

Instrumentation of the Säntis Tower for Lightning Current Measurement

THÈSE N° 5578 (2012)

PRÉSENTÉE LE 7 DECEMBRE 2012

À LA FACULTÉ DES SCIENCES ET TECHNIQUES DE L'INGÉNIEUR
LABORATOIRE DE RÉSEAUX ÉLECTRIQUES
PROGRAMME DOCTORAL EN GÉNIE ÉLECTRIQUE

ÉCOLE POLYTECHNIQUE FÉDÉRALE DE LAUSANNE

POUR L'OBTENTION DU GRADE DE DOCTEUR ÈS SCIENCES

PAR

Carlos Alberto ROMERO ROMERO

acceptée sur proposition du jury:

Dr S.-R. Cherkaoui, président du jury
Prof. F. Rachidi-Haeri, directeur de thèse
Prof. C. A. Nucci, rapporteur
Prof. M. Paolone, rapporteur
Prof. M. Rubinstein, rapporteur



ÉCOLE POLYTECHNIQUE
FÉDÉRALE DE LAUSANNE

Suisse
2012

To Nora

Résumé

La conception et la construction d'une nouvelle station expérimentale pour mesurer des courants de foudre sont l'objet de cette thèse. Un équipement avancé et moderne avec un système de contrôle à distance pour des mesures précises des paramètres du courant de la foudre a été utilisé pour l'instrumentation de la station Sântis.

La phénoménologie et la classification de décharges orageuses sont présentées au chapitre 2. Une vue d'ensemble des différents types de décharges, ainsi que leurs signatures typiques en matière de forme d'ondes de courant y sont décrits. Des mesures de courant de foudre obtenues à l'aide de différentes techniques sont également récapitulées. Un accent est mis sur le fait que, malgré un effort important pour obtenir des données expérimentales sur les courants de foudre en utilisant différentes techniques, le nombre de données disponibles reste limité et plus de données sont nécessaires pour mieux comprendre la physique de la foudre et mieux caractériser les paramètres du courant de foudre associés aux différents types de décharges de foudre entre nuage et sol.

Le chapitre 3 présente les caractéristiques d'un système dûment développé pour mesurer des formes d'onde de courant de foudre sur la tour Sântis en Suisse. Le système a été conçu en prenant en considération les contraintes CEM utilisant des fibres optiques comme infrastructure pour la transmission de signaux mesurés en soignant spécialement la conception du câblage, les boîtes de mesures, les systèmes de protection et le blindage. De plus, en raison des conditions extrêmes à l'intérieur de la tour, dans laquelle les températures varient de -15°C à $+35^{\circ}\text{C}$, un système comprenant un chauffage, un ventilateur, voies de ventilation de l'humidité et du matériel d'isolation thermique a été conçu pour maintenir la température dans des limites acceptables pour les composants et éviter de la condensation à l'intérieur des cartes imprimées.

Afin de surmonter la réponse limitée en haute fréquence des bobines de Rogowski, nous proposons de les combiner avec un capteur B-dot d'un design amélioré qui n'a pas les défauts des boucles conventionnelles. Le capteur conçu se caractérise par une fréquence de coupure supérieure de 20 MHz et une terminaison adapté de 50 Ohm.

Des tests des laboratoires effectués au laboratoire de compatibilité électromagnétique de l'EPFL démontrent l'efficacité de l'utilisation combinée de bobines de Rogowski et de capteurs B-Dot pour la mesure de courants de foudre.

Le système de mesure permet un entretien, un suivi et un contrôle à distance par internet. Le statut de chaque paire de capteurs en particulier est suivi et contrôlé à travers un système conçu et construit avec des modules National Instruments Compact-RIO reliés par un Ethernet 100Base-FX qui utilise des fibres optiques comme moyen de transmission.

Un logiciel d'analyse de données (SENDIS) a été développé pour analyser les données obtenues, pour extraire les paramètres statistiques et pour permettre le suivi, le contrôle et la programmation à distance des différentes composantes. Les algorithmes intégrés dans SENDIS permettent la détection de composants de courant (arc en retour, composants-M, courants continues) au sein de chaque éclair et l'extraction automatique des paramètres statistiques du signal de courant.

Au chapitre 4, nous présentons des distributions statistiques des paramètres de courant de foudre basées sur les formes d'ondes de courant des dérivées de courant mesurés sur le site de la tour Säntis en 2010 et 2011. 167 éclairs dont 2000 impulsions au total ont été analysés dans cette étude, constituant le plus grand ensemble de données au monde. Les distributions statistiques présentées dans ce chapitre sont associées avec des éclairs négatifs ascendants. Les données obtenues révèlent que nombre d'éclairs se caractérisent par une grande quantité de charge transférée (en excès de 50 C). Nous avons trouvé que la valeur médiane de la multiplicité d'éclair ou le nombre d'impulsions par éclairs s'élève à 8, une valeur nettement supérieure à celles associées aux éclairs descendants. D'une façon intéressante, 6 éclairs présentaient un nombre d'impulsions en excès de 40.

Le chapitre 5 contient une analyse de mesures de formes d'ondes de courant associées à des éclairs positifs et bipolaires enregistrés à la tour Säntis entre mai 2010 et janvier 2012. Le nombre total d'éclairs positifs enregistrés lors de la période en question s'élève à 30, alors que 3 éclairs ont été classifiés comme bipolaires. Nous avons trouvé un pourcentage d'éclairs

positifs (15%) nettement supérieur aux valeurs observées dans d'autres études durant les mois d'été (3% à 6.5%). Les dérivées temporelles des impulsions de courant associées à des traceurs par pas ascendants sont nettement supérieures à celles de l'impulsion principale. Les données que nous avons récoltées constituent la première preuve directement mesurée de composantes M des deux polarités pendant un courant de continuation transportant une charge positive au sol.

Les éclairs positifs observés se caractérisent par un pic médian de courant de 11.8 kA et une durée d'éclair médiane de 80 ms. Ces valeurs sont consistantes avec celles associées avec les données enregistrées à la tour Gaisberg en Autriche. D'un autre côté, la quantité de charge transférée est substantiellement supérieure dans notre ensemble de données avec une valeur médiane de 169 C (6 fois plus important que les valeurs obtenues à Monte San Salvatore et au Japon, et 3 fois plus important que les valeurs obtenues en Autriche).

8 éclairs sur 30 ont transporté une charge positive au sol en excès de 500 C. Les résultats obtenus confirment également les résultats de Saba et de ses collaborateurs selon lesquels les éclairs positifs peuvent combiner des pics élevés de courant avec des transferts de charge élevée (ou durée d'éclairs).

Dans le même chapitre, nous analysons trois éclairs bipolaires enregistrés durant la période étudiée pendant l'orage du 27 août 2011.

Au chapitre 6, nous présentons une évaluation de la performance du réseau européen de localisation de la foudre (EUCLID) utilisant les données de courant de foudre récoltées à la tour Sântis. L'efficacité de détection d'éclairs est estimée à 93% et l'erreur médiane de localisation est de 123 m. Les estimations de pics de courant d'EUCLID sont en moyenne supérieures au courant mesuré avec une erreur d'estimation médiane de pic de courant d'environ 60% pour des coups de plus de 10 kA.

Les mesures incluent 5 éclairs positifs typiques détectés avec succès par EUCLID. Les erreurs de localisation d'événements positifs vont de 1 à 3 km, avec une médiane de 960 m.

Liste de mots-clés:

Foudre, Champ électromagnétique, Tours élevées, Courants de canal-base, Tours Instrumentées, Décharges Orageuses Ascendantes, Eclairs Positifs, Eclairs Négatifs, Systèmes de Localisation de la foudre.

Abstract

In this thesis, a new experimental station was designed and built for the measurement of lightning currents. The station (Säntis Tower) was instrumented using advanced and modern equipment with remote monitoring for an accurate measurement of lightning current parameters.

In Chapter 2, we present the phenomenology and classification of lightning discharges. An overview of different types of discharges is given and their typical signatures in terms of current waveform were described. Lightning current measurements obtained using different techniques are also summarized. It is emphasized that, despite the important effort in obtaining experimental data on lightning currents using different techniques, the number of available data is still limited and more data are needed to better understand the physics of lightning and to better characterize the lightning current parameters associated with different types of cloud-to-ground lightning discharges.

Chapter 3 presents the characteristics of a system suitably developed to measure lightning current waveforms on the Säntis Tower in Switzerland. The system was designed considering the EMC constraints, using fiber optics as backbone for transmission of the measured signals and paying special attention to the design of the cabling, measurement boxes, protection systems and shielding. In addition, due to the harsh conditions inside the tower, where the temperature ranges from -15°C to $+35^{\circ}\text{C}$, a system comprising a heater, a ventilator, moisture exhaust holes, and a thermal insulation material was designed to keep the temperature within acceptable limits for the components and to avoid condensation inside the PCB cards.

In order to overcome the limited high frequency response of the Rogowski coils, we propose to combine them with an improved design of a B-dot sensor which does not have the

shortcomings of conventional loops. The designed sensor is characterized by an upper frequency cutoff of 20 MHz and a 50 Ohm matched termination.

Laboratory tests carried out in the high voltage laboratory of the EPFL show the effectiveness of the joint use of Rogowski coils and B-Dot sensors for the measurement of lightning currents.

The measurement system allows an over-the-Internet remote maintenance, monitoring and control overall system. In particular, the status of each pair of sensors is monitored and controlled by means of a system designed, and built, using National Instruments CompactRIO modules linked via 100Base-FX Ethernet, which uses fiber optics as a transmission medium.

A data analysis software (SENDIS) was developed to analyze the obtained data, to extract statistical parameters and to allow the remote monitoring, control and programming of the different components. Algorithms implemented in SENDIS allow the detection of current components (return stroke, M-component, continuous and continuing currents) within each flash and the automatic extraction of statistical parameters of the current.

In Chapter 4, we present statistical distributions of the lightning current parameters based on the lightning current and current-derivative waveforms measured at the Säntis Tower site in 2010 and 2011. The total number of flashes analyzed in this study was 167 which include nearly 2000 pulses, constituting the largest worldwide dataset. The statistical distributions are associated with upward negative flashes. The obtained data reveal that many flashes are characterized by a large amount of charge transfers (in excess of 50 C). The median value of the flash multiplicity or the number of pulses per flash was found to be 8, a value much larger than those associated with downward flashes. Interestingly, 6 flashes exhibited a number of pulses in excess of 40.

Chapter 5 presents an analysis of measured current waveforms associated with positive and bipolar flashes recorded on the Säntis tower from May 2010 till January 2012. The overall number of recorded positive flashes in the considered period was 30, while 3 flashes were classified as bipolar. The percentage of positive flashes (15%) was found to be considerably larger than the values observed in other studies in summer months (3% to 6.5%). The time-derivatives of the current pulses associated with upward stepped leaders are found to be much larger than those of the main pulse. Our recorded data constitute the first directly-measured evidence of M-components of both polarities during a continuing current lowering positive charge to ground.

The observed positive flashes are characterized by a median peak current of 11.8 kA, and a median flash duration of 80 ms. These values are consistent with those associated with the data recorded at the Gaisberg Tower in Austria. On the other hand, the amount of transferred charge was substantially larger in our dataset, with a median value of 169 C (6 times as large as the values obtained in Monte San Salvatore and in Japan, and 3 times as large as the value obtained in Austria). Eight flashes out of 30 transported positive charge to the ground in excess of 500 C. The obtained results confirm also the findings of Saba and co-workers according to which positive lightning flashes may combine high peak currents with high charge transfers (or flash durations).

In the same chapter, we analyze three bipolar flashes recorded during the considered time period which occurred during one storm on August 27, 2011.

In Chapter 6, we present an evaluation of the performance of the European Lightning Location Network (EUCLID) using the obtained data on lightning current measured on the Säntis Tower. The flash detection efficiency was estimated to be 93% and the median location error was 123 m. The EUCLID peak current estimates were on average larger than the measured current with a median peak current estimation error of about 60% for strokes over 10 kA. Measurements included five typical positive flashes successfully detected by EUCLID. The location errors for the positive events ranged from 1 to 3 km, with a median of 960 m.

Finally, in the Appendix, we present a thorough analysis of the noise source and characteristics affecting the measured signals at Säntis. We also describe appropriate signal processing methods, which are adopted and implemented to post-process the measured signals. The Appendix contains also a description of the data analysis software which was developed in the framework of this thesis to analyze the obtained data and to extract statistical parameters.

List of keywords:

Lightning, Electromagnetic Fields, Tall Towers, Channel-base currents, Instrumented Towers, upward flashes, downward flashes, positive flashes, negative flashes, lightning location systems

Acknowledgments

I would like to deeply thank the persons and organizations that made possible the development of the Sântis project. People that working with love and passion make dreams come true.

On the first place Professor Dr Farhad Rachidi who is the sum of many virtues in one human being. Outstanding researcher and eminent scientist, he kindly gave me his trust to develop the project and help me in every single step. Through these years Prof. Rachidi helped me to grow, always encouraging me while tolerating my complexities. Merci mon cher professeur.

To Professor Dr Mario Paolone, the non-stopping creator of ideas, intelligence, hard work and infinite kindness. A big thank you from my heart. When the problems came and we need a clear mind to orientate the technical and scientific issues Prof. Paolone always had the right response at the right time, even late at night, Sundays or any possible unconventional day.

I would like to express my sincere gratitude to Professor Dr. Marcos Rubinstein, an outstanding scientist that along with Prof. Rachidi conceived the Sântis project and who accepted me from the first time. Prof. Rubinstein offered to the project his limitless source of electromagnetic and lightning theory, ideas and kindness with me, his friendship and advices helped me passing all the required stages.

I would like to express all my gratitude to Dr. Felix Vega whose friendship and deep intelligence has illuminated my life for many years, to Nicolas Mora for being the available friend and electromagnetic handbook that I needed in many occasions, also to Prof. Dr.

Francisco Roman and Prof. José Ignacio Castañeda for their help and the precious opportunity to work and learn with you.

I thank also the opportunity to work with Prof. Dr. Abraham Rubinstein of the University of Applied Sciences of Western Switzerland, in Yverdon. The technical problems always were easier when discussing with a person of great talent and intelligence. I thank Abraham for his support and his friendship.

I am also grateful to Prof. Rachid Cherkaoui and Mme. Andrée Moinat always present to help in the hazardous and various situations of academics and life. Their collaboration and kindness made possible walking this path.

I would like to express my sincere gratitude to Dr. Pierre Zweiacker that helped through many stages of the experimental design and testing of the equipment.

Special thanks to for Bertrand Daout, Marc Sallin, Werner Hirschi and Fabrice Loup from Montena Technology who kindly supported the experiments and testing and always served as an advice in many stages of the project.

My warm gratitude to Prof. Carlo Alberto Nucci of the Department of Electrical Engineering of the University of Bologna, Italy, and Prof. Vladimir Rakov of the Department of Electrical and Computer Engineering of the University of Florida for their advices, contributions to the papers and kindness during the development of the data analysis and the conferences.

My sincere gratitude goes equally to Prof. Juan Ramon Mosig of the Laboratory of Electromagnetics and Acoustics (LEMA) of the EPFL for helping with material and ideas during this years.

Thanks a lot to Mr Eric Montandon (EMC Consulting, Worb, Switzerland) and Prof. Dr. Arturo Mediano for their help in the technical issues and development of the project and Dr. Armin Kaelin of Meteolabor for its help with the protection devices.

My sincere gratitude goes equally to Prof. Rajeev Thottappillil of the Ångström Laboratory of the University of Uppsala, Sweden, to Prof. Anja Skrivervik Favre of the Laboratory of Electromagnetics and Acoustics (LEMA) of the EPFL and Dr Markus Nyffeler From the Swiss Defense Procurement Agency (Armasuisse) in Spiez, Switzerland and to Dr José-Luis Bermudez and Dr William Chisholm of Kinectrics for the technical advices.

A Mr Jean-Paul Brugger, Mr Roland Dupuis and the personnel of the Atelier Mechanique of the EPFL for their support in realizing the mechanics and always available with the everyday problems of the experimental work.

My special gratitude to Dr Gerhard Diendorfer and Dr Wolfgang Schulz (ALDIS-OVE, Austria) and Marina Bernardi for your help, advices and providing the data that made possible some part of the work. To Prof. Vernon Cooray and Dr Liliana Arevalo (Ångström Laboratory, University of Uppsala, Sweden), Dr Fridolin Heidler (University of Federal Armed Forces, Munich, Germany), Prof. Joan Montanyà, (Universitat Politècnica de Catalunya, Terrassa, Spain), Prof. Silverio Visacro (Federal University of Minas Gerais, Brazil) and Prof. Alexandre Piantini (University of São Paulo, Brazil) for their participation in many papers, discussions and for your kindness during the conferences.

This work was financially supported by the Swiss National Science Foundation for Education and Research SER (Project No. C07.0037) and the Swiss National Science Foundation (Project No. 200021-122457) as well as the European COST Action P18.

Special thanks to the Iranian team Dr Abbas Mosaddeghi, Dr Hamid Shoory, Mehdi Mosaddeghi and Shahram Khazaei for their friendship.

Also would like to express my gratitude to my officemates Smorgonskiy Alexander and Omid Alizadeh Mousavi for your smiles, good mood and your continuous help.

A warm thank to Jean-Michel Buemi and Alejandro Salamanca that were always the helping hand with computers and life in general.

My sincere gratitude to my Farsi friends Ali Ahmadi Khatir, Amin Kaboli and Milad Daneshvari and also to Pirzadeh Bahareh for her Iranian language lessons and friendship

To my friends that always have been sharing good moments and many help on so many levels (listed without order) Mostafa Nick, Mokhtar Bozorg, Lazar Bizumic, Hossein Mahmoudimanesh, Reza Razzaghi, to the art of Lina Maria Hernandez, to my beloved friends Julian Quiroga, Diego Rincon and Leonel Meneses that came to visit and give moral support, to Dr Davide Pavanello for his scientific contributions, also special thanks to Paolo Romano and Diego Nicotra for their good advices on the Italian Lifestyle. And to Dr Ana Vukicevic, Simon Cottier, Maryam Bahramipanah, John Jairo Pantoja, Daniel Lopez, Dimitri Torregrossa, Francisco Santamaria, Anna Arestova, Jérôme Lovey, Mathilde Brocard, Ebru Karac, Sachiko Hirose, Daniel Burnier, Javier Serrano, Helin Zhou, Birgit Meyer, Roxanne Wuilloud, Dr Elvira Kaegi, Luis Panichelli, Eden Sorolla, Rolf Haubrichs, Dominique Zurcher, Théo Reichel, Jacques Falquet, Luis Díez Maroto, David Fernando Ariza, Dayana El Hage and Paola Cavadia.

To my wife Nora Kronig for her love for being my source and my root, and to my family Madeleine, Lea, Ilona, Mirza and Romain for being always there.

To my mother Gladys Romero and my father Hugo Romero, for their love and education, and to my cousin Ingrid Romero for their continuous support.

Table of Contents

- Résumé..... i
- Abstract v
- Acknowledgments..... ix
- Table of Contents xiii
- Chapter 1 Introduction..... 1
 - 1.1 Organization of the thesis 2
- Chapter 2. Lightning Current Measurements 5
 - 2.1 Introduction..... 5
 - 2.2 Lightning Phenomenology..... 6
 - 2.2.1 Cloud electrification and structure..... 6
 - 2.3 Breakdown Process 7
 - 2.4 Lightning Classification 7
 - 2.4.1 Classification based on discharge path 7
 - 2.4.2 Classification of CG and GC lightning based on transported charge..... 9
 - 2.5 Tower Effects..... 11
 - 2.6 Lightning Parameters Measurement and Estimation 12
 - 2.7 Instrumented Towers 12
 - 2.8 Triggered Lightning..... 14
 - 2.9 Lightning Location Systems 15
 - 2.10 Conclusion 16
- Chapter 3. Measurement System Design, Installation and Testing 17
 - 3.1 Introduction..... 17
 - 3.2 Selection of the Measurement Site: Analysis of Lightning Flash Density 18
 - 3.3 Säntis Tower 20
 - 3.4 Current Measurement Equipment 22

3.4.1	Rogowski Coils	23
3.4.2	Magnetic Derivative (B-Dot) sensor	25
3.5	Overall Measurement System Description	26
3.5.1	Measurement Boxes.....	27
3.5.2	Digitizers	31
3.5.3	Remote maintenance, monitoring and control system	32
3.6	Overall System Testing	33
3.6.1	Rogowski coils	33
3.6.2	B-Dot sensors calibration	34
3.7	System Installation	36
3.8	Data Analysis Software.....	40
3.9	Conclusions.....	40
Chapter 4.	Statistics of Negative Upward-Initiated Lightning to the Säntis Tower	41
4.1	Introduction.....	41
4.2	Lightning Current Parameters	42
4.3	Seasonal Flash Occurrence.....	42
4.4	Hourly Flash Occurrence	43
4.5	Statistics Calculation.....	45
4.5.1	Maximum Current Derivative.....	45
4.5.2	Peak Pulse Current	47
4.5.3	Current Risetime.....	48
4.5.4	Pulse Charge	53
4.5.5	Pulse Duration	55
4.5.6	Inter-pulse Interval.....	58
4.5.7	Total Flash Charge	59
4.5.8	Flash Multiplicity	62
4.6	Summary and Conclusions	63
Chapter 5.	Statistics of Positive and Bipolar Lightning Flashes Recorded on the Säntis Tower in 2010 and 2011.....	65
5.1	Introduction.....	65
5.2	Obtained Data	66
5.3	Classification of Current Waveforms Associated with Positive Flashes.....	68
5.3.1	Type I	68
5.3.2	Type II	71

5.4	Statistics of Positive Flashes	73
5.4.1	Peak Current	73
5.4.2	Total Transferred Charge.....	76
5.4.3	Flash Duration	78
5.4.4	Action Integral	80
5.4.5	Comparison with Observations at other Instrumented Towers	81
5.4.6	Bipolar Flashes.....	82
5.5	Conclusions.....	85
Chapter 6. An Evaluation of the Performance Characteristics of the European Lightning Location Network to Detect Upward Flashes Using Sántis Data		87
6.1	Introduction.....	87
6.2	Measurement Period.....	88
6.3	EUCLID Network	89
6.4	Flash Detection Efficiency	90
6.5	Location Accuracy.....	92
6.6	Peak Current Estimates	94
6.7	Conclusions.....	95
Conclusions and Perspectives		97
7.1	Summary	97
7.2	Original Contributions	101
7.3	Outlook and Future Work	102
References.....		105
Appendix: Signal Processing of the Sántis Measured Waveforms		117
8.1	Introduction.....	117
8.2	SENDIS Software for the Analysis, Post-Processing of the Sántis Data and Extraction of Statistical Parameters.....	117
8.3	Noise and Spectral Analysis.....	118
8.3.1	Example of measured data.....	118
8.3.2	Spectral Estimation.....	119
8.3.3	Non Parametrical Spectral Estimation	120
8.3.4	Definition of parameters	120
8.3.5	Parametrical Spectral Estimation	120
8.3.6	Spectral Leakage.....	121
8.3.7	Measurement Noise Types.....	122

8.3.8	Measurement System Signal Components	123
8.3.9	Quantification of Noise Using Spectral Analysis.....	123
8.3.10	Example 1: Synthetic White Noise Signals	124
8.3.11	Synthetic Pink Noise Signal.....	125
8.3.12	Example 2: Sinusoid plus Noise	125
8.3.13	Spectral Analysis of the Sántis Signals.....	126
8.3.14	Noise Characterization of the Sántis Signals	131
8.3.15	Loran-C Signals	134
8.3.16	Prony Method Spectral Estimation	135
8.3.17	Prony Signal Compression	137
8.4	Filtering.....	137
8.4.1	FIR.....	137
8.4.2	Zero-Phase Filtering.....	140
8.4.3	Amplitude Multiplication in ZPF	140
8.4.4	Transient Response of ZPF	143
8.4.5	Wavelet Analysis	143
8.4.6	Wavelet Power Spectrum.....	143
8.4.7	Wavelet Estimation of the Resonance Frequencies.....	145
8.4.8	Wavelet Filtering	147
8.4.9	Wavelet Baseline Detection (DC Removal)	148
8.5	Pulse Classification Algorithms.....	149
8.5.1	Stationarity Test	150
8.5.2	Semi-supervised Segmentation.....	150
8.5.3	Threshold Segmentation	151
8.5.4	Broken-Sticks Segmentation	152
8.6	Current Waveform Reconstruction	155
	References.....	158
	Curriculum Vitae.....	cv-i

Chapter 1

Introduction

Lightning influences our everyday life. This phenomenon feeds the global electric circuit, displacing charges on the atmosphere and interacting with ionosphere and magnetosphere electrical environment. Lightning is associated with planetary phenomena that shape life on the planet.

The study and understanding of lightning is important in areas that range from environment sciences to different engineering fields, on the side of either protection of large and small scale infrastructure (electrical, civil, telecommunications) against its harmful effects in form of direct and indirect coupling, or of its detection for meteorological purposes through lightning detection systems.

Currents and electromagnetic fields associated to lightning are an input to a significant number of calculations in the aforementioned engineering fields. The measurement of these variables along with their quantification in terms of lightning parameters help the scientific and engineering community to assess lightning effects and design effective protection systems.

One of the main difficulties in obtaining experimental data on lightning is that the probability of a natural lightning strike to a certain point is very low if this place has no distinctive features related to the surrounding environment. The observation of increased lightning frequency over tall metallic structures led researchers to instrument towers and buildings since the early 1920's.

Extensive experimental data recorded by Prof. Berger and his team on the top of two instrumented towers in Monte San Salvatore (Ticino) during 1950s and 1960s resulted in a complete statistical characterization of lightning current parameters, which are still considered to be the reference in lightning protection standards. However, the results obtained by Prof. Berger and his team suffered from the technological limitations of the instruments, in particular an insufficient frequency bandwidth of a few hundred kHz, despite the fact that the spectrum of lightning current exhibits significant frequencies up to a few MHz.

Recent experimental observations on tall telecommunication towers as well as theoretical analyses suggest, in addition, that the lightning current data obtained by means of instrumented towers might be affected by the presence of the tower itself. As a consequence, the adequacy of the statistical lightning current data, which are used extensively by researchers and engineers today has become questionable and there is an urgent need to obtain high-quality, directly-measured lightning data.

The mentioned considerations constitute the motivation for this thesis, the aim of which being to continue the pioneering work of Prof. Berger and build a new experimental station in Switzerland for the measurement of lightning currents, instrumented using advanced and modern equipment with remote monitoring for an accurate measurement of lightning current parameters.

1.1 Organization of the thesis

Chapter 2 presents an overview of lightning current measurements and constitutes the background of the thesis. The Chapter starts with a brief presentation of the phenomenology and classification of lightning discharges. An overview of different types of discharges is given and their typical signatures in terms of current waveforms are described. In the second part of the Chapter, a summary of lightning current measurements obtained using (i) instrumented towers, (ii) artificially-initiated lightning, and (iii) lightning location systems are presented.

Chapter 3 describes the measurement system design, installation and testing. First, an analysis of lightning flash density in Switzerland is presented, which revealed an exceptionally high lightning activity around the Säntis tower. Then, the designed equipment for the measurement of lightning current and its time-derivative are thoroughly described.

The description of the overall measurement system and its laboratory testing are also presented, as well as the installation of the equipment on the Sántis Tower.

Chapter 4 presents a statistical analysis of the obtained data for negative upward-initiated flashes measured at the Sántis tower. The period of analysis in our study extends from May 2010 to January 2012 during which a total number 167 negative flashes were recorded, including nearly 2000 pulses. The statistical analysis concern the seasonal and hourly flash occurrence, as well as the salient parameters of the lightning current, namely, maximum time derivative, peak current, pulse charge, duration and inter-pulse interval. The obtained data represents the largest dataset available in the literature for upward negative flashes.

Chapter 5 presents the statistics of positive and bipolar flashes recorded over the same period of analysis (May 2010 to January 2012). Among 201 flashes recorded during this period, 30 were of positive polarity (effectively transported positive charge to ground) and 3 were classified as bipolar. Even though positive lightning flashes are less frequent than negative ones, they are of particular interest for a number of reasons, most importantly because they are characterized by high peak currents and large impulse charges. As a result, they are a major concern for the designers of lightning protection systems of structures such as wind turbines and telecommunication towers.

Measurements of peak current, charge, duration and action integral for positive flashes are presented and discussed. A classification of current waveforms for positive flashes based on their signature is provided. The statistical data are put in context with other instrumented towers. The last part of the Chapter presents the measured bipolar flashes waveforms with their salient characteristics.

Chapter 6 presents the evaluation of the performance of the European Lightning Location Network (EUCLID) using the directly-measured lightning currents at the Sántis site. The basic aim of lightning location systems (LLS) is to provide density maps of lightning return strokes. However, more recently, LLS have also been used to estimate lightning current parameters. However, there is an inherent difficulty today in extracting lightning current parameters accurately from LLS data, since other unknown parameters – such as return stroke velocity – would affect the lightning current inferred from remote electromagnetic fields.

In the considered period of analysis (June 1st, 2010 to May 31st, 2011), 42 negative flashes were recorded on the Sántis Tower. From them, 37 could be correlated to EUCLID data by

comparison of the time-stamp provided by GPS time reference installed on the Sántis and the EUCLID time. The evaluation of the performance of EUCLID network in terms of detection efficiency, location accuracy and peak current estimates is presented and discussed.

In the **Appendix** of the thesis, we present a thorough analysis of the characteristics of the noise affecting the measured signals at Sántis. We also describe appropriate signal processing methods, which are adopted and implemented to post-process the measured signals. The Appendix contains also a description of the data analysis software which was developed in the framework of this thesis to analyze the obtained data and to extract statistical parameters. Finally, Summary and Conclusions along with perspective for future work are presented in **Chapter 7**.

Chapter 2.

Lightning Current Measurements

2.1 Introduction

The knowledge of the lightning current parameters is of primary importance for a number of reasons, in particular for a better understanding of the physics of the discharge, for evaluating its electromagnetic effects, for an effective protection design of electric and electronic systems and for the risk assessment related to lightning damages.

Lightning channel-base currents are obtained either by direct measurements using instrumented towers or from artificially initiated lightning by small rockets, or they can be estimated indirectly from the measurements of lightning electromagnetic fields.

Most of the models describing the electromagnetic field radiation by a lightning channel as well as those predicting the coupling of the radiated field to nearby transmission lines use as inputs measured direct lightning current waveforms or analytical representations of them, whose parameters come from statistical data obtained from tower measurements.

The aim of this Chapter is to present an overview of lightning current measurements obtained using the above-mentioned techniques. The Chapter starts first with a brief presentation of the phenomenology and classification of lightning discharges. An overview of different types of discharges is given and their typical signatures in terms of current waveform are described.

Then, in the second part of the Chapter, a summary of lightning current measurements obtained using (i) instrumented towers, (ii) artificially-initiated lightning, and (iii) lightning location systems are presented.

2.2 Lightning Phenomenology

2.2.1 Cloud electrification and structure

Among different clouds that could be electrified, cumulonimbus rain clouds are the main source of lightning phenomena (see e.g. [1, 2]), although in general, stratiform clouds ([1] pp. 91), covering territories hundreds of times larger than thunder clouds can, in some cases be highly charged [3] as shown during the 20 years studies and aircraft measurements of Imyanitov in Russia [4], studies that largely contributed to the understanding of cloud electrification process.

The charge separation, or cloud electrification [5] has been associated to phenomena of various origins, that range from microscale phenomena [6] to macroscale processes [7] or a combination of them ([5] Chapter 14 pp. 529).

Among the microscale phenomena are the precipitation theory involving collisions of hydrometeors in different phases [8], charge by induction, melting, freezing and capturing / releasing of free ions on charged aerosol particles [6]. Large scale phenomena are associated with phenomena of scales comparable to the cloud dipole, normally associated with air current convection transport of charge. Another large scale phenomena involves cosmic-ray particles that were shown to contribute to the electric field enhancement process [9], given the fact that multiple experiments (CLOUD experiment at CERN [10] and Russian Experiments at Moscow Central Aerological Observatory [11]) appear to confirm that cosmic rays are, if not the only, the main source of ion production in the lower atmosphere.

The net result of electrification is that an excess of charge develops and gets accumulated in different parts of the cloud, thus generating large electric fields and voltage gradients.

An excellent recent review of charging mechanisms can be found in [12] and some classic ones in [7, 13-15].

The cloud electrical distribution model is also still an object of research. In general the classical tripolar electric model (e.g. [1] pp. 86; [16]) provides a charge distribution compatible with various measurements campaigns and experiments (radar, ballooning, sounding) [17-19]. In this model, positive charges are located in the upper part of the cumulonimbus cloud, negative charges in the middle, and small pockets of positive charges in the cloud bottom, also called the p-regions. Recent studies suggest, however, that in some

cases the electrical structure of the thunderstorm cloud may be more complex than a dipole or a tripole, with reduced regions of alternate polarity in the cloud base [20-22].

It's important to underline that the cloud structure, geometry and thermodynamics are also dependent on the region topography and the relative earth position, as discussed by Krehbiel in ([23] Chap. 8) and confirmed in several studies [4, 24-26]. This fact makes difficult to generalize a single ideal cloud structure, and implies that these parameters might vary from site to another. Chapter 3 presents the salient characteristics of the Säntis site location and a later subsection in this chapter will briefly address this subject.

2.3 Breakdown Process

Prior to lightning discharge, the so-called preliminary breakdown marks the initiation of the process [27]. A gas discharge could be initiated when gas pressure and electric field exceed a threshold enough to start an electron avalanche and create a conductive channel or region. The most accepted theories for the breakdown are the emission of positive streamers from hydrometeors induced by high surrounding electric fields [27, 28] and the cosmic ray participation to runaway electron avalanches (the so-called runaway breakdown) [27, 29, 30]. Initial breakdown encompasses the formation of a single channel or a sequence of channels [31]. This can be distinguished as a train of microsecond-scale electric field pulses [31].

2.4 Lightning Classification

2.4.1 Classification based on discharge path

Lightning discharges can be classified in terms of their discharge paths: i) intracloud lightning, ii) inter-cloud or cloud-to-cloud lightning (CC), iii) cloud-to-ground (CG) and ground-to-cloud (GC) lightning, iv) cloud-to-air lightning, and, finally, iv) middle and upper atmospheric discharges [32].

Intracloud lightning (IC) is thought to account of the majority of the discharges [15]; it starts normally between the negative charge region and the main upper positive charge region of an electrified cloud. According to [33], leaders carrying negative charge propagate upward and horizontally into regions with positive charge, and positive leaders propagate downward and horizontally to regions with net negative charge. IC discharges are sometimes mixed with cloud-to-cloud discharges, but in general the latter has a larger spatial scale associated with mesoscale cloud systems [34].

Cloud-to-ground (CG) lightning is initiated when from a negative (or positive) charge region a downward stepped leader develops to progress from the cloud to the ground following the preliminary breakdown [1]. When the ionized channel approaches the ground, the electric field enhancement on protrusions generates one or several upward discharges called upward connecting leaders. When these two processes combine, an ionized channel is created and the deposited charge by the leader is neutralized by the return stroke travelling at a speed of about one third the speed of light. This sequence could be followed by a continuous current as evidenced by direct measurements using instrumented towers, characterized by a long lasting luminous segment on video observations [35] and with typical magnitudes of hundreds of amperes. A typical waveform associated with a downward negative flash is illustrated in Figure 2.2. After the connection of the stepped leader with the upward connecting discharge, the return stroke wavefront carries the ground potential up the stepped leader channel at a speed of typically one-third the speed of light. The negative charge deposited in the leader channel is lowered to ground through the highly conducting channel beneath the return stroke wavefront. This phase, the first return stroke, corresponds to a high amplitude current measured at ground level in the order of some tens of kAmps. The lightning flash may end after the return stroke current has ceased to flow. However, in most of the cases the flash may contain one or multiple subsequent strokes which occur after the propagation of downward dart leaders. The time between two successive pulses is typically some tens of ms during which we can have a zero-current interval or in some cases a continuing current with amplitudes of typically some hundreds of Amperes, sometimes with superimposed M-components (Rakov ([1] pp. 250).

A downward CG flash present a characteristic ramification pattern pointing to the earth, as photographed by many studies [36-39] whereas ground-to-cloud or upward-initiated lightning has characteristically an upward branching pattern [40]. Upward lightning is associated to tall grounded objects producing electric field enhancement on their tips, which can be high enough in some cases to generate upward positive or negative leaders that propagate from the ground to the cloud [41]. On the Säntis mast, a 124 m tall tower on top of a 2502 m ASL mountain which has been instrumented in the framework of the present thesis (see Chapter 3), most of the flashes are of upward type [42].

Extensive details of the electric field enhancement processes, the associated EM fields and the transmission line behavior of the tall structure from theory and experiments can be found in [43-46].

2.4.2 Classification of CG and GC lightning based on transported charge

Lightning discharges to the ground can also be classified depending on the polarity of the charge transferred to the ground, either positive, negative, or bipolar.

Positive lightning is generally associated with large currents, hundreds of millisecond scales and substantial charge transfers to ground, fact that marks the importance of their study for the design of protection systems for structures such as wind turbines. On the Sántis tower (see Chapter 3), charge transfers up to 1000 C for positive flashes have been recorded, which are comparable to large charge transfers presented by Miyake [47], Zhou [42] and reviewed by Nag and Rakov [48]. It has been observed that positive lightning is generally associated to cold seasons [49]. Another issue of positive flashes is related to its relatively slow risetime which, in general, produce a lesser distinctive electromagnetic footprint compared with fast and high current negative pulses, thus making difficult to discriminate this type of discharge by lightning location systems, which tend to misclassify them with intra-cloud discharges (e.g. [49, 50]).

Reported positive flashes in the literature are composed mainly by a single main event, in many cases with several superimposed M-component pulses and long continuing currents (CC). Continuing currents have also been measured, indirectly, using high speed cameras by Saba [51]. In [52] we propose a classification of the positive flashes according to their time domain characteristics. A typical upward positive waveform is presented in Figure 2.1.

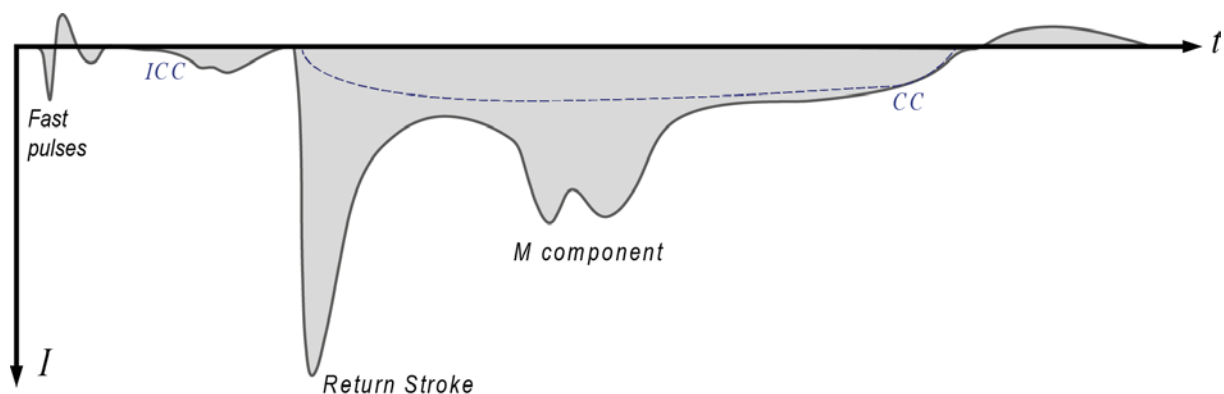


Figure 2.1. Typical current waveform associated with upward positive flashes. The duration of the waveform is typically some tens to some hundreds of milliseconds.

A reversal in the polarity of lightning current characterizes bipolar lightning. Different authors (e.g. [25, 49]) cite as probable origin for bipolar flashes currents of both polarities following a same channel to ground, but from different and oppositely charged regions in the cloud. In [49], Rakov classifies the bipolar discharges into 3 categories:

(1) Type one is associated with a polarity reversal during a slowly-varying (millisecond-scale) current component. The polarity reversal may occur one or more times and may involve an appreciable no-current interval between opposite polarity portions of the waveform.

(2) Type two of bipolar discharges is characterized by different polarities of the initial stage current and of the following return stroke or strokes.

(3) The third type of bipolar discharges involves return strokes of opposite polarity. Our measurements appear to be consistent with bipolar lightning statistics from other instrumented towers: 1.5% (3/201) of the total number of flashes at Säntis, 3% in Austria [53] and 6% in Monte San Salvatore [54].

As mentioned earlier, negative cloud-to-ground lightning is generally composed of multiple leader and return stroke sequences. The strokes are characterized by fast risetimes in the order of μs , amplitudes in order of a few tens of kA and durations of about 100 μs , thus transferring charges in the order of few Coulombs to tens of Coulombs at most.

The number of strokes per flash is generally called stroke multiplicity. The reported mean values reported in the literature range between 3 to 7 (e.g. [55, 56] [57] [37, 58]).

The current waveform signature of a typical upward negative flash is schematically illustrated in Figure 2.3. The current waveform starts with an initial continuous current (ICC), to which fast pulses and M-components can be superimposed. After the extinction of the ICC, sequences of downward leader / return strokes similar to downward flashes can occur. A continuing current with superimposed M-component pulses could also be present in between two consecutive strokes or at the end of the flash [59] [60]. Discussion on the differentiation between return stroke (RS) pulses and M components can be found in [61, 62].

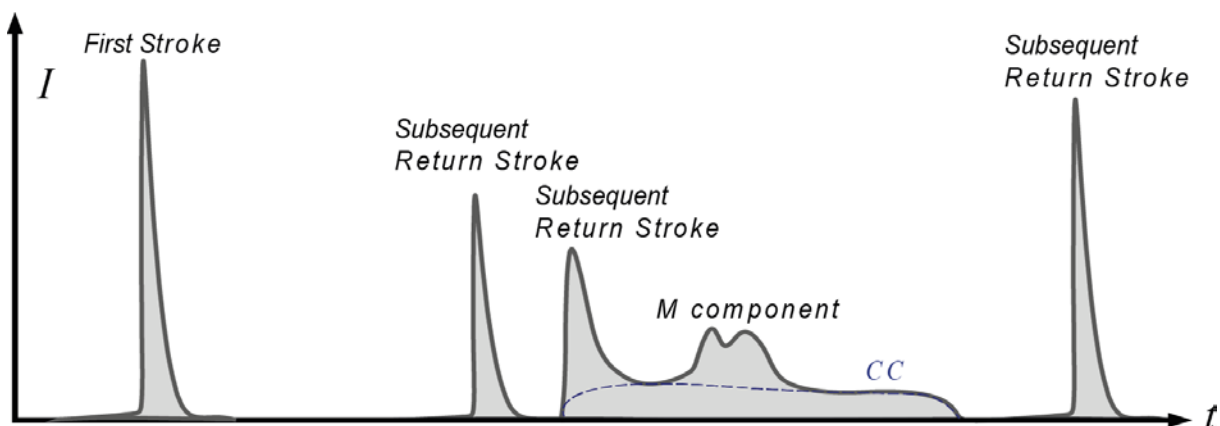


Figure 2.2. Typical current waveform associated with downward negative flashes.

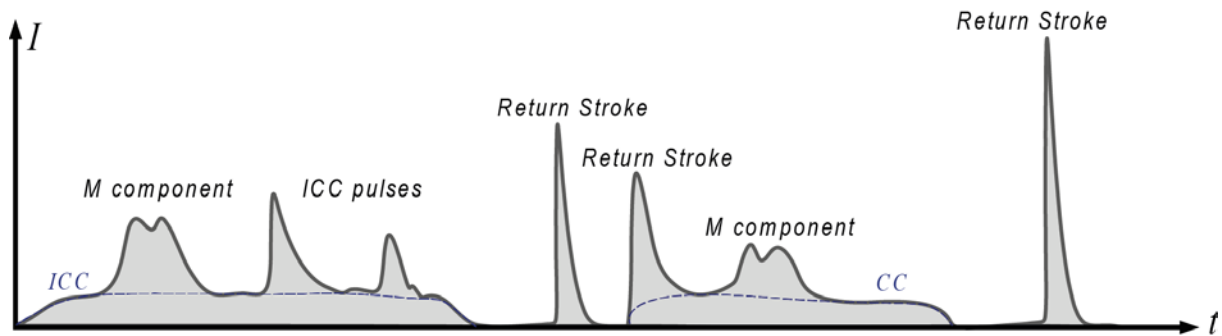


Figure 2.3. Typical current waveform associated with upward negative flashes.

2.5 Tower Effects

The presence of a tall tower has a tendency to increase substantially the local electric field magnitude and thus the probability that a downward stepped leader will terminate on the object ([1] pp. 50); this is essentially due to the fact that upward moving connecting leaders start earlier than from the surrounding ground [63]. Authors since Golde [64] realized that this enhancement of the electric fields decreases the critical ambient electric field necessary for inducing the inception of an upward leader. Objects of small or moderate heights (inferior to about 100 m) experience downward flashes, while tall structures of 100 m or taller, or moderate objects located on mountaintops experience essentially upward flashes (e.g. [46, 65, 66]).

Mountain height influences inversely the critical inception electric field. A discussion on this issue and the effect of space charge can be found in e.g. [67] or [68]). The concept of effective height is introduced to account for the enhancement of the electric field, caused by the presence of the mountain and the tower [65, 69]. Smorgonskiy et al. [70] have presented a method to evaluate the number of upward flashes initiated by a structure in a given geographical location.

Theoretical studies and experimental observations using tall towers have shown that measured currents along a tall structure might be affected by transient processes (e.g. [71]). Often, the tower has been included in the return stroke models in terms of a uniform transmission line [46, 71, 72] [73, 74]. An important question is to determine to which extent the lightning parameters might be affected by the tower transient processes and how to proceed to the decontamination of the measured waveform. For structure heights of about 100 m or less, such transient effects are supposed to be negligible, for typical lightning currents (e.g. [71]).

Chang [75] using data from CN tower points on the influence of tall towers on discharge polarity, but the results are not conclusive.

2.6 Lightning Parameters Measurement and Estimation

Three approaches can be used to obtain data on lightning currents:

- (1) Direct measurements using instrumented towers (e.g. [76-81]),
- (2) Direct measurements using the technique of artificial initiation of lightning (e.g. [82-84], and,
- (3) Indirect estimation of lightning current parameters from remote measurements of lightning electromagnetic fields assuming empirical (e.g. [85, 86]) or theoretical [87, 88]) relations between the lightning current and its associated electromagnetic fields.

2.7 Instrumented Towers

Given the low probability of measuring a direct current on a random point over the earth surface, and the fact that elevated grounded objects increase locally the electric field thus favoring the creation of upward leaders that effectively increase the probability of the creation of a channel [67], the idea of instrumenting those elevated objects provides a good way of measuring channel base currents. Another utility of instrumented towers is the calibration of LLS [50, 89] in terms of their detection efficiency, location accuracy, and peak current estimate.

Monte San Salvatore installation started in 1943 [90] when the Swiss High-voltage Research Committee in head of Dr. Karl Berger decided to initiate research activities on lightning on the mountain installing a masts of 70 m including the lightning rod and later a second mast of the same height in 1950 [91]. The two towers were separated 400 m but the second tower top was 47m lower than first tower [91]. Monte San Salvatore (45°58'37"N, 8°56'50"E) is 915 m ASL and 640 m over the Lake Lugano level on the southern border of the Alps where thunderstorm and rain clouds come from the Mediterranean [91]. Lightning currents were measured by means of a shunt below the needle of each tower. The reported median current values for downward negative first strokes was 30 kA for a total of 101 flashes, for downward negative subsequent strokes was 12 kA for 135 flashes [76]. It is likely that the values of the front duration and current derivative in Berger's data were affected to some extent by the

limited bandwidth of the used equipment [92]. This fact could also have affected, to a lesser degree, peak current values.

Morro do Cachimbo [93] station was instrumented in 1985 at 15 km of Belo Horizonte at 1.430m ASL (43°58'W, 20°00'S). The mast is a 60-m tall metallic structure. The station is 200 taller than the closest high point. Current measurements are performed via two current transformers of 25 V/kA and 5 V/kA at the base of the mast. There is a gap with a breakdown value of 10 kA that short circuits the shunt of small value for currents higher than its rating (see [93] Figure 3). Authors report values of 100 Hz and 10 MHz for the low and high cutoff frequencies of the current transformers. About 157 strokes were recorded during 13 years of operation. Visacro et al. ([93] pp. 4) report 33 video records of downward discharges, including 31 negative downward flashes and 2 positive flashes. The reported median negative current for first strokes is 46 kA and for subsequent strokes 16 kA (Table 2 and Table 4 of [93]).

The CN Tower is a 553 m mast in the city of Toronto, Canada (43°38'33"N 79°23'14"W). Lightning at CN Tower measurement station was observed since 1978. The instrumentation for measuring currents and fields was completed in 1991 [94, 95]. In 1997, the tower was updated with current derivative measuring system. The instrumentation consists of 3 m and 6 m long Rogowski coils, a fiber link, two magnetic field sensors, one electric field sensor, two video cameras and one high speed camera. The 3-m coil was installed at 474 m in a metallic structure that surrounded one fifth of the total metal mast, this coil was connected via a triax cable to the digitizer situated at 372 m. Authors report high noise coming from this arrangement (DC offset and high frequency) and a noise removal algorithm had to be implemented to clean-up the signals. The 6-m coil was installed at 500 m level and encircles the whole mast. This coil was connected to the digitizer via a fiber optic link. Their reported specifications of bandwidth and sensitivity for the 3-m coil are 40 MHz and 0.351 V/(A/ns). The 6-m Rogowski has the same reported 20 MHz bandwidth and a sensitivity of 1.19 V/(A/ns). The vertical resolution of the digitizers was 10 bits and the sample rate 100 MSPS with 128 kB / channel. Hussein [96] report that during 1992-2002 the number of flashes was 111. The reported median current for negative flashes (essentially of upward type) was 5 kA. The Gaisberg tower, a 100-m tall tower at 1287 m ASL close to Salzburg, Austria was instrumented since 1998. 457 upward initiated negative flashes were reported and analyzed in [81], and later 652 flashes were reported in [42]. The measurements were obtained with a shunt installed at 100 m with a bandwidth extending from DC to 3.2 MHz. In 2009, the

equipment were updated with fiber optic links (Nicolet ISOBE from DC to 15MHz) and 20 MS/s, 8 bit digitizers as reported in [42].

Another instrumented tower is the Ostankino tower ($55^{\circ}49'11''\text{N}$, $37^{\circ}36'42''\text{E}$) in Moscow. The tower is 540 m tall on which measuring sensors were installed at 533, 272 and 47 m [92]. In [97] the reported number of measured negative flashes were 58 at 533 m and 76 at 47 m. 6.7% (6/90) of the total flashes were bipolar [53]. Peak currents measured in the lower part of Ostankino tower were shown to be about a factor of two higher than the peak currents measured near the tower top (median peak currents at 47 and 533 m were 18 and 9 kA, respectively) [97].

First instrumented in 1978 and decommissioned in 1999, the Peissenberg tower [98] ($47^{\circ}48'08''\text{N}$, $11^{\circ}00'37''\text{E}$) is a 168-m tall mast located near Munich, Germany, at 950 m ASL and 250 m higher than surrounding ground. The tower was instrumented at two locations: (1) a current shunt with a bandwidth from 0.15 Hz up to 200 kHz and a current derivative sensor, located near the tower top; (2) A current sensor with a bandwidth from 100 Hz to 22 MHz and a current derivative sensor at 5 m. Fuchs [98] report 118 measured flashes between 1992 and 1998.

Other installations include the 200-m high Fukui tower in Japan [92], operational between 1989-2002, and measuring 18 positive flashes, 148 negatives and 47 bipolar [55]. A 40-m tall television tower in Italy instrumented in the 1970s by Delleria and Garbagnati measuring 42 downward negative flashes with a median first return stroke current of 33 kA and subsequent return stroke median current of 18 kA [77], and St. Chrischona tower in Switzerland, instrumented by E. Montandon commissioned by the Swiss PTT (Post, Telegram, Telegraph) company [99].

2.8 Triggered Lightning

Lightning can be artificially initiated using grounded rockets that when launched from the soil to a few hundred meters can produce a field enhancement on its tip enough to trigger a discharge via the creation of an upward positive leader that vaporizes a grounded rocket wire and bridges the gap between the cloud and ground [100]. The resulting leader/RS sequences are similar to those found in natural downward lightning with the difference that there is no natural first return stroke as described in [1]. Rocket triggering experiences, when done in favorable conditions, i.e. presence of cumulonimbus and ground static electric fields in the

order of -5 kV/m or lower (e.g. [101, 102]) are characterized by a high rate of success and provide with valuable simultaneous sets of experimental data which are useful to better understand the lightning phenomena.

It should be noted that (e.g. [103] [104] [92]) that triggered lightning has been reported to likely exhibit a larger number of strokes per flash, a higher dart leader velocity, and a shorter inter-stroke interval duration.

Triggered lightning experiences have been carried out in Florida [105-107], China [108, 109], Brazil [110], France [111, 112] and Japan [113] and [114].

2.9 Lightning Location Systems

Lightning locations system (LLS) networks like the NLDN in North America, and EUCLID in Europe, with hundreds of sensors detecting electric and magnetic fields represent an enormous potential for learning about lightning phenomena [92]. The basic aim of such systems is to provide density maps of lightning return strokes. However, more recently, LLS have also been used to estimate lightning current parameters. Because of the enormous amount of data they can provide and the possibility of offering local statistical data, it can be expected that LLS will become more and more important in the near future. However, there is an inherent difficulty today in extracting lightning current parameters accurately from LLS data, since other unknown parameters – such as return stroke velocity – would affect the lightning current inferred from remote electromagnetic fields. Despite of the variability of parameters such as the return stroke speed, Rachidi et al. [88] have shown that, for an assumed return-stroke model, the statistical estimation of the current is possible. They also show that for the transmission line (TL) model representing the return stroke, the equation permitting to infer the mean value of the return-stroke current from the mean value of electric or magnetic field and the mean value of speed has the same functional form as the well-known TL current—far field relationship. This result gives to some extent a theoretical justification to the use of lightning location systems to infer parameters of lightning current statistical distributions from measured fields alone [88].

Another important parameter that affects the relation between far radiated fields and return stroke currents is the propagation along a finitely conducting ground. As an example, the Austrian Lightning Detection System applies since 2001 a simplified compensation model to accounting for the propagation over a finite conductivity ground [115, 116].

Finally, another issue that hampers the use of LLS for estimating lightning current parameters is technological: most importantly the bandwidth of the electromagnetic field sensors, but also parameters (S parameters, VSWR) of the analog circuitry, temporal synchronization of the stations, and the vertical resolution of the digitizers.

2.10 Conclusion

The lightning current data gathered by Prof. Berger's team in Monte San Salvatore resulted in a complete statistical characterization of lightning current parameters. As mentioned earlier, however, the results were obtained with instruments with a frequency bandwidth of a few hundred kHz, an order of magnitude lower than the spectrum of the lightning current. Despite the important effort in obtaining experimental data on lightning currents using different techniques, the number of available data is still limited and more data are needed (i) to better understand the physics of lightning and the mechanisms at play for different types of discharges, (ii) to better characterize the lightning current parameters associated with different types of cloud-to-ground lightning discharges.

The objective of the present research project is to continue the pioneering work of Prof. Berger and build a new experimental station for the measurement of lightning currents, equipped with advanced and modern equipment with remote monitoring for an accurate measurement of lightning current parameters. For this purpose, the Säntis tower was found to be a unique structure to collect experimental information related to the lightning discharge. Thorough investigations on several towers located in different places in Switzerland resulted in the choice of the Säntis tower. The process of the site selection, the tower characteristics, and the design, construction and testing of the instrumentation and the deployment of the equipment on the tower will be presented in Chapter 3.

Chapter 3. Measurement System Design, Installation and Testing

3.1 Introduction

As discussed in Chapter 2, three approaches can be used to obtain data on lightning currents:

- (1) direct measurements using instrumented towers (e.g. [76, 78-81, 88, 117-119]),
- (2) direct measurements using the technique of artificial initiation of lightning by small rockets (e.g. [82, 84, 120]), and,
- (3) indirect estimation of lightning current parameters from remote measurements of lightning electromagnetic fields assuming empirical [86, 121] or theoretical [87, 88] relations between the lightning current and its associated electromagnetic fields.

Although each of the above-listed approaches have specific benefits and drawbacks, the statistical distributions of lightning current parameters are essentially based on experimental data obtained by means of instrumented towers.

The most complete description of lightning currents is due to Berger et al. [76] who used resistive shunts to measure natural lightning currents at the top of two 55-m tall towers located on Monte San Salvatore, in southern Switzerland. More recently, lightning current

and current derivative measurements have been obtained at the top of tall telecommunication towers (e.g., Austria [122], Germany [78], Switzerland [123], and Canada [117]).

A preliminary study on the analysis of lightning activity in several sites around tall structures¹ revealed an exceptionally high lightning activity around the Säntis tower located on the top of the Mount Säntis in the Appenzell region (Northeast Switzerland).

This chapter details the process of the site selection, describes the tower characteristics, presents the design, construction and testing of the instrumentation and the deployment of the equipment on the tower. The chapter is organized as follows.

Section 3.2 presents an analysis of lightning flash density in Switzerland, which resulted in the selection of the Säntis Tower, the characteristics of which is presented in Section 3.3. Section 3.4 describes the designed equipment for the measurement of lightning current and its time-derivative. The description of the overall measurement system and its laboratory testing are presented respectively in Sections 3.5 and 3.6. The installation of the equipment on the Säntis Tower is presented in Section 3.7. Finally, conclusions are given in Section 3.8.

3.2 Selection of the Measurement Site: Analysis of Lightning Flash Density

The selection of the Säntis Tower site followed an analysis of several candidate sites located in various Switzerland regions from which four of them four with high flash density are presented. Figure 3.1 shows the location of four of the studied tower sites, namely: Batinger Mountain (46.9792N, 7.52917E), Uetliberg Mountain (47.3525N, 8.4907E), San Salvatore Mountain (45.9787N, 8.9479E) and Säntis Mountain. The data were obtained using the database of EUCLID lightning location network.

¹ The study included 6 towers located in various regions of Switzerland, namely Monte San Salvatore, Barillette, Mont Pèlerin, Jungfrau, Swisscom-EPFL and Säntis.

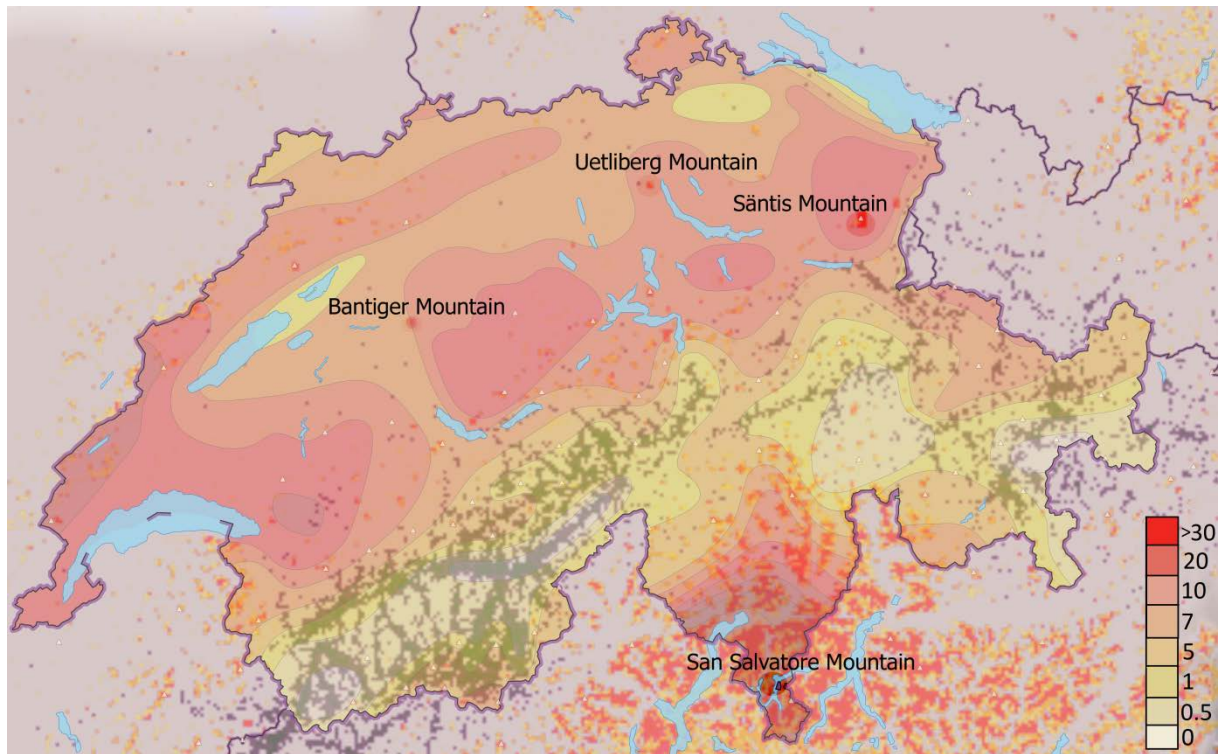


Figure 3.1. Annual ground flash density 1998-2008. Source Data: Federal Office of Meteorology and Climatology, MeteoSwiss Krähbühlstrasse 58, CH-8044 – Zürich

The mean annual ground flash density in Switzerland is shown on Figure 3.1. Notice that the main flash density is found over the Lemman plains, the Bern plains, the Ticino region and the Zürich region plains: places with significant contrast in relief (flat places with some relief).

The selection of the Sântis Tower site followed an analysis of several candidate sites located in various Switzerland regions from which four of them four with high flash density are presented in Figure 3.1, it is also shown the location of four of the studied tower sites, namely: Bantiger Mountain (46.9792N, 7.52917E), Uetliberg Mountain (47.3525N, 8.4907E), San Salvatore Mountain (45.9787N, 8.9479E) and Sântis Mountain. The data were obtained using the database of EUCLID lightning location network.

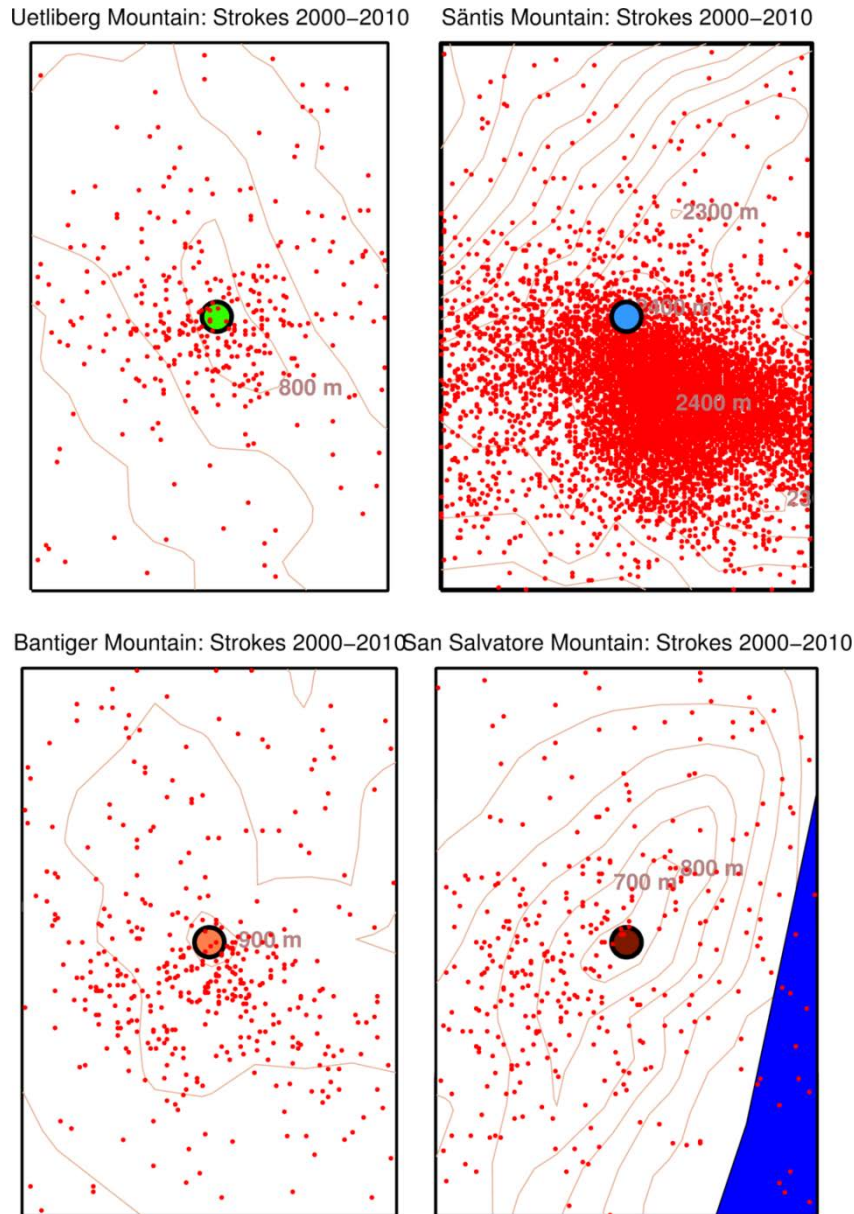


Figure 3.2. Swiss sites stroke impact map (2000 - 2010) for Uetliberg, Bantiger, San Salvatore and Säntis Mountain sites.
Source: EUCLID

Figure 3.2 presents the number of detected strokes between the years 2000-2010 around the four towers: Bantiger (187.7-m tall on the top of a 947-m mountain), Uetliberg (186.7-m tall on the top of a 869-m mountain), San Salvatore (70-m tall on the top of a 640-m mountain), and Säntis (124-m tall on the top of a 2502-m mountain). From the figure, it can clearly be seen that the Säntis Tower is by far the most frequently struck structure.

3.3 Säntis Tower

The 2502-m tall Mount Säntis (Alpstein Mountain complex) is located at $47^{\circ}14'57''\text{N}$ and $9^{\circ}20'32''\text{E}$ in the Appenzell region in the northeast of Switzerland. Mount Säntis is the most

prominent elevation within a circular radius of 30 km (the closest higher mountain is the 2645-m tall Schwarze Hörner – Corne Noire – located at $46^{\circ}58'38''\text{N}$, $9^{\circ}23'59''\text{E}$) at a distance of 35 km. The Säntis geographic site is peculiar as it is the highest peak next to a long plain that extends from this part of Switzerland to the South of Germany and that collides with the Alps as seen on Figure 3.3. These characteristics make the Mount Säntis a zone of strong foehn winds, formed when a humid air mass rise on the side of a mountain and exposed to strong winds get cooler and condensate, creating clouds and precipitations. The Säntis mountain region is a medium-high intensity precipitation area, heavily clouded all over the year.

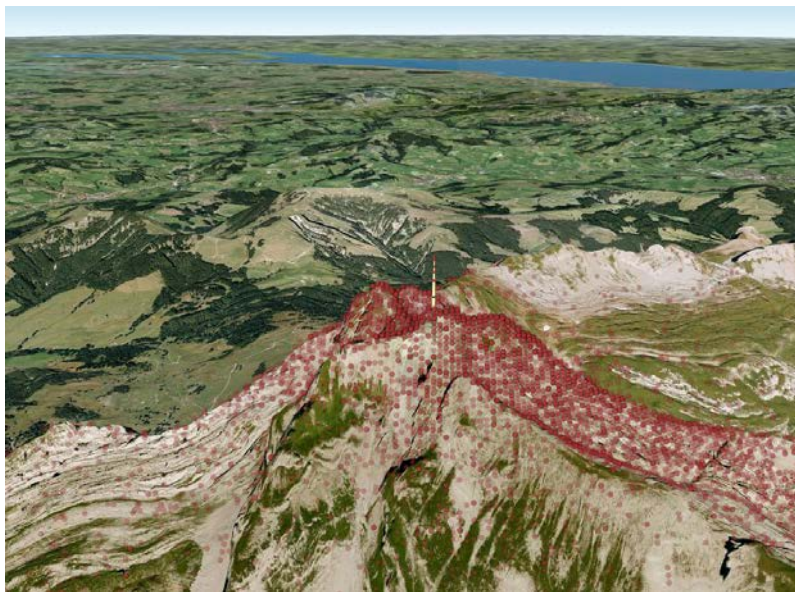


Figure 3.3. Säntis Mountain with tower view. In red the strokes measured by EUCLID from 2000-2012. Source: Google Maps™ mapping service and EUCLID

The Säntis Tower is a 124-meter tall tower sitting on the top of the Mount Säntis (see Figure 3.4). The tower has an inner conical thick metal hollow structure of a radius of 2 m at the base and of 1 m at its top. The outer dielectric Plexiglas structure has a radius of 3 m at the base and 1.5 m at the top and serves to isolate the electronic equipment and antennas from the elements as the structure serves mainly as a telecommunications tower and a climate station. The diameter of the tower base is sustained by a set of metal supports allowing the structure to slightly move under heavy winds. A CAD representation with representative dimensions of the tower is shown in Figure 3.5.

The high number of lightning discharges to the tower are somewhat related to a combination of different factors, such as the tall metallic structure on the top of a mountain, the local topography, meteorological factors.



Figure 3.4. The Säntis Tower

3.4 Current Measurement Equipment

Lightning currents are characterized by a typical frequency spectrum extending from DC to a few MHz. Broadband resistive shunts represent the ideal solution for the measurement of lightning currents as their output is a faithful reproduction of the current associated with various phases of a lightning discharge (in the case of upward discharges, i.e., the initial continuous current, superimposed pulses, and return strokes). However, such a solution was not possible to implement as it required the installation of the shunt on the top of the tower and does not allow measuring the current at other points along the tower.

Another solution often adopted for the measurement of lightning currents on instrumented towers is the use of Rogowski coils (e.g. on the CN Tower in Canada [117]). Rogowski coils can, in principle, have a frequency response down to the Hz or even mHz range and they should be able to record initial continuous currents associated with upward flashes (see i.e. [78]). However, their high frequency response is limited by the size of the sensor and by its resonance frequency, which might be as low as some hundreds of kHz. As a result, the current rise time and time-derivative might be affected by the high frequency shortcomings of Rogowski coils. In order to overcome the limited high frequency response of the Rogowski

coils, we proposed to use magnetic loops located very close to the tower to measure the high frequency content of the lightning current, assuming proportionality between magnetic field and current.

3.4.1 Rogowski Coils

Current sensors were installed on the Säntis Tower at two different heights (24 m and 82 m as seen in Figure 3.5), to provide not only a redundant measurement, but also as a means to evaluate the transient phenomena along the tower and allow the possible estimation of reflection coefficients at the boundaries of the structure [73]. Details of the coil transfer function, resonances and tests can be found in [124-126], in Section 3.6 (System Testing) and in [C. Romero, Internal Report (Säntis Measurement System Calibration)].

Three Rogowski coils were installed in the tower, namely, (i) a PEM® Rogowski coil at 82 m, (ii) a PEM® Rogowski coil at 24 m, and (iii) a ROCOIL® Rogowski coil at 24 m. The characteristics of the coils are given in Table I.

Table I: Characteristics of the two Rogowski coils

Parameter	ROCOIL @ 24 m	PEM @ 24 m	PEM @ 82 m
LF (-3dB)	0.1Hz	0.01Hz	0.01Hz
HF (-3dB)	5MHz	3MHz	3MHz
di/dt peak	100kA/us	150kA/us	150kA/us
Noise level	20mVp-p	2mVp-p	2mVp-p
Calibration Factor	Output 1: 1kA/V Output 2: 10kA/V	Output: 20kA/V	Output: 20kA/V
Diameter	3.72 m	3.72 m	1.62 m

The coils are characterized by resonance frequencies in the order of 1 MHz and are equipped with a resistor placed across the coil output to damp oscillations related to its resonance and analog integrators with low impedance output that feed a fiber optic link that transports the signal to a shielded room inside the tower compound. The location of the two sets of Rogowski coils can be seen in Figure 3.5.

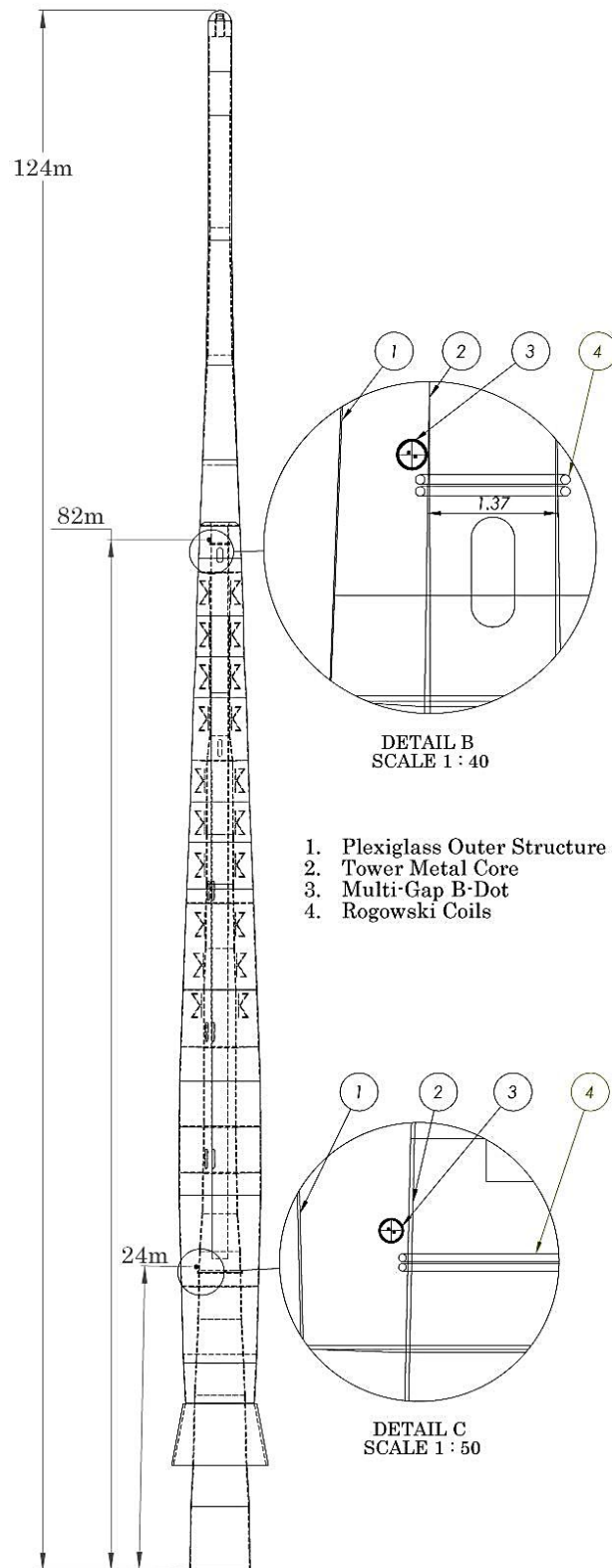


Figure 3.5. Sántis Tower CAD drawing, detailing the inner metallic core and the outer Plexiglas structure, the sensors placement and the overall tower dimensions. The scale of the details drawing refers to the scale of the main drawing.

3.4.2 Magnetic Derivative (B-Dot) sensor

In order to overcome the limited high frequency response of Rogowski coils, magnetic loops located very close to the tower mast were used, at a few meters distance from the axis, where dB/dt should be proportional to di/dt . A simple magnetic loop presents some disadvantages, namely the limitation of the high-frequency response by the resonance of the magnetic loop inductance and the capacitance of the connected cable, and the need of a high-impedance termination, which might result in contamination of the waveform through multiple reflections. To overcome these limitations, a new B-Dot sensor was designed based on Baum's studies [127-129]. Figure 3.6 shows the designed sensor which was manufactured at the Swiss Federal Institute of Technology in Lausanne. Details on its design and measurement can be found in [125] and the mathematics on the Appendix on the design of the B-Dot sensor.

The magnetic derivative sensor has an upper frequency cutoff of 20 MHz and a 50 Ohm matched termination. It also features a much better immunity against the electric field, compared to conventional loops [125]. The sensor is designed to withstand a maximum current steepness of 150-kA/ μ s, in agreement with the statistical parameters analyzed by Andersson and Eriksson in [118] that reports a 5 % percentile of events exceeding the value of 161.5-kA/ μ s corresponding to the maximum rate of rise of the current on the front (parameter TAN-G).

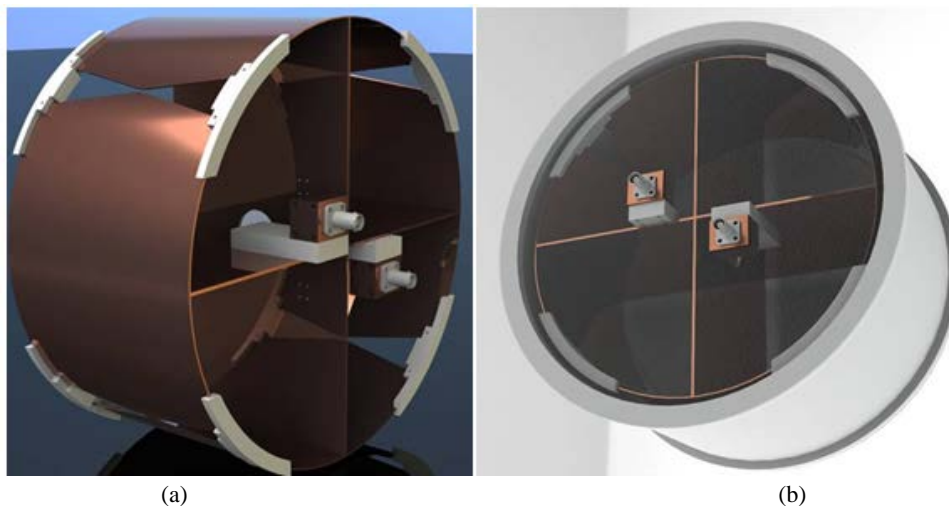


Figure 3.6. B-Dot sensor. (a) Detail of the conical transmission line gap used in it (b). Sensor with enclosure

Time domain numerical simulation of the B-Dot sensor was carried out using the CST Microwave Studio® software, applying different polarization plane waves and evaluating the output voltage on a test load. The transient solver was setup with a sigmoidal excitation waveform of DC to 300 MHz bandwidth; the solver steady state accuracy limit was -60-dB.

Figure 3.7(a) show the simulation setup for the 14cm radius loop and one of the applied E-H fields configuration. The upper simulation frequency was set to 2 GHz to provide an accurate spatial discretization of the loop including the measuring gap. The sensor output voltage obtained from the time domain simulation was then integrated and scaled to obtain the current. In Figure 3.7(b) the ratio between injected and measured current is plotted against the frequency. It can be seen that in the simulation the sensor follows the reference current up to a frequency of 50 MHz.

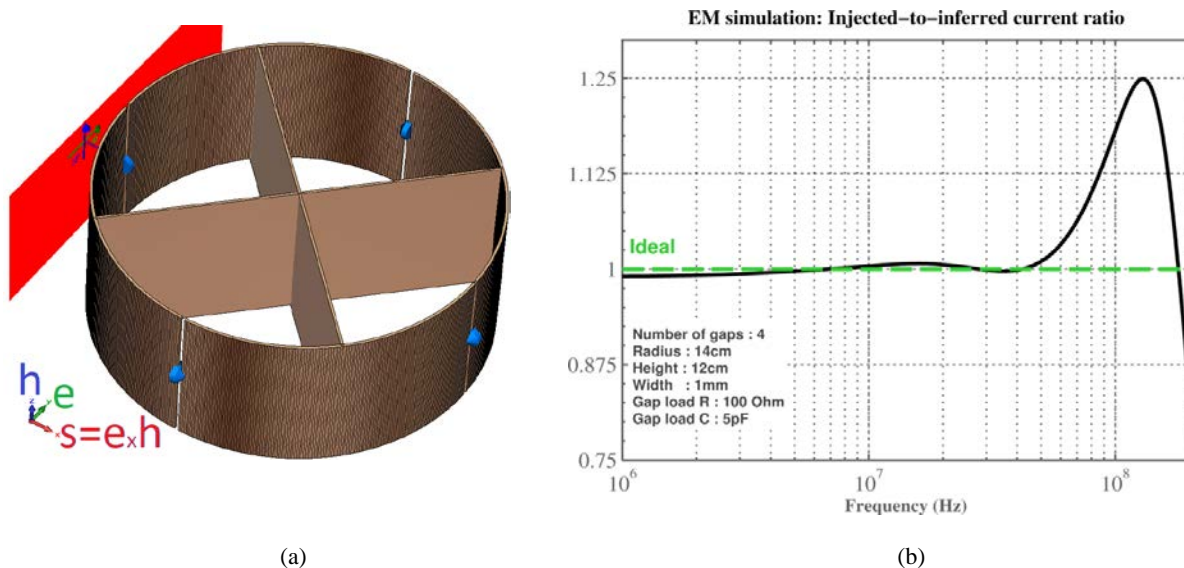


Figure 3.7. (a) Simulation setup for the electromagnetic simulation, showing the applied plane wave and the gaps charges (in blue) (b) Simulation of the magnetic loop (CST Microwave studio) showing the ratio between the injected current and the inferred current from B-Dot output voltage.

The complete calibration of the Rogowski and B-dot sensors can be found in an internal report document.

3.5 Overall Measurement System Description

A schematic diagram of the current measurement system is shown in Figure 3.8. The analog outputs of the sensors are relayed to a digitizing system by means of A/D – D/A 12-bit optical link characterized by an overall -3 dB bandwidth of DC to 25 MHz.

The status of each pair of sensors is controlled by means of a control system designed and built using National Instruments Compact-RIO modules linked via 100Base-FX fiber optics Ethernet. Such a system allows an over-the-Internet remote maintenance, monitoring and control overall system.

The control room consists of a local server running monitoring and storage tasks and a front-end station connected to the internet over a router and a standard ADSL link.

3.5.1 Measurement Boxes

The electronics are located near each measurement point on the tower inside specially-designed metallic boxes. These boxes were engineered to withstand the requirements of the tower conditions in terms of humidity, temperature, electromagnetic compatibility and space constraints.

The design of the boxes and their inner components were made using a CAD tool in order to assure the mechanical positioning, securing on the tower and to allow multi-domain (thermal, electromagnetic) simulations. Each box includes:

- A CompactRio FPGA-based system with a control loop that monitors and adjusts the heating and ventilation units. This unit also controls the DC power sources and the analog-to-fiber optic links. This system is linked to the recording and control room using a mono-mode fiber optic cable, which goes to a local computer used to monitor and control the measuring boxes subsystems.
- Analog-to-digital fiber optic converters that digitize the output of the integrators and magnetic loop and relay the signal to the control room.
- Analog integrators of the Rogowski coils.
- Power supply units for feeding the integrators with stable positive and negative voltage rails, making possible the measurement of positive and negative events.
- Heating and fan along with thermocouples for the temperature control of the boxes.
- Isolation transformer whose output feeds the internal AC power distribution system.
- Meteolabor® surge peak arresters at the input of the analog-to-fiber links.
- LAN / Fiber converter at the output of the CompactRio controller to isolate the remote controlling of the control units.

Figure 3.9 presents the CAD model of the box along with the aforementioned components. The design aspects of the electronic boxes are discussed on the following section.

3.5.1.1 EMC Design

The measurement box inside the tower might be exposed to the radiated fields of the telecommunication equipment in the tower and to the radiated fields from lightning. The Sântis boxes were designed as to minimize the coupling effects using EMC rules and components. The boxes were built and tested in the premises of the Montena EMC laboratories in Switzerland. The main components of the design are (see Figure 3.9(b)):

- Honeycomb pattern for the fan and exhausting holes (label 1 on the figure).

- Copper-beryllium finger gaskets for the box door.
- Filtered feed-through for the current and field signal inputs.
- A shielded isolation-transformer whose output feeds the internal AC power distribution system.
- Low pass through-hole waveguide filter for the fiber cabling (label 7 on the figure).

The box geometry, components configuration, and aperture lengths and distances were simulated using CST Microwave Studio®. Simulations showed a shielding effectiveness better than 60-dB at the chosen frequency range. The reported values of the shielding effectiveness measured at Montena EMC were 60-dB at $f < 100\text{ MHz}$, and 30-dB at $100\text{ MHz} < f < 1\text{ GHz}$. Other EMC mitigation measures used in the boxes include:

- Fast surge arresters at the input of the analog to fiber links, manufactured by Meteolabor®.
- LAN / Fiber converter at the output of the CompactRio controller to isolate the remote communication with the control room.
- Disjointed cabling system for the power and signal side inside the box

3.5.1.2 Thermal design

Due to the harsh conditions inside the tower, where the temperature ranges from -15°C to $+35^{\circ}\text{C}$, a system comprising a heater, a ventilator, moisture exhaust holes, and a thermal insulation material was designed to keep the temperature within acceptable limits for the components and to avoid condensation inside the PCB cards.

The thermal component design was based on analytical modeling and finite element simulation (FEM) using the SolidWorks flow simulation environment. The details of the thermal modeling can be found in [Carlos Romero, Internal report on the Thermal System Design]. For the simulation, an external air and box wall temperature of zero degrees was assumed and an internal heat source was set-up to simulate the heat exchange between the interior and the exterior of the box. In the first analysis, the air mass movement due to the fan was disregarded and, the system thermal steady state condition was investigated. In Figure 3.10(a), one can see the resulting temperature distribution in the case of no insulating material, where the internal temperature reaches zero degrees even with the heating system working at full power. In Figure 3.10(b), the simulation results in presence of a 2-cm thick foam material are presented. As it can be seen, the insulation layer is shown to be efficient in

maintaining the temperature within the operating ranges provided by manufacturers of the equipment installed inside the boxes. Multiple simulations were carried out to select the foam type and thickness of the foam to be installed in each box. The chosen material was a rigid fiber-glass sheet of 2cm thickness. The design was then built and validated at the EMC laboratory at EPFL. The effect of the fan was also assessed through numerical simulations obtained using SolidWorks. In Figure 3.11, the final selected fan at low and high speeds and its ability to reduce the system temperature of the boxes is represented using the results of the FEM simulation.

On the CompactRio system a temperature control system was implemented on the FPGA, whose inputs are the thermocouples measures and as outputs the relay-based control of the fan and heater. The control system maintains the temperature constant all year round.

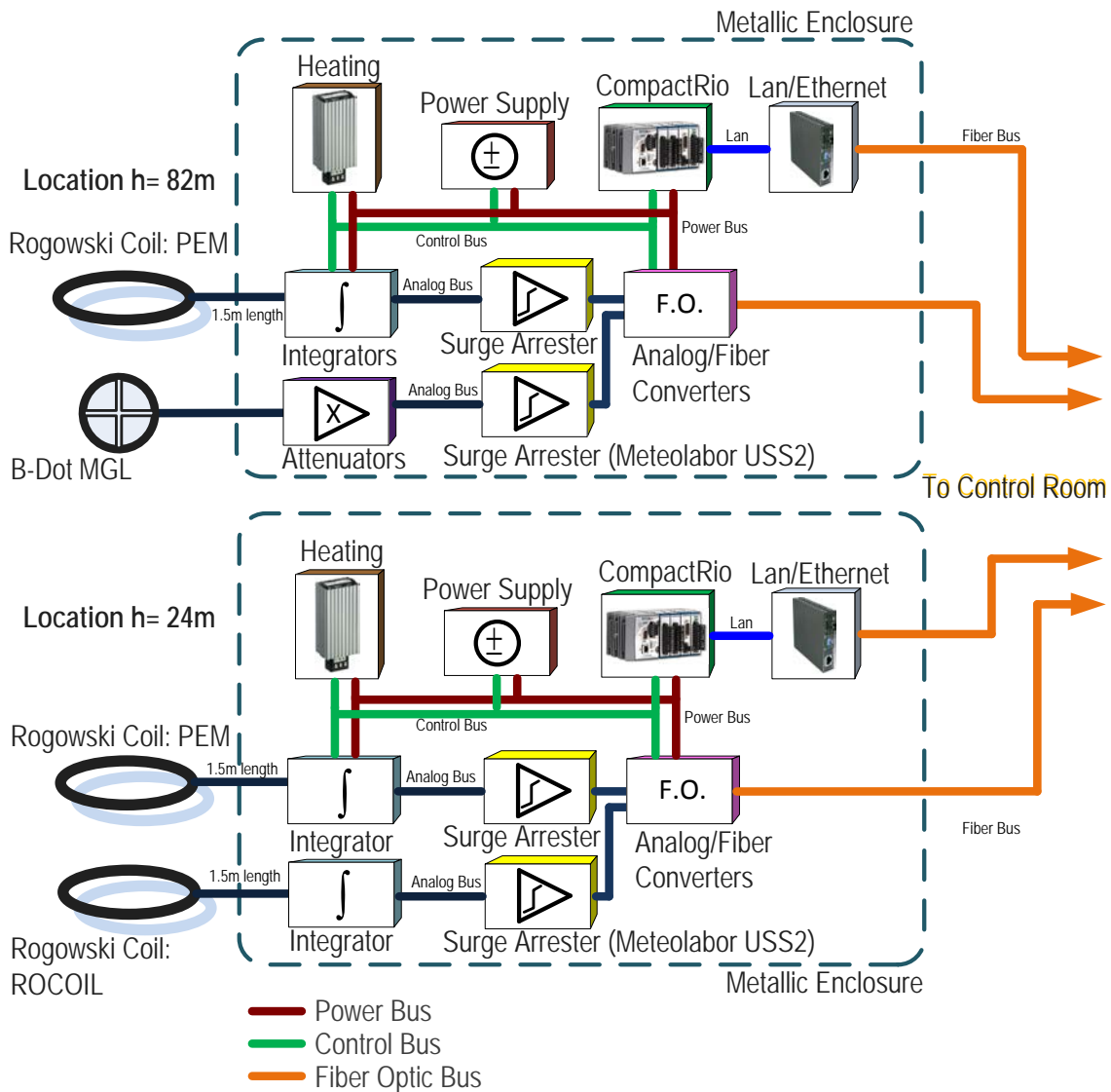


Figure 3.8. Electronic System Architecture

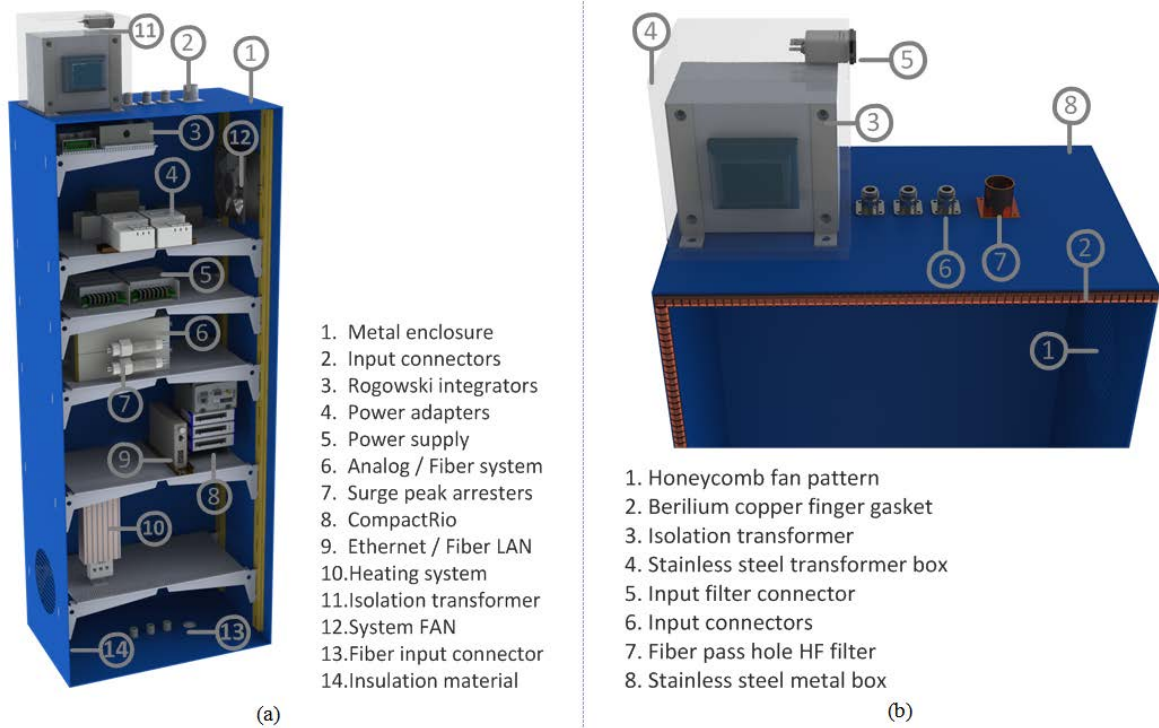


Figure 3.9. (a) CAD Model of the box and its component, (b) CAD Model of the EMC design components

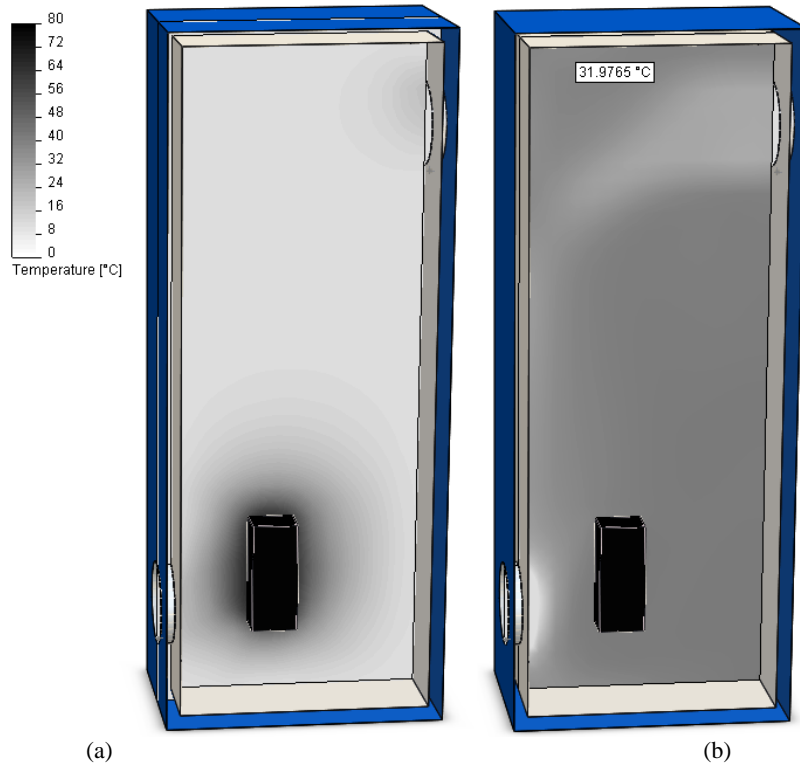


Figure 3.10. Comparison of the thermal behavior of the Sántis box under different insulation schemes (scale in °C). Simulation with outer 0°C air temperature. (a) Box with no insulating material. (b) Box with foam thermal insulator of 2 mm thickness

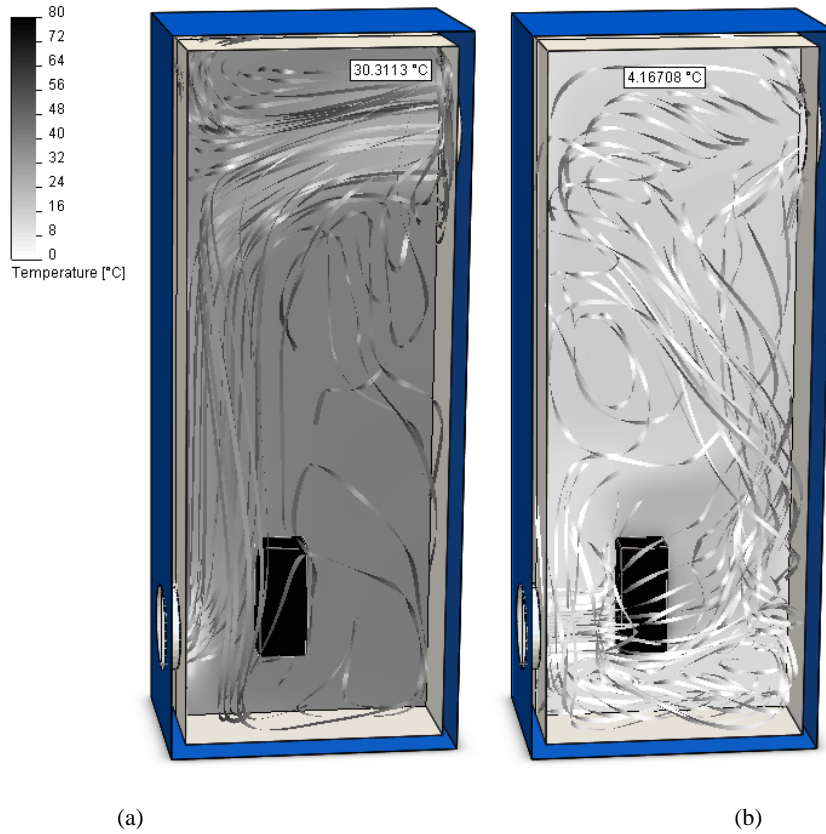


Figure 3.11. Fan influence on the thermal behavior of the measurement box (scale in °C). Outer air temperature was assumed to be 0°C. The simulations are carried out taking into account the presence of a 2-cm thick insulation material. (a) Fan at low speed. (b) Fan at full speed

3.5.2 Digitizers

The measured signals from the sensors are relayed to a high-speed digitizer via a fiber optic analog-to-digital / digital-to-analog link. The selected links, manufactured by Terahertz, are characterized by a -3dB frequency bandwidth of DC - 25 MHz with a sampling rate of 100 MS/s, a 12-bit resolution at $\pm 5V$, giving a signal-to-noise ratio $SNR_{max} = 74\text{-dB}$. These are connected to an 850 nm monomode industrial fiber.

Table II: Digitizer specifications

Number of channels	4
Number of digitizers	2
Sample Rate (Each channel)	100MS/s
Observation window	1.2 s
Pre-trigger	20% of the observation window
Resolution	14 bits
Input impedance	50Ω, 1MΩ (selectable)
Input voltage range	$\pm 10V$

A high-speed digitizer is connected to the fiber optic digital-to-analog converter in the control room. This is a National Instruments PCI-5122 which characteristics are given in Table II. The digitizer pre-trigger is configured as of 20% of the overall 1.2 seconds window, corresponding to 240 ms.

3.5.3 Remote maintenance, monitoring and control system

The Sântis distant measurement system required the development of specific functionalities to allow the remote monitoring, control and programming of the different components of the system.

These functionalities are characterized by a three-level hierarchical structure:

- Level #1 is the server that provides the backup storage of the measured lightning current waveforms. This server operates as a front-end, providing remote access to the data over the Internet.
- Level #2 is the measurement station composed of an industrial PC that hosts the two digitizers and the GPS card. It provides both measurement and storage functionalities and the dialog with the measurement boxes in the tower.

This computer hosts the two digitizers and implements the following functionalities:

- a) Triggering, measurement and storage of the current waveforms.
 - b) Acquisition of the UTC-GPS time stamp.
 - c) Backup of the measured current waveforms into the Level #1 server.
 - d) Remote control of the remote measurement boxes.
- Level #3 the local measurement at two heights, comprising: current sensors, electronics, protection, and control, this allows:
 - a) Voltage measurement and control of the power supply units connected to the Rogowski coil integrators and to the optical fiber link.
 - b) Temperature measurement and control of the shielded box equipment.
 - c) Communication with the measurement station to allow the remote control of thermal and analog / optical devices.
 - d) Remote programming and firmware updates

The Level #2 computer is an industrial PC equipped with high speed hard disk storage and a National Instruments PCI 5124 digitizers sampling at 100 MSPS, giving measuring window of 1.2 seconds per channel. Time stamping is provided by a Meinberg GPS 170 PCI card, with a maximum time uncertainty of 100 ns. Level #1 computer is a standard PC providing temporary backup storage and remote internet access.

A web interface allows the remote programming and monitoring of the system along with the possibility to plot data while it still remains locally stored on the backup server, without actually having to transfer the large data files. Recorded data files are sent over the Internet

link on a regular basis and ultimately be stored on servers belonging to the Swiss Federal Institute of Technology (EPFL), the University of Applied Sciences of Western Switzerland and the University of Bologna.

3.6 Overall System Testing

3.6.1 Rogowski coils

Although the Rogowski systems were provided with calibration certificates, their characteristics were verified first in the premises of the Montena EMC Laboratories and then, in the high voltage laboratory of the Swiss Federal Institute of Technology in Lausanne. Figure 3.12(a,b) show the comparison of each coil's output with the reference current waveform for tests carried out in Lausanne using a 2-kA current peak with a rise time of 1 μ s, generated by a 1.1-MV impulse generator. The reference current measure is provided by a Pearson 110T current transformer (CT) characterized by a 3dB bandwidth of 1 Hz – 20 MHz, usable rise time of 20 ns, maximum peak current of 5-kA and an overall accuracy of 1 %. The calibrations of the coils for higher current ranges (tens of kA) were done by making a few turns on the coils (as recommended by the manufacturers). The obtained results (not shown here for the sake of brevity) were similar to those presented in Figure 3.12. Figure 3.12(c,d) shows the magnitude of the Fourier transform of the reference current and the two Rogowski coils output and illustrates the fact that beyond 1 MHz the provided Rogowski coils are not able to reproduce with a high degree of accuracy the spectrum of the reference current (note that higher values are reported by the coil manufacturers as shown in Table I). It can also be seen that the PEM frequency response is much more accurate compared with the Rocoil's.

3.6.1.1 Rogowski coils noise

The measurement system underwent several tests during the spring and winter 2009 prior to its installation on the tower. Table III shows the measured noise floors for the full measured bandwidth (at a sampling frequency of 100MSPS) and Figure 3.14 an example noise estimation test. The RMS noise limits the measurement to 100A for the PEM Coils (they measure up to 100kA peak and 200pk-to-pk), so the unfiltered attained maximum resolution is about 1/1000 the maximum scale.

However, using numerical low pass filtering on the signals, we were able to measure continuing currents down to about 10-A (1/10000 the maximum full scale). Further details on

noise measurement mathematical details and the filters design can be found on the Appendix on Signal Processing of Sántis Signals.

3.6.2 B-Dot sensors calibration

The same setup used for testing the Rogowski coils was used to test the B-Dot sensors. The reference current was generated by a 1.1-MV impulse generator connected to a suspended wire. The B-Dot sensor was located at different distances from the conductor carrying the current. From the measurements, the agreement between the measured reference current and the inferred current obtained from the integration of the B-Dot sensor output was tested. Figure 3.13(a,b) illustrates one example of comparison.

On Figure 3.13(c), the Fourier Transform of the integrated output of the B-Dot sensor and that of the reference current are plotted. It can be seen that the B-Dot sensor reproduces satisfactorily the frequency content of the rise time reference current.

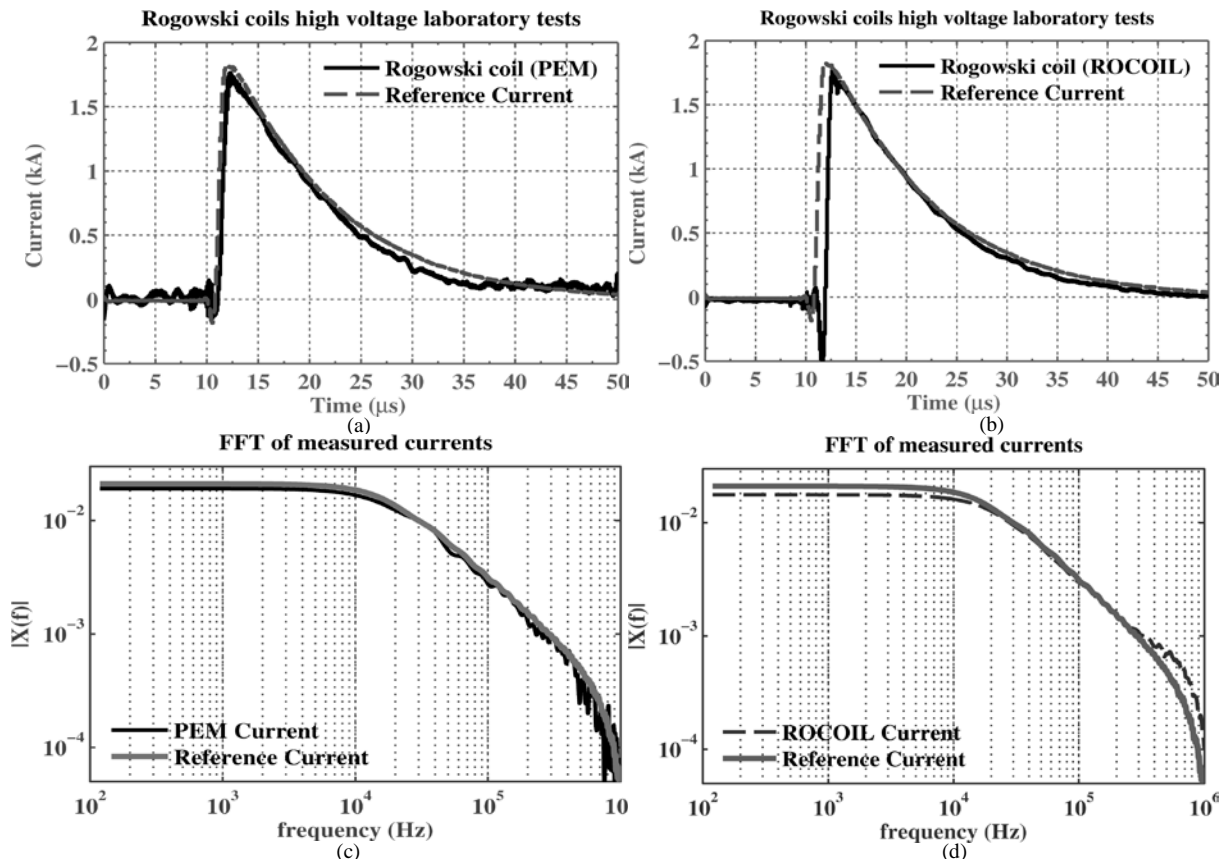


Figure 3.12. (a) Measurement comparison between a reference current using a calibrated current transformer (CT) against the two Rogowski coils (a) PEM coil (b) ROCOIL coil. (c) Fourier Transform of the measured currents using PEM coils and the reference CT. (d) Fourier Transform of the measured currents using ROCOIL coils and the reference CT.

Table II: Noise Estimation for the shown experiment over the full bandwidth (unfiltered signals)

Parameter	ROCOIL @ 24 m	PEM @ 24 m	PEM @ 82 m
LF (-3dB)	0.1Hz	0.01Hz	0.01Hz
HF (-3dB)	5MHz	3MHz	3MHz
di/dt peak	100kA/us	150kA/us	150kA/us
Noise level	20mVp-p	2mVp-p	2mVp-p
Calibration Factor	Output 1: 1kA/V Output 2: 10kA/V	Output: 20kA/V	Output: 20kA/V
Diameter	3.72 m	3.72 m	1.62 m

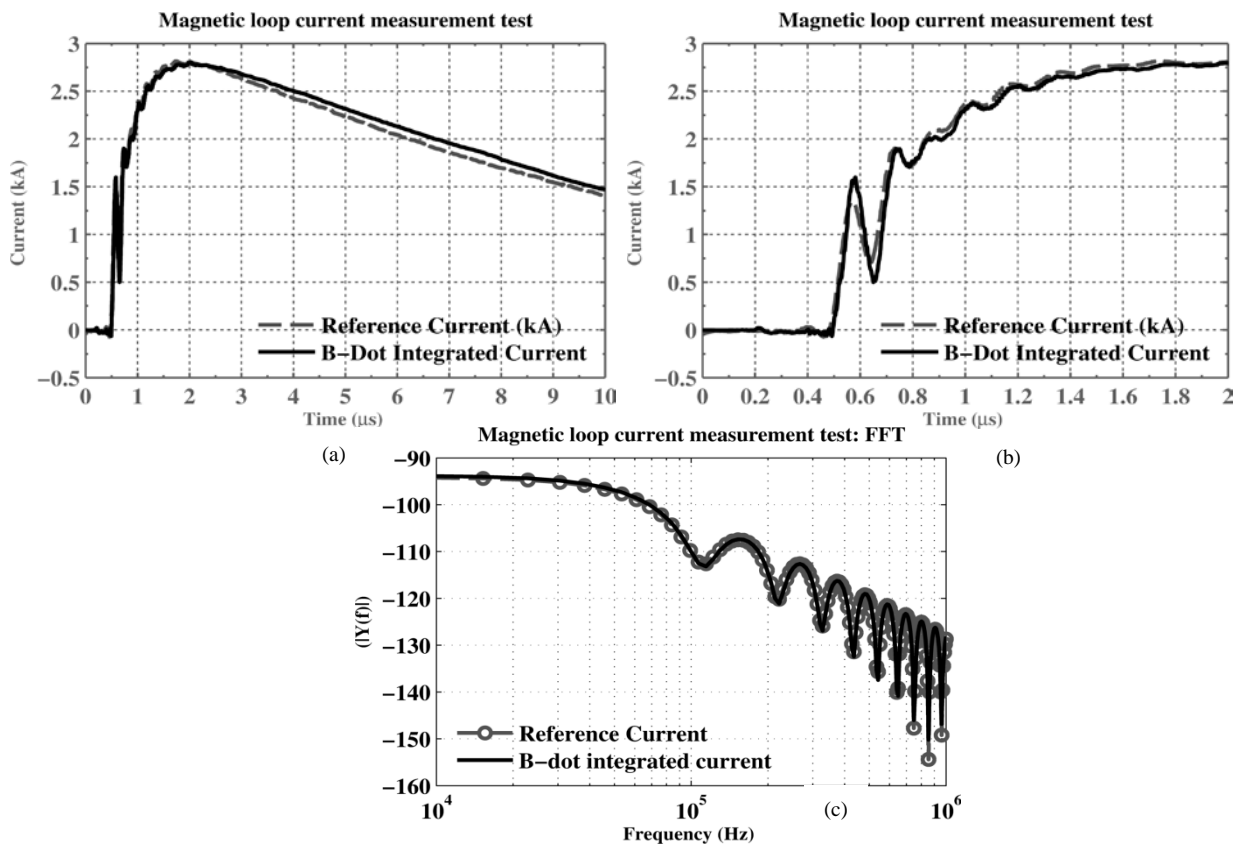


Figure 3.13.(a) Comparison between the measured reference current with a current transformer (CT) and the numerical integration of the B-Dot sensor (b) Detail of the first 2μs of (a). (c) FFT comparison of the measured reference current and B-Dot numerically integrated currents

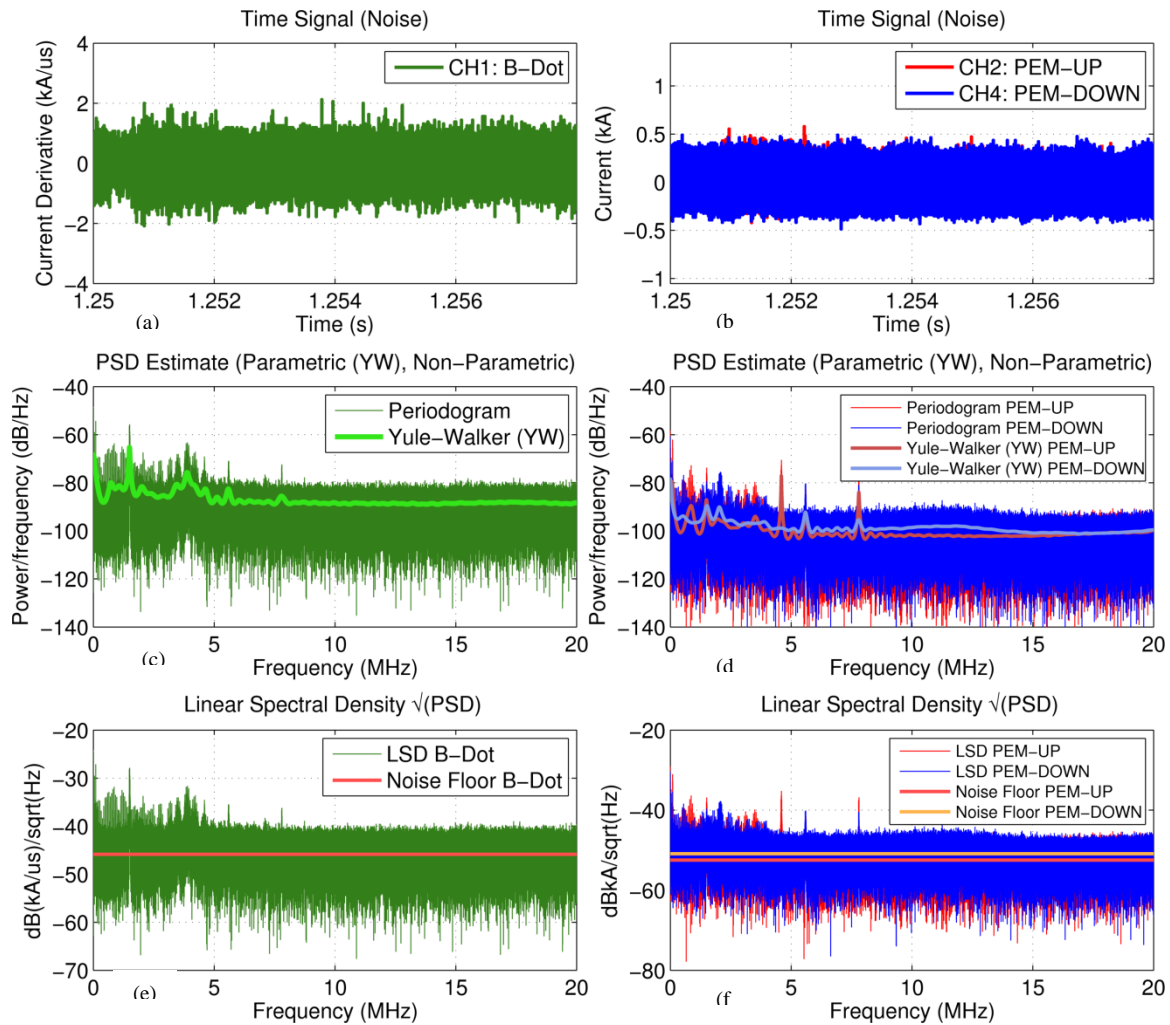


Figure 3.14. Sántis measurement system spectral noise estimation. (a) Time domain noise signal for B-Dot (b) Time domain noise signal for PEM coils (c) the estimated PSD for B-Dot (d) the estimated PSD for PEM coils (e) Linear Spectral Density for B-Dot showing the noise floor (f) Linear Spectral Density for PEM coils showing the noise floor.

3.7 System Installation

The system was installed on May 19, 2010 and is fully operational since then. Figure 3.15(a,b) present an inner view of the tower. Figure 3.16 presents a picture of the installed Rogowski coil and B-dot sensor on the top location (82 m) and Figure 3.17 shows two views of one of the two boxes containing the electronics box along with its components fixed inside the metallic structure of the tower.



(a)

(b)

Figure 3.15. Inner view of the tower (a) and the inner metallic structure (b).



Figure 3.16. Installed B-dot sensor and Rogowski coil around the inner metallic structure of the tower, upper measurement location (82 m).



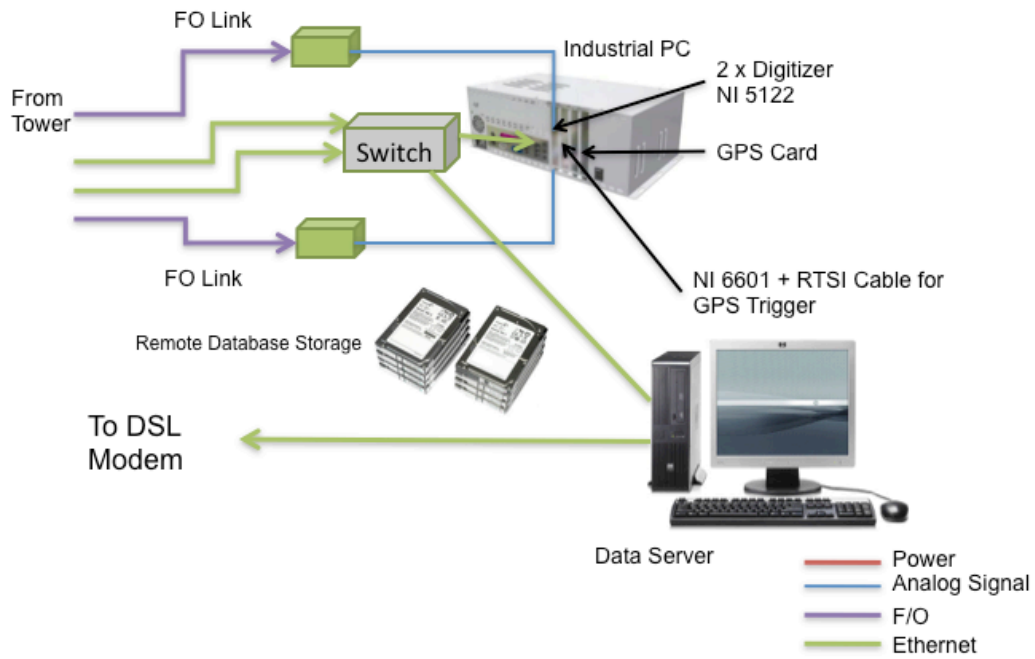
(a)



(b)

Figure 3.17. Pictures of the shielded measurement box installed inside the tower structure.(a) View of the lower part of the measurement box detailing the optic fiber output (b) view of the equipment inside the installed box

Figure 3.18a present a schematic diagram of the equipment on the control room, which includes the fibre optic links, the industrial PC with the digitizer boards and GPS card and the data server. The system is remotely accessible through a DSL connection and the control room system is also equipped with an uninterrupted power supply (UPS).



(a)



(b)

Figure 3.18. (a) Equipment in the control room of the Sântis Tower. Schematic diagram (a) and picture (b).

Since the installation of the system, a total number of 168 upward negative flashes and 33 upward positive flashes were successfully recorded with the system.

3.8 Data Analysis Software

A data analysis software (SENDIS) was developed to analyze the obtained data, to extract statistical parameters and to allow the remote monitoring, control and programming of the different components. The software is based on Matlab and designed using Object Oriented Programming. SENDIS' current capabilities include the opening, segmentation and processing of data files in the range of hundreds of millions of samples. The user can subsample the data for obtaining faster and overall views of the dataset. SENDIS makes it possible to segment the data for creating logical structured subsets and perform local processing on small clusters (such as return strokes). The software allows also to perform signal processing operations on the data, such as Wavelet, FIR and Zero-Delay filtering, integration, derivation, DC estimation and user-defined algorithms. The algorithms implemented in SENDIS allow the detection of current components (return stroke, M-component, continuous and continuing currents) within each flash and the automatic extraction of statistical parameters of the current.

3.9 Conclusions

The Sántis Tower has shown to be a unique structure to collect experimental data on lightning. The tower was instrumented to measure the lightning current at two different heights, 24 m and 82 m, using, at each height, two sensors, a Rogowski coil set up to measure the current itself and a specially-designed B-Dot sensor measuring the current derivative.

Special boxes were designed to house the electronics near the sensors. Criteria for the design included thermal and EMC constraints to deal with the electromagnetic and climatic environment in the tower.

The developed measurement system is characterized by a frequency bandwidth of 0.1 Hz to 1MHz for the Rogowski coil current measurements and 100 kHz to 20 MHz for magnetic field measurements.

Maintenance, monitoring and control tasks are carried out remotely using a remote control system over the Internet using a standard ADSL link on the Sántis.

The system was installed on the Sántis Tower in May 2010. Since then and until this date, more than 200 flashes were successfully recorded by the system.

Chapter 4. Statistics of Negative Upward-Initiated Lightning to the Säntis Tower

4.1 Introduction

This chapter discusses and presents statistical distributions of some of the lightning current parameters based on the lightning current and current-derivative waveforms measured at the Säntis Tower site [124-126, 130] in 2010 and 2011. The statistical distributions are associated to upward negative flashes.

The knowledge of the lightning channel-base current is of primary importance for the analysis of lightning interaction with electrical systems and structures, and the design of efficient protection systems.

Lightning channel-base currents are obtained either (i) by direct measurements using instrumented towers like those presented by Anderson and Eriksson (based on the measurement performed by Berger at Monte San Salvatore in Switzerland) [76], those obtained by Delleria and Garbagnati (based on the measurement performed at Monte Sasso di Pale and Monte Orsa in Italy) [119], and by other authors (e.g. [76, 78, 79, 81, 117]), or (ii) from artificially-initiated lightning by small rockets (e.g. [82, 84, 120]). Estimates of various lightning current parameters can also be obtained from the measurements of lightning electromagnetic fields assuming one or more empirical [86, 131] or theoretical relations [87, 132] between the lightning current and its associated electromagnetic fields.

The period of analysis in our study extends from May 2010 to January 2012 during which a total number of 201 flashes were successfully recorded on the Säntis. About 15% of the recorded flashes (namely 30) were of positive polarity, and 1.5% (3 flashes). The analysis presented in this chapter concern negative flashes (167 flashes).

4.2 Lightning Current Parameters

Figure 4.1 shows an example of a flash current record measured by one of the Rogowski coil located on the top measuring location (82 m). The current waveform is typical of upward negative flashes with an initial continuous current (ICC) of about 500 ms duration, and superimposed ICC pulses. The number of recorded ICC pulses is in excess of 30, with peak amplitudes ranging from about 1 kA to 14 kA. After the extinction of the ICC, a return stroke with a peak current of about 22 kA can be distinguished. The maximum steepness of the return stroke is about 56 kA/ μ s and the total transferred charge of this flash is 21 C.

For the statistical analysis of the parameters associated with current pulses, we considered together (i) return stroke pulses, namely pulses occurring after the extinction of the initial continuous current, and (ii) pulses superimposed with the initial continuous current fulfilling two conditions: a rise time lower than 8 μ s and an amplitude superior to 2-kA. These pulses are believed to be associated with the leader/return stroke mode of charge transfer, as opposed to slower pulses which are associated with M-component mode [133].

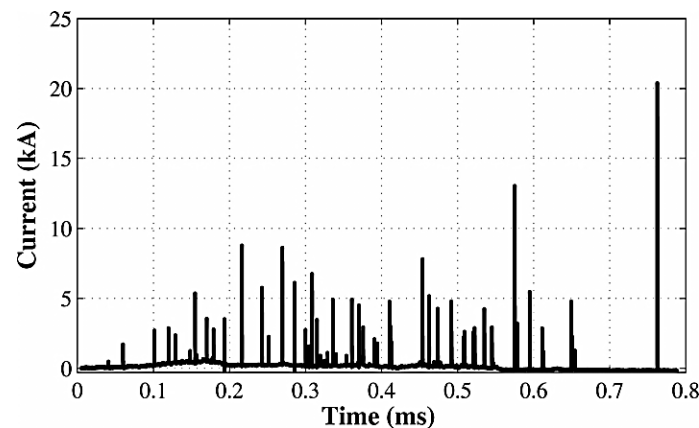


Figure 4.1. Typical current waveform measured at the Sântis Tower using a Rogowski coil located at 82 m above ground level. The flash occurred on October 12, 2010, at 19h52

4.3 Seasonal Flash Occurrence

For the duration of the presented measurement period (May 2010 to January 2012), a total of 201 flashes were recorded. All the observed flashes were apparently of upward type (initiated by upward leaders from the tower). Figure 4.2 and Figure 4.3 present respectively the monthly flash count spanned, and accumulated over the whole measurement period. The first measurement year is seen following the same seasonal pattern but during the adjusting time of the equipment (months of June and July 2010) not all the flashes were measured which is evident from Figure 4.2.

It can be seen on Figure 4.3 that negative flashes are mainly concentrated in the summer months during the convective season [134], August being the month during which most of negative flashes occurred (24 events in 2010 and 49 events in 2011). This distribution contrasts with the Gaisberg Tower measurements for which lightning strikes are quasi-uniformly distributed over the year [81]. Positive flashes on the Säntis follow the same seasonal pattern (see Chapter 5 for a detailed analysis of positive and bipolar flashes).

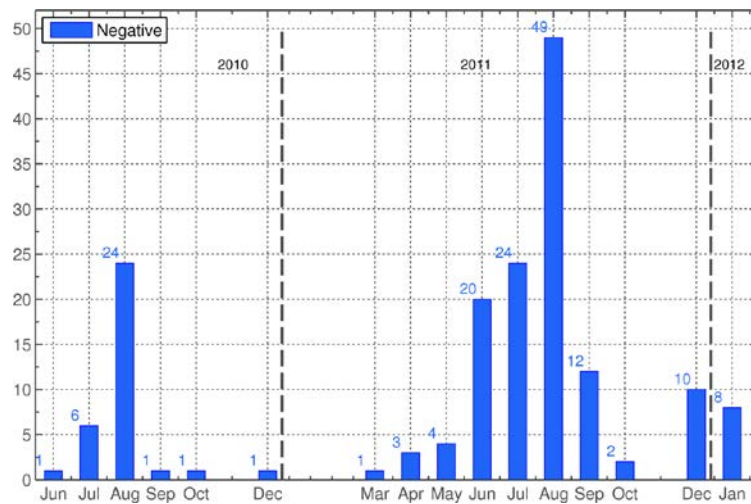


Figure 4.2 Negative Flashes count to the Säntis tower. June 2010 to January 2012.

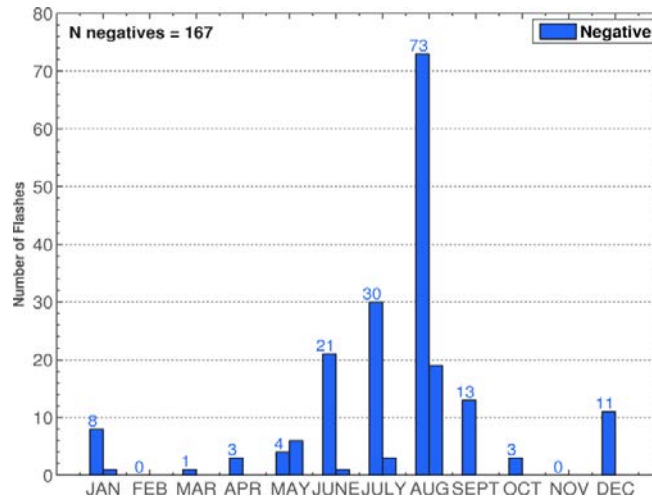


Figure 4.3. Monthly distribution of the number of negative flashes to the Säntis tower. June 2010 to January 2012.

4.4 Hourly Flash Occurrence

Figure 4.4 presents the hourly number of flashes at the Säntis tower from May 2010 to January 2012. It can be seen that most of the flashes occurred during the afternoon, mostly between 16:00 and 20:00. However, an appreciable number of flashes occurred in the morning, mostly between 6 and 10 AM. Figure 4.5 shows concurrently the hourly mean temperature, humidity and air pressure measured at Säntis station during the whole

measurement period and provided by the Meteosuisse meteorological service. The regression coefficients reveal that no clear pattern or correlation can be directly extracted from the comparison of alone environmental parameters with lightning, but nevertheless the highest zones of relative humidity, rain precipitation and measured atmospheric pressure are seen during the afternoon, coinciding with the highest flash daily occurrence period.

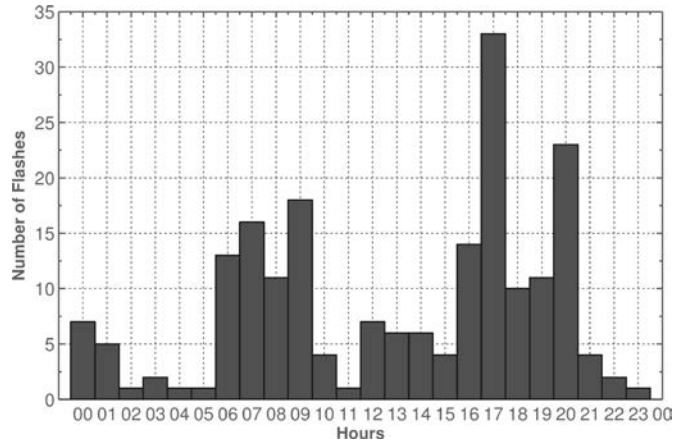


Figure 4.4. Hourly number of flashes at the Säntis tower from May 2010 to January 2012

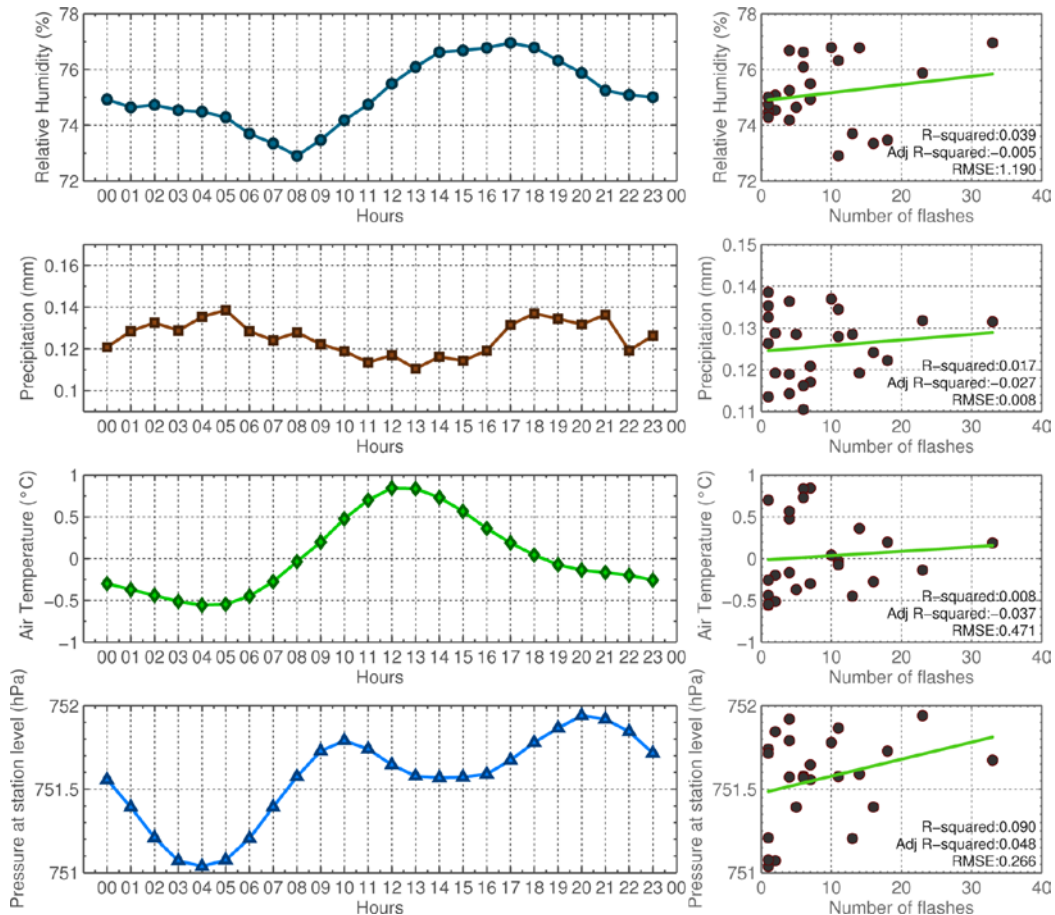


Figure 4.5 Hourly mean of different meteorological values measured at Säntis meteorological station from May 2010 to January 2012. Meteosuisse data (Federal Office of Meteorology and Climatology, Meteosuisse, Krähbühlstrasse 58 CH-8044 Zürich).

4.5 Statistics Calculation

The mathematical techniques applied in the derivation of the histograms, cumulative distributions (CDF) and probability plots are thoroughly described in an internal report [135]. The presented probability plots are constructed under the assumption of a lognormal distribution as in [1, 136, 137]. The straight lines on the probability plots are constructed from a maximum likelihood estimate of the lognormal parameters and the inter-quartile range (IQR) [135, 137]. The probability plots are calculated from the percentile calculation or ranking for the lognormal, based on the Hazen Score method [137].

The CDFs use both the lognormal percentile calculation and a Kaplan-Meier estimation of the empirical CDF [135, 137, 138]. The 95% confidence bounds for the Kaplan-Meier are plotted in all cases in order to illustrate the range in which the parameters are reliable up to this confidence level.

Probability plots which will be presented in this Chapter can reveal graphically goodness-of-fit but should not be used alone for the hypothesis rejection / acceptance of log-normality. In fact a Kolmogorov-Smirnov (KS) test [138] was used to check the validity of lognormal hypothesis under a certain confidence level.

4.5.1 Maximum Current Derivative

As indicated in Chapter 3 Section 3.4.2 and [124], the scaled B-dot sensor is directly used for the evaluation of the maximum current derivative statistical values. Figure 4.6 and Figure 4.7 present the probability plot and histogram of the maximum current derivative for a total number of $N=1851$ events. Note that this number is smaller than the total number of measured pulses, which is 1987. This is because the B-dot sensor cannot measure steepnesses lower than $2 \text{ kA}/\mu\text{s}$. The highest measured value for the maximum current derivative during the period of observation is $88.9 \text{ kA}/\mu\text{s}$. The straight lines in Figure 4.6 correspond to the ideal lognormal distribution (also superimposed in red to the histogram of Figure 4.7) and the IQR straight line. The median is found to be $19.9 \text{ kA}/\mu\text{s}$. Table 1 summarizes the statistical data for the maximum current derivative, in comparison with existing available data. It can be seen that the Säntis data are very similar to the data associated with the CN Tower.

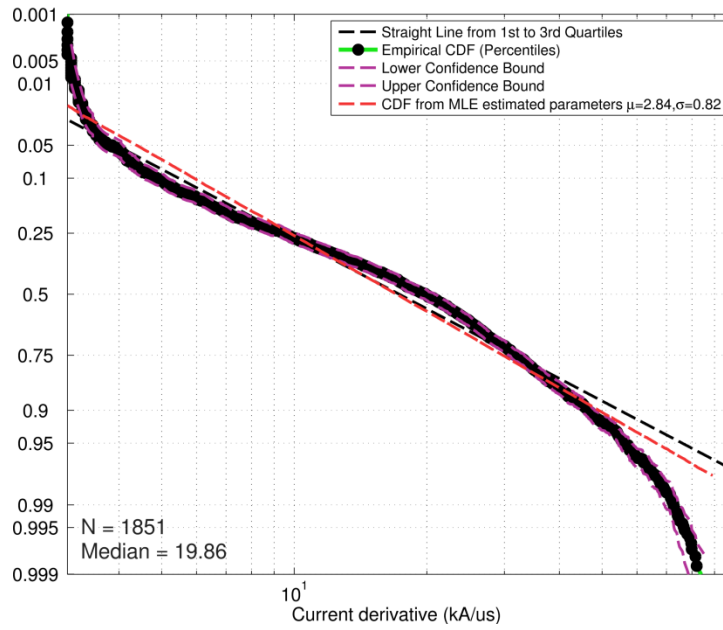


Figure 4.6. Maximum current derivative probability plot.

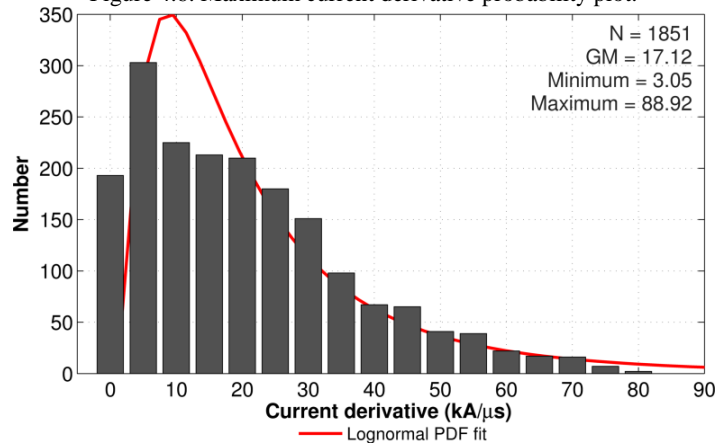


Figure 4.7. Maximum current derivative histogram.

TABLE I
STATISTICAL PARAMETERS OF PEAK CURRENT DERIVATIVE

Peak current derivative (kA/μs)						
Tower	Sample size	Percentage Exceeding Tabulated Value				
		95%	90%	50%	10%	5%
Empire State Building [139]	71	1.2	2.5	13.0	33	38
San Salvatore [140]	710	-	5.6	26	123	-
Peissenberg [141]*	125	-	-	11	-	87
CN Tower [94]	387	3.8	-	18.8	-	37
Säntis (This study)	1851	3.9	4.8	19.9	46.5	56.3

* for ICC pulses and return-stroke pulses

4.5.2 Peak Pulse Current

Figure 4.8 and Figure 4.9 present the probability plot and histogram of peak current for a total number of $N=1987$ events. The maximum measured value for the peak current during the period of observation is 26.5 kA. The labeled straight lines correspond to the ideal lognormal distribution and the IQR line. The median is 6.4 kA. Again, it can be seen from Table II that the obtained data at Säntis seem to be closest to the data associated with the CN Tower.

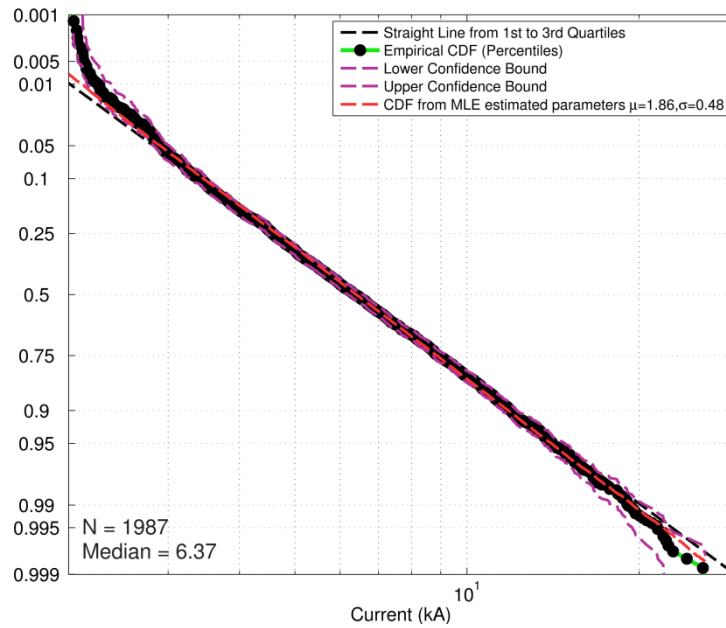


Figure 4.8. Peak current probability plot.

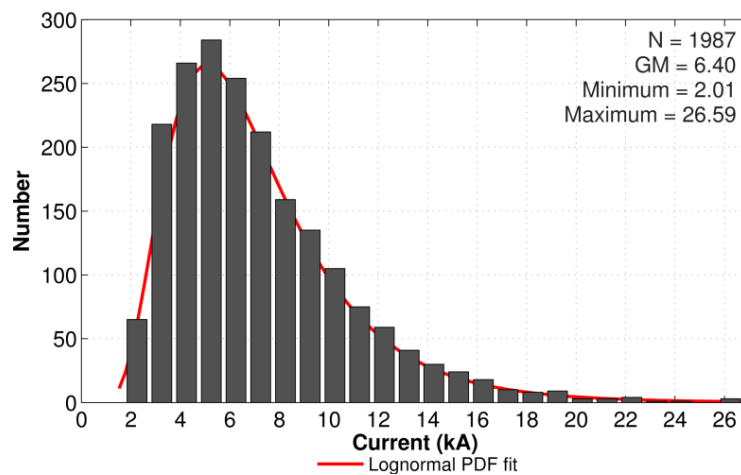


Figure 4.9. Peak current histogram

TABLE II
STATISTICAL PARAMETERS OF PEAK CURRENT

Peak current (kA)						
Tower	Sample size	Percentage <u>Exceeding</u> Tabulated Value				
		95%	90%	50%	10%	5%
Empire State Building [139]	82	-	4	5	10	-
San Salvatore [140]	176	-	4.2	10	25	-
Moscow Ostankino Tower [142] [◇]	58	-	4	9	19	-
Peissenberg [141]*	125	-	-	8.5	-	20
CN Tower [94] [◇]	387	1.3	-	5.1	-	16
Gaisberg Tower [81] [#]	476	3.5	4.2	9.2	18	22
Sântis (This study)	1987	2.9	3.4	6.4	11.9	14.1

[◇] Measurements at 533 m above ground

* for ICC pulses and return-stroke pulses

[#] Current pulses underwent a 250-kHz low pass filtering

4.5.3 Current Risetime

Estimates of the risetime of the measured lightning current pulses are useful in the determination of idealized lightning current waveforms, than can be used in many applications such as testing, electromagnetic simulation, power system protection planning [143], bandwidth estimation and sensor design([144] [127]).

This section presents a discussion on the influence of the definitions adopted to calculate the current risetime on the associated statistical distributions that can be inferred from a set of experimental data. In particular, two different definitions are considered in this study: (i) the t_{10-90} (sometimes referred to as T-10 [118]) and, (ii) the t_{mr} definition proposed by Baum [145] and discussed by Giri et al. [146, 147].

The t_{10-90} definition [6] is frequently used for lightning applications and lightning standards. This definition is illustrated in Figure 4.10 (adapted from [148]) and it is acceptable for monotonously rising waveforms. However, its application to current waveforms with early-time oscillatory behavior (such as those obtained from instrumented towers) might be problematic. Indeed, for pulses with fine structure in their rising part, both the 10% and the 90% values might be reached more than once, making the measurement of the t_{10-90} rise time ambiguous.

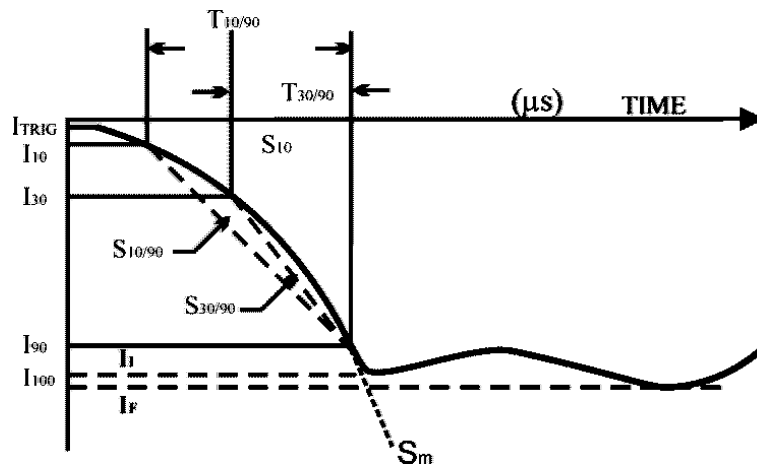


Figure 4.10 Definition of the t_{10-90} current risetime (Adapted from [148]). We use the absolute peak in the determination of the t_{10-90} risetime.

An alternative definition for the current risetime, used for instance, in Nuclear Electromagnetic Pulse (NEMP) studies is the risetime associated with the maximum rate of rise t_{mr} given by [146]:

$$t_{mr} = \frac{I_{peak}}{(di/dt)_{peak}} \tag{4.1}$$

To illustrate the difference between the two definitions, especially in the case where the waveform is characterized by a complex early-time behavior, we will consider the example shown in Figure 4.11a,b taken from our experimental dataset. The application of Equation 4.1 results in a rise time of 0.3 μs , while the use of the t_{10-90} definition yields a risetime of 0.7 μs .

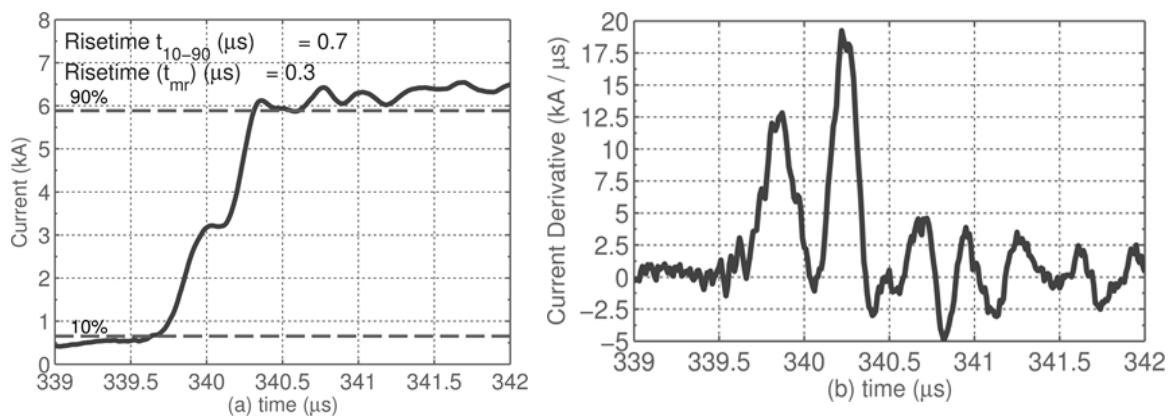


Figure 4.11. Illustration of the use of the two definitions for the determination of current risetime. (a) Current signal (b) Current derivative

Figure 4.12 and Figure 4.13 present the probability plot and histogram of t_{10-90} for a total of $N=1987$ events. Note that for the calculation of t_{10-90} , we considered the absolute peak and the instants when the 10% and 90% times are reached for the first time.

The statistical distributions for the risetime t_{mr} defined by Eq. 4.1 are presented in Figure 4.14 and Figure 4.15. Table 3 summarizes the statistical results associated with the two considered definitions.

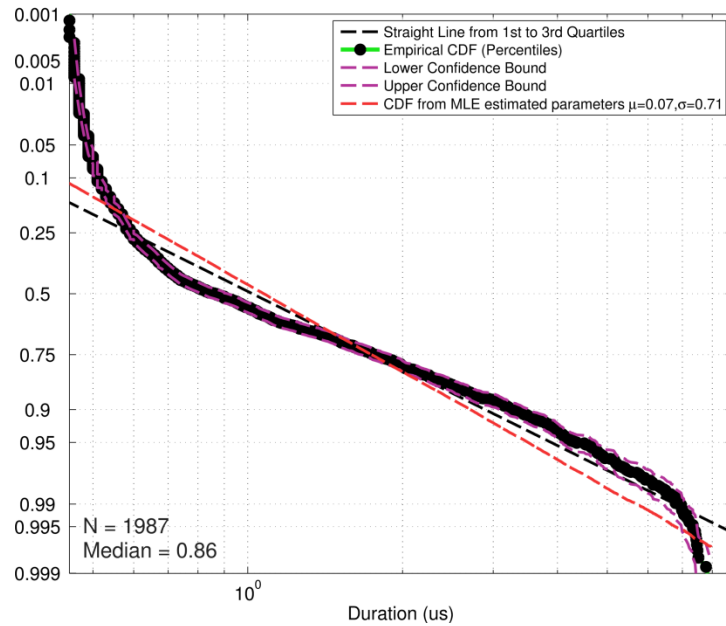


Figure 4.12. Probability plot for the t_{10-90} current risetime.

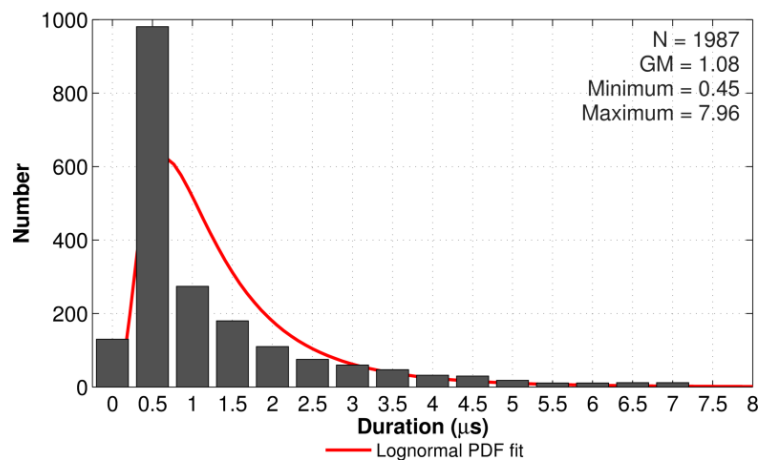


Figure 4.13. Histogram for the t_{10-90} current risetime.

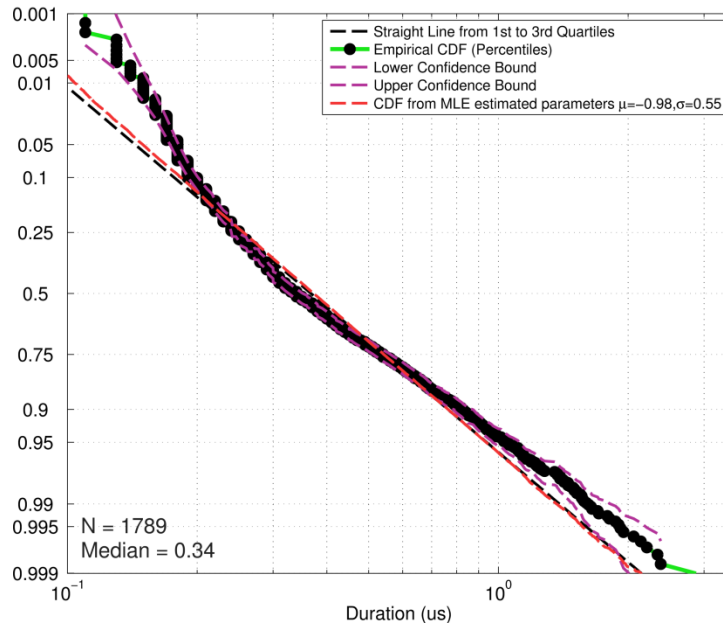


Figure 4.14. Probability plot for the t_{mr} current risetime.

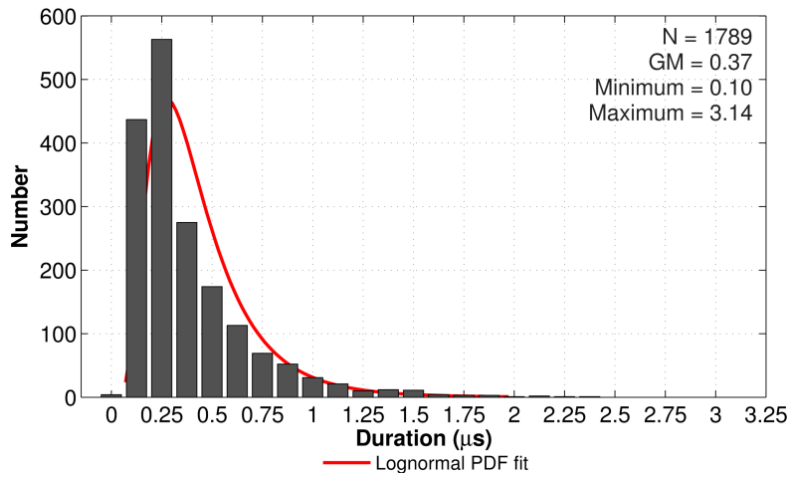


Figure 4.15. Histogram for the t_{mr} current risetime.

TABLE III
STATISTICAL PARAMETERS OF CURRENT RISETIME

Measure	Risetime						
	Parameter	N	Percentage <u>Exceeding</u> Tabulated Value				
			95%	90%	50%	10%	5%
$t_{10-90\%}$ (μs)	GM=1.08 Median=0.86 Max=7.96	1987	0.49	0.51	0.86	3.29	4.36
t_{mr} (μs)	GM=0.37 Median=0.34 Max=3.14	1789	0.18	0.19	0.34	0.82	1.05

It can be seen that the statistical values obtained for t_{mr} are substantially smaller than those for the classical t_{10-90} . The median and the geometrical mean of t_{10-90} (0.9 μs and 1.08 μs , respectively) are 3 times as large as those of the t_{mr} (0.3 μs and 0.37 μs).

The probability plots for the two definitions are plotted on the same graph for comparison in Figure 4.16.

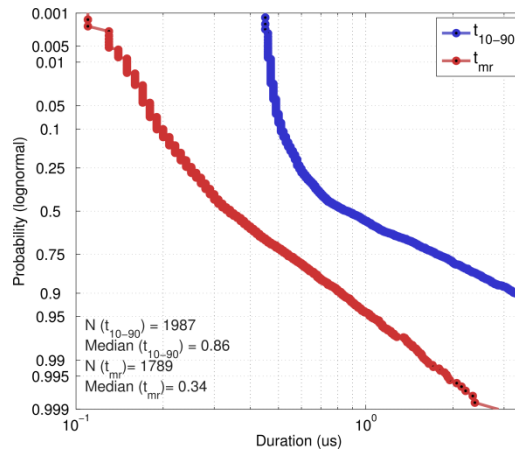


Figure 4.16. Probability plot for the t_{10-90} and t_{mr} .

It is worth noting that the t_{mr} definition does not always result in lower values compared with its t_{10-90} counterpart. An example in which the maximum peak is largely separated from the 90% point is shown Figure 4.17. In this case, the estimated t_{10-90} risetime is 11.9 μs , the maximum current is 2.05 kA and the maximum current derivative is 5.63×10^4 A/s, leading to a value of $t_{mr} = 36.43 \mu\text{s}$ which is over three times the t_{10-90} value.

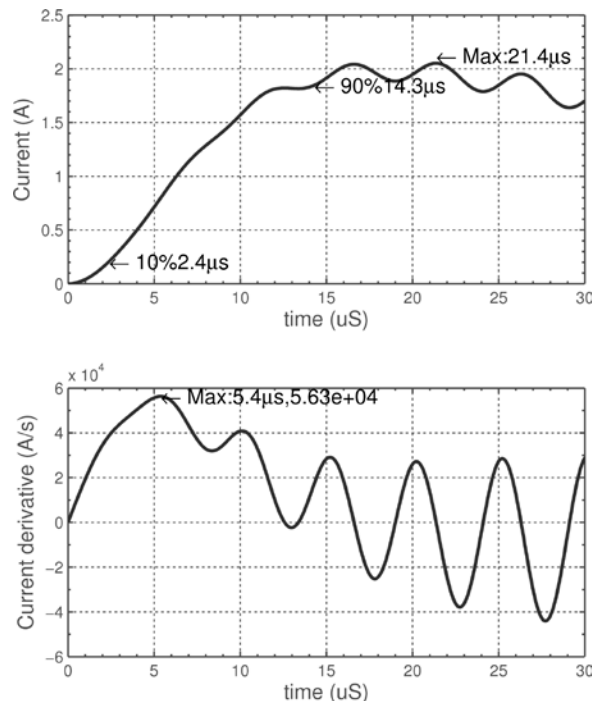


Figure 4.17. Synthetic waveforms of current and current derivative illustrating a case for which t_{mr} is larger than t_{10-90} .

The risetime is inversely related to the bandwidth of impulsive signals but the exact relation depends on the actual form of the frequency response of the signal.

To compare the ability of the two definitions (t_{mr} and t_{10-90}) in quantifying the maximum significant frequency of the spectrum, we evaluated for each pulse the maximum frequency that gives an inverse-FFT reconstruction with an error difference between the measured current and the reconstructed signal of less than 0.1%. Figure 4.18a and b present, for the whole Säntis dataset, the plots of $1/t_{mr}$ and $1/t_{10-90}$ as a function of the maximum frequency.

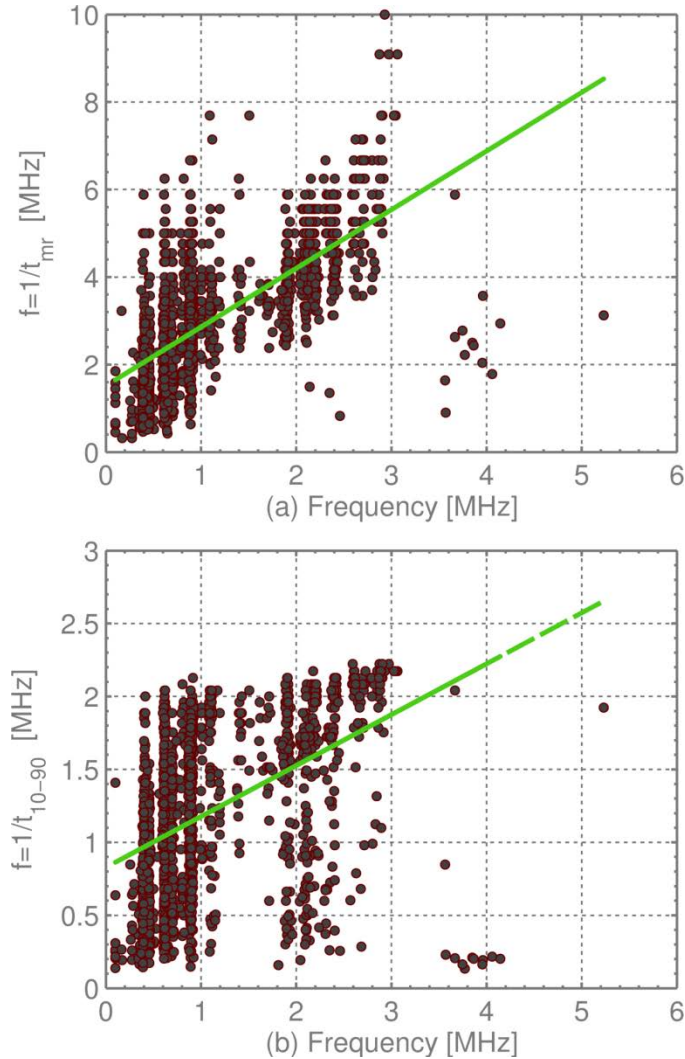


Figure 4.18. Relation between risetimes and bandwidth (a) $1/t_{mr}$ as a function of the maximum frequency and (b) $1/t_{10-90}$ as a function of the maximum frequency.

It can be seen that, overall, the t_{mr} definition is more consistent with the maximum frequency content of the signals, compared with the t_{10-90} . The calculated R^2 coefficients for t_{mr} and t_{10-90} are 0.47 and 0.21, respectively.

4.5.4 Pulse Charge

Figure 4.19 and Figure 4.20 present the probability plot and histogram of the transferred charge associated with each pulse for a total of $N=1987$ events. The median charge is 0.58 C.

Table IV presents a comparison of the obtained statistical data with available data in the literature. It can be seen that the obtained statistical data are very similar to those obtained recently at the Gaisberg Tower.

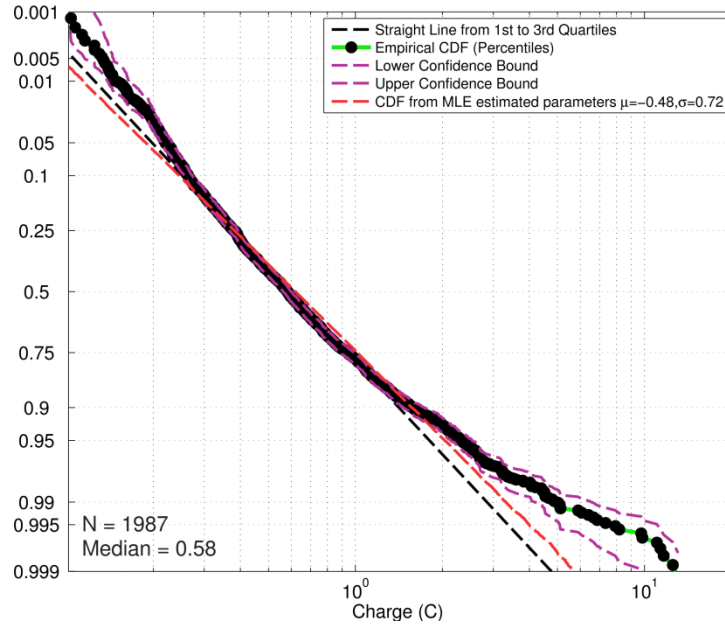


Figure 4.19. Pulse charge probability plot.

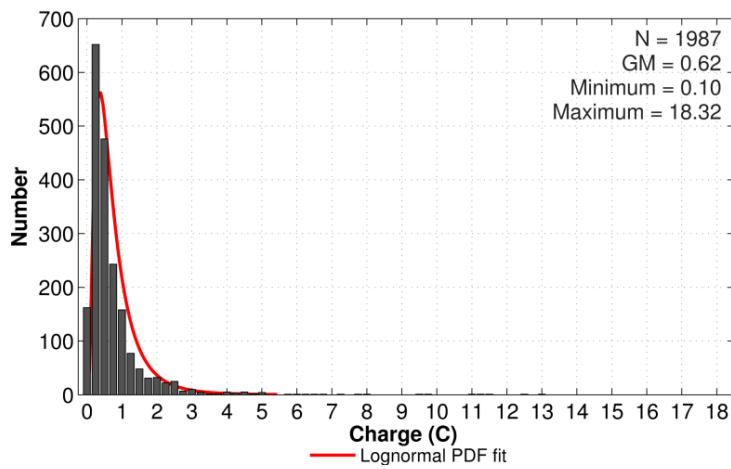


Figure 4.20. Pulse charge histogram.

TABLE IV
STATISTICAL PARAMETERS OF PULSE CHARGE

Pulse Charge (C)						
Tower	Sample size	Percentage <u>Exceeding</u> Tabulated Value				
		95%	90%	50%	10%	5%
Empire State Building [139]	81	-	-	0.15	1.3	-
San Salvatore [140]	579	-	0.14	0.77	4.1	-
Gaisberg Tower [8]	615	0.15	0.2	0.51	1.2	1.7
Säntis (This study)	1987	0.2	0.3	0.6	1.6	2.3

4.5.5 Pulse Duration

The pulse duration is defined as the time from the peak current point to the point where the current decays to 10% of this value. This definition is illustrated in Figure 4.21.

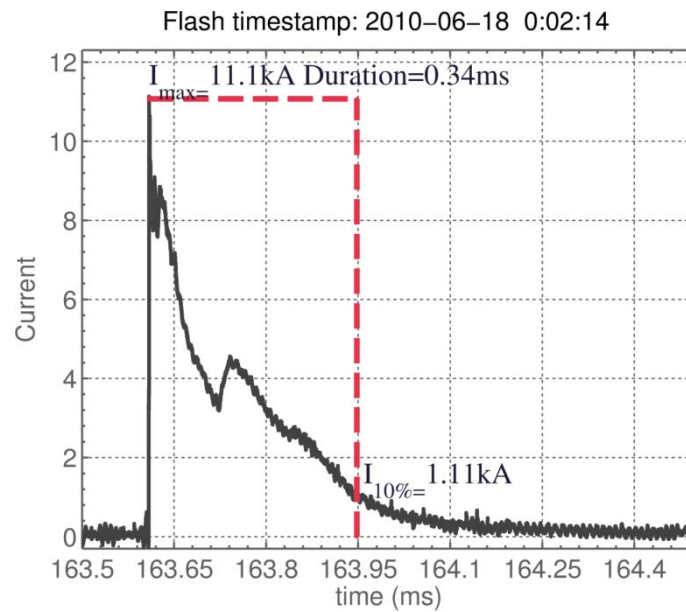


Figure 4.21. Definition of the pulse duration.

Figure 4.22 and Figure 4.23 present the probability plot and histogram of the pulse duration. The adopted definition is measured from the peak value to 10% of the pulse value. A total of N=1987 events are analyzed.

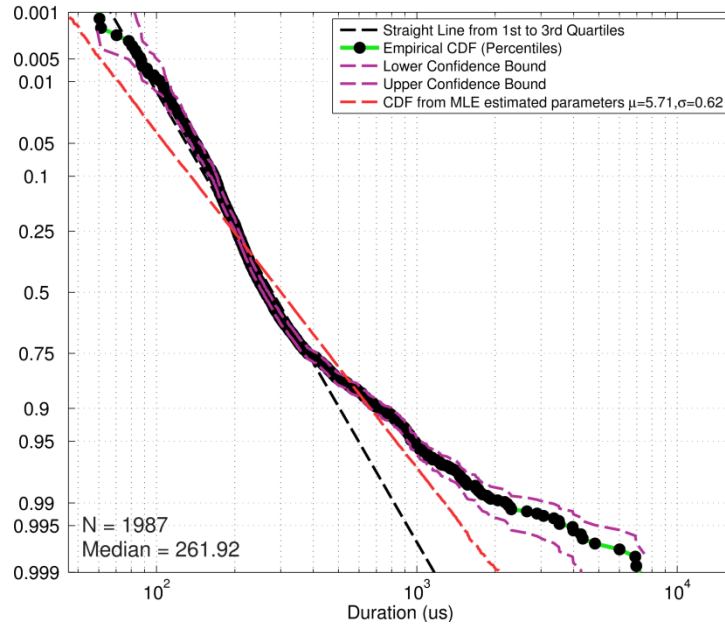


Figure 4.22. Pulse duration probability plot.

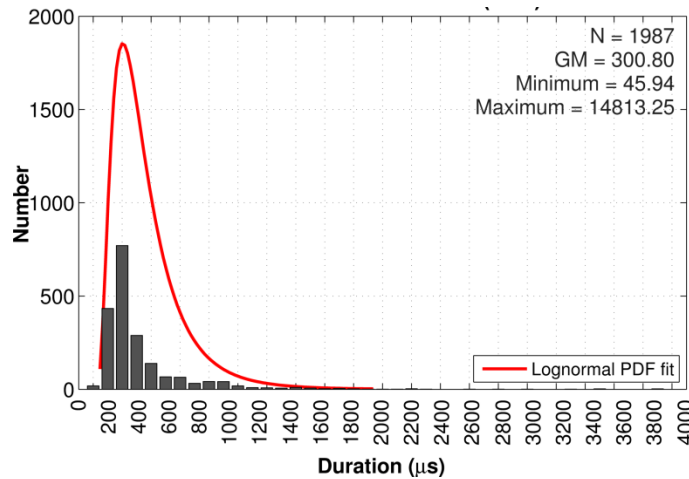


Figure 4.23. Pulse duration histogram.

Figure 4.24a and b present a scatter plot and a regression comparing the values of current peak and pulse duration as a function of transferred pulse charge. The data present a positive correlation for both figures.

Note that two pulses (Nodes 3240, 3241 as labeled in the Säntis database, and also visible on Figure 4.24a and b labels) associated with high charges correspond to a single flash occurred on 2011-17-13 at 17:36.36pm. The overall current measurement with this flash is presented in Figure 4.25a, and the detail of the aforementioned nodes is depicted in Figure 4.25b. This flash is characterized by a long initial continuous current of about 400 ms, followed by 4 return strokes. The overall charge transferred to ground for this flash is close to 200 C.

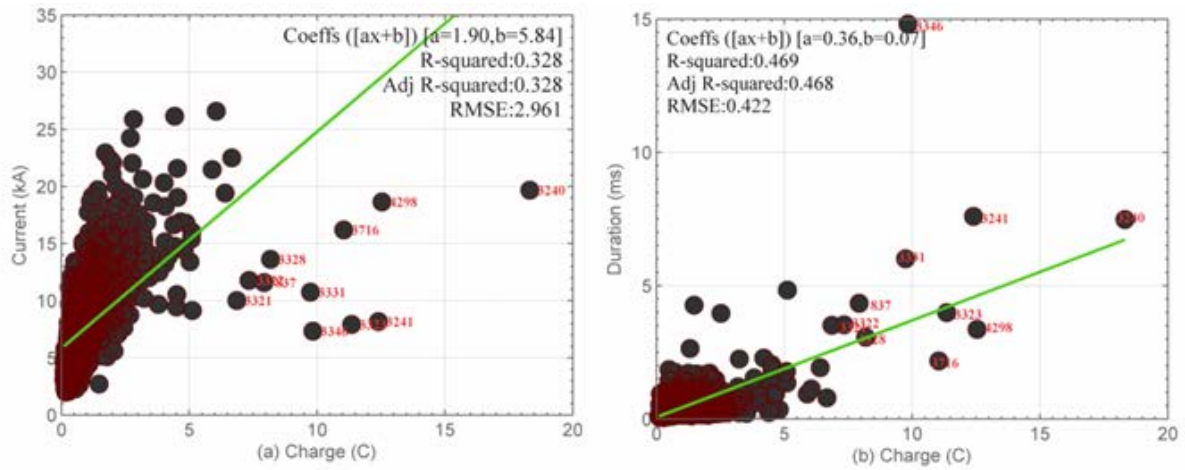


Figure 4.24. Comparison between the charge and other parameters

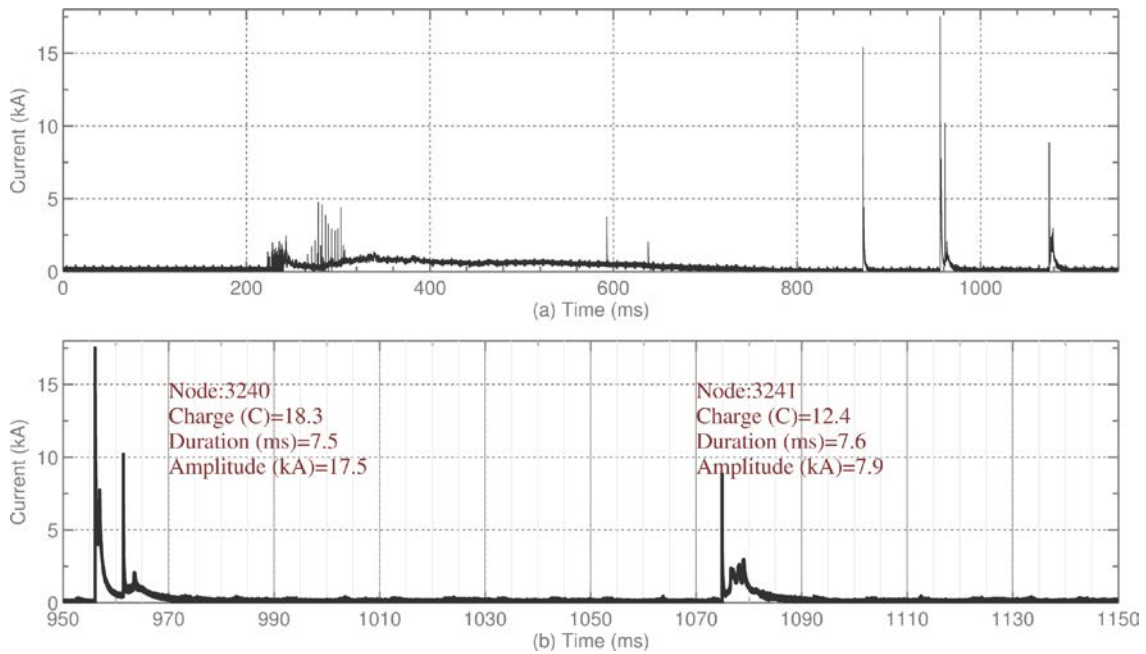


Figure 4.25. Example of a current waveform associated with an upward negative flash occurred on 2011-07-13 at 17:36.26. (a) Overall flash current. (b) Details of the last two pulses (return strokes).

The event corresponding to the pulse with the longest duration is presented in Figure 4.26. The measured pulse duration is 14.8 ms. Note that the long pulse duration is due to the presence of a continuing current which followed the main pulse.

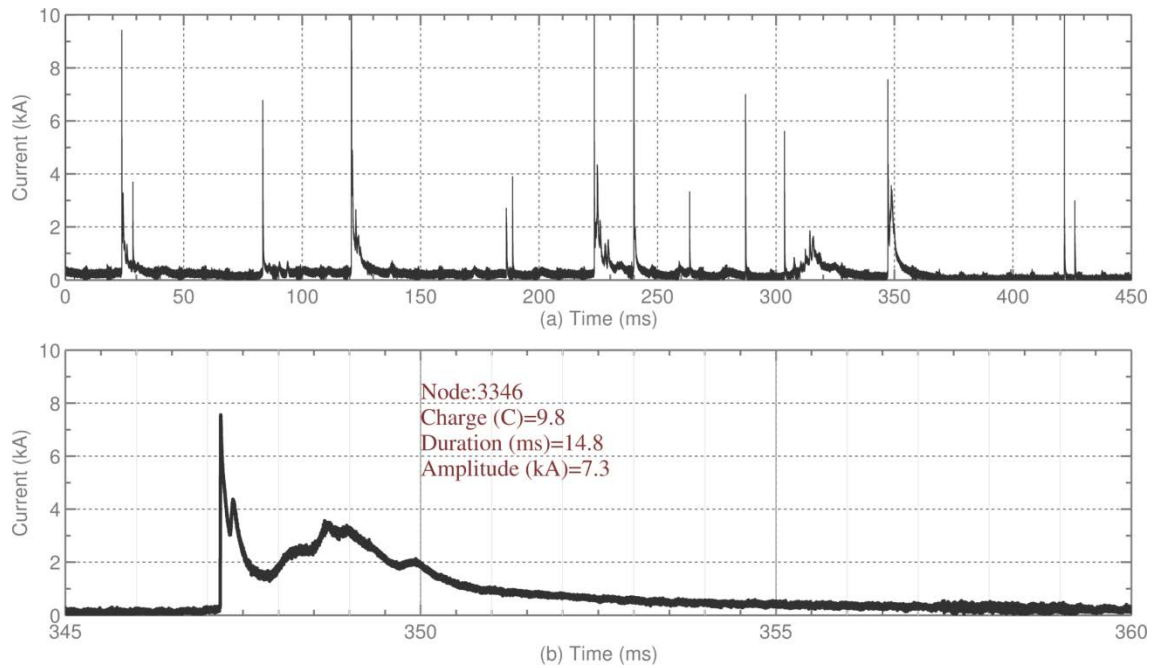


Figure 4.26. Flash occurred on 2011-07-23 at 17:40.57. (a) Current for the overall flash (b) Detail of the pulse occurred at about 350 ms, with the longest pulse duration.

4.5.6 Inter-pulse Interval

Figure 4.27 and Figure 4.28 present the probability plot and histogram of the inter-pulse interval for a total number of 1820 pulses. The obtained value for the median (17.2 ms) is consistent with the value reported at Gaisberg Tower (17.3 ms) [8].

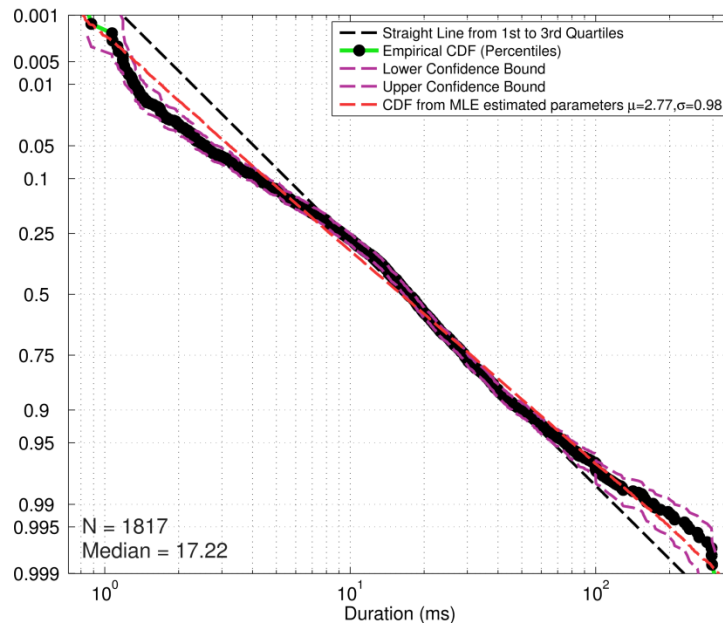


Figure 4.27. Inter-pulse interval probability plot.

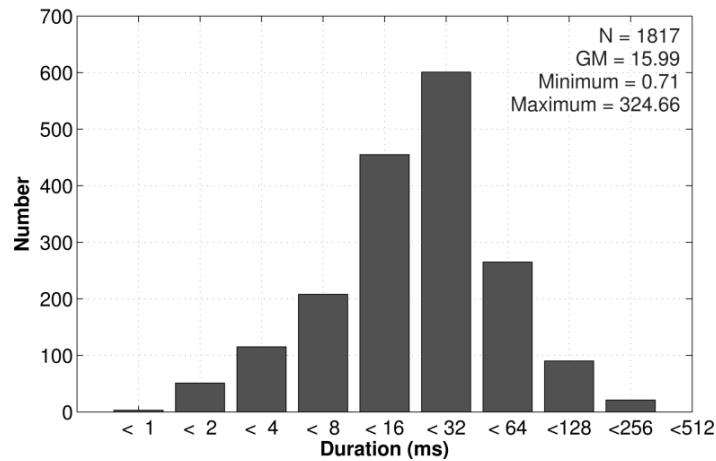


Figure 4.28. Inter-pulse interval histogram.

4.5.7 Total Flash Charge

The noise level associated with the measurement system does not allow us to accurately characterize flashes with a relatively low initial continuous current. As a result, no statistical data will be presented for the total transferred charge associated with the flashes. Table V presents the data for the total transferred charge, total flash duration and the ICC duration for 4 flashes. The associated current waveforms and charge calculation are presented in Figure 4.29, Figure 4.30, Figure 4.31 and Figure 4.32. It is interesting to observe that, at least in some cases, large amount of charge transfers (in excess of 50 C) can be associated to upward negative flashes.

TABLE V
SUMMARY OF ESTIMATED PARAMETERS FOR THE TOTAL FLASH CHARGE IN 4 EVENTS

Flash	Total Charge (C)	Total Duration (ms)	ICC current duration (ms)
Flash # 8 2010-07-26 at 17:42	101	1100*	400
Flash # 70 2011-06-22 at 17:21	92	800	700
Flash # 90 2011-07-13 at 16:20	60	550	300
Flash # 92 2011-07-13 at 17:38	181	1100*	800

* The digitizers maximum measurement window associated couldn't cover the whole flash duration

All these four were measured during the convective season (July 2011 and June 2012). The main charge transfer is due to the long initial continuous current, while the individual strokes contribute marginally to the total charge.

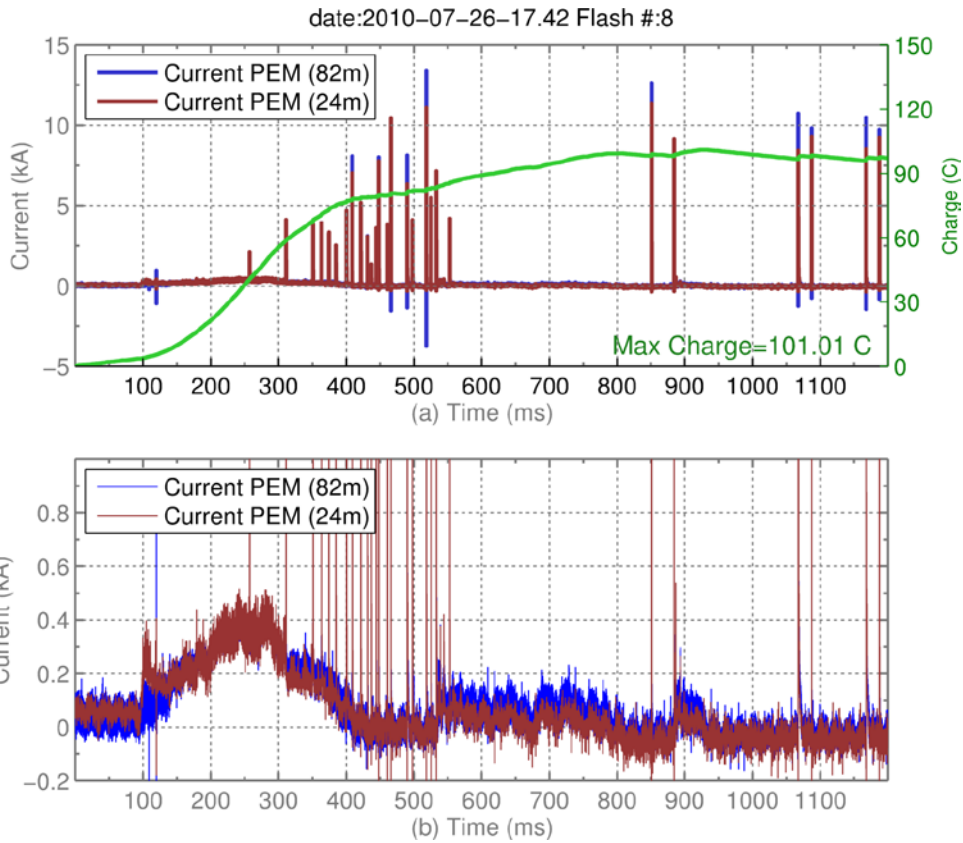


Figure 4.29. Flash # 8 2010-07-26 at 17:42 (a) Flash current for current channels at the two tower heights, the integrated charge value is plotted on the right (b) Detail of the current values up to 1 kA.

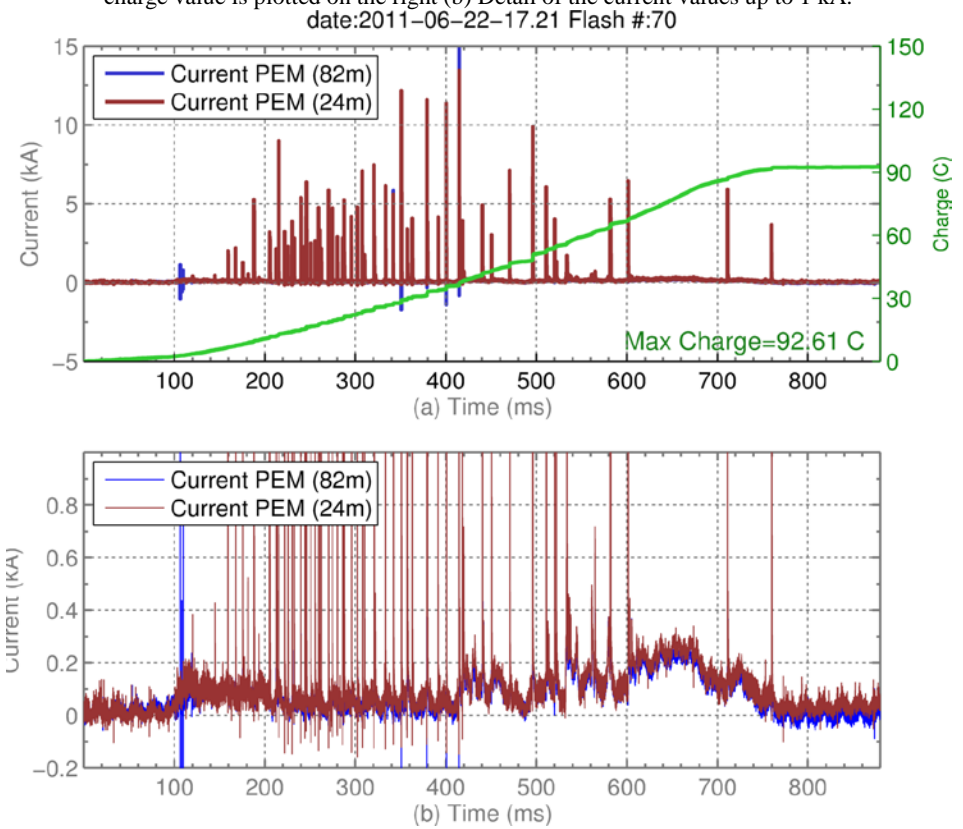


Figure 4.30. Flash # 70 2011-06-22 at 17:21 (a) Flash current for current channels at the two tower heights, the integrated charge value is plotted on the right (b) Detail of the current values up to 1 kA.

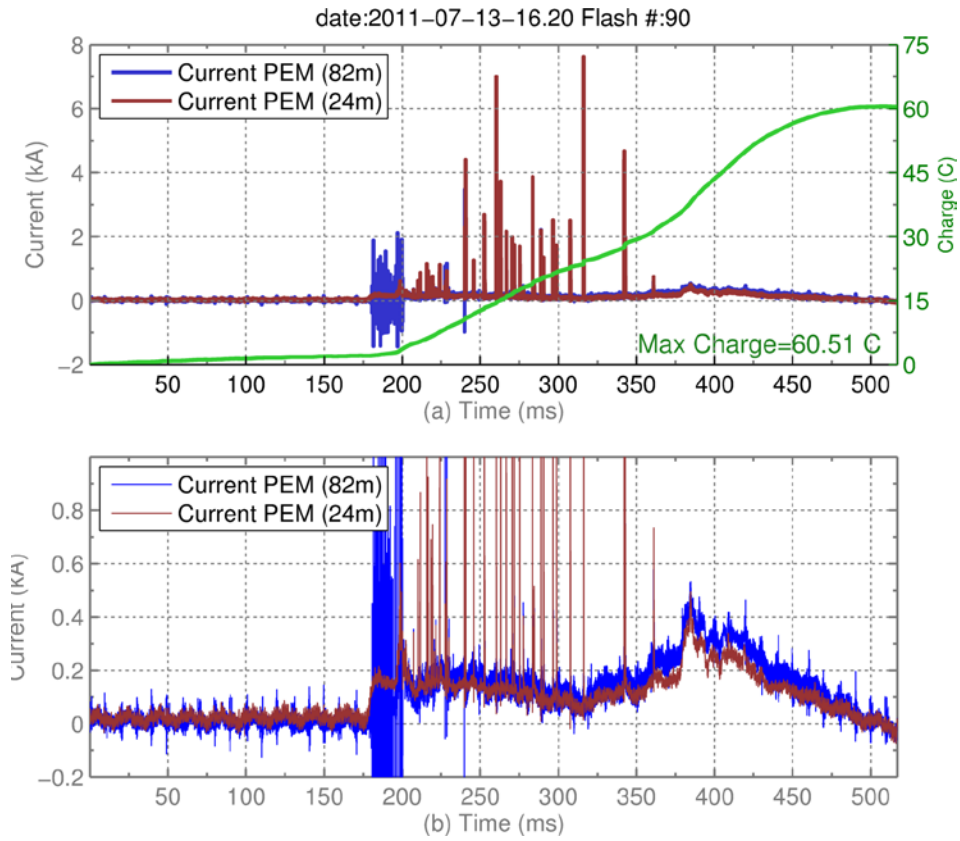


Figure 4.31. Flash # 90 2011-07-13 at 16:20 (a) Flash current for current channels at the two tower heights, the integrated charge value is plotted on the right (b) Detail of the current values up to 1 kA.

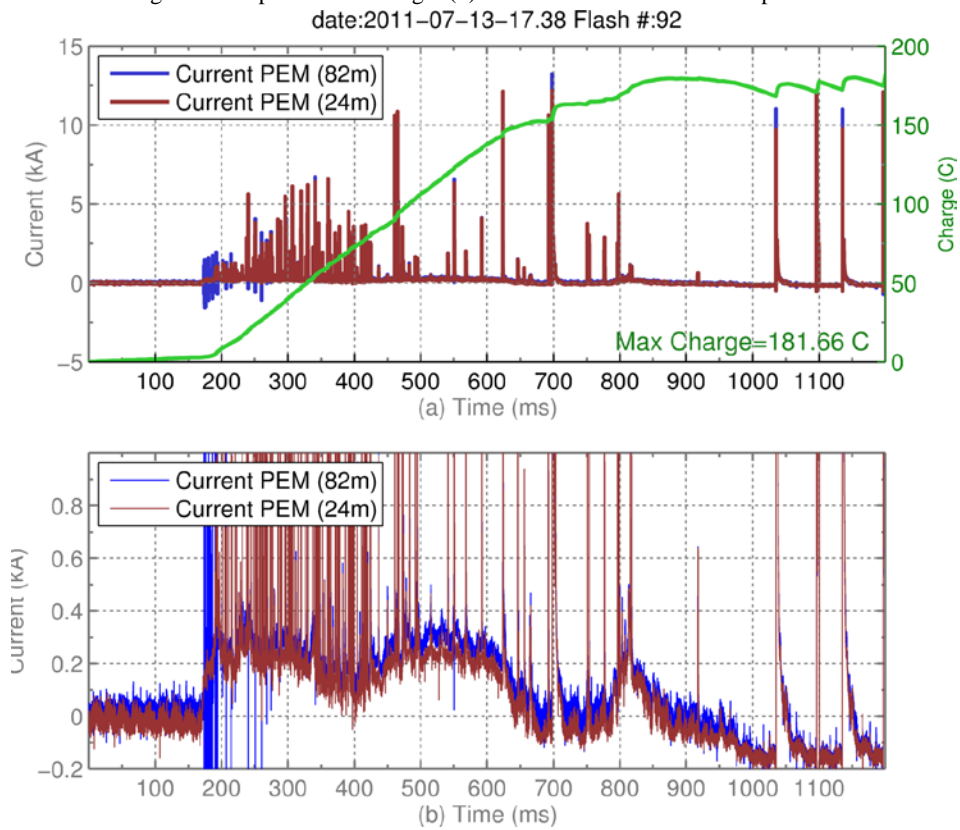


Figure 4.32. Flash # 92 2011-07-13 at 17:38 (a) Flash current for current channels at the two tower heights, the integrated charge value is plotted on the right (b) Detail of the current values up to 1 kA.

4.5.8 Flash Multiplicity

The histogram of the flash multiplicity or the number of pulses per flash is presented in Figure 4.33. It presents a lognormal distribution with a median of 8 pulses per flash. It is worth noting that the flash multiplicity is determined considering all the pulses of each flash satisfying two conditions that are indicative of leader/return-stroke mode of charge transfer [133], namely a risetime lower than 8 μ sec and an amplitude superior to 2-kA.

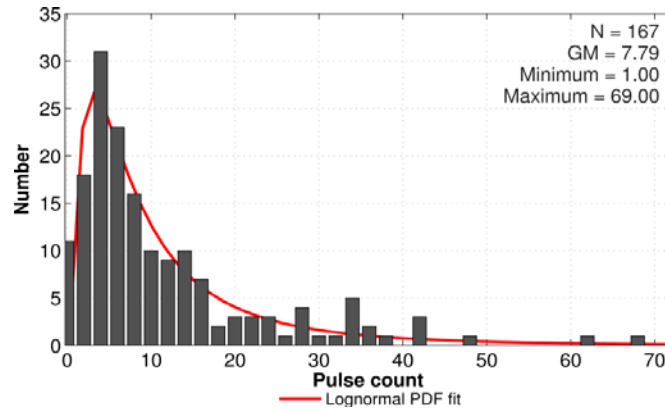


Figure 4.33. Flash multiplicity histogram.

Figure 4.34 shows a flash with large pulse multiplicity (62), along with expanded views of the first 320 ms and the time window between 350 and 450 ms.

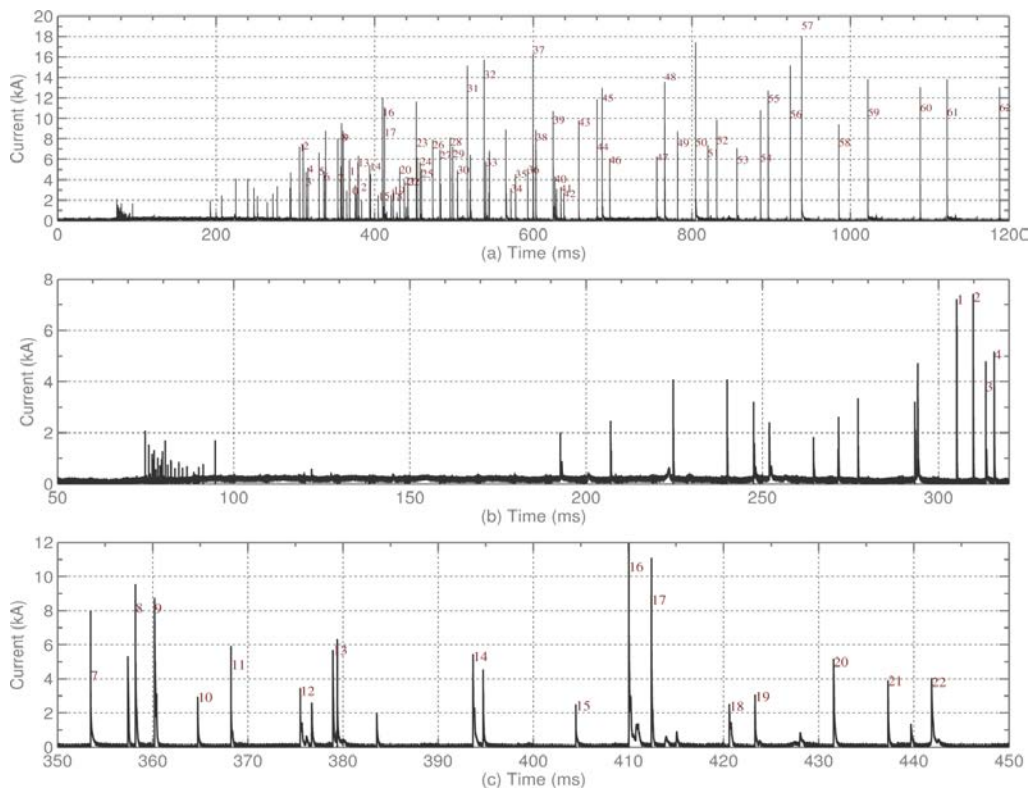


Figure 4.34. Flash with large multiplicity (62) occurred on 2011-08-27 at 09:24.16 am. Classified pulses are numbered on figure. (a) Overall flash current (b) Expanded view of first 320 ms (c) Expanded view of time window between 350- 450ms.

4.6 Summary and Conclusions

In this Chapter, we presented statistical distributions of the lightning current parameters based on the lightning current and current-derivative waveforms measured at the Sántis Tower site in 2010 and 2011. The total number of flashes analyzed in this study was 167 which include nearly 2000 pulses. The statistical distributions are associated with upward negative flashes.

It is shown that negative flashes are mainly concentrated in the summer months during the convective season. This distribution contrasts with the Gaisberg Tower measurements for which lightning strikes are quasi-uniformly distributed over the year. Most of the flashes occurred during the afternoon, mostly between 4 and 8 PM. however, an appreciable number of flashes occurred in the morning, mostly between 6 and 10 AM.

Table VI summarizes the obtained statistical data on lightning current parameters. It is worth noting that the obtained data constitutes the largest dataset available to this date. The obtained data were compared to and found, in general, to be consistent with published data associated with measurements obtained at other sites. The statistical data on the current risetime are quite unique. Two different definitions were used to determine the current risetime. The first is the t_{10-90} risetime, frequently used in lightning applications and lightning standards. The second definition is the risetime associated with the maximum rate of rise t_{mr} given by the ratio of the current peak to the current maximum derivative. The obtained statistical values for t_{mr} were found to be substantially smaller than those for the classical t_{10-90} . In particular, the median value of t_{10-90} (equal to $0.9 \mu\text{s}$) was found to be 3 times as large as that of the t_{mr} (equal to $0.3 \mu\text{s}$) and the same ratio was observed for the geometrical means ($1.08 \mu\text{s}$ and $0.37 \mu\text{s}$).

The noise level associated with the measurement system did not allow us to accurately characterize flashes with a relatively low initial continuous current. As a result, no statistical data were presented for the total transferred charge associated with the flashes. Nevertheless, it was found that many flashes were characterized by a large amount of charge transfers (in excess of 50 C). The main charge transfer is due to the long initial continuous current, while the individual strokes contribute marginally to the total charge.

The median value of the flash multiplicity or the number of pulses per flash was found to be 8, a value much larger than those associated with downward flashes.

TABLE VI
SUMMARY OF STATISTICAL PARAMETERS OF LIGHTNING CURRENTS ASSOCIATED WITH UPWARD NEGATIVE
FLASHES MEASURED AT SÄNTIS TOWER

Parameter	Sample size	Percentage <u>Exceeding</u> Tabulated Value				
		95%	90%	50%	10%	5%
Peak current derivative kA/ μ s	1851	3.9	4.8	19.9	46.5	56.3
Peak current kA[140]	1987	2.9	3.4	6.4	11.9	14.1
t_{10-90} μ s	1987	0.49	0.51	0.86	3.29	4.36
t_{mr} μ s	1789	0.18	0.19	0.34	0.82	1.05
Pulse Charge C	1987	0.2	0.3	0.6	1.6	2.3
Inter-pulse Interval ms	1817	2.57	4.15	17.2	50.1	75.1
Flash Multiplicity Count	167	1	2.2	8	29	37
Stroke Duration μ s	1978	141	166	262	724	978

Chapter 5. Statistics of Positive and Bipolar Lightning Flashes Recorded on the Söntis Tower in 2010 and 2011

5.1 Introduction

This chapter presents an analysis of measured current waveforms associated with positive and bipolar flashes recorded on the Söntis tower from May 2010 till January 2012. The overall number of recorded flashes in the considered period was 201, of which 30 were of positive polarity (effectively transported positive charge to ground) and 3 were classified as bipolar.

Even though positive lightning flashes are less frequent than negative ones, they are of particular interest for a number of reasons, most importantly:

- (1) Positive flashes are characterized by high peak currents and large impulse charges [149]. As a result, they are a major concern for the designers of lightning protection systems of structures such as wind turbines and telecommunication towers.
- (2) Their electromagnetic field waveforms are often characterized by a complex structure that makes them difficult to detect and classify by lightning location systems [149].
- (3) It has been found that positive lightning flashes are related to the initiation of transient luminous events in the middle atmosphere (e.g. [150, 151]).

Furthermore, experimental data on positive lightning are very limited and often controversial [149]. A better understanding of positive lightning is therefore needed for studying cloud electrification mechanisms, charge distribution in thunderclouds, lightning discharges in the middle and upper atmosphere and improved lightning protection of systems [149].

Except for a handful studies (e.g. [76, 152-154]) presenting directly measured current waveforms associated with positive flashes, most of the recent studies on the physics and characterization of positive lightning are based either on remote electric field measurements (e.g. [58, 155, 156]), high-speed video observations (e.g. [151, 157-160]), or a combination of the two (e.g. [161]).

As for the negative flashes discussed in Chapter 4, positive flashes observed on the Säntis Tower (see Figure 5.1) are also concentrated in the summer months, August being the month during which most of the positive flashes occurred (6 events in 2010 and 16 events in 2011).

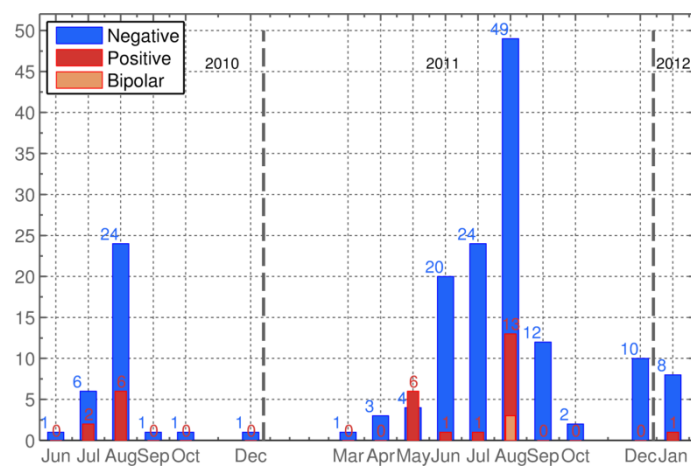


Figure 5.1. Flashes count to the Säntis tower. June 2010 to January 2012.

5.2 Obtained Data

Table I presents values for the current peak, total transferred charge, duration and action integral for all recorded positive flashes. All recorded positive flashes were composed of a single main pulse, except those recorded on August 1, 2010 and August 3, 2011 (11:51) that contained two pulses.

The observed current waveforms were classified into two types, as described in the following two subsections. Note that, throughout this chapter, negative current polarity indicates positive charge transfer to ground.

TABLE I. CURRENT PEAK, TOTAL TRANSFERRED CHARGE AND FLASH DURATION OF POSITIVE FLASHES RECORDED ON THE SÁNTIS TOWER

Flash Number	Number and Time tag (dd.mm.yy hh.mm)	I_p (kA)	Q (C)	Duration (ms)	Action Int. ($\times 10^3$ A ² s)	Type
1	21.07.2010 19:05	42.6	280.9	111	1.700	1
2	21.07.2010 19:31	18.0	84.0	51	0.295	1
3	01.08.2010 20:00	0.7	2.7	15	0.001	2
4	01.08.2010 20:02	2.39*	16.7	77	0.013	2
5	01.08.2010 20:06	1.5	6.8	40	0.003	2
6	15.08.2010 14:34	13.2	189.1	55	0.798	2
7	15.08.2010 14:37	3.8	134.8	83	0.210	2
8	30.08.2010 04:42	6.4	153.4	68	0.366	2
9	01.05.2011 12:36	11.8	8.3	9	0.024	2
10	20.05.2011 15:29	21.6	30.2	12	0.219	2
11	22.05.2011 23:48	11.7	31.4	17	0.058	2
12	26.05.2011 17:53	1.8	19.5	60	0.013	2
13	26.05.2011 18:00	16.6	14.8	15	0.056	1
14	26.05.2011 18:03	31.5	41.1	40	0.135	1
15	06.06.2011 10:36	12.3	80.6	100	0.116	2
16	08.07.2011 01:06	11.9	899.6	370	4.001	2
17	03.08.2011 11:51	92.8	404.2	50	4.185	2
18	03.08.2011 12:16	3.9	15.0	25	0.013	2
19	27.08.2011 05:43	12.0	853.3	250	4.787	2
20	27.08.2011 06:00	8.0	363.9	300	0.602	2
21	27.08.2011 06:02	5.0	460.0	270	0.994	2
22	27.08.2011 06:30	25.7	913.3	260	7.193	2
23	27.08.2011 06:37	12.8	15.0	15	0.020	2
24	27.08.2011 06:46	21.9	902.0	200	7.097	2
25	27.08.2011 06:47	10.8	701.8	210	3.905	2
26	27.08.2011 06:48	10.4	537.7	240	2.342	2
27	27.08.2011 06:50	12.1	700.9	250	3.319	2
28	27.08.2011 08:38	9.3	184.7	170	0.662	2
29	27.08.2011 08:47	8.0	225.7	165	0.424	2
30	05.01.2012 17:21	11.4	512.5	165	2.799	2

*) corresponds to the second, highest peak.

5.3 Classification of Current Waveforms Associated with Positive Flashes

5.3.1 Type I

The first type of observed waveforms is characterized by three stages [52]: (1) an initial, slowly rising portion lasting a few milliseconds, (2) the main pulse, and (3) a long continuing current, as usually observed in positive lightning (e.g. [152] and Chapter 5 of [1]). Prior to the start of the initial, slowly rising portion, the current waveforms are characterized by an oscillatory waveform during which highest currents steepness occur.

A representative example of a waveform of the first type is shown in Figure 5.2, which presents the current waveform associated with a positive flash recorded on July 21, 2010. The long continuing current is clearly discernible in Figure 5.2a.

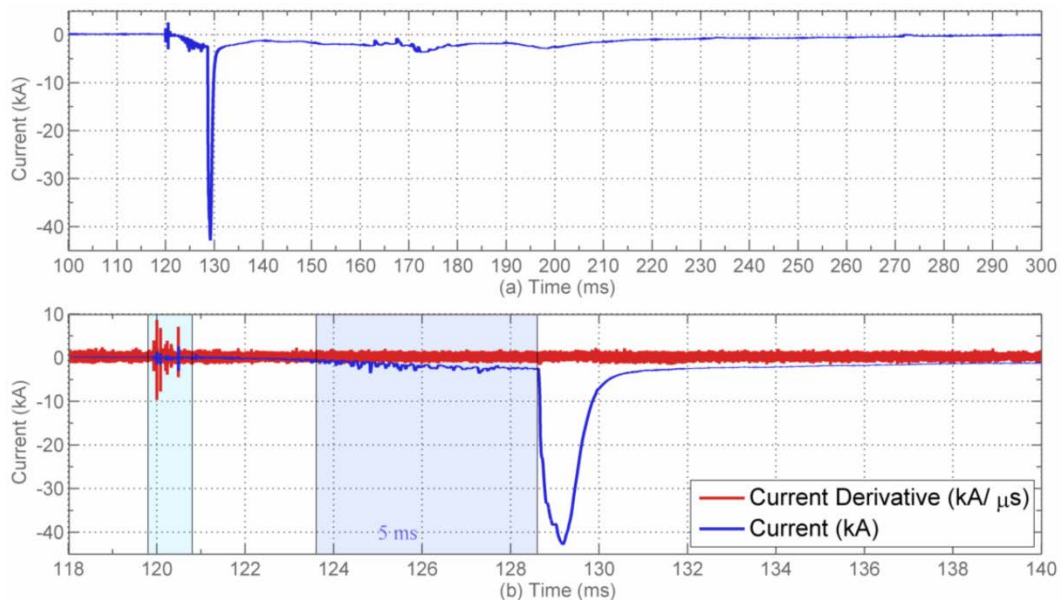


Figure 5.2. Current waveform associated with a positive flash recorded on July 21, 2010, 19:05. (a) Current waveform for the whole flash. (b) Expanded view of the first 20 ms.

An expanded view of the current waveform is shown in Figure 5.2b in which the initial, slowly rising portion is seen to last for about 5 ms at the end of which the current reaches a value of about 2 kA. This slowly rising portion around 120 ms contains some fine structure. The main pulse has a peak value of 43 kA and a zero-to-peak risetime of about 538 μ s. The total charge transferred to ground is 280 Coulombs.

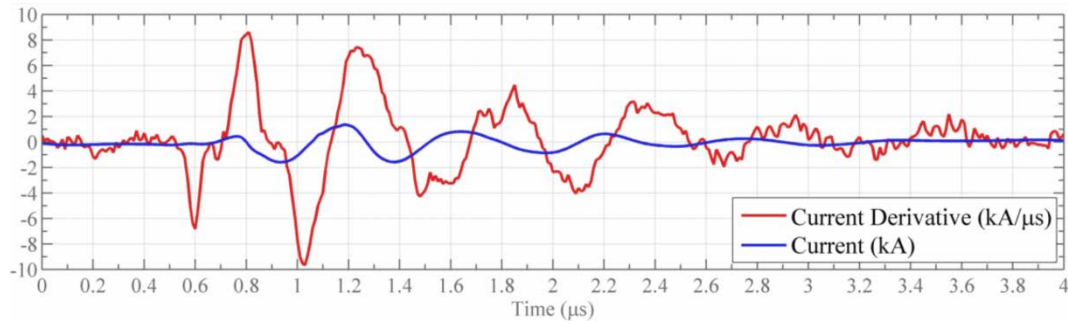


Figure 5.3. Expanded view of the fastest pulse occurring at about 120 ms. Note that the values on the time axis of this figure are relative values.

In Figure 5.2b, we have also shown the time-derivative of the current measured by the B-dot sensor. It can be seen that the highest steepness occurs about 3 ms prior to the initial slowly rising portion of the current. This might be either associated with the onset of the upward negative leader or it may be induced in the tower by cloud discharges.

Figure 5.3 shows a detailed view of the fastest of these pulses (which occurred at a time of about 120 ms), where the time-derivative of the current measured by the B-dot sensor is also shown. Note that in Figure 5.3, the values on the time axis are not absolute values. It can be seen that the current and the current derivative are characterized by an oscillatory waveform with a frequency of about 2.3 MHz, which corresponds to a wavelength of about 130 m.

Figure 5.4 presents another positive flash of the first type recorded on the same day (July 21st). The initial, slowly rising portion lasts about 10 ms, at the end of which the current reaches a value of 1 kA. The peak value of the main pulse is 18 kA, its zero-to-peak risetime is about 80 μ s and the total transferred charge to ground is 84 Coulombs. An expanded view of the initial 4 ms of the main current pulse is shown in Figure 5.4b in which relatively slow subsidiary peaks are visible after the initial peak.

Positive and negative M-component-like pulses are discernible in the continuing current (between 150 and 200 ms), as can be seen in Figure 5.4. The occurrence of M-components in positive flashes was reported recently by Campos et al. [159] who analysed the luminosity-versus-time profiles obtained through video observations. Our recorded data appear to confirm the findings of Campos and co-workers and, to the best of the authors' knowledge, our data constitute the first direct evidence of M-component-like current pulses in positive flashes, except for that seen in Figure 5.1 of [1] and discussed in [150].

It is worth noting that this flash can be viewed as bipolar. An expanded view of a portion of the continuing current is plotted in Figure 5.5, showing a polarity change occurring at about 170 ms (due to an M-component-like pulse).

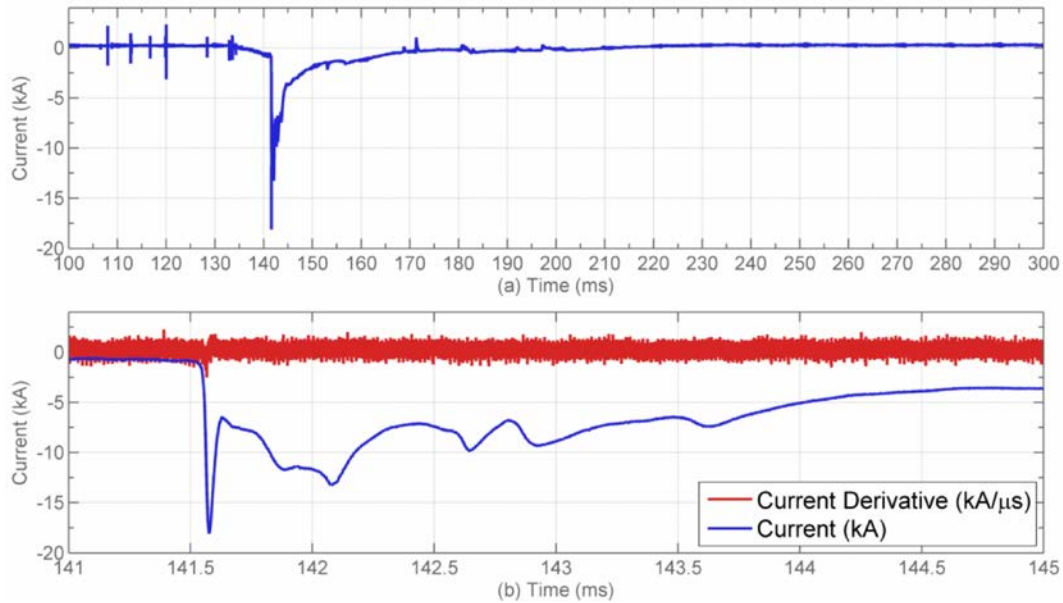


Figure 5.4. Current waveform associated with a positive flash recorded on July 21, 2010, 19:31.

Note also that initial fast pulses can be seen at about 107 ms, 120 ms and right prior to the initial slow rise of the pulse. Figure 5.6 shows an expanded view of the highest initial pulse occurred at about 120 ms. Again, the oscillations can be associated either with the onset of the upward negative leader or may be induced in the tower by cloud discharges. Another likely explanation is the attempted leader process that was observed to occur prior to formation of sustained upward positive leader in rocket-triggered lightning (see for example, Figs. 7.9 and 7.10 of [1]).

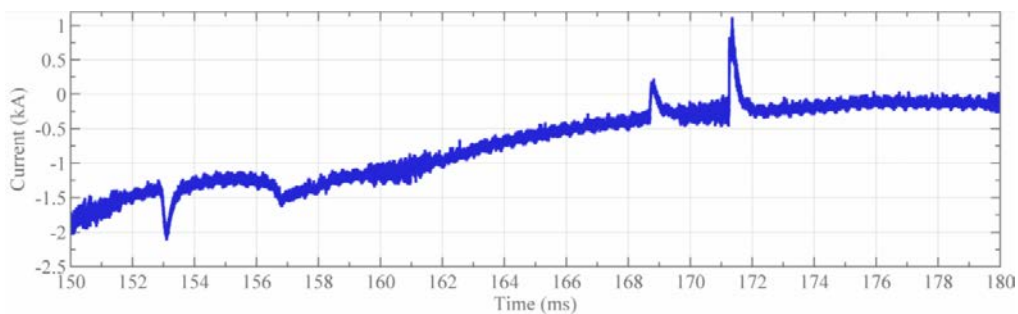


Figure 5.5. Expanded view of the current waveform of Figure 5.4 showing the zero-crossing due to positive-polarity pulse at about 170 ms.

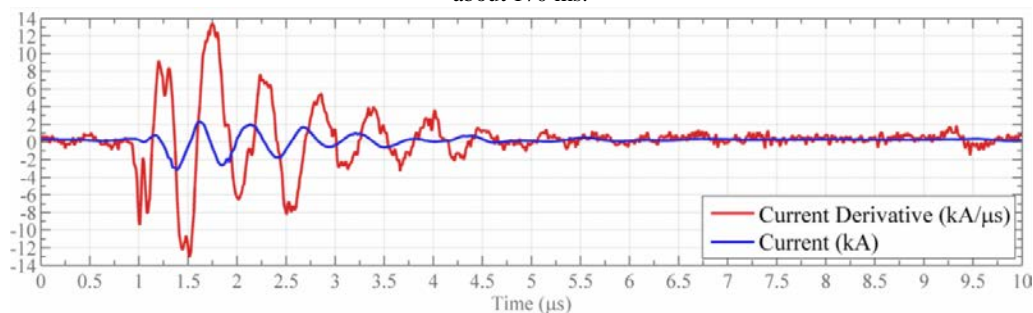


Figure 5.6. Expanded view of the fastest pulse of the current waveform of Figure 5.4 occurring at about 120 ms (blue). Note that the values on the time axis of this figure are relative values. The current derivative is also plotted in red.

5.3.2 Type II

The second type of observed positive flashes is characterized by an initial slowly rising portion with a moderate peak current (not exceeding a few kAmps) and the presence of successive pulses separated by a time interval of some tens of μs , which may be due to an upward negative stepped leader [100, 153, 154].

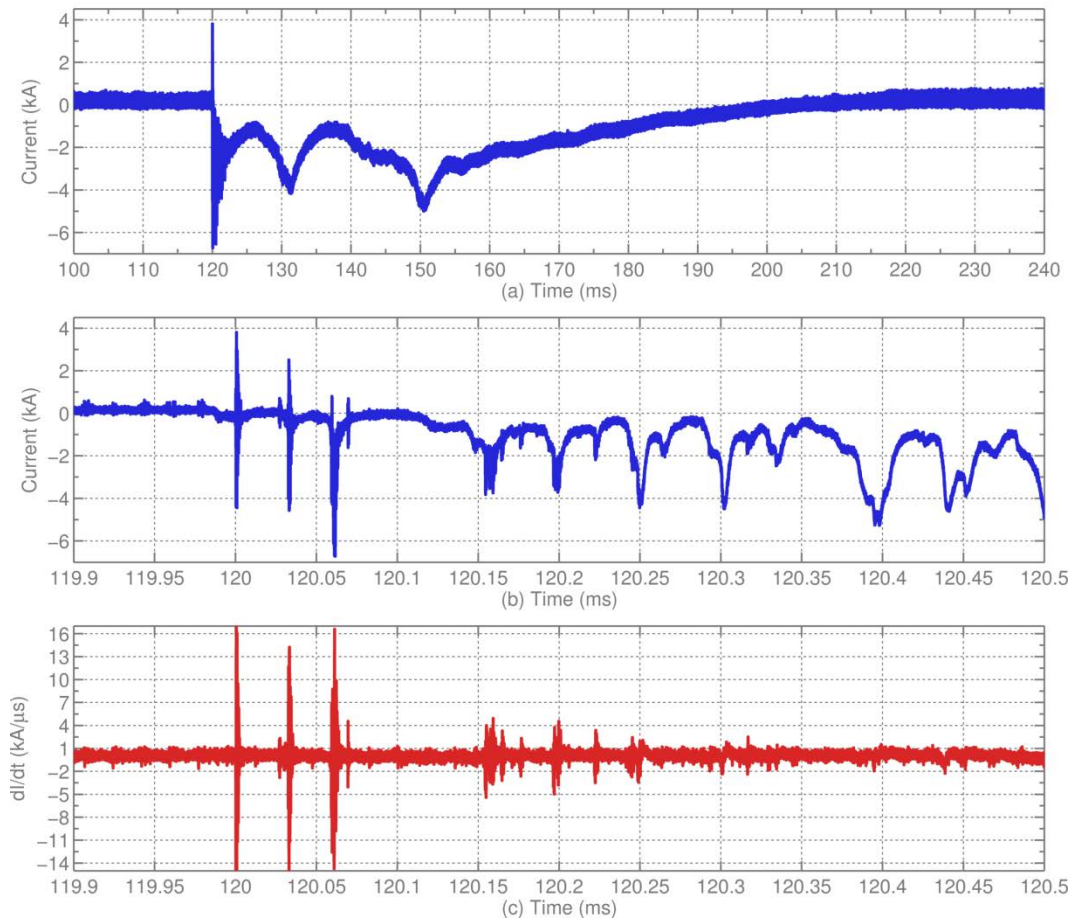


Figure 5.7. Current waveform associated with a positive flash recorded on August 30, 2010 at 04:42. (a) Overall flash (b) Detail of the current between 119.9 and 120.5ms (c) Detail of the current derivative between 119.9 and 120.5ms.

Figure 5.7 presents a current waveform associated with a positive flash of the second type recorded on August 30, 2010 with a current peak of 6.2 kA. The main pulse is followed by 2 M-component-type pulses. Figure 5.7b presents an expanded view of the initial part of the current in which successive pulses separated by a time interval of about 50 μs are seen. In Figure 5.7c, we have plotted the time-derivative of the current measured using the B-dot sensor. It can be seen that the highest steepnesses (in excess of 15 kA/ μs) are associated with the initial pulses.

Figure 5.8 present a detailed view of the pulses occurred at about 120 ms. The values on the time scale are relative values.

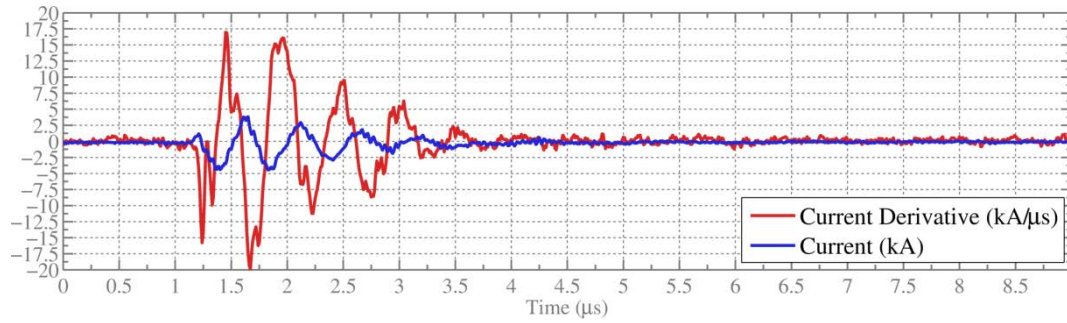


Figure 5.8. Expanded view of the fastest pulse of the current waveform and its time-derivative of Fig. 7 occurring at about 120 ms. Note that the values on the time axis of this figure are relative values.

Figure 5.9 shows the current associated with a two-pulse positive flash recorded on August 1, 2010. Note that the peak values are relatively small (3 kA and 2.3 kA). Fast repetitive impulses are clearly noticeable in the rising portion of the first pulse (see Figure 5.9b). They are absent in the second, larger pulse (at about 180 ms) of this flash. The zero-to-peak risetime of this second pulse is about 8 ms.

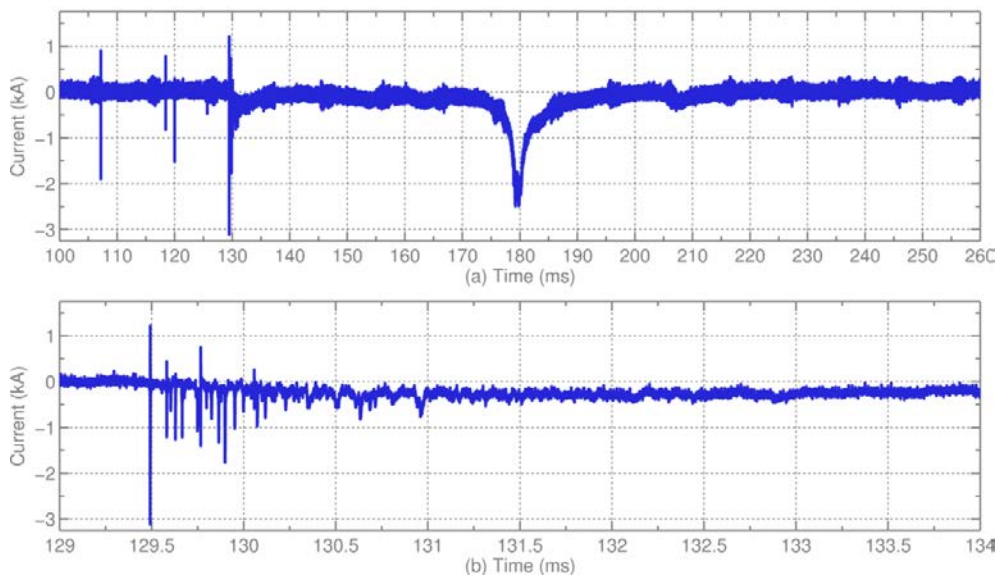


Figure 5.9. Current waveform of a positive flash recorded on August 1, 2010 at 20:02. (a) Overall flash (b) Detail of the current between 129 and 134 ms.

A last example of a current waveform associated with the second observed type is shown in Figure 5.10. Again, this current is characterized by a relatively low peak value (3.8 kA), a relatively long risetime (12 ms) and fast pulses in the rising part of the waveform.

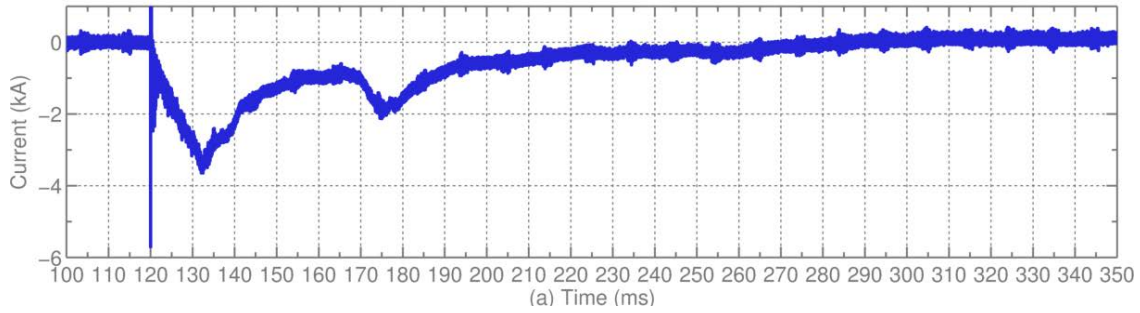


Figure 5.10. Current waveform of a positive flash recorded on August 15, 2010 at 14:37.

The recorded data contain the first directly-measured evidence of M-components of both polarities during a continuing current lowering positive charge to ground.

5.4 Statistics of Positive Flashes

The mathematical techniques applied in the statistical analysis are the same as those applied for the negative flashes analysis (See Chapter 4, Section Statistics Calculation).

Table I summarizes the values of peak current, charge, duration and action integral associated with recorded positive flash waveforms. In this section, we present the statistics associated with the salient parameters of the positive flashes, by making reference to available data obtained at other instrumented towers.

5.4.1 Peak Current

Figure 5.11 presents the cumulative distribution function of the peak current I . The CDF is defined as [162]

$$CDF_x(I) = P(X \leq I) \quad 5.1$$

The empirical CDF of Figure 5.11 is obtained using the percentiles table [163]. The 95% confidence bounds are drawn for reference along with the lognormal CDF defined in Equation 5.2 and plotted using the parameters (μ, σ) approximated by a lognormal maximum-likelihood estimation (MLE) of the data of Table I.

$$CDF_x = \frac{1}{2} \operatorname{erfc} \left(-\frac{\ln(I) - \mu}{\sigma\sqrt{2}} \right) \quad 5.2$$

Figure 5.12 and Figure 5.13 present the probability plot and associated histogram. Notice that the MLE-estimated σ in Figure 5.11 matches the standard deviation of the logarithm of the data (normal domain) on Figure 5.12.

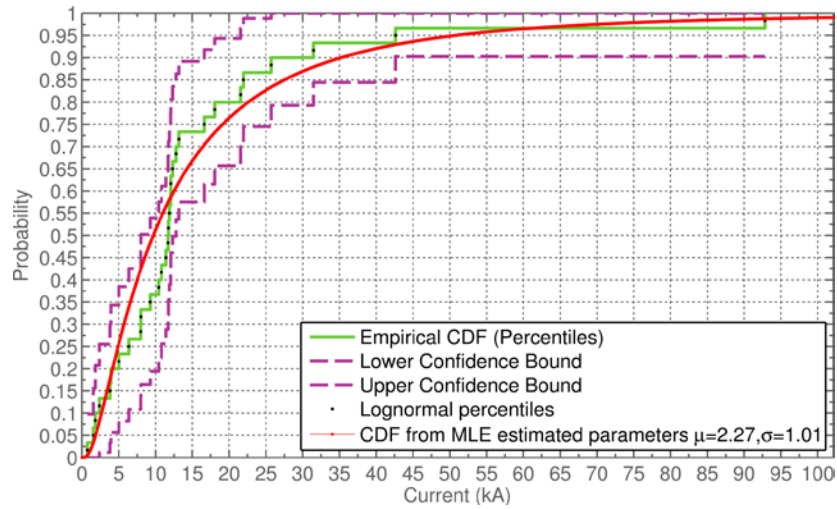


Figure 5.11. Empirical CDF along with its confidence bounds and lognormal CDF with MLE-estimated parameters for the peak current. The exceeding probability ranges labels are calculated from the MLE-estimated CDF.

The difference between the ideal lognormal CDF and the empirical CDF is due to the small sample size ($n=30$).

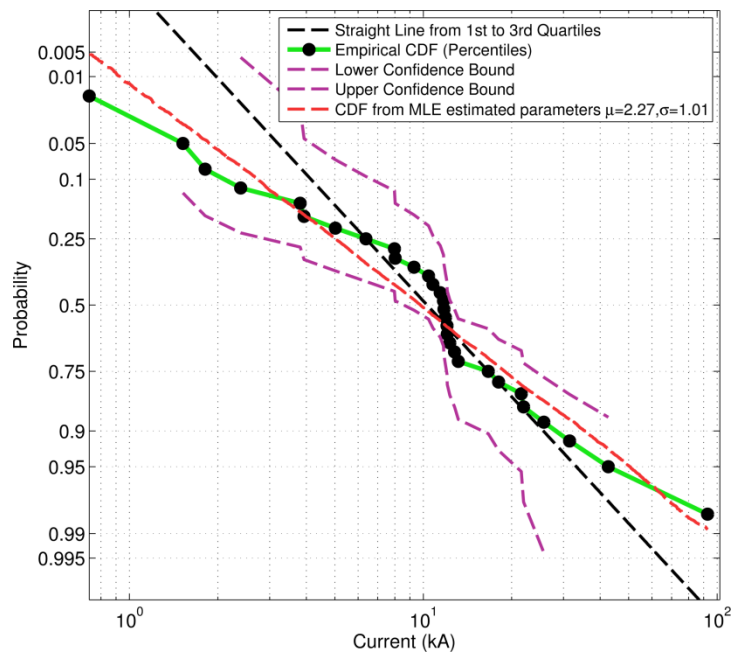


Figure 5.12. Peak current cumulative frequency distribution.

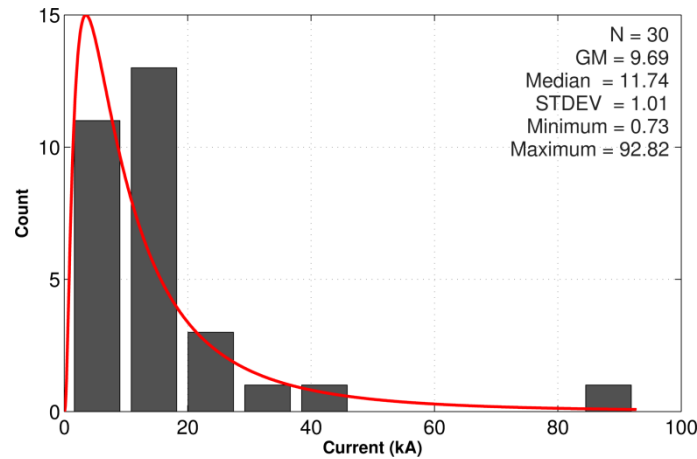


Figure 5.13. Peak current histogram. The MLE estimated PDF is superimposed as a continuous curve.

The maximum measured value for the peak current during the period of observation is 93 kA. The waveform associated with this flash (classified as type 1 and occurred on August 3, 2011 at 11:51) is presented in Figure 5.14. Note that the waveform is characterized by a very complex waveshape including two pulses (of peak amplitude 93 kA and 72 kA, respectively) separated by 1 ms, and followed by a series of fast pulses superimposed to a long continuing current-like waveform.

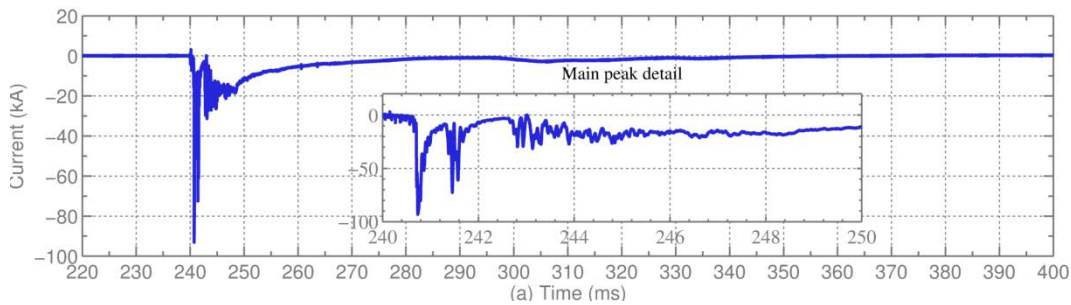


Figure 5.14. Current waveform associated with a positive flash that occurred on August 3, 2011 at 11:51. This is the largest measured current in the period of analysis. An expanded view of the first 10 ms of the waveform is presented in the inset of the figure.

TABLE II. STATISTICAL PARAMETERS OF CURRENT PEAK

		Peak current (kA)				
Tower	Sample size	Percentage <u>Exceeding</u> Tabulated Value				
		95%	90%	50%	10%	5%
Sântis (This study)	30	1.52	2.1	11.74	28.6	42.63

Table II summarizes statistical data associated with the current peak. The median is found to be 11.74 kA.

5.4.2 Total Transferred Charge

Figure 5.15 present the CDF plot of the total transferred charge. In the same figure, we have plotted the empirical CDF, the 95% confidence bounds and the lognormal CDF approximation and plotted using the parameters indicated on the figure (from maximum-likelihood estimation).

Figure 5.16 and Figure 5.17 show respectively the probability plot and the histogram of the transferred charge.

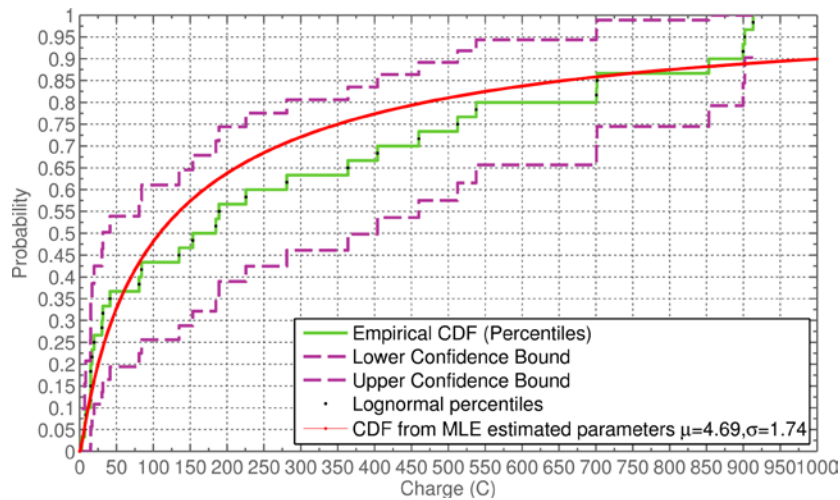


Figure 5.15. Empirical CDF along with its confidence bounds and lognormal CDF with MLE-estimated parameters for the charge. The exceeding probability ranges labels are calculated from the MLE-estimated CDF.

The median is found to be 317 C and the statistical data for the charge are given in Table III.

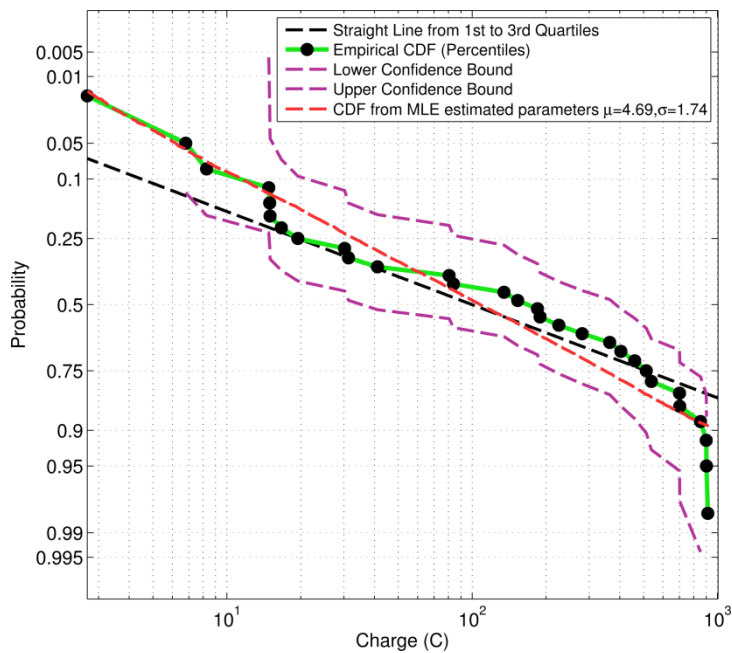


Figure 5.16. Probability plot of transferred charge.

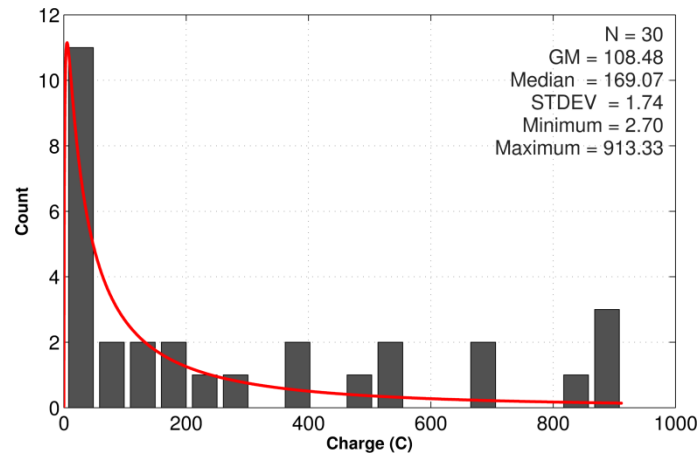


Figure 5.17. Charge histogram. The MLE estimated PDF is superimposed as a continuous curve.

TABLE III: STATISTICAL PARAMETERS OF TOTAL TRANSFERRED CHARGE

		Peak charge (C)				
Tower	Sample size	Percentage Exceeding Tabulated Value MLE				
		95%	90%	50%	10%	5%
Säntis (This study)	30	6.8	11.5	169	876	901

Examples of flashes transferring large amounts of charge are presented in Figure 5.18 and Figure 5.19. Figure 5.18 illustrates a type-1 flash during which 280 C of charge was transferred to ground. Figure 5.19 shows a 6 kA peak, type-2 flash with an associated transferred charge of over 150 C. In these figures, vertical lines show the times corresponding to 10%, 50% and 90% of the total transferred charge.

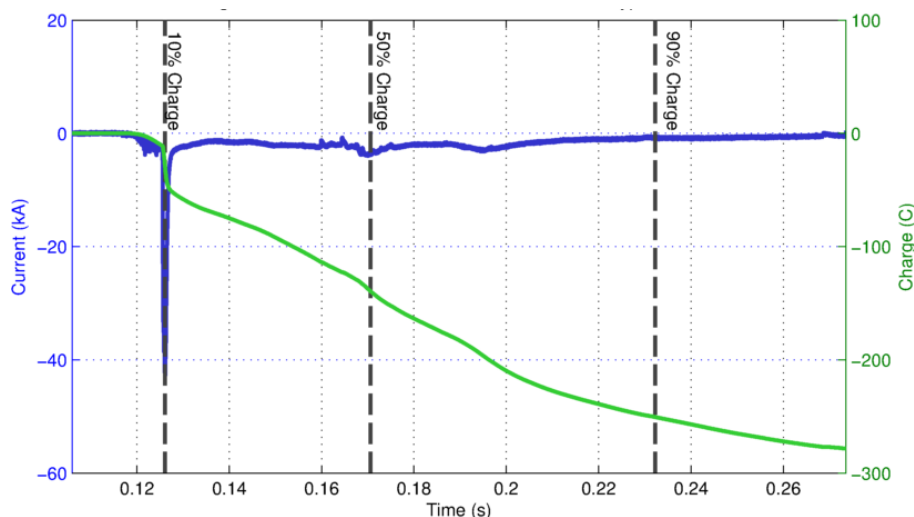


Figure 5.18. Flash (#1) classified as Type 1. Occurred on 2010-07-21 19:05.

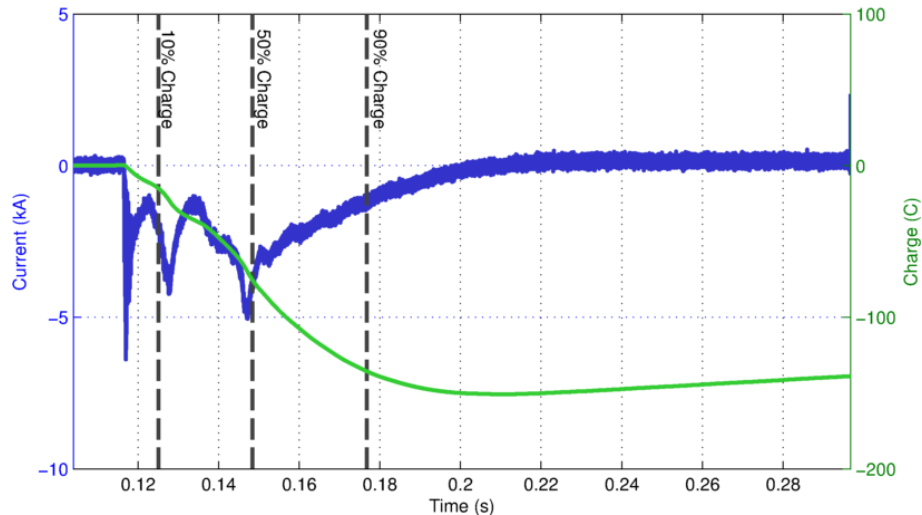


Figure 5.19. Flash (#8) classified as Type 2. Occurred on 2010-08-30 4:42.

It is worth observing that 8 flashes out of 30 transported positive charge to the ground in excess of 500 C (see Table I). The largest amount of transferred charge measured in the period of analysis corresponds to a flash occurred on August 27, 2011 which is shown in Figure 5.20.

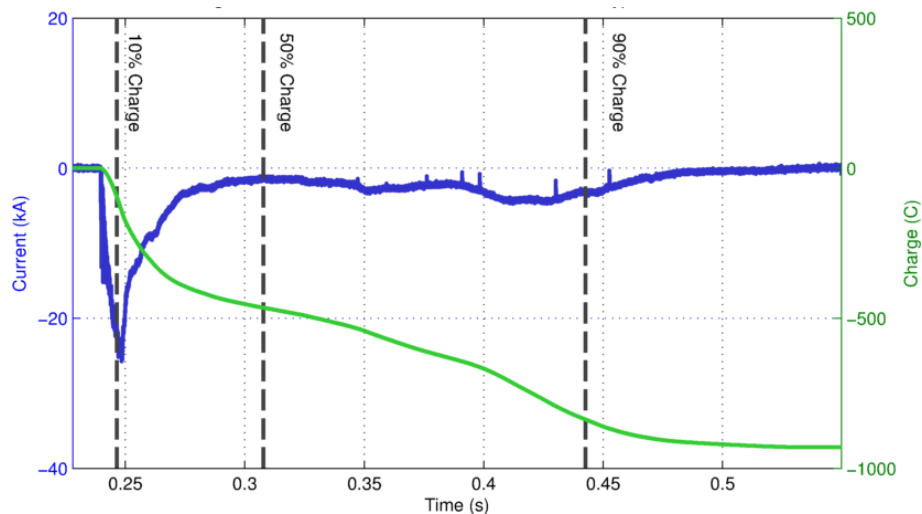


Figure 5.20. Flash (#22) occurred on 2011-08-27 6:30 with a total charge transferred of 913 C.

The amount of charge transferred during this flash (913 C) is very close to the highest charge transfer ever measured of about 1000 C, reported by Miyake et al. [47] for positive and negative winter lightning in Japan.

5.4.3 Flash Duration

Figure 5.21 presents the CDF plot of the flash duration and Figure 5.22 and Figure 5.23 present the probability plot and the histogram.

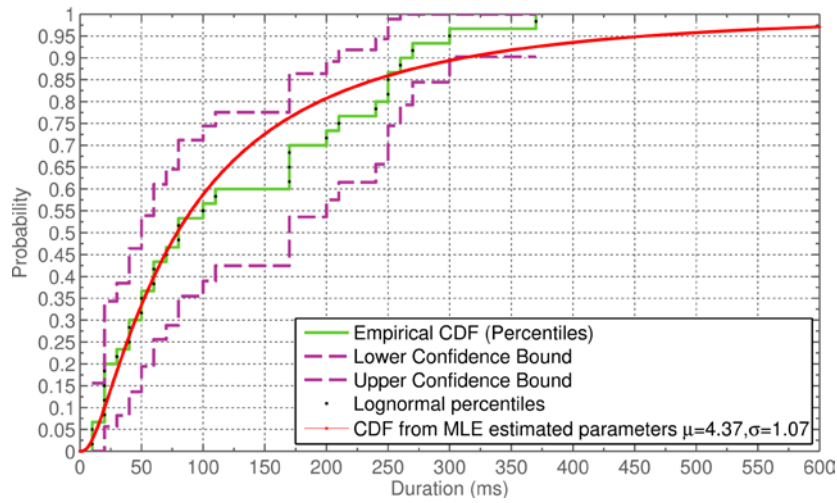


Figure 5.21. Empirical CDF along with its confidence bounds and lognormal CDF with MLE-estimated parameters for the flash duration

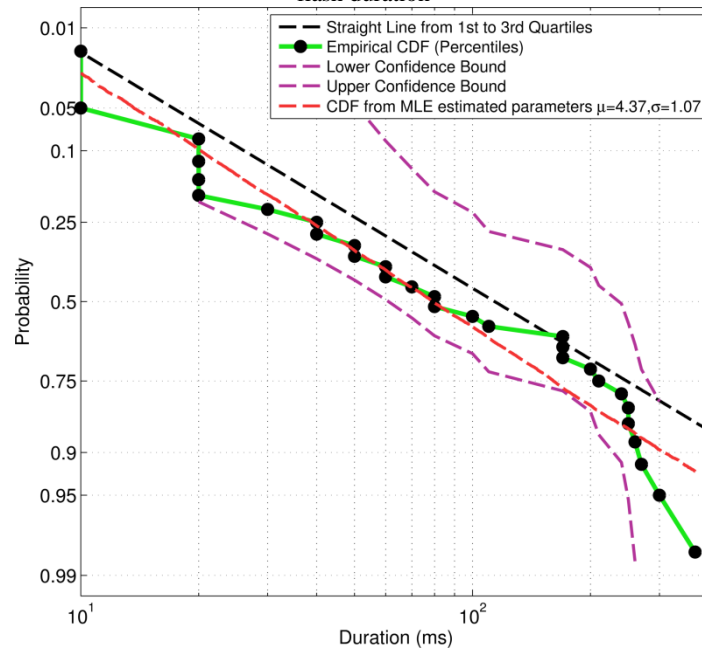


Figure 5.22. Probability plot of flash duration

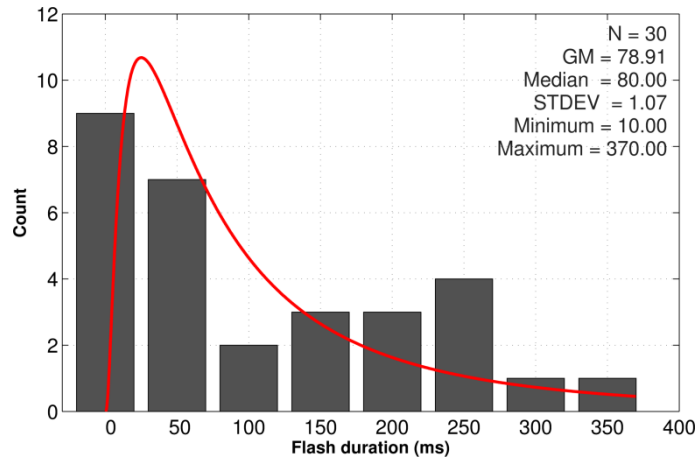


Figure 5.23. Flash duration histogram.

TABLE IV. STATISTICAL PARAMETERS OF FLASH DURATION

Flash Duration (ms)						
Tower	Sample size	Percentage <u>Exceeding</u> Tabulated Value MLE				
		95%	90%	50%	10%	5%
Sántis (This study)	30	10	20	80	265	300

The median duration is found to be 80 ms and the statistical parameters are given in Table IV.

5.4.4 Action Integral

The histogram of action integral of the Sántis positive flash currents is presented in Figure 5.24. The measured values are characterized by a median value of $0.4 \times 10^3 \text{ A}^2\text{s}$ and a maximum value of $7.19 \times 10^3 \text{ A}^2\text{s}$. These values are significantly larger than those associated with the 10-year data obtained at the Gaisberg Tower [42], with a median of $0.16 \times 10^3 \text{ A}^2\text{s}$ and a maximum of $2 \times 10^3 \text{ A}^2\text{s}$. Two thirds of the observed values remain, nevertheless, below $1 \times 10^3 \text{ A}^2\text{s}$.

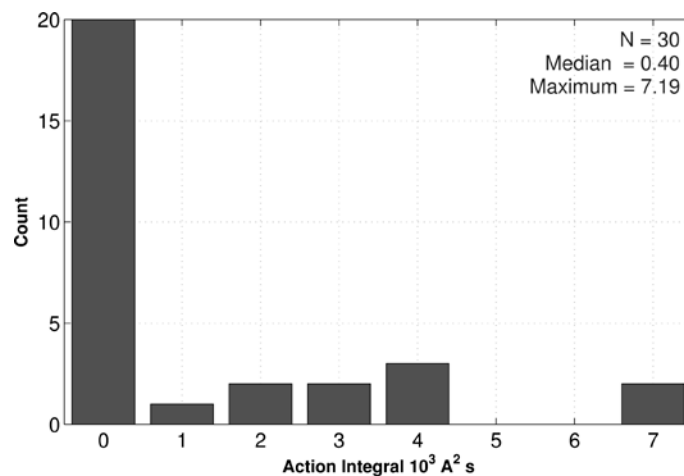


Figure 5.24. Action Integral Histogram

Figure 5.25 presents the variation of the peak current as a function of the charge and flash duration, the obtained results confirm the findings of Saba et al. [37] according to which positive lightning flashes may combine high peak currents with high charges (or flash duration).

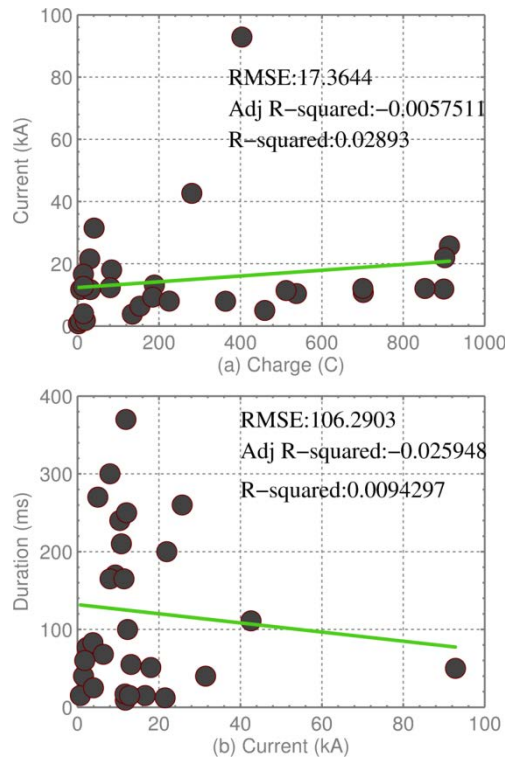


Figure 5.25. (a) Peak current versus transferred charge (b) Peak current versus duration.

5.4.5 Comparison with Observations at other Instrumented Towers

Table V presents a summary of the median value of the peak current, transferred charge and flash duration obtained in this study and compared to the available data obtained in Switzerland (Monte San Salvatore) [54], Japan [164] and at the Gaisberg Tower, Austria [42] for upward positive flashes. The sample size is given in the parenthesis.

It can be seen that the median values for the peak current and the flash duration are consistent with the data obtained recently in Austria. It is worth noting that, Zhou et al. [42] defined two parameters associated with the peak current: (i) the so-called pulse peak current which is the absolute maximum value of the current reported in Table I, and (ii) the so-called flash peak current which corresponds to the peak current associated with the low frequency filtered waveform, the median of which was 5.2 kA. The amount of transferred charge is substantially larger in our obtained dataset, with a median value of 169 C. This value is about 6 times as large as the values obtained in Monte San Salvatore [140] and in Japan [164], and about 3 times as large as the value obtained in Austria [42].

TABLE V. SUMMARY OF CURRENT PARAMETERS (MEDIAN VALUES) OF UPWARD POSITIVE FLASHES AND COMPARISON WITH AVAILABLE DATA. THE SAMPLE SIZE IS GIVEN IN THE PARENTHESIS

Tower	Peak Current (kA)	Flash Duration (ms)	Charge Transfer (C)
Monte San Salvatore, Switzerland [54]	1.5 (132)	72 (138)	26 (137)
Nikaho Kougen Wind Farm, Japan [164]	6.5 (16)	40 (16)	30.2 (16)
Gaisberg Tower, Austria [42]	11* (25)	82 (25)	58 (25)
Säntis Tower, Switzerland	11.8 (30)	80 (30)	169 (30)

*) this value corresponds to the maximum peak current (called the pulse peak current in [42]). Zhou et al. [42] define also the flash peak current associated with the slowly varying current in which fast pulses were filtered out.

5.4.6 Bipolar Flashes

During the period of analysis, three bipolar flashes were recorded at Säntis which correspond to 1.5% (3/201) of the total number of flashes². This number is lower than those reported in previous studies in Austria (3%, [53]) and in Monte San Salvatore (6%, [54]). All three flashes occurred in the morning of August 27, 2011.

Two of the recorded bipolar flashes (shown in Figure 5.27 and Figure 5.28) correspond to the type 2 of the classification provided by Rakov [1], the third one corresponding to the type 3 (seen on Figure 5.26).

Figure 5.26 presents the first measured bipolar flash composed by an initial negative stroke of 7 kA with a slow risetime of about 100 μ s preceded by two fast oscillations visible on the

² It is worth noting, as mentioned previously, that the flash presented in Figure 5.7 can also be viewed as bipolar. The waveform shows indeed a polarity change due to an M-component-like pulse.

current derivative channel (Figure 5.26b), then a main positive pulse appears transferring 150 C in about 70 ms. The main positive pulse has a moderate peak current composed of two successive peaks (12.5 kA and 6 kA) being the second peak the main contributor of charge.

The second measured bipolar pulse is shown in Figure 5.27, where two current channels are plotted, the PEM Rogowski coil (with gain 20 kA / V) and the ROCOIL Rogowski coil (with gain 1 kA / V). The current is characterized by an initial positive excursion of about 5 kA peak associated with a charge transfer of about 300 C. A change on the polarity is seen at, followed by a long continuing current lasting about 300 ms, superimposed to which multiple small impulses can be seen (see Figure 5.26b). A relatively slow negative pulse of 3 kA peak and 175 μ s risetime (shown in Figure 5.26c) occurred 500 ms after the start of the event.

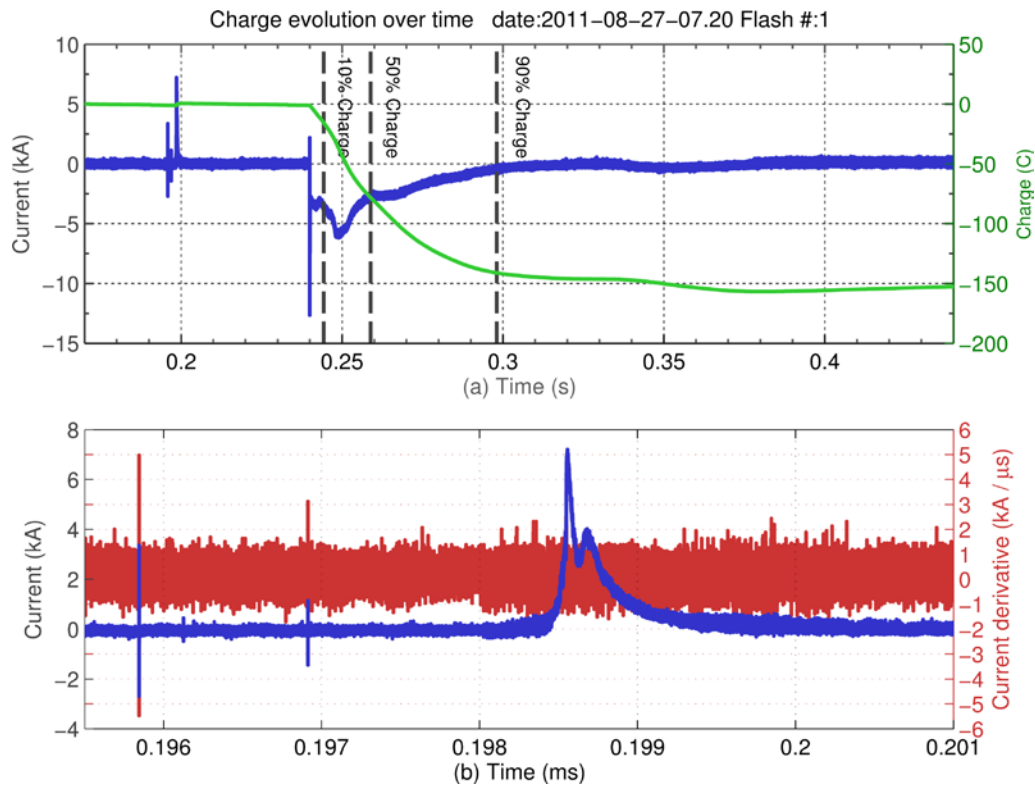


Figure 5.26. Current waveform associated with a bipolar flash (#1 out of 3) that occurred on August 27, 2011 at 07:20. (b) Expanded view of the negative pulse.

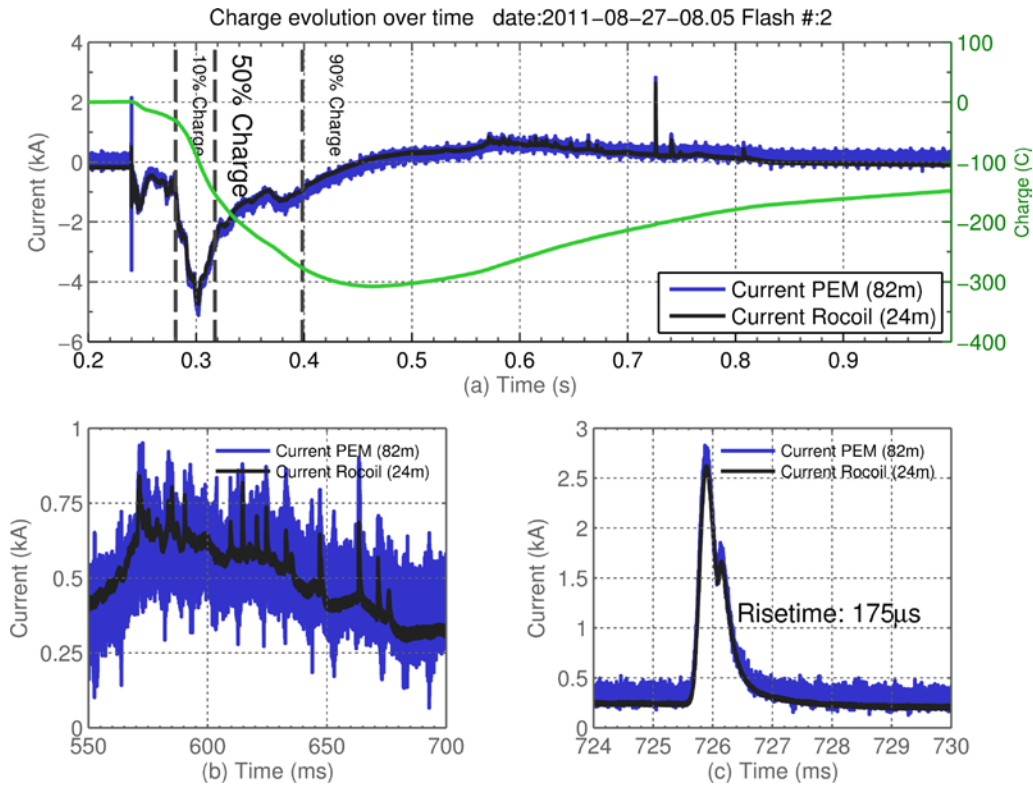


Figure 5.27. Current waveform associated with a bipolar flash (#2 out of 3) that occurred on August 27, 2011 at 08:05. (b) Expanded view of the region between 500 and 700 ms (c) Expanded view of the negative pulse.

Figure 5.28 presents the third measured bipolar current waveform occurred on August 27, 2011 at 08:42. The flash is composed of an initial stage of positive polarity (typical of positive flashes of type 2) with a peak current of about 10 kA. About 80 ms after the extinction of the continuing current, a 14-kA peak negative return stroke was measured. An expanded view of the negative return stroke is presented in Fig. 10b. The net transferred charge for the bipolar flash presented in Figure 5.28 is positive and equal to about 170 C.

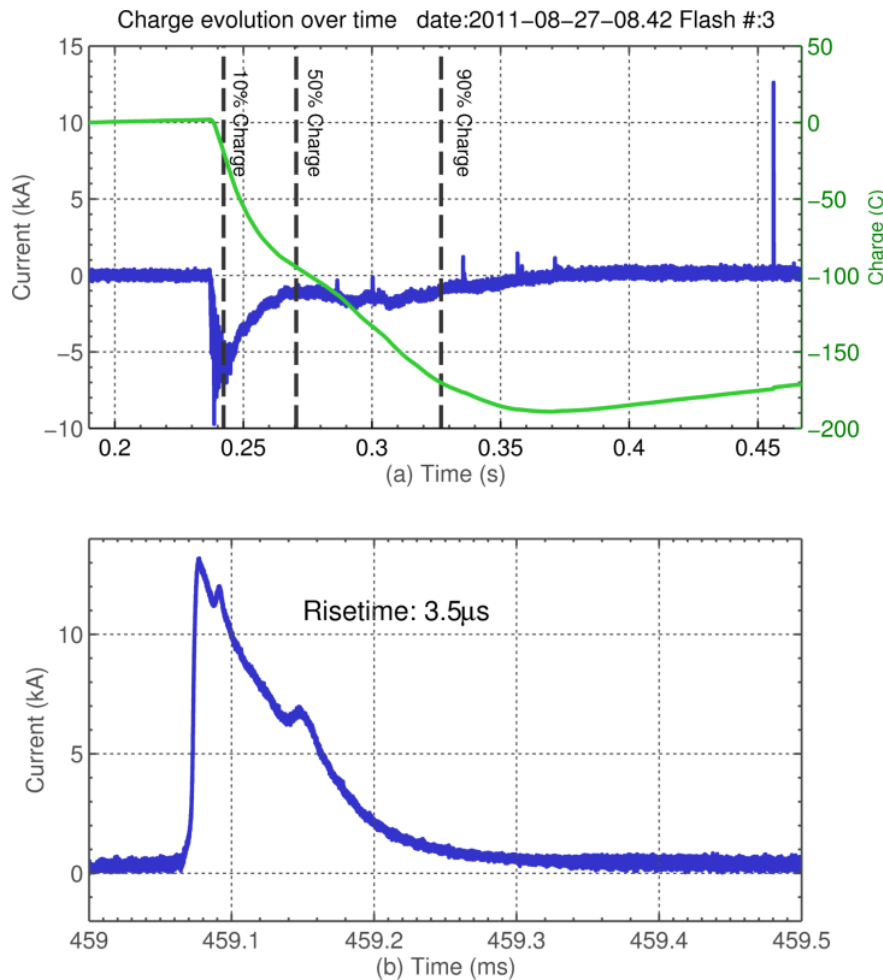


Figure 5.28. Current waveform associated with a bipolar flash (#3 out of 3) that occurred on August 27, 2011 at 08:42. (b) Expanded view of the negative return stroke

5.5 Conclusions

In this Chapter, an analysis of the measured current waveforms associated with positive and bipolar flashes recorded on the Säntis tower, Switzerland, from May 2010 till January 2012 was presented. The overall number of recorded flashes in the considered period was 201, of which 30 were of positive polarity (effectively transported positive charge to ground) and three were bipolar. The recorded positive flashes were mainly concentrated in the summer months, August being the month during which most of them occurred (6 events in 2010 and 16 events in 2011). The percentage of positive flashes (15%) is considerably larger than the values observed in other studies in summer months (3% to 6.5%).

The observed current waveforms were classified into two types. The first type is characterized by three stages: (1) an initial, slowly rising portion lasting a few milliseconds, (2) the main pulse, and (3) a long continuing current that may contain several pulses of both polarities characteristic of M components. The second type of observed positive flashes is

characterized by (i) the absence of any initial slowly rising portion, (ii) lower peak currents, and (iii) presence of successive pulses which may be due to an upward stepped leader.

The time-derivatives of the current pulses associated with upward stepped leaders are found to be much larger than those of the main pulse. All the observed flashes contained a single main pulse, except for one flash of the second type, which featured two pulses. Our recorded data constitute the first directly-measured evidence of M-components of both polarities during a continuing current lowering positive charge to ground.

The observed positive flashes are characterized by a median peak current of 11.8 kA, and a median flash duration of 80 ms. These values are consistent with those associated with the data recorded at the Gaisberg Tower in Austria. On the other hand, the amount of transferred charge is substantially larger in our dataset, with a median value of 169 C (6 times as large as the values obtained in Monte San Salvatore and in Japan, and 3 times as large as the value obtained in Austria). Eight flashes out of 30 transported positive charge to the ground in excess of 500 C. The obtained results confirm also the findings of Saba et al. according to which positive lightning flashes may combine high peak currents with high charge transfers (or flash durations).

The three bipolar flashes recorded during the considered time period occurred during one storm occurred on August 27, 2011. The relative number of bipolar flashes (1.5%) is found to be lower than the values reported in previous studies in Austria and in Switzerland (3 to 6%). On the basis of the classification proposed by Rakov, two of the three observed bipolar flashes belonged to Type 2 and one to Type 3.

Chapter 6. An Evaluation of the Performance Characteristics of the European Lightning Location Network to Detect Upward Flashes Using Säntis Data

6.1 Introduction

The assessment of the performances of lightning location systems can be evaluated by means of directly measured events provided by either instrumented towers (e.g. [165-167]) or rocket-triggered lightning [168]. Diendorfer et al. [166] compared lightning peak currents measured at the Gaisberg tower (100-m tall) to correlated lightning peak currents reported by the Austrian Lightning Detection and Information System (ALDIS). They reported very good agreement, the differences between the directly-measured and ALDIS-estimates being in the range of measurement errors of both systems. Rachidi et al. [88] derived equations to infer the mean value of the return stroke current from the mean values of the peak remote field and the return stroke speed. The derived equations were validated using simultaneous measurements of return stroke current, electric fields at 5 km, and return stroke speeds associated with triggered lightning and reported by Willett et al. in [169]. Jerauld et al. [168] evaluated the performance characteristics of the U.S. National Lightning Detection Network (NLDN) [170] using rocket-triggered lightning data acquired during the summers 2001-2003 at Camp Blanding, Florida, reporting a tendency of NLDN to underestimate peak currents with a median peak current estimation error of about -18 %. This underestimation has been shown to

result from propagation model parameters that were not well-suited to the NLDN sensor baseline distances [171]. More recently, Nag et al. [172] presented a similar analysis using the Camp Blanding data acquired during 2004-2009. The reported flash and stroke detection efficiencies were 92% and 76%, respectively, while the median absolute location error was 308 m. The median NLDN-estimated peak current error was -6.1% . Pavanello et al. [173] used directly-measured lightning currents at the top of the CN Tower (553 m) to evaluate the performance of the North American Lightning Detection Network (NALDN) in terms of current peak estimates. They showed that the NALDN inferred values overestimate the actual current peaks for strikes to very tall towers by a factor of about 3 to 4 because the presence of the tall struck object is not included in the NALDN current peak estimation algorithm. However, correcting the NALDN estimates by using the tower correction factors proposed either by [174] or [89] results in an excellent estimation of the lightning current peaks.

In this Chapter, we use the data obtained at Säntis Tower from June 1st, 2010 to May 31st, 2011 to evaluate the performance of the EUCLID lightning detection network (<http://www.euclid.org>) in terms of detection efficiency, location accuracy and peak current estimates. We also discuss some limitations in detecting strokes in upward-initiated lightning flashes.

6.2 Measurement Period

In the considered period (June 1st, 2010 to May 31st, 2011), 57 flashes were recorded at the Säntis Tower out of which 15 were of positive polarity. From the 42 negative flashes, 37 could be correlated to EUCLID data by comparing the time-stamp provided by the GPS time reference installed on the Säntis and the EUCLID time. Specifically, events from Säntis and EUCLID were considered synchronized if the two following criteria were satisfied: i) the GPS time stamps were within a time window of few ms and ii) the pattern of strokes time stamps provided by EUCLID and Säntis data fits within the μs range. Note that data provided by the EUCLID lightning location system (LLS) are restricted to a circular area of 5 km radius centered in the location of the Säntis Tower. Concerning the time synchronization, it is worth observing that the trigger of the measurement system of the Säntis tower makes use of a threshold-based logic applied to the time derivative signal of the lightning current that is directly measured by means of a B-Dot sensor. Such a logic results into a time delay that, as

expected, depends on the waveform of the lightning current time derivative. However, such a time delay is, for typical values of current time derivatives, within $0.1 - 1 \mu\text{s}$.

6.3 EUCLID Network

EUCLID (European Cooperation for Lightning Detection) is a consortium of 16 European national lightning detecting networks with the aim to identify and detect lightning all over the European area (<http://www.euclid.org>). Presently, the complete network consists of 138 sensors contributing to the detection of lightning. The location of the sensors is shown on Figure 6.1.

For cloud-to-ground (CG) lightning, an overall flash detection efficiency of 98% and a stroke detection efficiency of 84% has been determined for the EUCLID network based on video studies in Austria [175]. Very similar values of detection efficiency are observed for lightning to the Gaisberg Tower [39] for upward flashes including at least one return stroke. For the location of Sântis Tower, the overall performance of the EUCLID network for CG lightning should be very much the same as observed in Austria. For upward initiated lightning from a tall tower, the detection efficiency of these kinds of networks is affected by the occurrence of ICC pulses with longer current risetimes, and more generally with waveshapes very different from those associated with downward flashes for which they are calibrated.

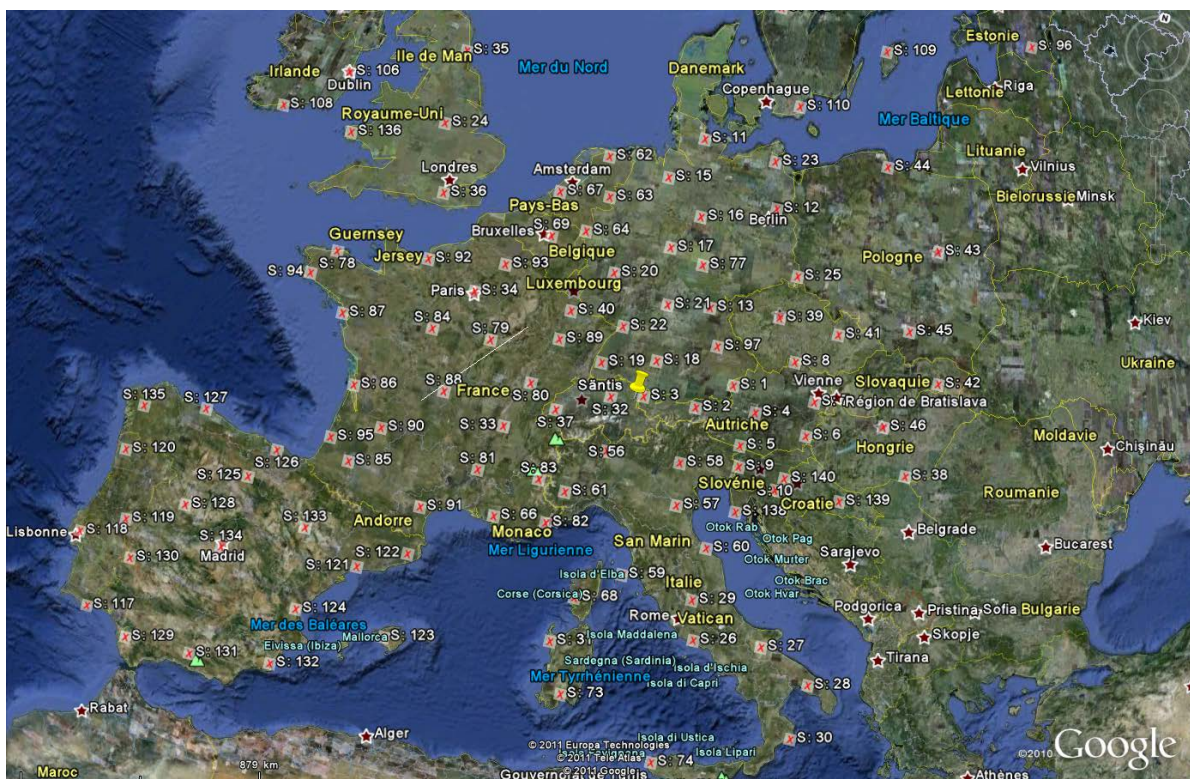


Figure 6.1. Location of EUCLID network sensors (Image from Google Earth and data provided by ALDIS)

6.4 Flash Detection Efficiency

Table 1 presents the flash detection efficiency for the negative flashes to the Sántis Tower observed in the mentioned period during which 42 flashes were recorded at Sántis.

TABLE I. FLASH DETECTION EFFICIENCY (FDE) OF THE EUCLID NETWORK ASSOCIATED WITH NEGATIVE LIGHTNING FLASHES TO THE SÁNTIS TOWER, JUNE 2010-MAY 2011.

Number of Sántis Tower measured negative flashes	42
Number of EUCLID detected flashes	37
Flash Detection Efficiency	88%
Flash Detection Efficiency, excluding flashes containing ICC pulses only	93%

Out of the 42 flashes, 37 were detected by the EUCLID network. It should be noted that among the 5 flashes which were missed by EUCLID, two were characterized by only an ICC without return strokes (these flashes are referred to as ICC_p [39, 175]). As mentioned before, ICC pulses often feature longer risetimes (small di/dt) and are not associated with sufficient radiation to be detected by lightning location systems. These two flashes are shown in Figure 6.2a,b.

Figure 6.3 presents the EUCLID pulse detection efficiency as a function of pulse peak current measured at Sántis (the minimum considered current peak in the analysis was 2 kA for the Sántis data). Even though the number of data point is insufficient, especially for high peak currents (see Figure 6.4), the data suggest a clear increase of the pulse detection efficiency as a function of peak current.

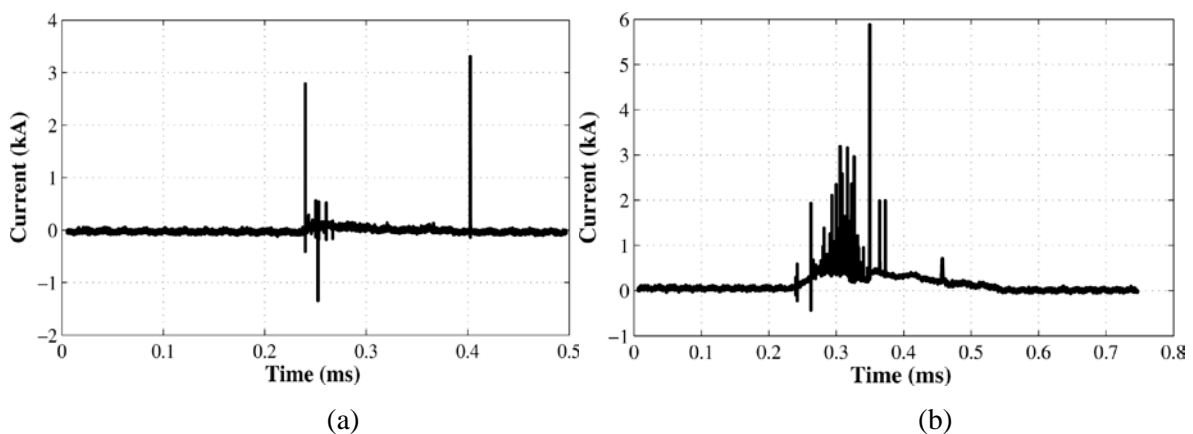


Figure 6.2. The two ICC_p type flashes which were missed by EUCLID. None of them contained any return strokes. (a) April 12, 2011 at 17:34, (b) April 28, 2011 at 16:25.

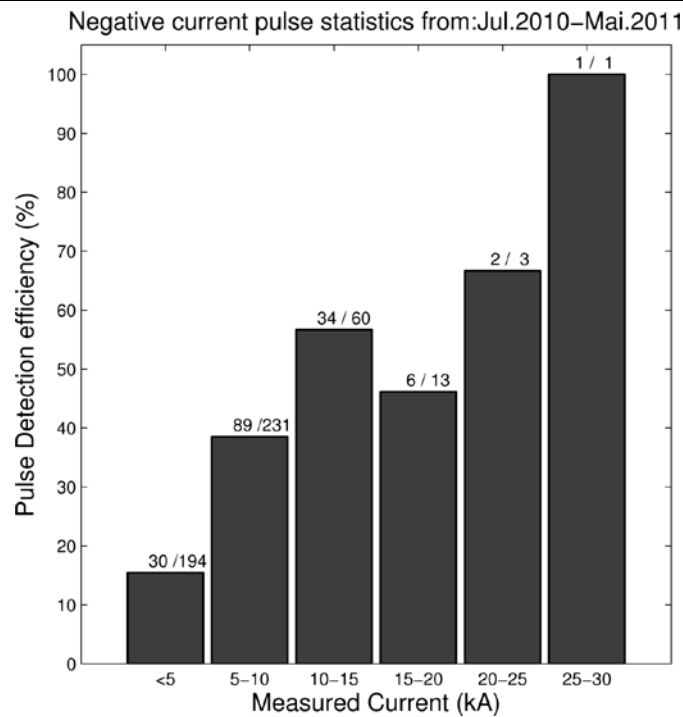


Figure 6.3. EUCLID detection efficiency as a function of pulse peak current measured at Sântis (bin size of 5 kA).

We have to note that the data shown in Figure 6.3 are a combination of return strokes and ICC-pulses and therefore the reduced detection efficiency for lower amplitudes in this preliminary comparison is most likely caused by the high number of ICC-pulses with long risetimes in this low amplitude range.

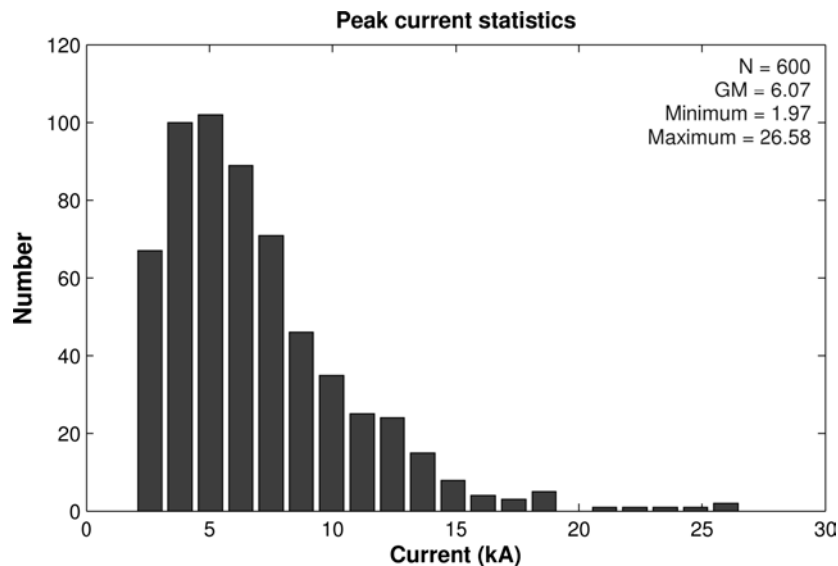


Figure 6.4. Peak current histogram (Sântis measurements)

Regarding the positive flashes, out of the 15 recorded events, only four were characterized by typical positive current waveshapes [130]. The current peaks associated with these four single-stroke flashes were 43, 18, 16 and 31 kA. For all of these flashes we can find time correlated EUCLID detected strokes. At this time it is unclear whether EUCLID located the

main channel attached to the tower top or located some recoil streamers within the cloud above the tower. The 43-kA event is plotted in Figure 6.5. It is worth noting that the M-component-like pulse that occurred at about 170 ms was detected by EUCLID and classified as a second stroke.

It is also worth noting that some of the upward flashes from the tower can be triggered by nearby cloud-to-ground or intracloud discharges some tens of ms prior to the start of the upward leader from the tower [40]. The uncertainty in the time correlation being in the order of ms, it is therefore possible that, in some cases, the located events at some km distance from the Säntis are the triggering events and not the discharges to the tower. Although we expect these events to be rare, they might have some influence on the estimated detection efficiency, location accuracy and peak current estimations of the system.

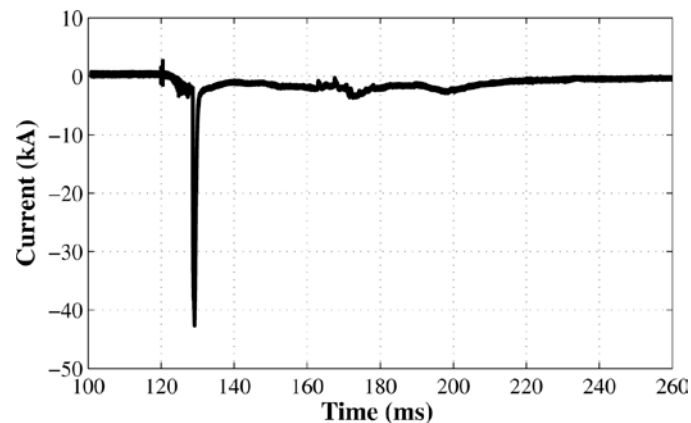


Figure 6.5. Current waveform associated with a positive flash recorded on July 21, 2010, 19:05. The M-component-like pulse that occurred at about 170 ms was detected by EUCLID and classified as a second stroke.

6.5 Location Accuracy

Figure 6.6 presents a plot of pulse locations estimated by EUCLID. The median of the absolute error for the location (defined as the distance between the Säntis Tower location and the median of EUCLID's stroke locations) of negative flashes is 126 m.

Sântis strokes map from:Jul.2010–Mai.2011

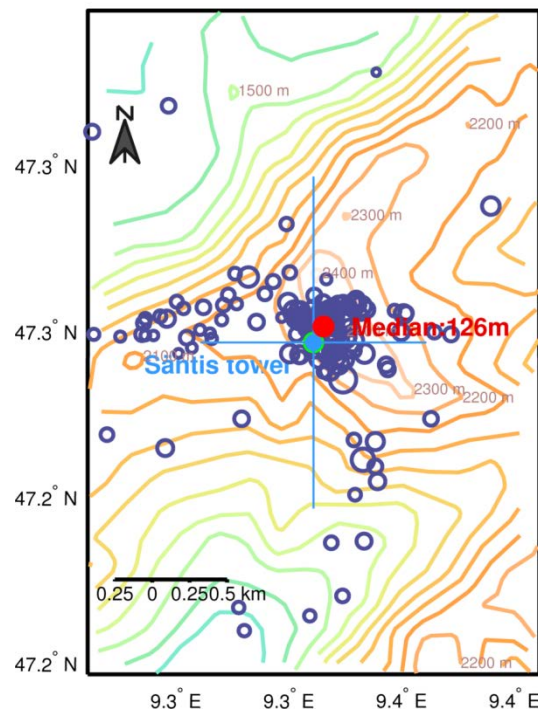


Figure 6.6. Plot of EUCLID stroke locations for flashes recorded from June 2010 to June 2011. The size of the circles is proportional to the current peak estimated by EUCLID.

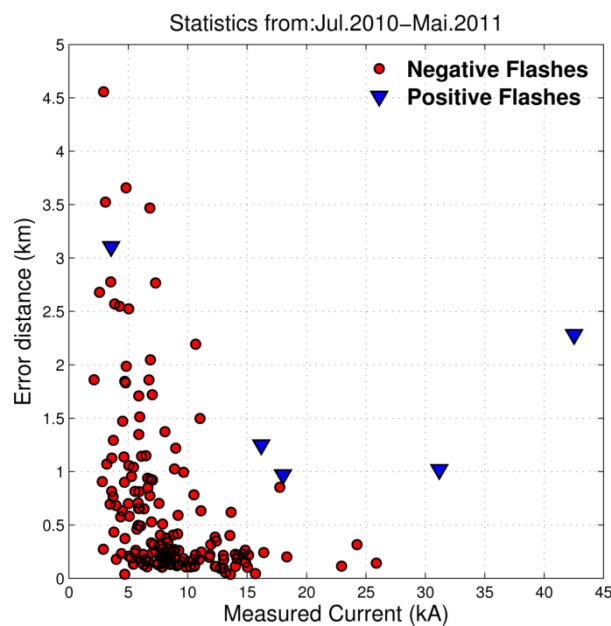


Figure 6.7. EUCLID absolute location error versus Sântis Tower measured peak current.

Figure 6.7 shows EUCLID’s absolute location error versus the peak current measured on the Sântis tower. The majority of large location errors are for current peaks lower than 10 kA. For negative current peaks larger than 15 kA, the location errors do not exceed 1 km. For positive flashes, the dataset is limited to 5 events. The location errors for these positive events range from 1 to 3 km, with a median of 959 m.

Figure 6.8 shows the arithmetic mean of the absolute location error as a function of current peak ranges. It can be seen that the error's mean value remains below 500 m for current peaks larger than 10 kA.

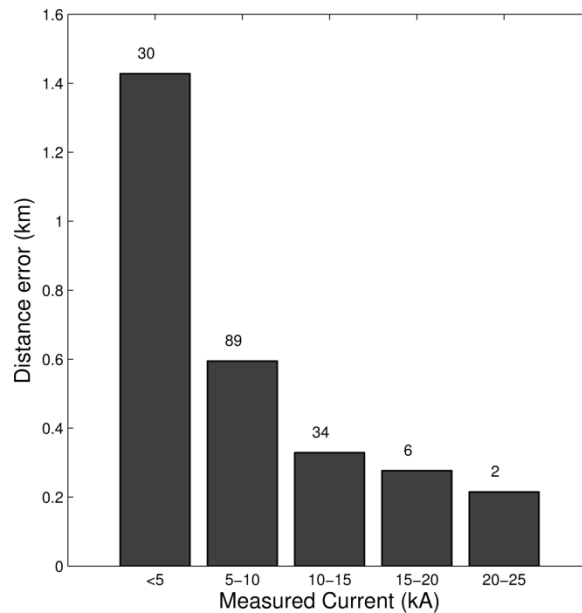


Figure 6.8. Arithmetic mean of EUCLID absolute location error versus Sántis peak current. Only negative flashes are considered here.

6.6 Peak Current Estimates

Figure 6.9 presents the EUCLID peak current estimates versus directly measured peak currents at the Sántis Tower (recorded at the height of 82 m) for both negative and positive events. Note that we obtained nearly identical results using current peaks measured at the lower height. It should be noted that no distinction was made between return strokes and ICC pulses (with rise times smaller than 8 μ s). It can be seen that the LLS peak current estimates are on average larger than the measured current.

Figure 6.10 shows the median and standard deviation of the EUCLID peak current estimation errors as a percentage of the directly measured Sántis current ranges. For current peaks larger than 10 kA, the absolute percentage error is about 50 to 60%. Note that these errors are significantly larger than those reported by Diendorfer et al. [166, 176] using Gaisberg Tower data.

For the five positive events, the median of the absolute error of EUCLID peak current estimation as a percentage of the directly measured Sántis current is 46%.

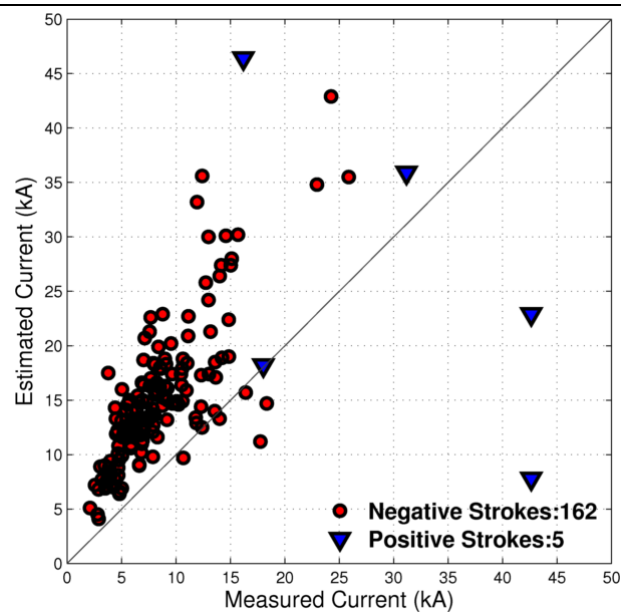


Figure 6.9. EUCLID peak current estimated versus peak current directly measured at Sántis Tower.

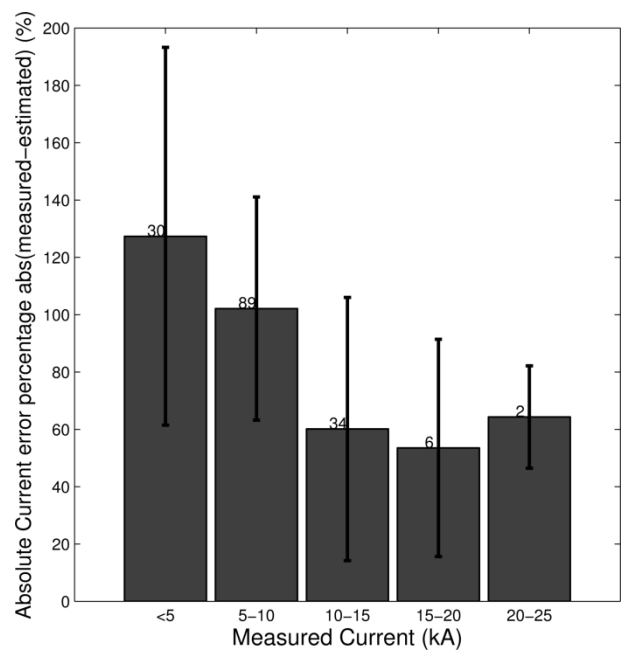


Figure 6.10. Arithmetic mean and standard deviation of EUCLID peak current estimation errors (magnitude) given as a percentage of the directly measured Sántis current ranges. Only negative flashes are considered here.

6.7 Conclusions

In this Chapter, we used the obtained data on lightning current measured on the Sántis Tower from June 1st, 2010 to May 31st, 2011 to do an evaluation of the performance of the EUCLID lightning detection network in terms of detection efficiency, location accuracy and peak current estimates for these tower initiated lightning events. In the considered period, 57 flashes were recorded on the Sántis Tower out of which 15 were of positive polarity. From

them, 37 could be correlated to EUCLID data by comparison of the time-stamp provided by GPS time reference installed on the Sántis and the EUCLID time.

The flash detection efficiency was estimated to be 93% and the median location error was 123 m. The majority of large location errors were for current peaks lower than 10 kA. For negative current peaks larger than 15 kA, the location errors did not exceed 1 km.

The EUCLID peak current estimates were on average larger than the measured current with a median peak current estimation error of about 60% for strokes over 10 kA.

Measurements included five typical positive flashes successfully detected by EUCLID. The location errors for the positive events ranged from 1 to 3 km, with a median of 960 m.

Conclusions and Perspectives

7.1 Summary

The aim of this thesis was to build a new experimental station in Switzerland for the measurement of lightning currents, instrumented using advanced and modern equipment with remote monitoring for an accurate measurement of lightning current parameters.

Chapter 2 presented the phenomenology and classification of lightning discharges. An overview of different types of discharges was given and their typical signatures in terms of current waveform were described. Lightning current measurements obtained using instrumented towers, artificially-initiated lightning, and lightning location systems were also summarized. It was emphasized that, despite the important effort in obtaining experimental data on lightning currents using different techniques, the number of available data is still limited and more data are needed to better understand the physics of lightning and to better characterize the lightning current parameters associated with different types of cloud-to-ground lightning discharges.

Chapter 3 presented the characteristics of a system suitably developed to measure lightning current waveforms on the Säntis Tower in Switzerland. We first described the configuration of the system then presented the characteristics of the measurement equipment, in terms of bandwidth and accuracy, inferred by means of experimental tests.

The system was designed considering the EMC constraints, using fiber optics as backbone for transmission of the measured signals and paying special attention to the design of the cabling, measurement boxes, protection systems and shielding. In addition, due to the harsh conditions inside the tower, where the temperature ranges from -15°C to $+35^{\circ}\text{C}$, a

system comprising a heater, a ventilator, moisture exhaust holes, and a thermal insulation material was designed to keep the temperature within acceptable limits for the components and to avoid condensation inside the PCB cards.

In order to overcome the limited high frequency response of the Rogowski coils, we proposed to use magnetic loops located very close to the tower. We showed that the use of conventional loops (B-Dot sensors) might be inadequate on the one hand because of the limitation of their high-frequency response by the resonance of the magnetic loop inductance and the capacitance of the connected cable. On the other hand, conventional loops require the use of a high-impedance termination, which might result in contamination of the waveform through multiple reflections when relatively long cables are used.

We proposed to use an improved design for the B-Dot sensor based on the works of Baum which does not have the above-mentioned shortcomings. Specifically, the inductance is lowered by extending the vertical dimension of the loop, with the overall effect of extending the operating frequency range. To overcome the integrating behavior of the loop when connected to low-impedance loads (such as 50 Ohm), an arrangement of 100-Ohm-impedance cables connected across conical-transmission-line gaps is proposed. The designed sensor is characterized by an upper frequency cutoff of 20 MHz and a 50 Ohm matched termination.

Laboratory tests carried out in the high voltage laboratory of the EPFL showed the effectiveness of the joint use of Rogowski coils and B-Dot sensors for the measurement of lightning currents.

The measurement system allows an over-the-Internet remote maintenance, monitoring and control overall system. In particular, the status of each pair of sensors is monitored and controlled by means of a system designed, and built, using National Instruments CompactRIO modules linked via 100Base-FX Ethernet, which uses fiber optics as a transmission medium.

A data analysis software (SENDIS) was developed to analyze the obtained data, to extract statistical parameters and to allow the remote monitoring, control and programming of the different components. The software is based on Matlab and designed using Object Oriented Programming. SENDIS' current capabilities include the opening, segmentation and processing of data files in the range of hundreds of millions of samples. The user can subsample the data for obtaining faster and overall views of the dataset. SENDIS makes it possible to segment the data for creating logical structured subsets and perform local

processing on small clusters (such as return strokes). The software allows also to perform signal processing operations on the data, such as Wavelet, FIR and Zero-Delay filtering, integration, derivation, DC estimation and user-defined algorithms.

Algorithms implemented in SENDIS allow the detection of current components (return stroke, M-component, continuous and continuing currents) within each flash and the automatic extraction of statistical parameters of the current.

In Chapter 4, we presented statistical distributions of the lightning current parameters based on the lightning current and current-derivative waveforms measured at the Sántis Tower site in 2010 and 2011. The total number of flashes analyzed in this study was 167 which include nearly 2000 pulses, constituting the largest worldwide dataset. The statistical distributions are associated with upward negative flashes.

Negative flashes were found to be mainly concentrated in the summer months during the convective season. This distribution contrasts with the Gaisberg Tower measurements for which lightning strikes are quasi-uniformly distributed over the year. Most of the flashes occurred during the afternoon, mostly between 4 and 8 PM. However, an appreciable number of flashes occurred in the morning, mostly between 6 and 10 AM. The obtained data were compared to and found, in general, to be consistent with published data associated with measurements obtained at other sites. Two different definitions were used to determine the current risetime. The first is the t_{10-90} risetime, frequently used in lightning applications and lightning standards. The second definition is the risetime associated with the maximum rate of rise t_{mr} given by the ratio of the current peak to the current maximum derivative.

The noise level associated with the measurement system did not allow us to accurately characterize flashes with a relatively low initial continuous current. As a result, no statistical data were presented for the total transferred charge associated with the flashes. Nevertheless, it was found that many flashes were characterized by a large amount of charge transfers (in excess of 50 C); The main charge transfer being due to the long initial continuous current, while the individual strokes contribute marginally to the total charge.

The median value of the flash multiplicity or the number of pulses per flash was found to be 8, a value much larger than those associated with downward flashes. Interestingly, 6 flashes exhibited a number of pulses in excess of 40.

Chapter 5 presented an analysis of measured current waveforms associated with positive and bipolar flashes recorded on the Säntis tower from May 2010 till January 2012. The overall number of recorded positive flashes in the considered period was 30, while 3 flashes were classified as bipolar. The recorded positive flashes were mainly concentrated in the summer months, August being the month during which most of them occurred (6 events in 2010 and 16 events in 2011). The percentage of positive flashes (15%) was found to be considerably larger than the values observed in other studies in summer months (3% to 6.5%).

The time-derivatives of the current pulses associated with upward stepped leaders were found to be much larger than those of the main pulse. All the observed flashes contained a single main pulse, except for one flash of the second type, which featured two pulses. Our recorded data constitute the first directly-measured evidence of M-components of both polarities during a continuing current lowering positive charge to ground.

The observed positive flashes were characterized by a median peak current of 11.8 kA, and a median flash duration of 80 ms. These values are consistent with those associated with the data recorded at the Gaisberg Tower in Austria. On the other hand, the amount of transferred charge was substantially larger in our dataset, with a median value of 169 C (6 times as large as the values obtained in Monte San Salvatore and in Japan, and 3 times as large as the value obtained in Austria). Eight flashes out of 30 transported positive charge to the ground in excess of 500 C. The obtained results confirm also the findings of Saba and co-workers according to which positive lightning flashes may combine high peak currents with high charge transfers (or flash durations).

The three bipolar flashes recorded during the considered time period occurred during one storm occurred on August 27, 2011. The relative number of bipolar flashes (1.5%) was found to be lower than the values reported in previous studies in Austria and in Switzerland (3 to 6%).

Chapter 6 presented an evaluation of the performance of the European Lightning Location Network (EUCLID) using the obtained data on lightning current measured on the Säntis Tower from June 1st, 2010 to May 31st, 2011. In the considered period, 57 flashes were recorded on the Säntis Tower out of which 15 were of positive polarity. From them, 37 could be correlated to EUCLID data by comparison of the time-stamp provided by GPS time reference installed on the Säntis and the EUCLID time.

The flash detection efficiency was estimated to be 93% and the median location error was 123 m. The EUCLID peak current estimates were on average larger than the measured current

with a median peak current estimation error of about 60% for strokes over 10 kA. For negative current peaks larger than 15 kA, the location errors did not exceed 1 km.

Measurements included four typical positive flashes successfully detected by EUCLID. The location errors for the positive events ranged from 1 to 3 km, with a median of 960 m. For the five positive events, the median of the absolute error of EUCLID peak current estimation as a percentage of the directly measured Söntis current was 46%.

In the **Appendix** of the thesis, we presented a thorough analysis of the characteristics of the noise affecting the measured signals at Söntis. We also described advanced signal processing methods, which were adopted and implemented to post-process the measured signals.

7.2 Original Contributions

The main original contributions of this thesis are summarized in what follows.

- Design, development, testing and installation of a complete system for the measurement of lightning currents at the Söntis tower. The system is designed to be operational in a harsh electromagnetic and environmental conditions, and it allows an over-the-Internet remote maintenance, monitoring and control.
- An improved design for the B-Dot sensor based on the works of Baum which does not have the shortcomings of conventional magnetic loops. The proposed combined use of the B-dot sensor and Rogowski coils allowed to obtain a faithful measurement of lightning currents in a frequency range of 0.01 Hz to 20 MHz.
- A complete statistical analysis of upward negative flashes. The obtained data represents today the largest dataset worldwide.
- Our data constitute the first directly-measured evidence of M-components of both polarities during a continuing current lowering positive charge to ground. Our data showed, in addition, that positive flashes may combine high peak currents with high charge transfers (or flash durations). As a result, they should be considered as a major concern for the designers of lightning protection systems of structures such as wind turbines and telecommunication towers.
- The performance evaluation of the European lightning detection network using ground-truth data obtained at Söntis tower.

7.3 Outlook and Future Work

The Sántis tower was instrumented in May 2010 and during its two first years of operation, more than 200 flashes were successfully recorded. The recorded flashes contain more than 2000 current pulses, constituting the largest available database in the literature, while the system remains operational and the number of data is constantly increasing.

The system has a robust base in terms of installed measurement device specifications and cabling and it has been working steadily since its installation, withstanding the changing temperatures and high fields produced by lightning and high power antenna transmitters installed on the tower.

The design provides the possibility of installing additional sensors as the measurement boxes and fiber optic links can accommodate further equipment.

One major limitation of the present system is the noise level which does not allow us to accurately characterize flashes with a relatively low initial continuous current. As a result, statistical data could not be obtained so far for the total transferred charge associated with the flashes. Furthermore, an accurate measurement of the initial continuous current is a must because it allows discriminating upward and downward flashes. Therefore, there is a need in enhancing the measurement system to make it possible to accurately measure initial continuous currents down to some tens of Amperes. Several options are under studies, namely the use of Hall effect sensors or magnetometers.

Another enhancement of the measurement system would be the installation of a high-speed camera to measure the lightning path trajectory. We plan also, in the near future, to develop and install electric and magnetic field sensors at different distances to the Sántis tower, to measure simultaneously electromagnetic fields radiated by strikes to the Sántis tower. These data would be extremely valuable, in particular to evaluate the propagation effects on mountainous regions and helping to calibrate lightning location systems.

The performance analysis of the European lightning detection network has revealed the need of a better calibration for low intensity and/or positive flashes to increase their efficiency in terms of location accuracy and peak current estimates. The obtained data on positive flashes could definitely be used for this purpose. And in general, experimental data on positive lightning being very limited and often controversial, the data could lead to physical insights into the physics of this type of discharge and to their better understanding.

The software design provides a stable and expandable platform based on proven technologies, the actual use of databases and well known programming languages. The modular construction of the algorithms will allow further improving the analysis and producing statistical data in a more efficient way, even when working with hundreds of millions of samples per channel.

The current data storage system allows to store data in distributed servers to assure the availability and safety of the stored records over time. However, the increasing amount of data will require some investments to provide extended server capacity and backup features.

The application of compression algorithms such as Prony or Matrix Pencil Method should be considered in the future to ease the storage and processing of the data.

Measured waveforms characterized by particularly fast risetimes might, in principle, be affected by transient processes along the tower. This phenomenon can be analyzed in the future thanks to the simultaneous measurement of the current at two different heights.

The tower with its proven sensors can be used for testing innovative techniques of measuring currents, such as fiber optic sensors, which might be used in the future in replacement of the Rogowski coils which suffer from shortcomings at very low and high frequencies.

References

- [1] V. A. Rakov and M. A. Uman, *Lightning: physics and effects*: Cambridge University Press, 2003.
- [2] R. A. Houze, *Cloud Dynamics*: Academic Press, 1994.
- [3] T. R. Shepherd, W. D. Rust, and T. C. Marshall, "Electric Fields and Charges near 0°C in Stratiform Clouds," *Monthly Weather Review*, vol. 124, pp. 919-938, 1996/05/01 1996.
- [4] I. M. Imyantov and E. V. Chubarina, *Electricity of the free atmosphere: by I.M. Imyantov and E.V. Chubarina. Translated from Russian*, 1967.
- [5] D. Lamb and J. Verlinde, *Physics and Chemistry of Clouds*: Cambridge University Press, 2011.
- [6] A. J. Illingworth, "Charge Separation in Thunderstorms: Small Scale Processes," *J. Geophys. Res.*, vol. 90, pp. 6026-6032, 1985.
- [7] E. R. Williams, "Large-Scale Charge Separation in Thunderclouds," *J. Geophys. Res.*, vol. 90, pp. 6013-6025, 1985.
- [8] R. F. Griffiths and J. Latham, "Electrical corona from ice hydrometeors," *Quarterly Journal of the Royal Meteorological Society*, vol. 101, pp. 395-395, 1975.
- [9] L. I. Dorman, *Cosmic Rays in Magnetospheres of the Earth and Other Planets*: Springer Science+Business Media B.V., 2009.
- [10] J. Kirkby, J. Curtius, J. Almeida, E. Dunne, J. Duplissy, S. Ehrhart, *et al.*, "Role of sulphuric acid, ammonia and galactic cosmic rays in atmospheric aerosol nucleation," *Nature*, vol. 476, pp. 429-433, 2011.
- [11] V. I. Ermakov, G. A. Bazilevskaya, P. E. Pokrevsky, and Y. I. Stozhkov, "Ion balance equation in the atmosphere," *J. Geophys. Res.*, vol. 102, pp. 23413-23419, 1997.
- [12] C. P. R. Saunders, "Charge separation mechanisms in clouds," *Space Science Reviews*, vol. 137, pp. 335-353, 2008.
- [13] R. Lhermitte and E. Williams, "Cloud electrification," *Rev. Geophys.*, vol. 21, pp. 984-992, 1983.
- [14] B. J. Mason, *The physics of clouds*: Clarendon Press, 1971.
- [15] V. Cooray, *The Lightning Flash*: IEE, 2003.
- [16] E. R. Williams, "The Tripole Structure of Thunderstorms," *J. Geophys. Res.*, vol. 94, pp. 13151-13167, 1989.

-
- [17] T. C. Marshall and M. Stolzenburg, "Estimates of cloud charge densities in thunderstorms," *J. Geophys. Res.*, vol. 103, pp. 19769-19775, 1998.
- [18] Q. Mo, J. H. Helsdon, Jr., and W. P. Winn, "Aircraft observations of the creation of lower positive charges in thunderstorms," *J. Geophys. Res.*, vol. 107, p. 4616, 2002.
- [19] G. Simpson and G. D. Robinson, "The Distribution of Electricity in Thunderclouds, II," *Proceedings of the Royal Society of London. Series A. Mathematical and Physical Sciences*, vol. 177, pp. 281-329, February 24, 1941 1941.
- [20] W. D. Rust and T. C. Marshall, "On abandoning the thunderstorm tripole-charge paradigm," *J. Geophys. Res.*, vol. 101, pp. 23499-23504, 1996.
- [21] M. Stolzenburg, W. D. Rust, and T. C. Marshall, "Electrical structure in thunderstorm convective regions 3. Synthesis," *J. Geophys. Res.*, vol. 103, pp. 14097-14108, 1998.
- [22] S. D. Pawar and A. K. Kamra, "Evolution of lightning and the possible initiation/triggering of lightning discharges by the lower positive charge center in an isolated thundercloud in the tropics," *J. Geophys. Res.*, vol. 109, p. D02205, 2004.
- [23] N. R. C. G. S. Committee and A. G. Union, *The Earth's Electrical Environment*: National Academy Press, 1986.
- [24] X. Qie, T. Zhang, C. Chen, G. Zhang, T. Zhang, and W. Wei, "The lower positive charge center and its effect on lightning discharges on the Tibetan Plateau," *Geophys. Res. Lett.*, vol. 32, p. L05814, 2005.
- [25] K. Narita, Y. Goto, H. Komuro, and S. Sawada, "Bipolar Lightning in Winter at Maki, Japan," *J. Geophys. Res.*, vol. 94, pp. 13191-13195, 1989.
- [26] J. Whiteway, C. Cook, M. Gallagher, T. Choularton, J. Harries, P. Connolly, *et al.*, "Anatomy of cirrus clouds: Results from the Emerald airborne campaigns," *Geophys. Res. Lett.*, vol. 31, p. L24102, 2004.
- [27] R. Solomon, V. Schroeder, and M. B. Baker, "Lightning initiation—conventional and runaway-breakdown hypotheses," *Quarterly Journal of the Royal Meteorological Society*, vol. 127, pp. 2683-2704, 2001.
- [28] D. Petersen, M. Bailey, J. Hallett, and W. H. Beasley, "Laboratory investigation of positive streamer discharges from simulated ice hydrometeors," *Quarterly Journal of the Royal Meteorological Society*, vol. 132, pp. 263-273, 2006.
- [29] A. V. Gurevich, G. A. Mesyats, K. P. Zybin, A. G. Reutova, V. G. Shpak, S. A. Shunailov, *et al.*, "Real-time observation of runaway-electron breakdown of air in the laboratory conditions," in *Plasma Science (ICOPS), 2011 Abstracts IEEE International Conference on*, 2011, pp. 1-1.
- [30] G. Milikh and R. Roussel-Dupré, "Runaway breakdown and electrical discharges in thunderstorms," *J. Geophys. Res.*, vol. 115, p. A00E60, 2010.
- [31] A. Nag and V. A. Rakov, "Pulse trains that are characteristic of preliminary breakdown in cloud-to-ground lightning but are not followed by return stroke pulses," *J. Geophys. Res.*, vol. 113, p. D01102, 2008.
- [32] C. J. Rodger, "Red sprites, upward lightning, and VLF perturbations," *Rev. Geophys.*, vol. 37, pp. 317-336, 1999.
- [33] W. P. Winn, G. D. Aulich, S. J. Hunyady, K. B. Eack, H. E. Edens, P. R. Krehbiel, *et al.*, "Lightning leader stepping, K changes, and other observations near an intracloud flash," *J. Geophys. Res.*, vol. 116, p. D23115, 2011.
- [34] R. A. Maddox, D. M. Rodgers, and K. W. Howard, "Mesoscale Convective Complexes Over the United States During 1981— Annual Summary," *Monthly Weather Review*, vol. 110, pp. 1501-1514, 1982/10/01 1982.

-
- [35] L. Weitao, Z. Enwei, Z. Yang, Z. Baoyou, Z. Dong, and Z. Yijun, "Correlation analysis between channel current and luminosity of continuous/continuing current process in an artificially triggered lightning flash," in *Lightning (APL), 2011 7th Asia-Pacific International Conference on*, 2011, pp. 322-326.
- [36] K. Berger, "Mesungen und Resultate der Blitzforschung auf dem Monte San Salvatore bei Lugano, der Jahre 1963-1971," *Bulletin SEV*, vol. 63, pp. 1403-1422, 1972.
- [37] M. M. F. Saba, M. G. Ballarotti, and O. Pinto, Jr., "Negative cloud-to-ground lightning properties from high-speed video observations," *J. Geophys. Res.*, vol. 111, p. D03101, 2006.
- [38] T. A. Warner, R. E. Orville, J. L. Marshall, and K. Huggins, "Spectral (600–1050 nm) time exposures (99.6 μs) of a lightning stepped leader," *J. Geophys. Res.*, vol. 116, p. D12210, 2011.
- [39] W. Schulz, H. Pichler, and G. Diendorfer, "Evaluation of 45 negative flashes based on E-field measurements, video data and lightning location data in Austria," in *30th Int. Conf. on Lightning Protection (ICLP)*, Cagliari, Italy, 2010.
- [40] T. A. Warner, K. L. Cummins, and R. E. Orville, "Comparison of Upward Lightning Observations From Towers in Rapid City, South Dakota with National Lightning Detection Network Data - Preliminary Findings," in *3rd International Symposium on Winter Lightning (ISWL2011)*, Sapporo, Japan, 2011.
- [41] Y. Baba and V. A. Rakov, "Lightning electromagnetic environment in the presence of a tall grounded strike object," *J. Geophys. Res.*, vol. 110, p. D09108, 2005.
- [42] H. Zhou, G. Diendorfer, R. Thottappillil, H. Pichler, and M. Mair, "Characteristics of upward positive lightning flashes initiated from the Gaisberg Tower," *J. Geophys. Res.*, vol. 117, p. D06110, 2012.
- [43] Y. Baba and M. Ishii, "Numerical electromagnetic field analysis of lightning current in tall structures," *IEEE Transactions on Power Delivery*, vol. 16, pp. 324-8, 2001.
- [44] A. Mosaddeghi, D. Pavanello, F. Rachidi, and M. Rubinstein, "Electric and Magnetic Fields at Very Close Range from a Lightning Strike to a Tall Object," in *19th International Zurich Symposium on Electromagnetic Compatibility*, Singapore, 2008.
- [45] J. L. Bermudez, F. Rachidi, W. Janischewskyj, A. M. Hussein, M. Rubinstein, C. A. Nucci, *et al.*, "On the Enhancement of Radiated Electric and Magnetic Fields Associated with Lightning Return Strokes to Tall Structures," in *IEEE International Conference on Electromagnetic Compatibility*, Montreal, Canada, 2001, pp. 1005-8.
- [46] F. Rachidi, "Modeling Lightning Return Strokes to Tall Structures: A Review," *Journal of Lightning Research*, vol. 1, pp. 16-31, January 2007.
- [47] K. Miyake, T. Suzuki, and K. Shinjou, "Characteristics of winter lightning current on Japan Sea Coast," *Power Delivery, IEEE Transactions on*, vol. 7, pp. 1450-1457, 1992.
- [48] A. Nag and V. A. Rakov, "Positive lightning: An overview, new observations, and inferences," *J. Geophys. Res.*, vol. 117, p. D08109, 2012.
- [49] V. A. RAKOV, *A review of positive and bipolar lightning discharges* vol. 84. Boston, MA, ETATS-UNIS: American Meteorological Society, 2003.
- [50] C. Romero, M. Paolone, F. Rachidi, M. Rubinstein, A. Rubinstein, G. Diendorfer, *et al.*, "Preliminary comparison of data from the Sântis Tower and the EUCLID lightning location system," in *Lightning Protection (XI SIPDA), 2011 International Symposium on*, 2011, pp. 140-145.
- [51] M. M. F. Saba, O. Pinto, Jr., and M. G. Ballarotti, "Relation between lightning return stroke peak current and following continuing current," *Geophys. Res. Lett.*, vol. 33, p. L23807, 2006.

-
- [52] C. Romero, M. Paolone, F. Rachidi, M. Rubinstein, V. A. Rakov, A. Rubinstein, *et al.*, "Current waveforms associated with positive flashes recorded on the Säntis tower in summer 2010," in *Lightning Protection (XI SIPDA), 2011 International Symposium on*, 2011, pp. 1-6.
- [53] H. Zhou, G. Diendorfer, R. Thottappillil, H. Pichler, and M. Mair, "Characteristics of upward bipolar lightning flashes observed at the Gaisberg Tower," *J. Geophys. Res.*, vol. 116, p. D13106, 2011.
- [54] K. Berger, "Blitzstrom-Parameter von Aufwärtsblitzen," *Bull. Schweiz. Elektrotech. Ver.*, vol. 69, pp. 353-60, 1978.
- [55] V. A. Rakov, "Lightning Phenomenology and Parameters Important for Lightning Protection," in *9th International Symposium on Lightning Protection (SIPDA)*, Foz do Iguaçu, Brazil, 2007.
- [56] N. Kitagawa, M. Brook, and E. J. Workman, "Continuing Currents in Cloud-to-Ground Lightning Discharges," *J. Geophys. Res.*, vol. 67, pp. 637-647, 1962.
- [57] V. A. Rakov and M. A. Uman, "Some properties of negative cloud-to-ground lightning flashes versus stroke order," *Journal of Geophysical Research*, vol. 95, pp. 5447-53, 1990.
- [58] V. Cooray and H. Pérez, "Some features of lightning flashes observed in Sweden," *J. Geophys. Res.*, vol. 99, pp. 10683-10688, 1994.
- [59] N. Aleksandrov, É. Bazelyan, and M. Shneider, "Effect of continuous current during pauses between successive strokes on the decay of the lightning channel," *Plasma Physics Reports*, vol. 26, pp. 893-901, 2000.
- [60] D. M. Jordan, V. P. Idone, R. E. Orville, V. A. Rakov, and M. A. Uman, "Luminosity characteristics of lightning M components," *J. Geophys. Res.*, vol. 100, pp. 25695-25700, 1995.
- [61] V. A. Rakov, D. E. Crawford, K. J. Rambo, G. H. Schnetzer, M. A. Uman, and R. Thottappillil, "M-component mode of charge transfer to ground in lightning discharges," *J. Geophys. Res.*, vol. 106, pp. 22817-22831, 2001.
- [62] L. Z. S. Campos, M. M. F. Saba, and C. Schumann, "Characterization of M Components in Positive Lightning from High-Speed Video and Electric Field Data," in *3rd International Symposium on Winter Lightning (ISWL2011)*, Sapporo, Japan, 2011.
- [63] G. Diendorfer, "Lightning initiated from tall structures — A review," in *Lightning Protection (XI SIPDA), 2011 International Symposium on*, 2011, pp. 298-303.
- [64] R. H. Golde, "Lightning and tall structures," *Electrical Engineers, Proceedings of the Institution of*, vol. 125, pp. 347-351, 1978.
- [65] H. Zhou, N. Theethayi, G. Diendorfer, R. Thottappillil, and V. Rakov, *On estimation of the effective height of towers on mountaintops in lightning incidence studies* vol. 68. Amsterdam, PAYS-BAS: Elsevier, 2010.
- [66] A. Mosaddeghi, F. Rachidi, M. Rubinstein, F. Napolitano, D. Pavanello, V. Shostak, *et al.*, "Radiated Fields from Lightning Strikes to Tall Structures: Effect of Upward Connecting Leader and Reflections at the Return Stroke Wavefront " *IEEE Transactions on Electromagnetic Compatibility*, in press, 2011.
- [67] M. Becerra, V. Cooray, S. Soula, and S. Chauzy, "Effect of the space charge layer created by corona at ground level on the inception of upward lightning leaders from tall towers," *J. Geophys. Res.*, vol. 112, p. D12205, 2007.

-
- [68] C. J. Biagi, M. A. Uman, J. Gopalakrishnan, J. D. Hill, V. A. Rakov, T. Ngin, *et al.*, "Determination of the electric field intensity and space charge density versus height prior to triggered lightning," *J. Geophys. Res.*, vol. 116, p. D15201, 2011.
- [69] G. Diendorfer and W. Schulz, "Lightning incidence to elevated objects on mountains," in *24th ICLP (International Conference on Lightning Protection)*, Birmingham, U.K., 1998, pp. 173-5.
- [70] A. Smorgonskiy, F. Rachidi, M. Rubinstein, G. Diendorfer, W. Schulz, and N. Korovkin, "A new method for the estimation of the number of upward flashes from tall structures," in *Lightning Protection (XI SIPDA), 2011 International Symposium on*, 2011, pp. 97-100.
- [71] V. A. Rakov, "Transient response of a tall object to lightning," *Electromagnetic Compatibility, IEEE Transactions on*, vol. 43, pp. 654-661, 2001.
- [72] J. L. Bermudez, F. Rachidi, W. Janischewskyj, A. M. Hussein, M. Rubinstein, D. Pavanello, *et al.*, "Influence of the Height of an Elevated Strike Object on the Enhancement of Lightning Radiated Fields," in *2003 IEEE Bologna PowerTech Conference*, Bologna, Italy, 2003, pp. 503-507.
- [73] J. L. Bermudez, M. Rubinstein, F. Rachidi, F. Heidler, and M. Paolone, "Determination of Reflection Coefficients at the Top and Bottom of Elevated Strike Objects Struck by Lightning," *Journal of Geophysical Research*, vol. 108, pp. 4413, doi: 10.1029/2002JD002973, 2003.
- [74] A. Mosaddeghi, F. Rachidi, M. Rubinstein, D. Pavanello, V. Shostak, W. Janischewskyj, *et al.*, "On the effect of possible reflections at the return stroke wavefront on radiated fields from lightning strikes to tall structures," in *X International Symposium on Lightning Protection (SIPDA)*, Curitiba, Brazil, 2009.
- [75] J.-S. Chang, T. G. Beuthe, L. Seto, A. Duft, N. Hayashi, W. Chisholm, *et al.*, "AN INVESTIGATION OF THE POSSIBLE RELATIONSHIPS BETWEEN THUNDERCLOUD ELECTRIC FIELDS AND THE LIGHTNING PARAMETERS FOR TALL STRUCTURES," *J. Geophys. Res.*, vol. 94, pp. 13197-13205, 1989.
- [76] K. Berger, R. B. Anderson, and H. Kroninger, "Parameters of lightning flashes," *Electra. no.*, vol. 41, pp. 23-37, 1975.
- [77] E. Garbagnati and G. B. Lo Piparo, "Parameters von Blitzstroemen," *Elektro-Technische Zeitschrift ETZ-A*, vol. 103, pp. 61-65, 1982.
- [78] F. Heidler, J. Wiesinger, and W. Zischank, "Lightning Currents Measured at a Telecommunication Tower from 1992 to 1998," in *14th International Zurich Symposium on Electromagnetic Compatibility*, Zurich, Switzerland, 2001, p. 6.
- [79] S. Visacro, J. A. Soares, M. A. O. Schroeder, L. C. L. Cherchiglia, and V. J. de Sousa, "Statistical analysis of lightning current parameters: Measurements at Morro do Cachimbo Station," *Journal of Geophysical Research*, vol. 109, D01105, doi:10.1029/2003JD003662, 2004.
- [80] J. Takami and S. Okabe, "Observational Results of Lightning Current on Transmission Towers," *IEEE Transactions on Power Delivery*, vol. 22, pp. 547-556, 2007.
- [81] G. Diendorfer, H. Pichler, and M. Mair, "Some Parameters of Negative Upward Initiated Lightning to the Gaisberg Tower (2000 - 2007)," *IEEE Transactions on Electromagnetic Compatibility*, 2009.
- [82] C. Leteinturier, C. Weidman, and J. Hamelin, "Current and Electric Field Derivatives in triggered Lightning Return Strokes," *Journal of Geophysical Research*, vol. 95, pp. 811-828, 1990.

-
- [83] V. A. Rakov, "Lightning discharges triggered using rocket-and-wire techniques," *recent res. Devel. Geophysics*, vol. 2, pp. 141-171, 1999.
- [84] V. A. Rakov, M. A. Uman, D. Wang, K. J. Rambo, D. E. Crawford, and G. H. Schnetzer, "Lightning properties from triggered-lightning experiments at Camp Blanding, Florida (1997-1999)," in *25th ICLP (international conference on lightning Protection)*, Rhodes, Greece, 2000, pp. 54-59.
- [85] J. C. Willett, J. C. Bailey, and E. P. Krider, "A class of unusual lightning electric field waveforms with very strong HF radiation," *Journal of Geophysical Research*, vol. 94, pp. 16,255-67, 1989.
- [86] V. A. Rakov, R. Thottappillil, and M. A. Uman, "On the empirical formula of Willett et al. relating lightning return-stroke peak current and peak electric field," *Journal of Geophysical Research*, vol. 97, pp. 11527-33, 1992.
- [87] F. Rachidi and R. Thottappillil, "Determination of lightning currents from far electromagnetic fields," *Journal of Geophysical Research*, vol. 98, pp. 18315-20, 1993.
- [88] F. Rachidi, J. L. Bermudez, M. Rubinstein, and V. A. Rakov, "On the estimation of lightning peak currents from measured fields using lightning location systems," *Journal of Electrostatics*, vol. 60, pp. 121-129, 2004.
- [89] Y. Baba and V. A. Rakov, "Lightning strikes to tall objects: Currents inferred from far electromagnetic fields versus directly measured currents," *Geophys. Res. Letters*, vol. 34, pp. 1-5, 2007.
- [90] F. J. de Miranda, O. Pinto Jr, and M. M. F. Saba, "A study of the time interval between return strokes and K-changes of negative cloud-to-ground lightning flashes in Brazil," *Journal of Atmospheric and Solar-Terrestrial Physics*, vol. 65, pp. 293-297, 2003.
- [91] K. Berger, "Novel observations on lightning discharges - Results of research on Mount San Salvatore," *Journal of the Franklin Institute*, vol. 283, pp. 478-525, 1967.
- [92] F. Rachidi, "The Quandary of Direct Measurement and Indirect Estimation of Lightning Current Parameters," ed, 2004.
- [93] S. Visacro, A. Soares, Jr., M. A. O. Schroeder, L. C. L. Cherchiglia, and V. J. de Sousa, "Statistical analysis of lightning current parameters: Measurements at Morro do Cachimbo Station," *J. Geophys. Res.*, vol. 109, p. D01105, 2004.
- [94] A. Hussein, W. Janischewskyj, M. Milewski, V. Shostak, W. A. Chisholm, and J. S. Chang, "Current waveform parameters of CN Tower," *Journal of Electrostatics*, vol. 60, pp. 149-162, 2004.
- [95] W. Janischewskyj, A. M. Hussein, V. Shostak, I. Rusan, J. X. Li, and J. S. Chang, "Statistics of lightning strikes to the Toronto Canadian National Tower (1978-1995)," *Power Delivery, IEEE Transactions on*, vol. 12, pp. 1210-1221, 1997.
- [96] A. M. Hussein, W. Janischewskyj, M. Milewski, V. Shostak, and J. S. Chang, "Waveform parameters of fields generated by lightning strokes to the CN tower and to objects in its vicinity," in *Power Tech Conference Proceedings, 2003 IEEE Bologna*, 2003, p. 8 pp. Vol.4.
- [97] V. A. Rakov, "Transient response of a tall object to lightning," *IEEE Transactions on Electromagnetic Compatibility*, vol. 43, pp. 654-61, 2001.
- [98] F. Fuchs, E. U. Landers, R. Schmid, and J. Wiesinger, "Lightning current and magnetic field parameters caused by lightning strikes to tall structures relating to

- interference of electronic systems," *Electromagnetic Compatibility, IEEE Transactions on*, vol. 40, pp. 444-451, 1998.
- [99] E. Montandon and B. Beyeler, "Lightning induced voltages on electrical installations on a swiss ptt instrumented tower in st. chrischona , switzerland," in *22nd International Conference on Lightning Protection*, Budapest, Hungary, 1994, p. 6.
- [100] V. A. Rakov, D. E. Crawford, V. Kodali, V. P. Idone, M. A. Uman, G. H. Schnetzer, *et al.*, "Cutoff and reestablishment of current in rocket-triggered lightning," *J. Geophys. Res.*, vol. 108, p. 4747, 2003.
- [101] J. D. Hill, J. Pilkey, M. A. Uman, D. M. Jordan, W. Rison, and P. R. Krehbiel, "Geometrical and electrical characteristics of the initial stage in Florida triggered lightning," *Geophys. Res. Lett.*, vol. 39, p. L09807, 2012.
- [102] M. Rahman, V. Cooray, V. A. Rakov, M. A. Uman, P. Liyanage, B. A. DeCarlo, *et al.*, "Measurements of NOX produced by rocket-triggered lightning," *Geophys. Res. Lett.*, vol. 34, p. L03816, 2007.
- [103] V. A. Rakov, "Parameters of Rocket-Triggered Lightning," *International Journal of Plasma Environmental Science and Technology (IJPEST)*, vol. 4, pp. 80-85, 2010.
- [104] D. M. Jordan, V. P. Idone, V. A. Rakov, M. A. Uman, W. H. Beasley, and H. Jurenka, "Observed Dart Leader Speed in Natural and Triggered Lightning," *J. Geophys. Res.*, vol. 97, pp. 9951-9957, 1992.
- [105] R. J. Fisher, G. H. Schnetzer, R. Thottappillil, V. A. Rakov, M. A. Uman, and J. D. Goldberg, "Parameters of triggered-lightning flashes in Florida and Alabama," *Journal of Geophysical Research*, vol. 98, pp. 22887-902, 1993.
- [106] V. A. Rakov, C. T. Mata, A. G. Mata, M. A. Uman, and K. J. Rambo, "Recent triggered-lightning experiments at the ICLRT at Camp Blanding, Florida," in *VII International Symposium on Lightning Protection (SIPDA)*, São Paulo, Brazil, 2003, pp. 144-150.
- [107] M. A. Uman, V. A. Rakov, E. J. Rambo, T. W. Vaught, M. I. Fernandez, D. J. Cordier, *et al.*, "Triggered-lightning experiments at Camp Blanding, Florida (1993-1995)," *Transactions of the Institute of Electrical Engineers of Japan, Part B*, vol. 117, pp. 446-52, 1997.
- [108] X. Liu, C. Wang, Y. Zhang, Q. Xiao, D. Wang, Z. Zhou, *et al.*, "Experiment of artificially triggering lightning in China," *J. Geophys. Res.*, vol. 99, pp. 10727-10731, 1994.
- [109] J. Yang, X. Qie, G. Zhang, Q. Zhang, G. Feng, Y. Zhao, *et al.*, "Characteristics of channel base currents and close magnetic fields in triggered flashes in SHATLE," *J. Geophys. Res.*, vol. 115, p. D23102, 2010.
- [110] O. Pinto Jr, I. R. C. A. Pinto, M. M. F. Saba, N. N. Solorzano, and D. Guedes, "Return stroke peak current observations of negative natural and triggered lightning in Brazil," *Atmospheric Research*, vol. 76, pp. 493-502, 2005.
- [111] R. P. Fieux, C. H. Gary, B. P. Hutzler, A. R. Eybert-Berard, P. L. Hubert, A. C. Meesters, *et al.*, "Research on Artificially Triggered Lightning in France," *Power Apparatus and Systems, IEEE Transactions on*, vol. PAS-97, pp. 725-733, 1978.
- [112] P. Depasse, "Statistics on artificially triggered lightning," *J. Geophys. Res.*, vol. 99, pp. 18515-18522, 1994.
- [113] H. Akiyama, K. Ichino, and K. Horii, "Channel Reconstruction of Triggered Lightning Flashes With Bipolar Currents From Thunder Measurements," *J. Geophys. Res.*, vol. 90, pp. 10674-10680, 1985.

-
- [114] M. Kobayashi, H. Sasaki, and K. Nakamura, "Rocket-triggered lightning experiments on zinc oxide arresters and their applications to power transmission lines," *Electrical Engineering in Japan*, vol. 122, pp. 25-33, 1998.
- [115] G. Diendorfer, W. Schulz, and V. A. Rakov, "Lightning characteristics based on data from the Austrian lightning locating system," *IEEE Transactions on Electromagnetic Compatibility*, vol. 40, pp. 452-64, 1998.
- [116] G. Diendorfer, "Lightning properties derived from lightning location systems and tower measurements," *Invited Talk presented at the 9th Int. Conference on EMI&EMC (INCEMIC 2006), Bangalore, India, 2006*.
- [117] A. M. Hussein, W. Janischewskyj, J. S. Chang, V. Shostak, W. A. Chisholm, P. Dzurevych, *et al.*, "Simultaneous measurement of lightning parameters for strokes to the Toronto Canadian National Tower," *Journal of Geophysical Research*, vol. 100, pp. 8853-61, 1995.
- [118] R. B. Andersson and A. J. Eriksson, "Lightning parameters for engineering application," *Electra*, vol. 69, pp. 65-102, 1980.
- [119] E. Garbagnati, E. Giudice, and G. B. Lopiparo, "Messung von Blitzströmen in Italien — Ergebnisse einer statistischen Auswertung," *ETZ*1978.
- [120] V. A. Rakov, M. A. Uman, K. J. Rambo, M. I. Fernandez, R. J. Fisher, G. H. Schnetzer, *et al.*, "New insights into lightning processes gained from triggered-lightning experiments in Florida and Alabama," *Journal of Geophysical Research*, vol. 103, pp. 14117-30, 1998.
- [121] J. C. Willett, J. C. Bailley, V. P. Idone, A. Eybert-Berard, and L. Barret, "Submicrosecond Intercomparison of Radiation Fields and currents in triggered Lightning Return Strokes Based on the Transmission-Line Model," *Journal of Geophysical Research*, vol. 94, pp. 13,275 - 13,286, 1989.
- [122] G. Diendorfer, M. Mair, W. Schulz, and W. Hadrian, "Lightning current measurements in Austria-experimental setup and first results," in *25th ICLP (International Conference on Lightning Protection)*, Rhodes, Greece, 2000, pp. 44-47.
- [123] E. Montandon and B. Beyeler, "The lightning measuring equipment on the swiss PTT telecommunications tower at st. chrischona, switzerland," *telecom recherches et développement, St. Chrischona, Switzerland*29.04.94 1994.
- [124] C. Romero, A. Rubinstein, M. Paolone, F. Rachidi, M. Rubinstein, P. Zweiacker, *et al.*, "Instrumentation of the Säntis Tower in Switzerland for lightning current measurements," *International Journal of Plasma Environmental Science & Technology*, vol. 4, pp. 79-85, 2010.
- [125] C. Romero, A. Mediano, A. Rubinstein, F. Rachidi, M. Rubinstein, M. Paolone, *et al.*, "Measurement of lightning currents using a combination of Rogowski coils and B-Dot sensors," in *30th International Conference on Lightning Protection (ICLP)*, Cagliari, Italy, 2010.
- [126] C. Romero, M. Paolone, M. Rubinstein, F. Rachidi, A. Rubinstein, G. Diendorfer, *et al.*, "A System for the Measurements of Lightning Currents at the Säntis Tower," *Electric Power System Research Journal*, 2011.
- [127] C. E. Baum, "Maximizing Frequency Response of a B-dot Loop: Note 8," *Sensor and Simulation Notes*1964.
- [128] C. E. Baum, E. Breen, J. Giles, J. O'Neill, and G. Sower, "Sensors for electromagnetic pulse measurements both inside and away from nuclear source regions," *IEEE Transactions on Antennas and Propagation*, vol. 26, pp. 22-35, 1978.

-
- [129] C. E. Baum, "A Conical-Transmission-Line Gap for a Cylindrical Loop, Sensor and Simulation Note 42," 1967.
- [130] C. Romero, M. Paolone, F. Rachidi, M. Rubinstein, A. Rubinstein, P. Zweigacker, *et al.*, "Current Waveforms Associated with Positive Flashes Recorded on the Sântis Tower in Summer 2010 " in *XI International Symposium on Lightning Protection (SIPDA)*, Fortaleza, Brazil, 2011.
- [131] V. A. Rakov, R. Thottappillil, and M. A. Uman, "Electric field pulses in K and M changes of lightning ground flashes," *Journal of Geophysical Research*, vol. 97, pp. 9935-50, 1992.
- [132] J. L. Bermudez, F. Rachidi, W. Janischewskyj, V. Shostak, M. Rubinstein, D. Pavanello, *et al.*, "Determination of Lightning Currents from Far Electromagnetic Fields: Effect of a Strike Object," *Journal of Electrostatics*, vol. 65, pp. 289-295, May 2007.
- [133] D. Flache, V. A. Rakov, F. Heidler, W. Zischank, and R. Thottappillil, "Initial-stage pulses in upward lightning: Leader/return stroke versus M-component mode of charge transfer to ground," *Geophys. Res. Lett.*, vol. 35, L13812, doi:10.1029/2008GL034148, 2008.
- [134] E. E. Ávila, R. E. Bürgesser, N. E. Castellano, A. B. Collier, R. H. Compagnucci, and A. R. W. Hughes, "Correlations between deep convection and lightning activity on a global scale," *Journal of Atmospheric and Solar-Terrestrial Physics*, vol. 72, pp. 1114-1121, 2010.
- [135] C. Romero, "Internal Rapport: On the Lognormal Probability Plot," 2012.
- [136] P. Chowdhuri, J. G. Anderson, W. A. Chisholm, T. E. Field, M. Ishii, J. A. Martinez, *et al.*, "Parameters of lightning strokes: a review," *Power Delivery, IEEE Transactions on*, vol. 20, pp. 346-358, 2005.
- [137] E. T. Lee and J. W. Wang, *Statistical Methods for Survival Data Analysis*: J. Wiley, 2003.
- [138] *Biostatistics: A Foundation for Analysis in the Health Sciences 8E with SPSS Student Software Version 16. 0*: John Wiley & Sons, Incorporated, 2008.
- [139] J. H. Hagenguth and J. G. Anderson, "Lightning to the Empire State Building," *AIEE Trans.*, vol. 71, pp. 641-9, 1952.
- [140] K. Berger, "Blitzstrom-Parameters von Aufwärtsblitzen," *Schweiz. Elektrotech.*, vol. 69, 1978.
- [141] F. Fuchs, "Overall experimental setup for the lightning current and LEMP research at the mountain Hoher Peissenberg," in *24th ICLP (International Conference on Lightning Protection)*, Birmingham, U.K., 1998, pp. 95-100.
- [142] B. N. Gorin and A. V. Shkilev, "Measurements of lightning currents at the Ostankino tower," *Elektrichestvo*, vol. 8, pp. 64-5, 1984.
- [143] V. Cooray, *Lightning Protection*: IET, 2010.
- [144] C. E. Baum, L. Carin, and A. P. Stone, *Ultra-Wideband, Short-Pulse Electromagnetics 3*: Plenum Press, 1997.
- [145] C. E. Baum, "Some Considerations Concerning Analytic EMP Criteria Waveforms," *Theoretical Notes*, vol. Note 285 (www.ece.unm.edu/summa/notes), 1976.
- [146] D. V. Giri, W. D. Prather, and C. E. Baum, "The Relationship Between NEMP Standards and Simulator Performance Specifications," *Sensor and Simulation Notes*, vol. Note 538 (www.ece.unm.edu/summa/notes), 2009.
- [147] D. V. Giri, "Effective Rise Time Resulting from a Convolution of Waveforms with Exponential and Gaussian Rise Characteristics," *Measurement Notes* vol. Note 33 (www.ece.unm.edu/summa/notes), 1987.

-
- [148] "IEEE Guide for Improving the lightning performance of electric power overhead distribution lines (IEEE Std. 1410)," ed: IEEE, 2004.
- [149] V. A. Rakov, "A Review of Positive and Bipolar Lightning Discharge," *Bull. Am. Meteor. Soc.*, vol. 84, pp. 767-776, 2003.
- [150] S. A. Yashunin, E. A. Mareev, and V. A. Rakov, "Are lightning M components capable of initiating sprites and sprite halos?," *J. Geophys. Res.*, vol. 112, p. D10109, 2007.
- [151] M. M. F. Saba, W. Schulz, T. A. Warner, L. Z. S. Campos, C. Schumann, E. P. Krider, *et al.*, "High-speed video observations of positive lightning flashes to ground," *Journal of Geophysical Research*, vol. 115, D24201, 2010.
- [152] Y. Goto and K. I. Narita, "Electrical characteristics of winter lightning," *Journal of Atmospheric and Terrestrial Physics*, vol. 57, pp. 449-458, 1995.
- [153] A. Wada, A. Asakawa, and T. Shindo, "Characteristics of lightning flash initiated by an upward leader in winter," in *23rd International Conference on Lightning Protection*, Florence, Italy, 1996.
- [154] G. Diendorfer, H. Pichler, and M. Mair, "Characteristics of positive upward lightning measured on an instrumented tower," in *28th International Conference on Lightning Protection (ICLP)*, Kanazawa, Japan, 2006, pp. 79-82.
- [155] D. Fuquay, "Positive Cloud-to-Ground Lightning in Summer Thunderstorms," *Journal of Geophysical Research*, vol. 87, pp. 7131-7140, 1982.
- [156] M. Ishii, K. Shimizu, J. Hojo, and K. Shinjo, "Termination of multiple-stroke flashes observed by electromagnetic field," in *24th International Conference on Lightning Protection (ICLP)*, Birmingham, UK, 1998.
- [157] M. M. F. Saba, K. L. Cummins, T. A. Warner, E. P. Krider, L. Z. S. Campos, M. G. Ballarotti, *et al.*, "Positive leader characteristics from high-speed video observations," *Geophys. Res. Lett.*, vol. 35, p. L07802, 2008.
- [158] M. M. F. Saba, L. Z. S. Campos, E. P. Krider, and O. Pinto, Jr., "High-speed video observations of positive ground flashes produced by intracloud lightning," *Geophys. Res. Lett.*, vol. 36, p. L12811, 2009.
- [159] L. Z. S. Campos, M. M. F. Saba, O. Pinto Jr, and M. G. Ballarotti, "Waveshapes of continuing currents and properties of M-components in natural positive cloud-to-ground lightning," *Atmospheric Research*, vol. 91, pp. 416-424, 2009.
- [160] S. A. Fleenor, C. J. Biagi, K. L. Cummins, E. P. Krider, and X.-M. Shao, "Characteristics of cloud-to-ground lightning in warm-season thunderstorms in the Central Great Plains," *Atmospheric Research*, vol. 91, pp. 333-352, 2009.
- [161] X. Kong, X. Qie, and Y. Zhao, "Characteristics of downward leader in a positive cloud-to-ground lightning flash observed by high-speed video camera and electric field changes," *Geophys. Res. Lett.*, vol. 35, p. L05816, 2008.
- [162] S. Miller and D. Childers, *Probability and Random Processes: With Applications to Signal Processing and Communications*: Elsevier Science, 2012.
- [163] J. M. Chambers, *Graphical methods for data analysis*: Wadsworth International Group, 1983.
- [164] T. M. M. Miki, A. Asakawa, Y. Asuka and N. Honjo, "Observation of Lightning Flashes to Wind Turbines," *30th International Conference on Lightning Protection (ICLP)*, Cagliari, Italy, 2010.
- [165] C. Romero, M. Paolone, F. Rachidi, M. Rubinstein, A. Rubinstein, G. Diendorfer, *et al.*, "Preliminary comparison of data from the Säntis Tower and the EUCLID

- lightning location system," in *Lightning Protection (XI SIPDA), 2011 International Symposium on*, 2011, pp. 140-145.
- [166] G. Diendorfer, W. Hadrian, F. Hofbauer, M. Mair, and W. Schulz, "Evaluation of lightning location data employing measurements of direct strikes to a radio tower," Session 2002 CIGRE, Paris, France 2002.
- [167] W. Schulz and G. Diendorfer, "Lightning peak currents measured on tall towers and measured with lightning location systems," in *18th International Lightning Detection Conference ILDC 2004*, Helsinki, Finland, 2004.
- [168] J. Jerauld, V. A. Rakov, M. A. Uman, K. J. Rambo, and D. M. Jordan, "An evaluation of the performance characteristics of the U.S. National Lightning Detection Network in Florida using rocket-triggered lightning," *Journal of Geophysical Research*, vol. 110, 2005 2005.
- [169] J. C. Willett, J. C. Bailey, V. P. Idone, A. Eybert-Berard, and L. Barret, "Submicrosecond Intercomparison of Radiation Fields and Currents in Triggered Lightning Return Strokes Based on the Transmission-Line Model," *J. Geophys. Res.*, vol. 94, pp. 13275-13286, 1989.
- [170] K. L. Cummins, W. L. Hiscox, A. E. Pifer, and M. W. Maier, "Performance analysis of the U.S. National Lightning Detection Network," in *9th International Conference on Atmospheric Electricity*, International Commission on Atmospheric Electricity, St. Petersburg, Russia, 1992.
- [171] K. L. Cummins, J. A. Cramer, C. J. Biagi, E. P. Krider, J. Jerauld, M. A. Uman, *et al.*, "The U.S. National Lightning Detection Network: Post-upgrade status," in *2nd Conf. on Meteorological Appl. of Lightning Data, AMS Annual Meeting*, Atlanta, US, 2006.
- [172] A. Nag, S. Mallick, V. A. Rakov, J. S. Howard, C. J. Biagi, J. D. Hill, *et al.*, "Evaluation of U.S. National Lightning Detection Network performance characteristics using rocket-triggered lightning data acquired in 2004-2009," *J. Geophys. Res.*, vol. 116, p. D02123, 2011.
- [173] D. Pavanello, F. Rachidi, W. Janischewskyj, M. Rubinstein, V. Shostak, C. A. Nucci, *et al.*, "On the Current Peak Estimates Provided by Lightning Detection Networks for Lightning Return Strokes to Tall Towers," *IEEE Transactions on Electromagnetic Compatibility*, vol. 51, pp. 453-458, 2009.
- [174] J. L. Bermudez, F. Rachidi, W. Janischewskyj, V. Shostak, M. Rubinstein, D. Pavanello, *et al.*, "Far-field - current relationship based on the TL model for lightning return strokes to elevated strike objects," *IEEE Transactions on Electromagnetic Compatibility*, vol. 47, pp. 146-159, February 2005 2005.
- [175] G. Diendorfer, "LLS Performance validation using lightning to Towers," in *21st International Lightning Detection Conference (ILDC) & 3rd International Lightning Meteorology Conference (ILMC)*, Orlando, Florida, 2010.
- [176] G. Diendorfer and H. Pichler, "Properties of lightning discharges to an instrumented tower and their implication on the location of those flashes by lightning location systems," in *6th International Workshop on Physics of Lightning, Assoc. pour la Promotion des Echanges entre la Rech. et l'Ind.*, Guadeloupe, France, 2004.

Appendix: Signal Processing of the Sántis Measured Waveforms

8.1 Introduction

The Sántis Tower measuring system uses a combination of Rogowski coils and magnetic field sensors [1] to record lightning current and its time derivative. The measured waveforms are contaminated with noise (due to external sources and internal sources, namely quantization noise). They might also be affected by possible reflections related to transient processes along a tall object [2-7].

In this Appendix, we present a thorough analysis of noise source and characteristics, as well as appropriate signal processing methods, which are adopted and implemented to post-process the measured signals.

8.2 SENDIS Software for the Analysis, Post-Processing of the Sántis Data and Extraction of Statistical Parameters

The measurement system installed on the Sántis tower records each flash over a period of 1.2 seconds with a sampling rate of 100 MSamples/sec. Considering that we have four measurement channels, the required memory for each flash is about 1 Gbyte. As a result, ordinary software could not be used for the visualization, processing and analysis of the results. A specific data analysis software (SENDIS) was developed in the framework of this thesis to analyze the obtained data and to extract statistical parameters. The software is based on Matlab and designed using Object Oriented Programming. SENDIS' current capabilities include the opening, segmentation and processing of data files in the range of hundreds of millions of samples. The user can subsample the data for obtaining faster and overall views of

the dataset. SENDIS makes it possible to segment the data for creating logical structured subsets and perform local processing on small clusters (such as return strokes). The software allows also to perform signal processing operations on the data, such as Wavelet filtering, FIR filtering, Zero-Delay Filtering, integration, derivation, DC estimation and user-defined algorithms.

Algorithms implemented in SENDIS allow the detection of current components (return stroke, M-component, continuing current) within each flash and the automatic extraction of statistical parameters of the current. In what follows, algorithms and signal processing tools used and implemented in SENDIS will be detailed.

8.3 Noise and Spectral Analysis

8.3.1 Example of measured data

One example of a measured flash current is shown on Figure 1. Figures 2 and 3 illustrate two different pulses from the given flash. Parameters like maximum current, pulse duration, and current derivative from large pulses (Figure 2a) can be clearly distinguished without filtering but detailed analysis related to the fast transient part (detailed in Figure 2b) might require some processing to remove noise from real signal characteristics. Furthermore for small pulses (Figure 3), it is even more important to clean the signal in a way that preserves its inherent characteristics (amplitude, frequency, delay and phase) to extract its salient parameters.

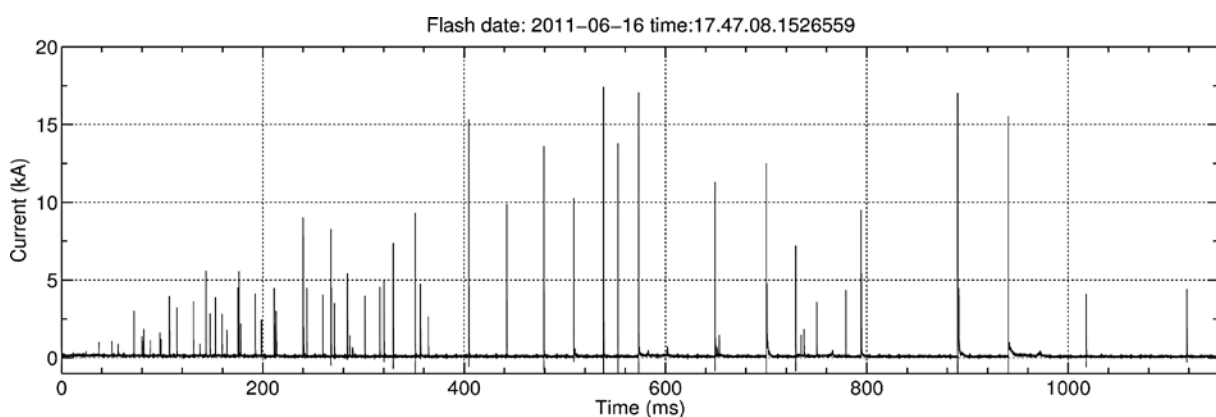


Figure 1. Example of a lightning flash current measured waveform.

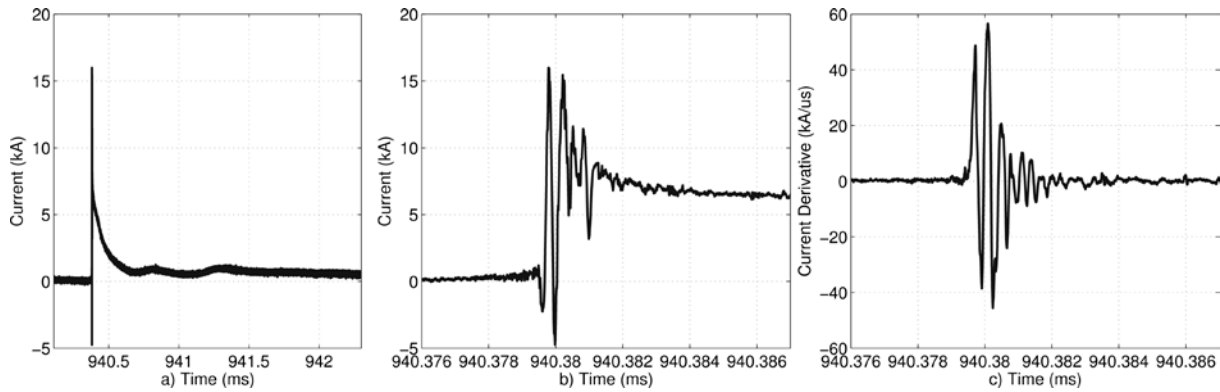


Figure 2 (a,b,c). Expanded view of a pulse of the flash presented in Fig. 1. (a) Pulse current. (b) Expanded views of the rising part of the current, and (c) its time derivative.

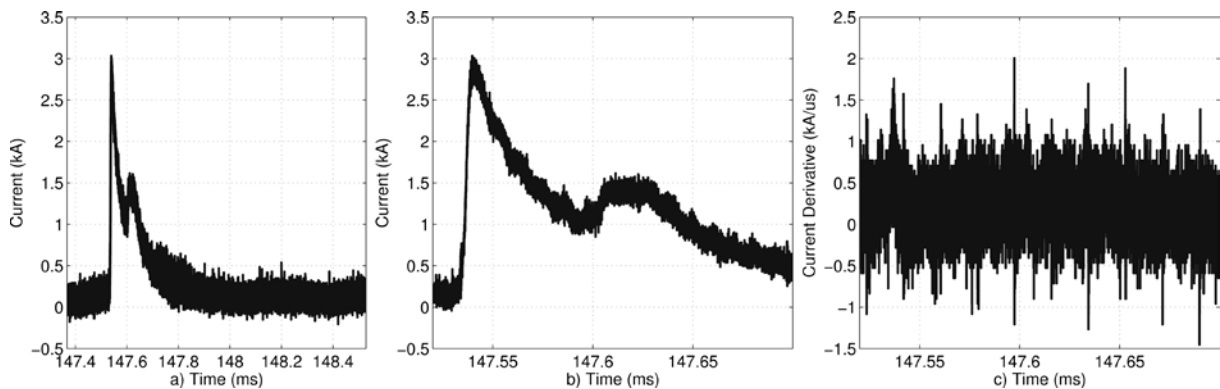


Figure 3 (a,b,c). Expanded view of a small pulse of the flash presented in Fig. 1. (a) Pulse current. (b) Expanded views of the rising part of the current and (c) its time derivative.

Appropriate signal processing methods should therefore be applied to extract the primary parameters of the lightning current from the measured waveforms, filtering out the external noise, as well as the internal noise from the measurement system.

The proposed algorithms and mathematical tools will be discussed in what follows, after a brief review of fundamental theory with illustrative examples.

8.3.2 Spectral Estimation

A frequency domain transformation of the time-domain signal is useful for a number of reasons such as the selection of the filtering algorithm. The spectral estimation algorithms should be carefully applied because of the inherent non-periodic nature of the measured signals and the resultant expected spectral leakage associated with the discrete Fourier transform (DFT) [8].

8.3.3 Non Parametrical Spectral Estimation

Non parametrical methods do not assume any underlying model of the random process under study, which can even be non-stationary [9]. In particular, the selected methods will use the information obtained after applying a DFT algorithm, which in this case will be the fast Fourier transformation (FFT).

8.3.4 Definition of parameters

The mean-squared spectrum (MSS) estimates the power at specific frequencies and it's often used for deterministic signal analysis [10]; it can be obtained from the Fourier transform using Equation 1.1:

$$MSS(f) = \frac{|\mathcal{F}(y(t))|^2}{N} \text{ [Watts]} \quad 1.1$$

where $(y(t))$ corresponds to a time-domain signal, $\mathcal{F}(\cdot)$ corresponds to the Fourier transform of the signal and N corresponds to the number of samples.

Another useful measure often applied to stochastic signals is the Power Spectral Density (PSD). The PSD can be obtained from the Fourier transform of the autocorrelation function of the signal (if the signal comes from a wide-sense stationary random process i.e. one whose joint probability distribution does not change when shifted in time or space) [10] as expressed in Equation 1.2

$$PSD(f) = \int_{-\infty}^{\infty} R(\tau) e^{-2\pi i f \tau} d\tau = \mathcal{F}(R(\tau)) \text{ [Watts/Hertz]} \quad 1.2$$

A supplementary calculated measure it's the Linear Spectral Density (LSD), corresponding to the square root of the PSD with units in dB/\sqrt{Hz} .

One basic quantity resulting from the PSD is the signal noise power in a frequency band [10] Equation 1.3, which can be obtained by integrating the PSD (in this case single sided for the positive frequencies):

$$P = \int_{F_1}^{F_2} PSD(f) df \quad 1.3$$

8.3.5 Parametrical Spectral Estimation

As opposed to non-parametric spectral estimation methods, parametric methods are based on the assumption of an underlying model, such as autoregressive (AR), moving average (MA), or ARMAX [11]. Once the parametric model is chosen, their parameters are estimated

typically using an error minimization technique [12]. This makes the parametric spectral estimation heavily dependent on the underlying model and its degrees of freedom. In this work, the selected spectral estimation model is the Yule-Walker because of its efficiency in handling large datasets and because it always produces an underlying stable model [13].

In many cases, the two methods (non-parametrical and parametrical) are presented concurrently in order to compare their respective estimations.

8.3.6 Spectral Leakage

When the discrete summation of the DFT algorithm is applied on finite signals over non integer periods, some spectral lines appear at frequency components that are not harmonics of the fundamental. Therefore the overall power is not well estimated. A simple example of this effect is shown in Figure 4, where the FFT on the same signal, but in one case sampled longer than a period, displays spectral lines that shouldn't exist for a perfect sinusoid. The importance of pointing the leakage phenomena comes from the fact that the measured signals on-the-field are not periodic, and as DFT-based measures are extensively used, they will likely present leakage.

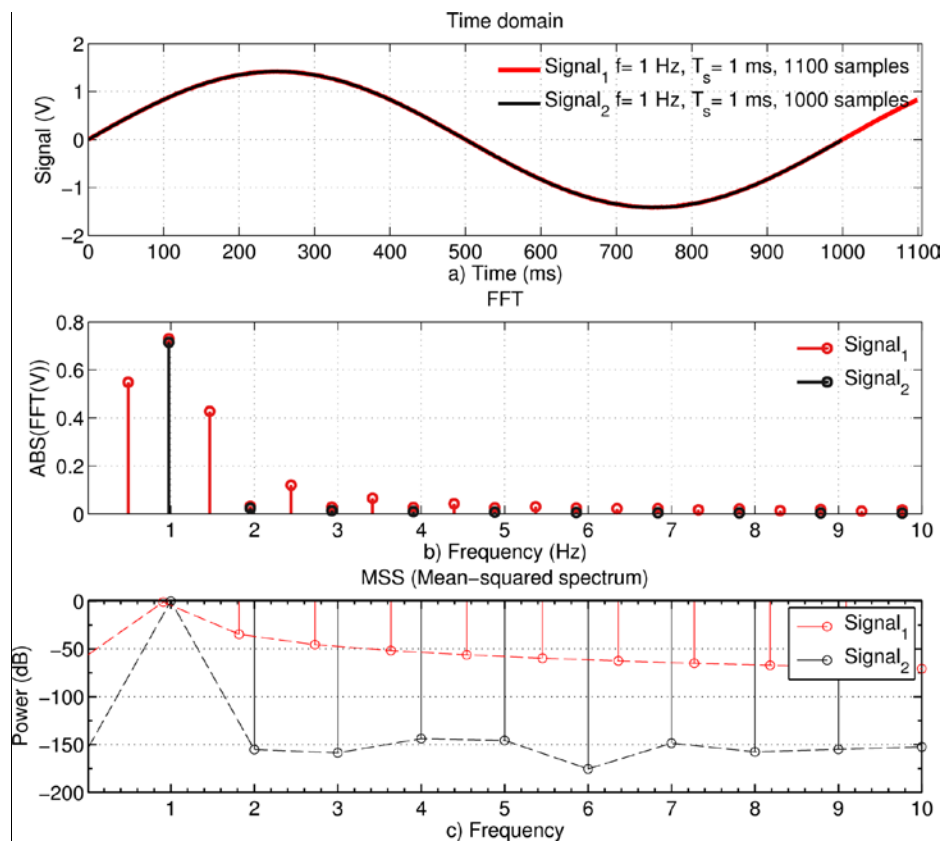


Figure 4 Spectral Leakage Effect on a sinusoidal signal (a)Time domain (b) FFT (c) MSS

To alleviate leakage it's necessary to apply a window to the signals in order to improve the spectral estimation. Some common windows are Blackman, Hamming, and Kaiser. Each has different figures of merit and tradeoffs as detailed in [14]. Examples of different windows are depicted in Figure 5, where it's seen that the pass-band and stop-band transitions, lengths and flatness are particular to each method. A detailed study on the windows behavior and characteristics can be found on [15].

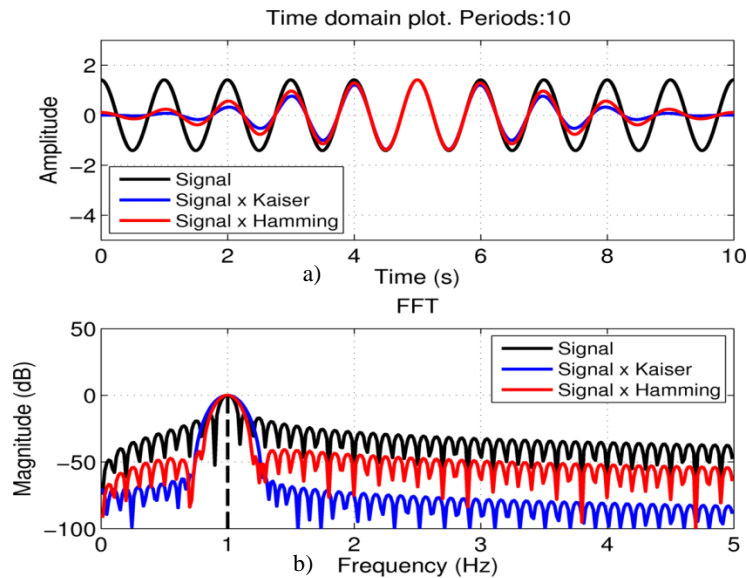


Figure 5. Effect of windowing the time signals on a generated signal (a) Effect on time (b) Effect on frequency

After testing different windows on the measured data, a Kaiser window was selected for the spectral analysis, in particular because of the transient behavior of the current and magnetic field derivative waveforms featuring resonant frequencies [14, 16]. Windowing is integrated on the developed software for the spectral estimation module.

8.3.7 Measurement Noise Types

Unwanted noise from the measurement system can be classified according to its characteristics. The following list was adapted from [17]:

- White noise: random noise which has an impulse autocorrelation function and a flat power spectrum. White noise theoretically contains all frequencies in equal power.
- Band-limited white noise: Similar to white noise, this is a noise with a flat power spectrum and a limited bandwidth that usually covers the limited spectrum of the device or the signal of interest. The autocorrelation of this noise is sinc-shaped.
- Narrowband noise: A noise process with a narrow bandwidth such as 50/60 Hz from the electricity supply.

- Colored noise: A non-white noise or any wideband noise whose spectrum has a non-flat shape. Examples are pink noise (also called $1/f$ noise), brown noise and autoregressive noise.
- Impulsive noise: Consists of short-duration pulses of random amplitude, time of occurrence and duration.
- Transient noise pulses: Consist of relatively long duration noise pulses such as clicks, burst noise etc.
- Quantization noise: comes from the discretization of analog signals and is proportional to the number of used bits and the linearity of the converters.

Examining the frequency spectrum behavior of noise signals allows its identification to one of the mentioned forms of noise, and the design of filters allowing its minimization [9] (linear filters, Wiener filters, etc.).

8.3.8 Measurement System Signal Components

The Sántis measurement system consists of a combination of Rogowski coils and B-dot sensors, each with a given transfer function. The Rogowski coils are characterized by a frequency response ranging from a few mHz to about 2 MHz. A resonance at 1.2 MHz was detected during the coil's characterization [1]. The B-dot sensor's usable frequency response was determined, both by simulations and measurements, to be in the range from 100 KHz to about 20 MHz [18].

Note that we did not consider in the analysis other signal components associated with transient processes along the tower. Indeed, these transient effects should be in general negligible for a tower height of 124 m [2].

8.3.9 Quantification of Noise Using Spectral Analysis

To validate the results of the selected methods for noise characterization, synthetic waveforms with chosen noise parameters are generated. Then, estimation algorithms are applied to these waveforms and approximations of the original, known parameters are obtained. Finally, the selected methods are applied to the Sántis measured waveforms and the results are commented.

8.3.10 Example 1: Synthetic White Noise Signals

A stationary realization of a white-noise signal with zero mean and $\sigma=0.3$ is shown in Figure 6a. The sampling frequency is 10 MHz. The three sigma lines are also shown in the same figure. The corresponding histogram is shown in Figure. 7b. The mean-square spectrum (MSS) is plotted as a function of frequency in Figure 6c. The MSS was obtained by applying a Fourier transform to the autocorrelation function. Figure 6d shows the power spectral density (PSD) (independent of the sampling frequency) and Figure 6e shows the Linear Spectral Density (LSD) extensively used in electronic literature for device characterization.

From the figures, it's clear the constant power-over-frequency characteristic of the generated noise realization.

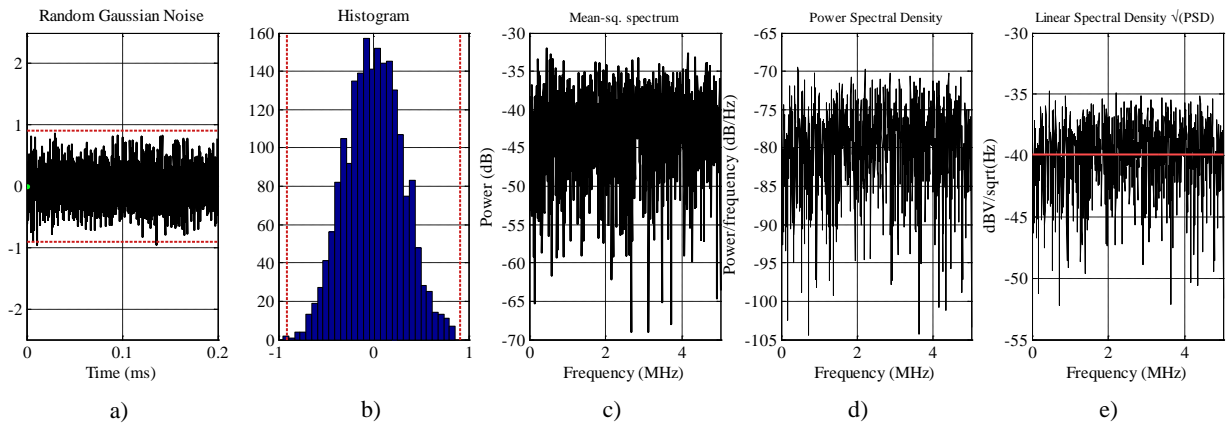


Figure 6 White Noise signal (a) with its associated histogram (b), Mean square spectrum (c), power spectral density (d) and linear spectral density (e).

The estimation of the noise power comes from Equations 1.1, 1.2 and 1.3, then calculating the integral of the PSD in the frequency range that gives the variance [10] (and square rooted the standard deviation σ); this integral is calculated numerically on the shown data obtaining:

$$\sigma_{estimated} = 0.29$$

Recall that synthetic noise was generated with $F_s = 10MHz$ and $\sigma=0.3$. From the Linear Spectral Density (LSD) curve (red line in Figure 6e) a constant noise in frequency of $-40dBV/\sqrt{Hz}$ is observed, a value that can also be obtained from the estimated σ as follows:

$$Noise_{[Vsqrthz]} = \sqrt{\frac{\sigma_{estimated}^2}{F_s}} = 91.70\mu V/\sqrt{Hz}$$

$$LSD = 10 \log(Noise) = -40.3dB$$

which corresponds to the value of the Figure 6e.

8.3.11 Synthetic Pink Noise Signal

A realization of a pink noise is shown in Figure 7. Its $1/f$ frequency decay is noticeable from its power density estimation (see Figure 7d). Such signals are associated with shot noise, reverberation and electrostatic discharges measured in communication channels [19]. They are difficult to filter given their non-stationary character.

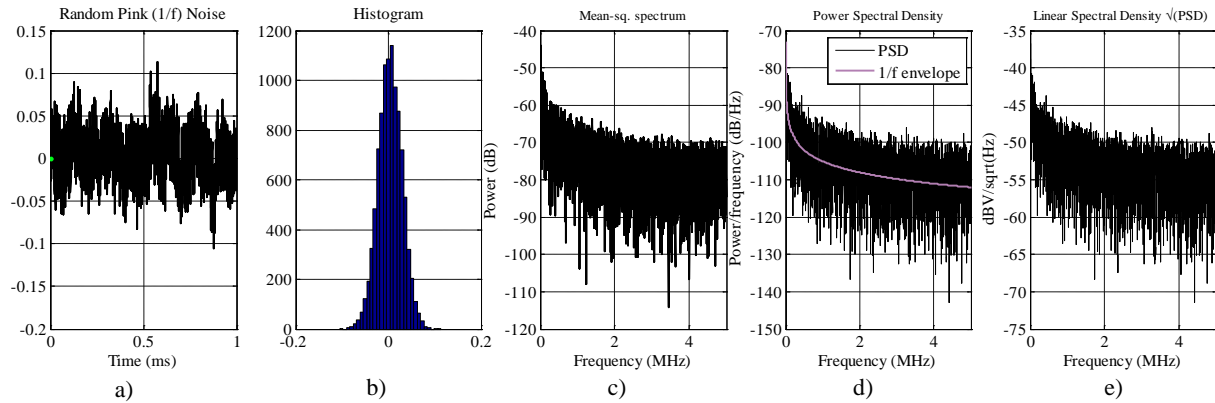


Figure 7 Pink Noise signal (a) with its associated histogram (b), Mean square spectrum (c), power spectral density (d) and linear spectral density (e).

8.3.12 Example 2: Sinusoid plus Noise

In order to illustrate the noise spectral estimation algorithm when noise is superimposed with signals, two sinusoids (0.2MHz and 0.4MHz) of amplitudes 1 and 2 volts, respectively, are added with the same amount of white noise used in the first example (see Figure 8a). Observe that for these amplitudes, the Mean Squared Spectrum plot (Figure 8b) approximates accurately their power in dB: -3dB and 3dB respectively (corresponding to $10\log(A^2/2)$ from each sinusoid, and marked by red dotted lines for clarity in Figure 8b). The result of the noise estimation (red line) on Figure 8d retrieves precisely the same values of estimated noise on the LSD as in the Example 1.

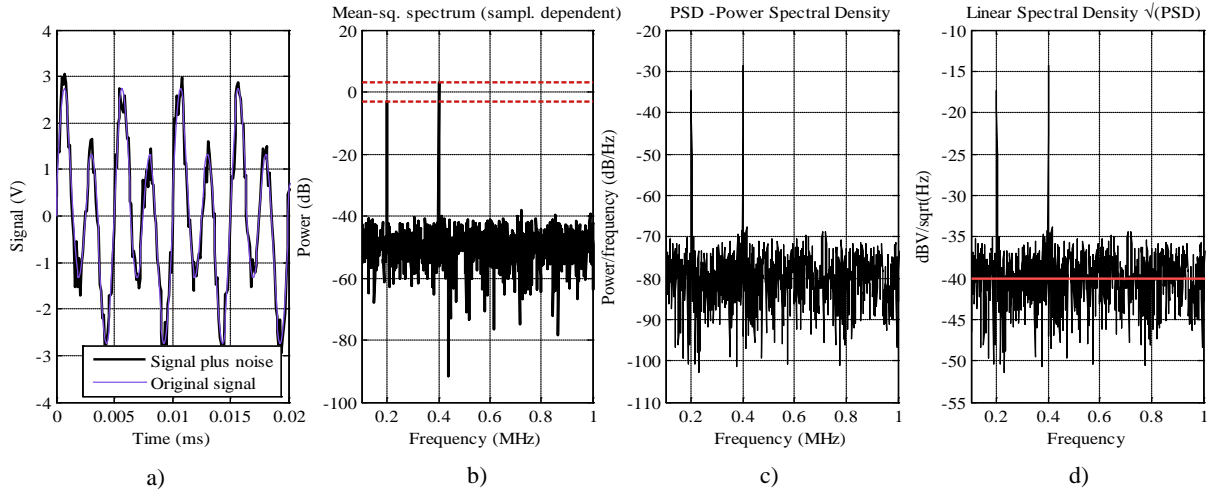


Figure 8 Sinusoid plus noise signal (a) with its associated histogram (b), Mean square spectrum (c), power spectral density (d) and linear spectral density (e).

The described methods will be now used to estimate the noise in the Sántis measurement system.

8.3.13 Spectral Analysis of the Sántis Signals

The current configuration of the Sántis measurement system comprises four measured signals [20]. The characteristics of the measuring sensor associated to each are presented in Table I.

TABLE I.
CHARACTERISTICS OF THE MEASUREMENT SYSTEM.

Sensor	Sensitivity	Min. Range	Max. Range	Bandwidth
B-dot sensor	91.131 (kA/us) / V	5 kA/us	250 kA/us (theoretical)	150KHz- 20MHz
Rogowski coil (1) PEM	20 kA/V	-	100 kA	0.01Hz- 1.2MHz
Rogowski coil (2) PEM	20 kA/V	-	100 kA	0.01Hz- 1.2MHz
Rogowski coil ROCOIL	1 kA/V	-	5 kA	0.01Hz- 1.2MHz

The complete measurement chain is depicted in Figure 9.

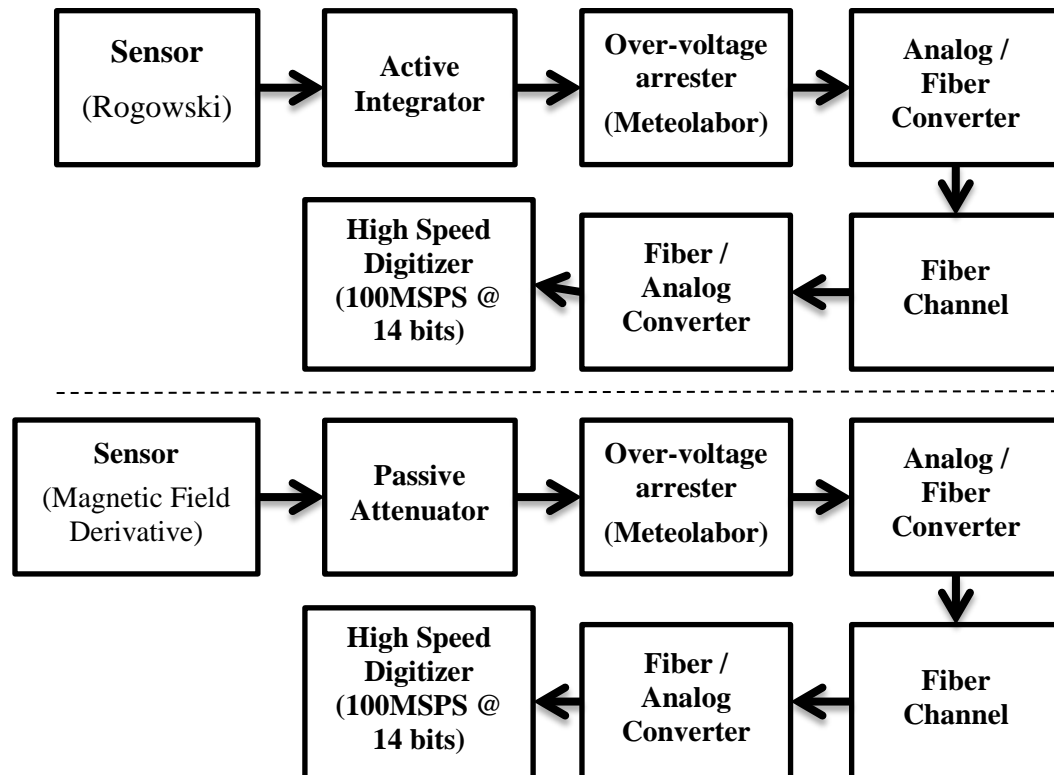


Figure 9. Sántis measurement system chain.

The signal out of the Rogowski coil is integrated using an analog active integration circuit. Then, the integrated signal is converted and relayed via fiber cables to the digitizer. The input of the electro-optical converter is protected using an overvoltage arrester (Meteolabor USS-2-V-BNC).

The signal out of the B-dot sensor goes through a passive 50 dB attenuator before being relayed to the digitizer through a fiber optic link.

An example of the parametric and non-parametric estimates of the PSD is shown in Figure 10 for the current and current-derivative channels associated with a flash occurred on 2012-01-05. The considered frequency range is up to 10 MHz and expanded views of the first 2 MHz are also shown separately. Notice that the current derivative has an expected larger frequency content (see right column), whereas the current signals coming from the Rogowski sensors have most of their energy concentrated on the first MHz of the spectrum and multiple resonance frequencies are observed at about 1MHz.

Further insight into the frequency content of a single pulse can be obtained using a spectrogram by means of a STFT [9]. Figure 11b shows the STFT for a single pulse of the same flash where peaks matching the peak frequencies (1.5MHz, 4.5MHz) in Figure 10 can be observed. Furthermore, they appear to be persistent over the whole duration of the pulse.

The energy is essentially concentrated in the rising part of the wave (Figure 11b). This behavior of the observed frequency peaks in the time-frequency diagram suggest that those are not associated with the Rogowski resonant frequency (only).

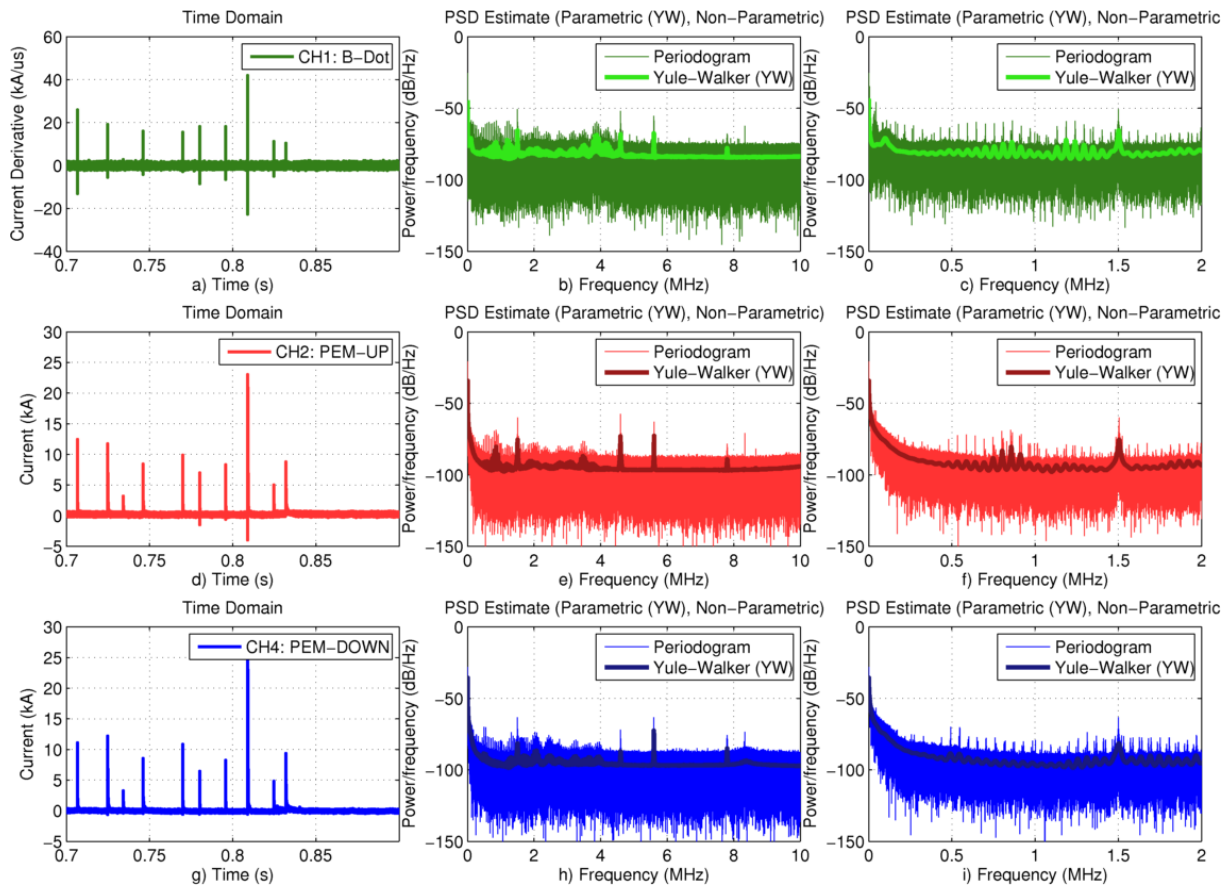


Figure 10. PSD (non-parametric and parametric) of the current derivative and the two current channels for a flash occurred on 2012-01-05 at 17:02. Left column (figures a,d,h): measured signal, middle column: PSD over 10 MHz, right column: expanded view of PSD for the first 2 MHz.

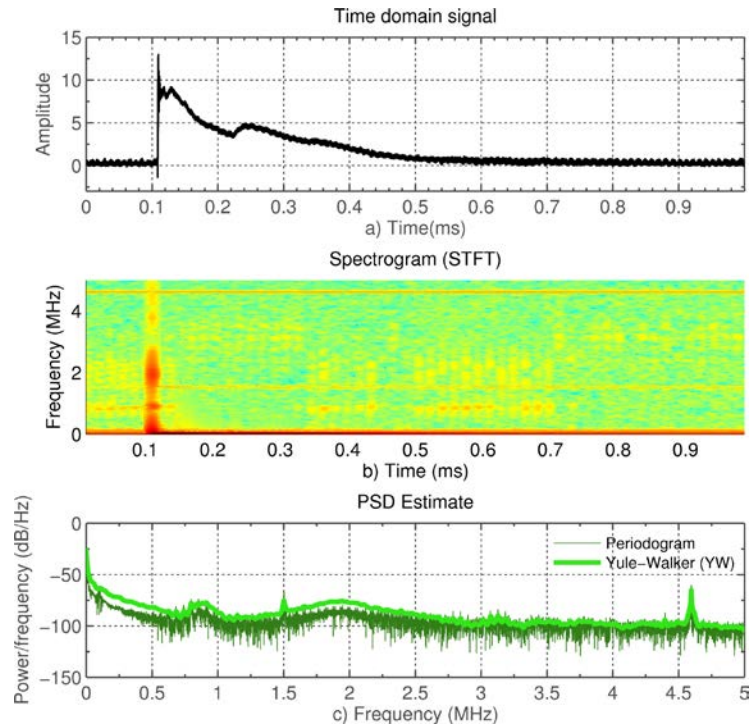


Figure 11. Expanded view of a single pulse associated with the same flash of Fig. 11 (a), along with its spectrogram (b) and PSD estimates (c).

To confirm the observations, the same analysis was repeated for the entire dataset, consisting of 1987 pulses. The results are presented in Figures 13, 14, and 15. They reveal peaks on both current and current derivate signals, whose main frequencies are located at 1.5MHz, 4.6MHz, 5.6MHz and 7.8MHz. They are seen consistently and cannot be associated with multiples of the sampling frequency of the fiber optic link (100MSPS) or the digitizer (100MSPS).

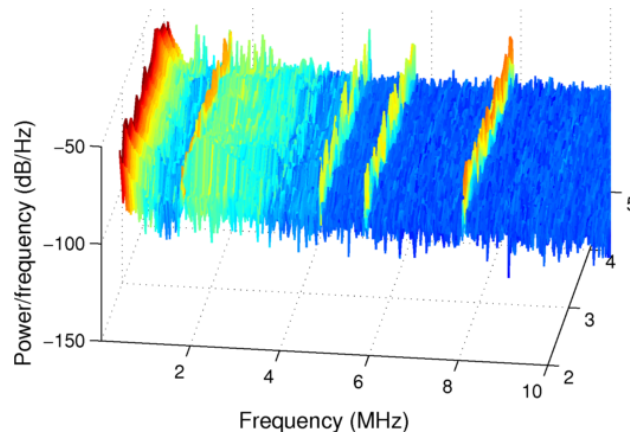


Figure 12. 3D view spectrogram for current pulses.

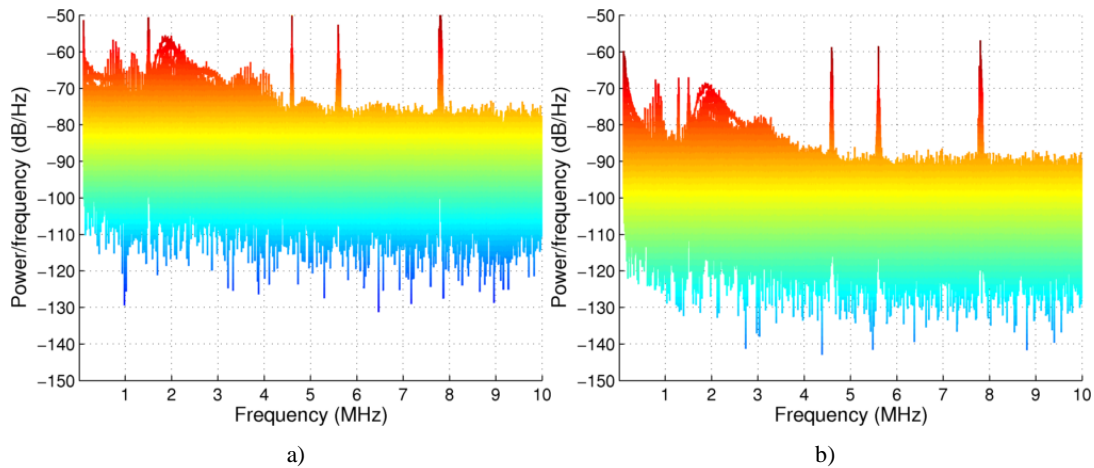


Figure 13. Front view spectrograms for current pulses (a) and their time-derivatives (b).

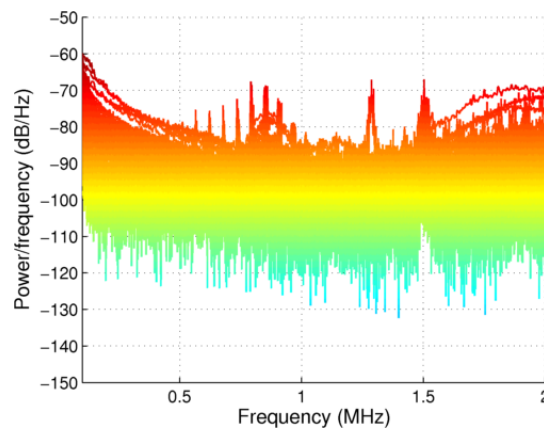


Figure 14. Spectrogram for thousands of current pulses showing the first 2MHz and the 1.5MHz resonance.

The origins of the observed peaks in the MHz region are currently unknown. They are, however, certainly related to an external continuous source and they are not associated with the measured lightning signals. Indeed, those peaks are present even when no lightning current is transiting the tower, as can be seen on the STFT-based time-frequency analysis of a measured noise signal, presented in Figure 15.

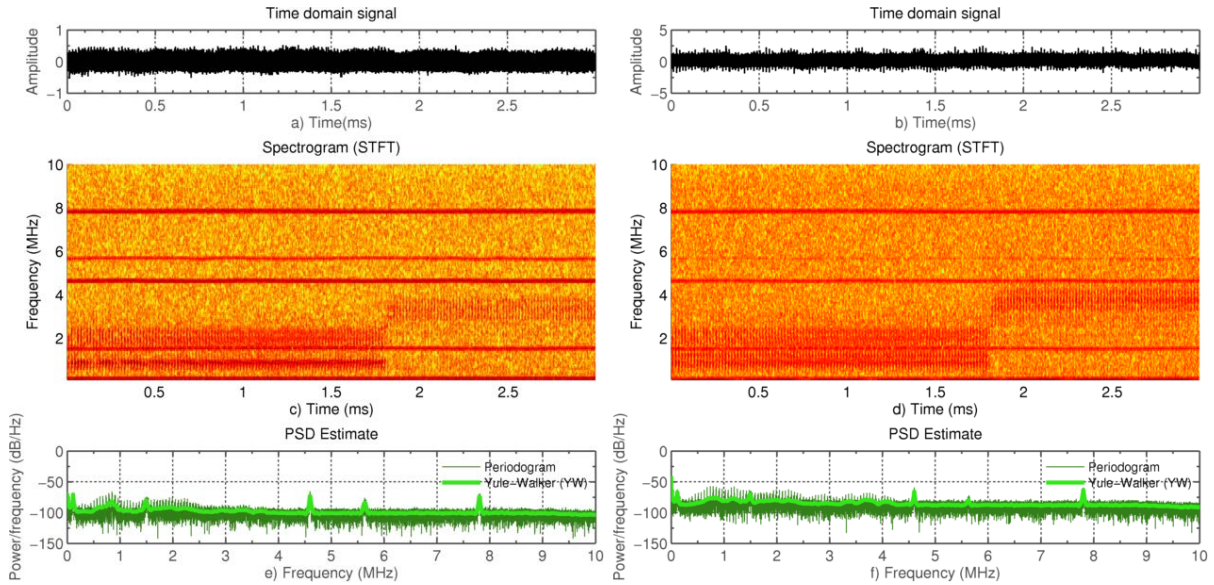


Figure 15. Time-frequency plot of a noise signal picked by the Rogowski coil (left column figures a,c,e) and its time derivative picked by the B-dot sensor (right column figures b,d,f). Both signals show resonance peaks associated to external noise.

The observed resonances cannot be originated from the Rogowski coil resonances, since they are equally observed on the output signals of all the three coils (characterized by different characteristics and physical sizes) as well as on the output signal of the B-dot sensor.

8.3.14 Noise Characterization of the Sántis Signals

We assume that the measured noise is a stationary stochastic process. Samples from hundreds of collected signals were processed using the previously described algorithms. One example of a noise sample signal and its spectral estimation is shown in Figure 16. The noise parameters over the full bandwidth (sampling frequency 100MSPS) for the considered noise signal shown in Figure 16 are summarized in Table II.

TABLE II.

NOISE ESTIMATION FOR THE NOISE SIGNAL PRESENTED IN FIGURE. 17 OVER THE FULL BANDWIDTH

Channel	Noise (rms) ($\sigma_{estimated}$)	Noise/sqrt(Hz) [dB]
Noise CH1 (kA/uS) (B-Dot)	0.31722	-45.8
Noise CH2 (kA) (PEM-UP)	0.07198	-52.5
Noise CH4 (kA) (PEM-DOWN)	0.12280	-50.9
Noise CH3 (kA) (ROCOIL)	0.00559	-64.1

The average noise estimates over the full bandwidth done for 500 noise samples along the entire Sántis database are presented in Table III.

TABLE III.
NOISE ESTIMATION OVER THE FULL BANDWIDTH

Channel	Noise (rms)	Noise/sqrt(Hz) [dB]
Noise CH1 (kA/uS) (B-Dot)	0.35	-44.56
Noise CH2 (kA) (PEM-UP)	0.100	-50
Noise CH4 (kA) (PEM-DOWN)	0.100	-50
Noise CH3 (kA) (ROCOIL)	5e-03	-63

It is important to underline that the obtained noise levels correspond to the full bandwidth. A denoising process via filtering can improve (lower) the effective measured noise by reducing the effective bandwidth.

The obtained results for filtered waveforms are summarized on Table IV. The selected upper frequency limits for the filters are chosen according to the bandwidth of the sensors. As expected, the resulting noise levels are significantly lower than the noise over the full bandwidth. It should be noted that in practice, over 99% of the noise (or peak-to-peak worst case scenario) is within six times the rms noise (6σ) [21]. These values are also reported in Table III.

TABLE IV.
NOISE ESTIMATION USING FILTERED WAVEFORMS

Channel	Bandwidth	Noise (rms)	Noise pk-to-pk (6σ)
Noise CH1 (B-Dot)	20MHz	0.22-kA/us	1.32-kA/us
Noise CH2 (PEM-UP)	1.5MHz	0.015-kA	0.09-kA
Noise CH4 (PEM-DOWN)	1.5MHz	0.015-kA	0.09-kA
Noise CH3 (ROCOIL)	1.5MHz	0.000765-kA	0.0046-kA

Examples of denoising on measured lightning waveforms are shown in Figure 17.

It is worth noting that the resulting filtered waveforms depend on the characteristics of the selected filters (phase, group delay, pass-band gain, stop-band attenuation). This will be discussed in Section 8.4.

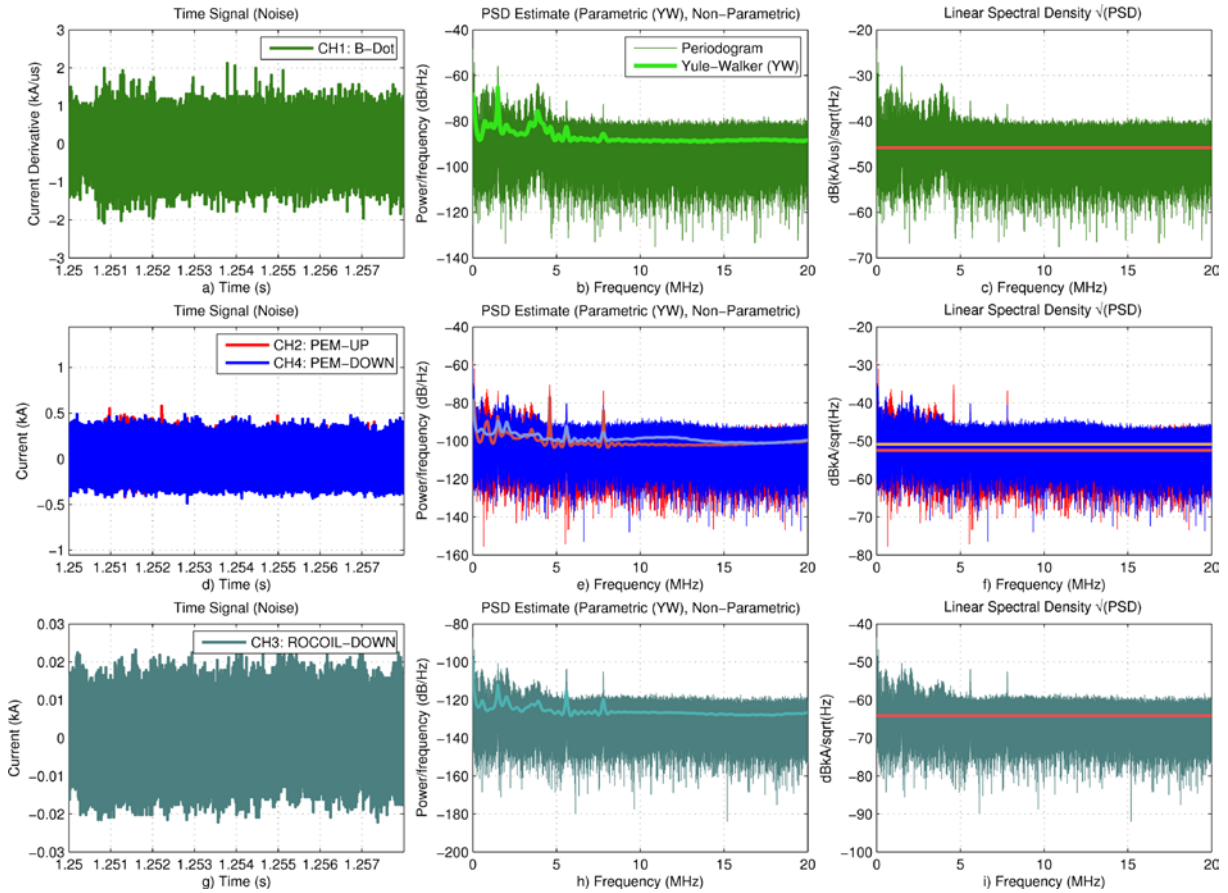


Figure 16. Sántis measurement system spectral noise estimation.

Left panel (Figures a,d,g): Time domain noise signal measured with the instrumentation. Center panel (Figures b,e,h): the estimated PSD. Right panel (Figures c,f,i): the estimated LSD.

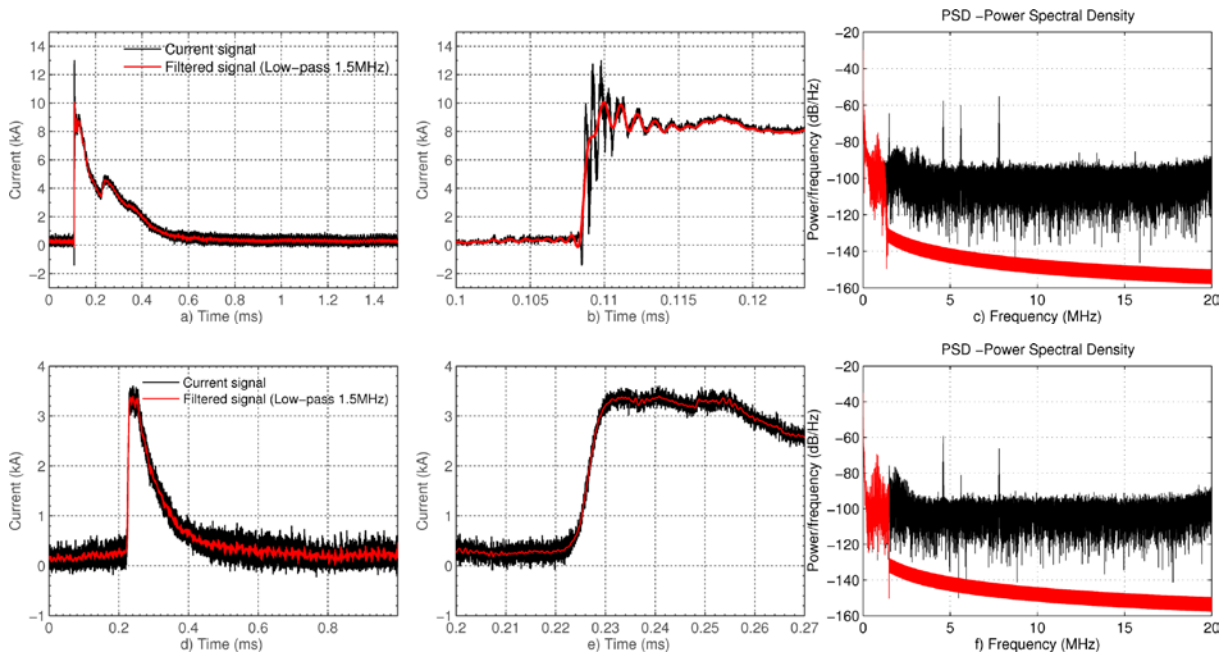


Figure 17. Denoising of measured waveforms using a low-pass 1.5 MHz filter. (a) Fast current pulse, (b) expanded view over the rising portion, (c) PSD. (d) Slow current pulse, (e) expanded view over the rising portion, (f) PSD. Black curve: raw data. Red curve: filtered data.

8.3.15 Loran-C Signals

Through the characterization process of the measured noise, a 100-kHz signal of about 20 and 30 dB larger than the base noise floor appeared consistently on the measurement channels, as shown in Figure 18. The signal appeared to be the Loran-C radio-navigation signal which uses the frequency band of 90–110 kHz¹.

Liatos and Hussein [22] found the same kind of noise component on the measured waveforms obtained at the CN Tower in Toronto over thirteen years of measurement.

The closest transmitters to the Sântis tower are reported in Table V along with their associated power and distance to the Sântis tower. Most of transmitters in Switzerland, Germany and Italy are decommissioned waiting for a modernization of the standard since 2010.

TABLE V.
LORAN-C TRANSMITTERS

Station	Country	LAT (WGS84)	LON (WGS84)	Power (kw)	Distance to Sântis (km)
LESSAY	France	49° 08' 55.224" N	001°30' 17.029" W	250	849
SOUSTONS	France	43° 44' 23.099" N	001° 22' 49.584" W	250	926
SYLT	Germany	54° 48' 29.975" N	008° 17' 36.856" E	250	855

¹ <http://www.loran-europe.eu>

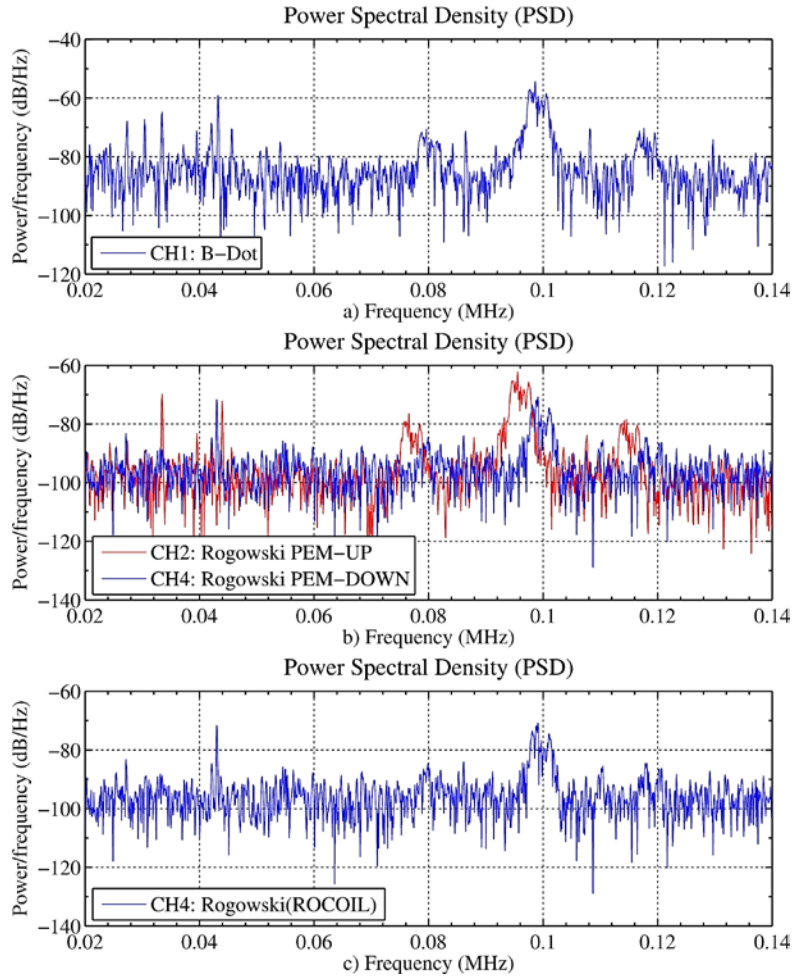


Figure 18. Detail of the PSD showing a signal in the band 90 - 100 KHz associated with a Loran-C signal

8.3.16 Prony Method Spectral Estimation

The Prony method [23] decomposes a given signal using a series of damped complex exponentials, offering a level of abstraction superior to the Fourier decomposition [24]:

$$y[n] = \sum_{i=1}^M a_i z_i^{n-1} \text{ with } a_i, z_i \in \mathbb{C} \quad 1.4$$

Being n the discrete sampling variable.

The developed Prony algorithm is based on the Matrix Pencil Algorithm [25] and Singular Value Decomposition and it's efficient with large signals via matrix regularization.

The following example depicts the representation of a time domain waveform coming from a synthetically generated damped sinusoid of 50Hz plus noise. In the considered case shown in Figure 19, the Prony method directly finds the coefficients via the implemented algorithm

when the signal is noiseless (Figure 19a) and finds a good approximation to the noisy case (Figure 19b). Figure 19c and 20d show the estimated frequencies from the Prony estimation.

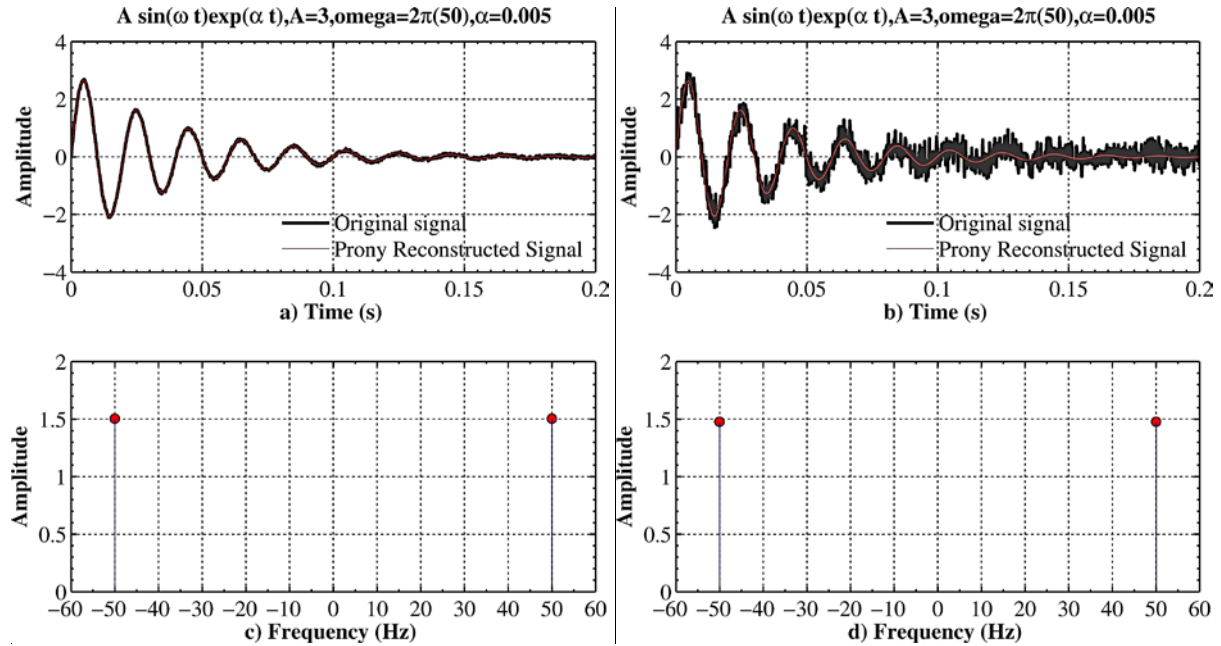


Figure 19. Example of signal reconstruction using the Prony method with different levels of noise. (a) a noiseless damped sinusoid, (b) noisy damped sinusoid, (c) and (d) estimated frequencies from the Prony method for the noiseless and noisy signals.

The Prony method is very efficient in representing complex signals with a reduced number of terms [24]. Its main problem is the computational complexity in making the estimation of the complex parameters via an error minimization algorithm, thus requiring spectral decompositions and matrix inversions, which makes it prohibitive for signals with large number of samples and large number of discrete frequencies corresponding to higher degrees of freedom [26].

Figure 20 shows a comparison between an original measured waveform for the current and its Prony representation, notice that the presented Prony representation uses only 200 coefficients.

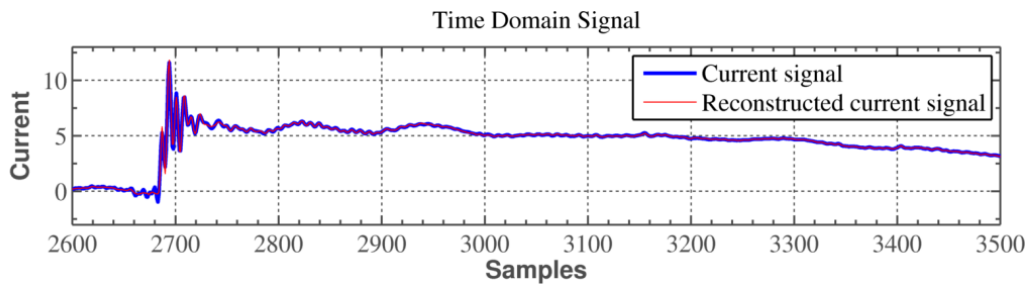


Figure 20. Signal reconstruction using the Prony method

8.3.17 Prony Signal Compression

The Prony method is also useful in finding compact representation of time varying signals. As an example, the Prony representation of the signal presented in Figure 20 uses only 200 coefficients, a sufficient number to represent a signal of 20.000 data samples. This corresponds to a compression rate of 100.

8.4 Filtering

Different filtering schemes have been tested on the database, the results are commented regarding their characteristics and how they impact the current waveform integrity.

8.4.1 FIR

A digital filter scheme consists on a discrete function of the form [9]

$$y[n] = \frac{1}{b_0} \left[\sum_{i=0}^N a_i x[n-i] - \sum_{j=0}^M b_j y[n-j] \right] \quad 1.5$$

This function generalizes the finite (FIR) and infinite IIR response filter representations. In particular the discrete coefficients a_i, b_i and orders N, M of the filter quantified via the design method (Butterworth, Elliptic, Equiripple, etc.), determine the pass-band and stop-band attenuations, the ripple in the same bands, the steepness of the transition between bands, the group delay, the step response and the stability [9]. The aim is to compare different design methods and adapt the design requirements to the measured current and current derivative signals.

Selecting the filter requires a compromise between the order and pass-band ripple for different design methods, a selection of which is presented in Figure 21.

After applying different types of filters to measured waveforms, the Chebyshev Type II was selected because of its maximum flatness on the band-pass which allows preserving the current amplitudes and fields while having a moderate transition band distance.

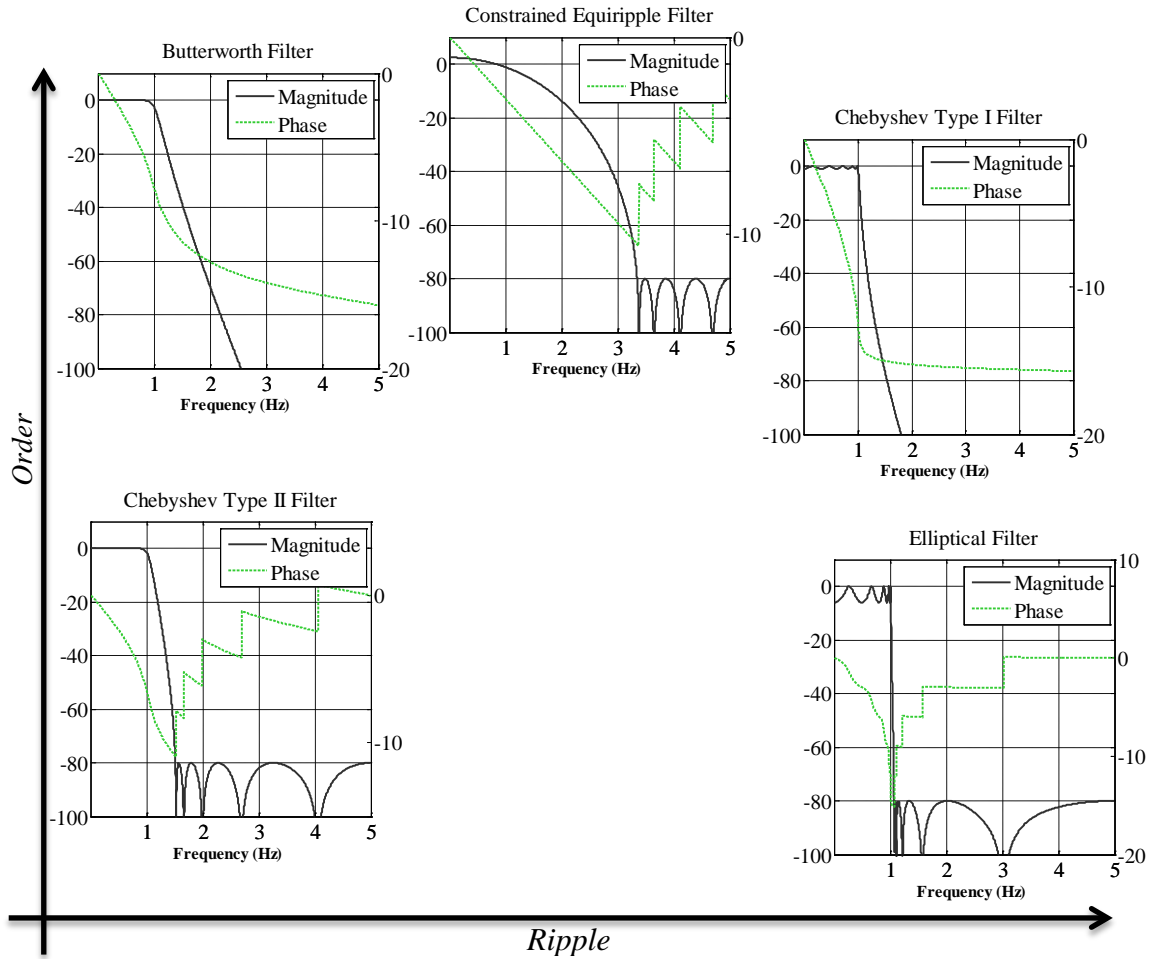


Figure 21. Filter design comparison regarding the magnitude and phase. Abscissa: Ripple, Ordinate: filter order

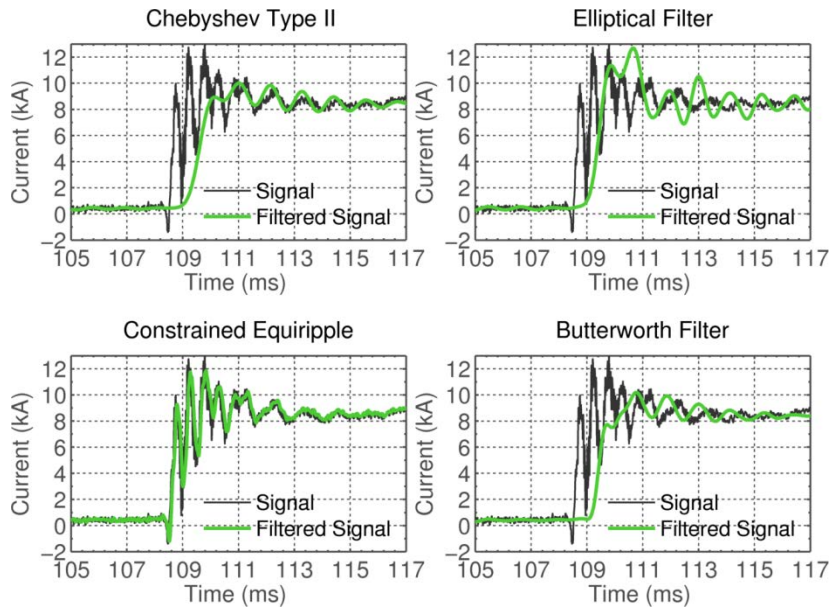


Figure 22. Comparison of different filter schemes on a measured current signal

Maintaining the pass-band signal amplitude response, allows the calculation of accurate amplitude statistics while filtering, which effectively shortens noise bandwidth and eliminate undesired bands.

The second basic comparison done in Figure 22 is the group delay effect on the output signal, which results on different frequencies getting delayed unevenly (in samples). In particular we need linear phase over the band-pass domain, thus zero or constant group delay, which on the Figure 22 comparison corresponds to the Constrained Equiripple Filter. However this filter doesn't correspond to a very low ripple characteristic with controlled gain on the pass-band response and the transition band is rather wide.

Figure 23 demonstrates additionally the undesirable group delay of the Chebyshev Type II filter. It could then be possible to search more elaborate filter design algorithms (such as multirate filters or a carefully designed cascade filter) but a tradeoff will always exist between the transition band size and the group delay, and in general we cannot afford to delay the signal nor changing its amplitude when making temporal comparison between channels and extracting statistics. The solution to use the Chebyshev Type II and correct its phase response comes in the form of a zero-phase filtering (ZPF), what could be applied due the offline nature of the measured signals. The ZPF design is detailed in the next subsection.

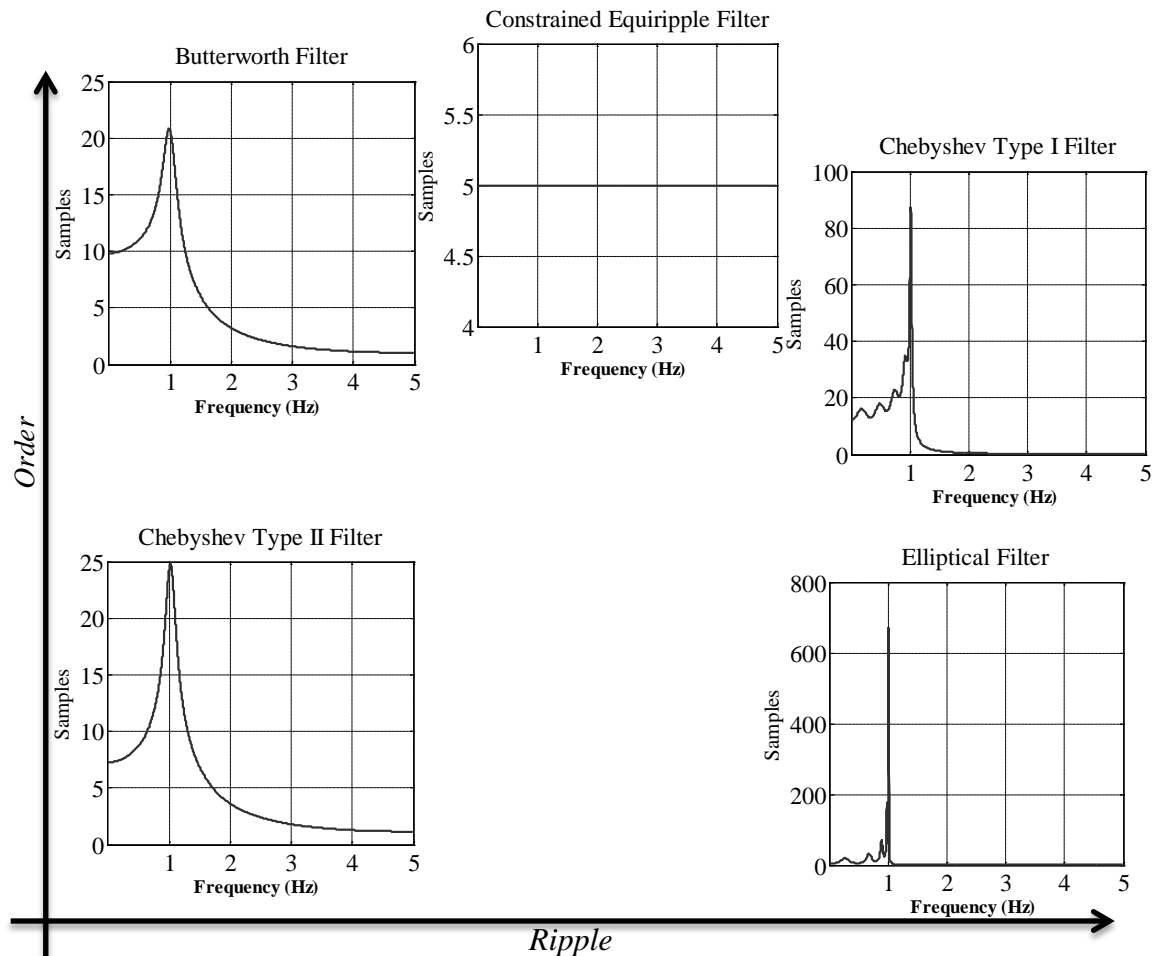


Figure 23. Filter design comparison regarding the group delay. Abscissa: Ripple, Ordinate: filter order

8.4.2 Zero-Phase Filtering

Zero-phase filtering (ZPF) prevents temporal signal delay while allowing even nonlinear phase and group delays. An example of the application of a linear phase filter compared with a zero-phase implementation is presented in Figure 24, where it can be seen that the FIR linear phase implementation results in a time-delay of the filtered signal.

The use of ZPF in lightning applications has already been proposed in [27, 28]. There are, however, two important issues associated with the use of ZPF which call for special care: the multiplication of the amplitude response and the transient phenomena on the signal start and end edges. These issues will be discussed in the following two subsections.

8.4.3 Amplitude Multiplication in ZPF

The ZPF filter convolves the selected filter coefficients sum ($G(n)$) to the input signal $x(n)$

$$y_{forward}[n] = G(n) * x(n) \quad 1.6$$

And then this signal is time reversed

$$y_{reversed}[n] = y_{forward}[-n] \quad 1.7$$

The selected filter is applied again

$$y_{second}[n] = G(n) * y_{reversed}[n] \quad 1.8$$

The final step is to reverse the resulting signal [15]

$$y[n] = y_{second}[-n] \quad 1.9$$

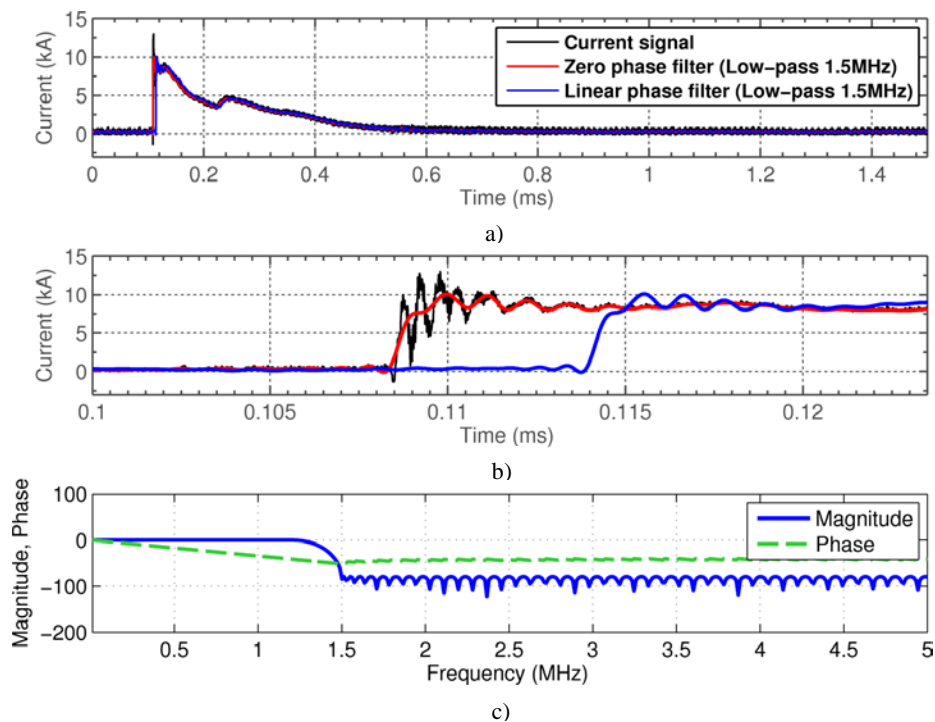


Figure 24. Zero-phase filter signal displacement behavior. a) Comparison between a measured current signal pulse, the result of zero phase filter on the signal (low pass at 1.5MHz) and a low-pass linear phase filter at the same frequency over the whole pulse duration. b) Detail of the risetime part of the three waveforms. c) Phase and frequency response of the low-pass filter

The main problem it's that the band-pass amplitude or gain should be as close to one, because when reversing the signal, the gain gets multiplied by the same value (squared). An example with a low order (and low delay) filter is shown on the Figure 25, where the FIR filter has a fixed gain (around 1.1) and its seen clearly that the zero phase response further amplify the amplitude. A closed demonstration of the amplitude multiplication can be found in [29].

This problem restricts even further the choice of the filter architecture, making necessary to choose a filter with a very flat pass-band amplitude response. In the end a ZPF Chebyshev type II was chosen due its characteristics. An example of the final implemented filtering scheme is shown in Figure 26 where is seen that the filtering process don't change neither the delay nor the phase (delay) response.

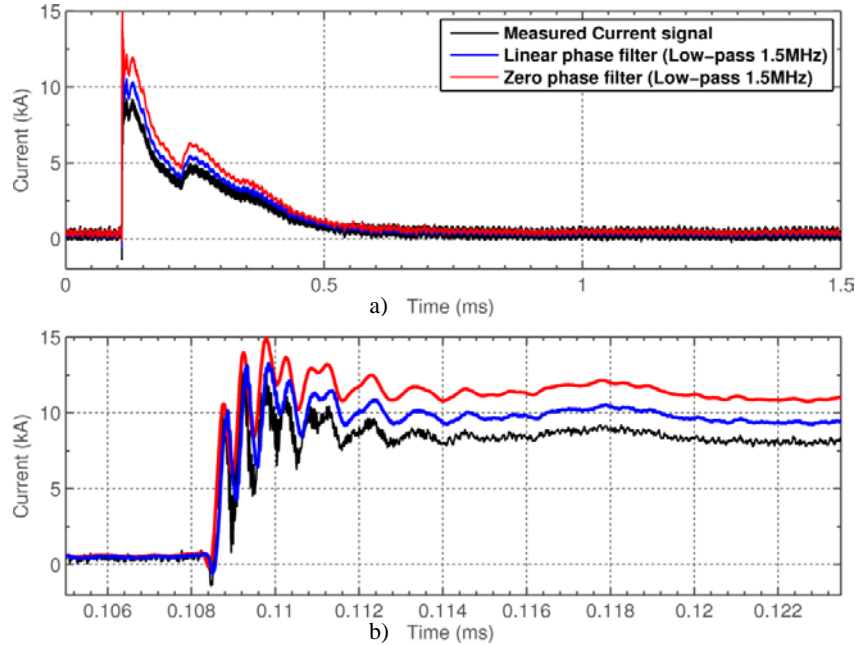


Figure 25. Amplitude multiplication in an incorrect ZPF implementation of a linear phase filter with non-unity gain in the pass-band a) Overall pulse b) detail of the risetime part (labels are the same as in part a))

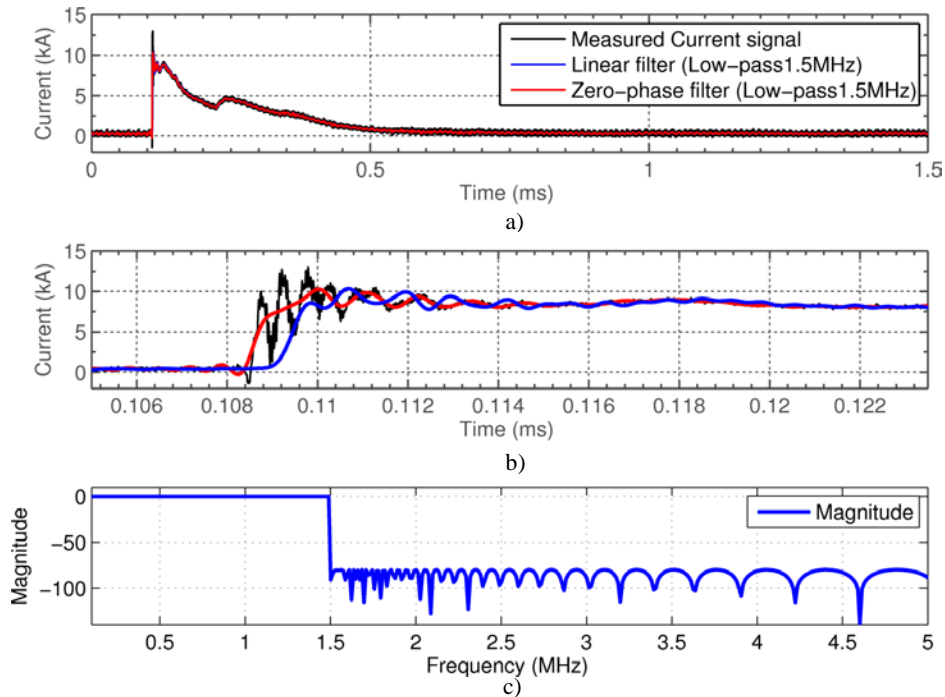


Figure 26. ZPF implementation used in the Sántis processing of the current signal (in black) a) Overall pulse b) detail of the risetime part (labels are the same as in part a))

8.4.4 Transient Response of ZPF

A potential problem is the step response of ZPF that alters the left and right edges of the signals [30], what in our case is not a huge concern as the signal on the edges is mainly composed of white noise and in any case no pulse is left or found on the borders of the analysis windows. An in-depth study of this problem and a solution can be found in [31].

8.4.5 Wavelet Analysis

The Wavelet-based analysis has been widely used in the lightning community for several areas such as lightning detection systems, mainly in the denoising process of the measured waveforms and in the extraction of signal components [32, 33], protection of power networks [34-36], modeling and characterization of lightning signals [37]. A good review on the use of Wavelet in lightning-related studies can be found in [38].

8.4.6 Wavelet Power Spectrum

The continuous-wavelet transform (CWT) can be written as the integral of the product between the signal $x(t)$ and the wavelet family $\Psi(a, b)$ [36]. The wavelet family of functions depends on a scaling factor (a) and a translation factor (b) that compress and scale the kernel (mother) wavelet in time.

$$CWT(a, b) = \frac{1}{\sqrt{a}} \int_{-\infty}^{\infty} x(t) \Psi^* \left(\frac{t-b}{a} \right) dt, (a, b) \in \mathbb{R} \quad 1.10$$

In contrast to the Fourier transform, the family of functions Ψ is not necessarily defined *a priori*, so they can be latter chosen to have desirable properties such as an approximate band-pass behavior in frequency. For an adequate wavelet analysis, the mother wavelet must fulfill the admissibility conditions, i.e. having a vanishing Fourier transform in zero frequency or equivalently a zero average value in the time domain which can be expressed as [39]:

$$|\Psi(\omega)|^2|_{\omega=0} = 0 \quad 1.11$$

This property implies that the wavelet has a band-pass spectrum because $\Psi(\omega)$ must be band-limited. A bank of band-pass filters with different frequencies and bandwidths can then be obtained by varying the scaling and translation factors of the selected Wavelet. As a result, a complete representation of the signal in frequency can be obtained in a tree-like fashion with a finite number of levels. The Wavelet transform can therefore improve one of the downsides of the STFT (used in Section 8.3.13 for time-frequency representation of pulses), namely the

inverse relation between the time resolution and frequency resolution [35]. In the same way a spectrogram was associated to the STFT, a scalogram can be defined for the CWT using a weighted sum of the squared wavelet coefficients.

Different wavelet families are associated with different time-frequency relations, therefore choosing the family depends on the compromise between time localization (ability to distinguish when in time a frequency change has occurred) and frequency localization (the capacity to distinguish close frequencies). The selected family is the Morlet kernel because of its regularity and good frequency localization ability for transient signals. Morlet signal in time domain is a cosine function multiplied by a Gaussian function and is a band-pass filter in the frequency domain [40]. An example of the capabilities of the wavelet transform is presented in Figure 27, where two synthetic sinusoids are generated with the aim of distinguishing their respective frequencies (1MHz and 2MHz with a sampling frequency of 100MHz). The figure shows how the Fourier-based spectral estimation (Figure 27c) fails to localize the frequencies whereas the wavelet transform accurately localize the two and display the time-frequency behavior of the signal.

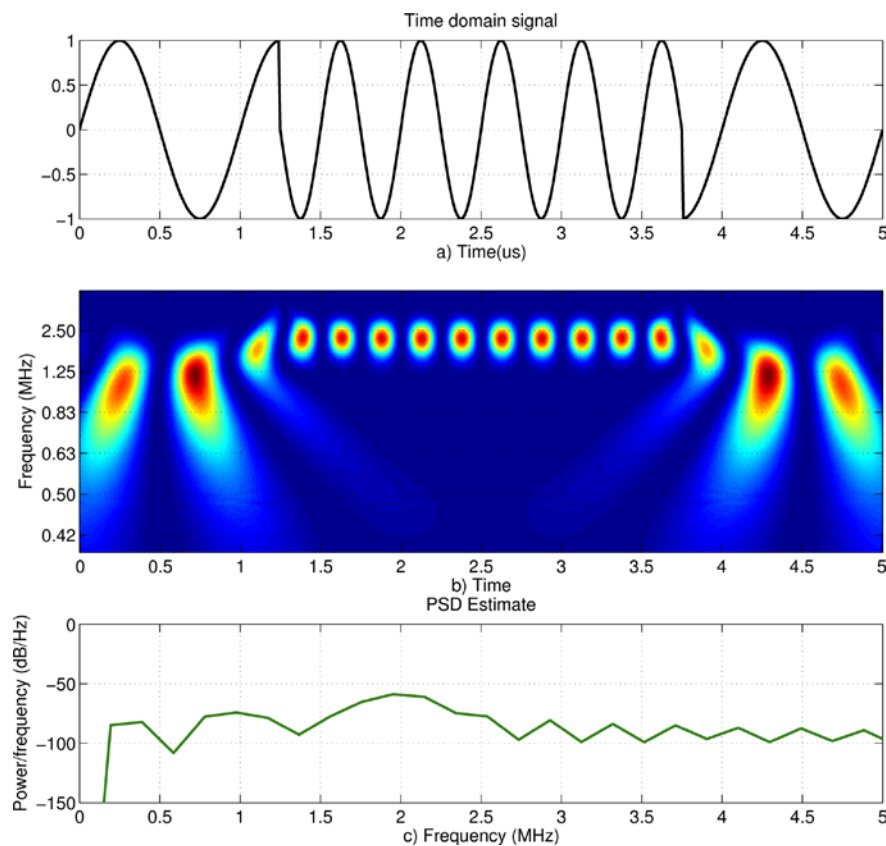


Figure 27. A synthetic signal consisting of two sinusoids ($f_1=1\text{MHz}$, $f_2=2\text{MHz}$) (a), its scalogram (b), and its Fourier-based spectral estimation (c).

The scales-frequencies equivalence approximation (SF diagram) (see Figure 28d for an example applied to a measured current pulse) can be obtained from the wavelet tree decomposition by associating the center frequency of each decomposition level to an equivalent frequency.

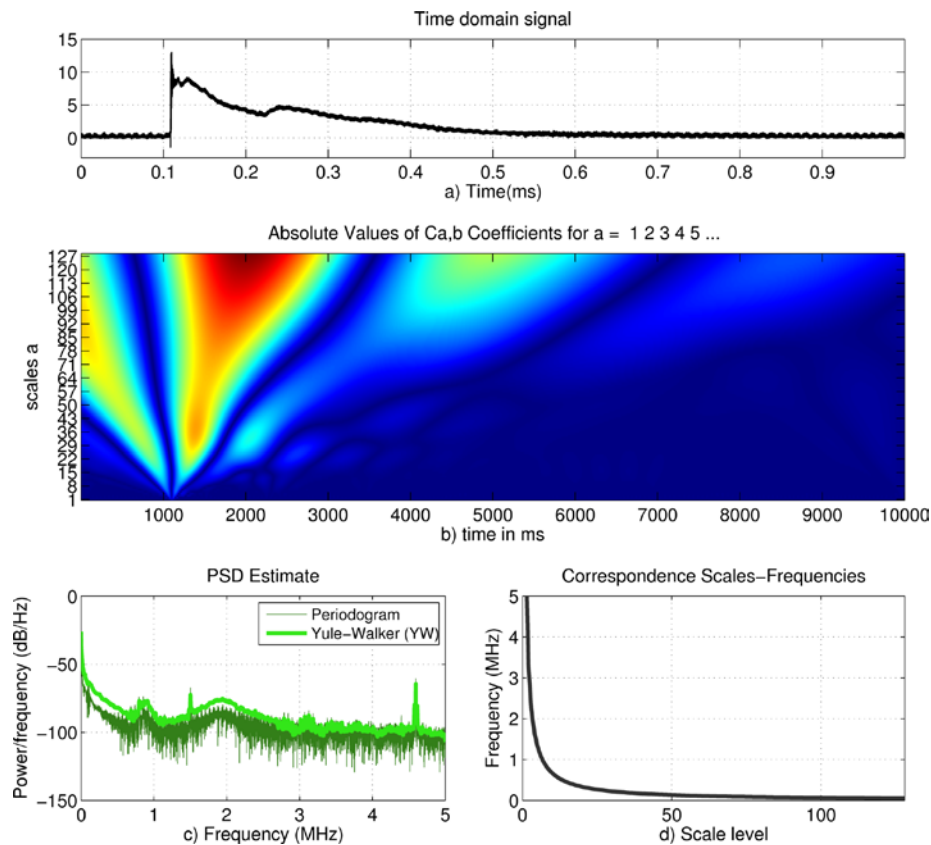


Figure 28. Wavelet spectral estimation of a current pulse. (a) measured time domain signal, (b) scalogram, (c) Fourier-based spectral estimation and, (d) the correspondence between wavelet scales and frequencies based on a Morlet kernel wavelet via a SF diagram.

The scalogram on the figure shows clearly the instant at which the peak current occurs and its associated low scale (high frequency) content but also a low frequency wave (the overall structure of the pulse) that, in this case, can be assimilated to multiple Morlet low frequency wavelets. These power spectrum figures for current pulses are comparable to those obtained by Miranda, Sharma and Cooray [38, 41].

8.4.7 Wavelet Estimation of the Resonance Frequencies

One interesting application of wavelets is the estimation of resonances frequencies in the measured waveforms, given that the analysis should be done on short time windows, limited to the duration of the current risetime or the current derivative signal. Figure 29 presents a superimposed plot of several current and current derivative signals for the early times (about 3

microseconds). We can distinguish a ringing phenomenon with a frequency of about 2 to 2.5 MHz. Currently, the origin of this high frequency oscillation is unknown. It could be related to the transient process along the tower structure, and/or the attachment process between the descending dart leader and a connecting leader starting from the top of the tower. It is worth noting that similar oscillations have been observed at Gaisberg and Peissenberg instrumented towers (G. Diendorfer, personal communication).

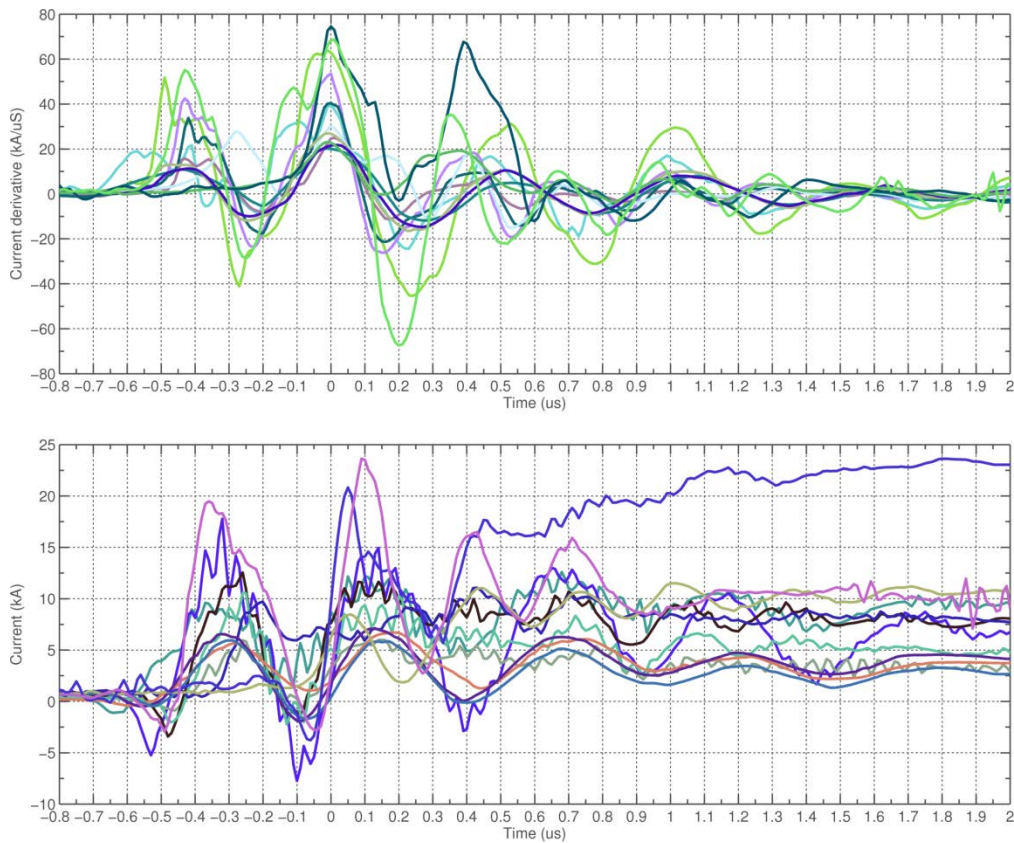


Figure 29. Superposition of several current derivative (up) and current signals (down).

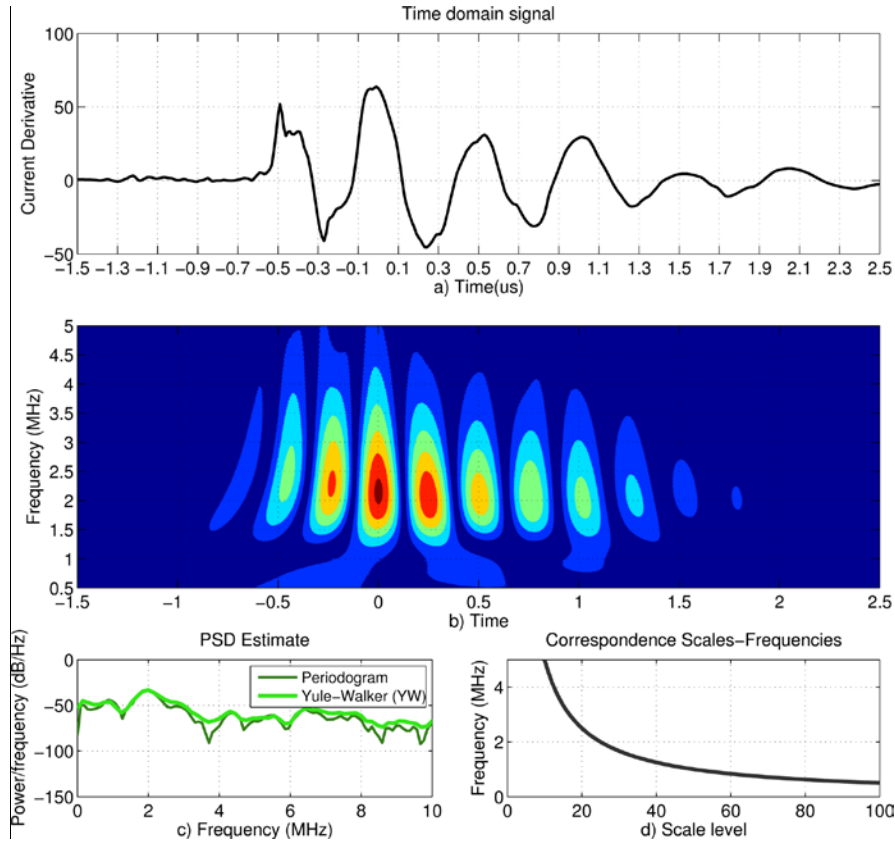


Figure 30. Wavelet spectral estimation of a current derivative signal. (up) time signal (middle) scalogram (down) Fourier-based spectral estimation and the correspondence between wavelet scales and frequencies based on a Morlet kernel wavelet via SF diagram.

8.4.8 Wavelet Filtering

Wavelet filtering technique can be achieved by applying a threshold to the decomposition coefficients and then reconstructing the signal from them [42]. This is equivalent to a low-pass filtering; however, more complex schemes can be considered by changing the weight in different decomposition levels [43]. The selected wavelet filter is based on algorithms used for lightning signal denoising [44, 45] and the assumed noise estimation parameters were obtained in Section 8.3.14.

A representative example is presented in Figure 31 where it can be seen that the wavelet filter is able to reduce the noise while keeping the fast details of the signal.

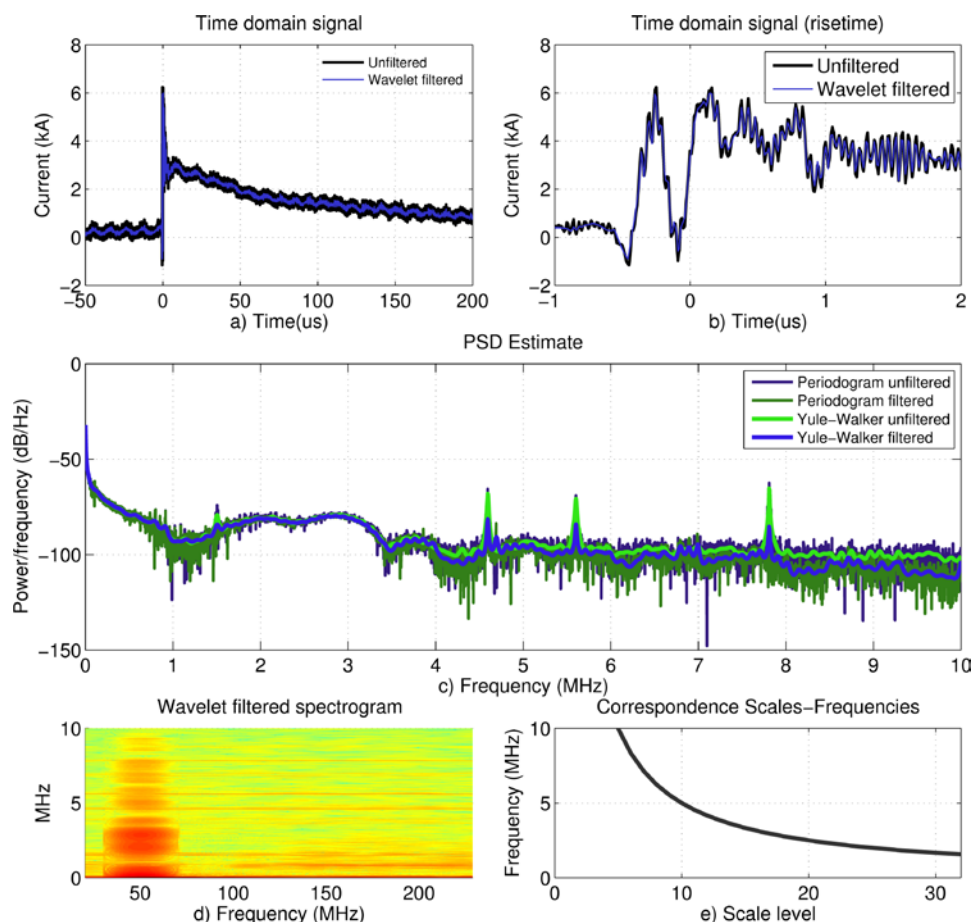


Figure 31. Wavelet filtering of a measured current signal. (a) time signal (b) detail of the rise time (c) Spectral estimation comparison of filtered and wavelet filtered (d) spectrogram (e) correspondence scales-frequencies via SF diagram

8.4.9 Wavelet Baseline Detection (DC Removal)

For positive and negative pulses, the baseline detection algorithm should allow to detect the DC components in a robust way. The idea of wavelet-based baseline detection uses the decomposition levels associated with frequencies close to DC, retrieved via the higher-order decomposition levels. A bi-orthogonal wavelet was used for this purpose to avoid time delays [39]. The decomposition level was chosen according to a scale-frequency (SF) diagram (See for example Figure 32) to keep frequencies less than 0.5Hz. The baseline detection algorithm was used as a stage in other DSP operations and it can be applied either to the entire flash or single pulses. An example of the DC estimation and removal is depicted on Figure 32.

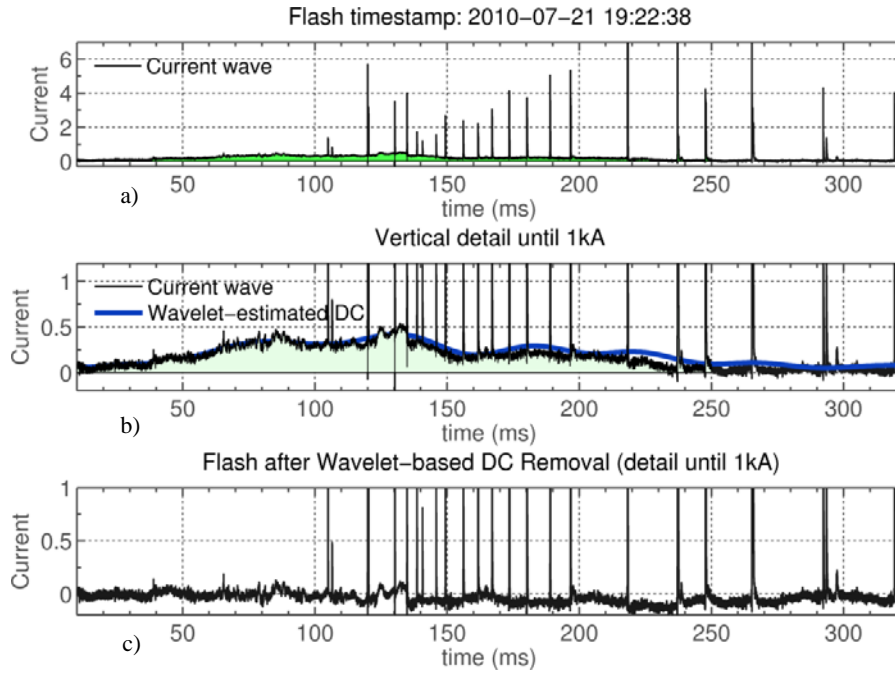


Figure 32. Wavelet-based DC estimation algorithm (a) current time signal with shadowed DC content (b) detail of the first kA with the superimposed estimation curve (c) result of the DC removal.

8.5 Pulse Classification Algorithms

Segmentation of entire flashes into pulses is required in order to identify each pulse and extract their statistical parameters. Consider the current pulse presented in Figure 33a where we can define three pulse regions as illustrated in the figure.

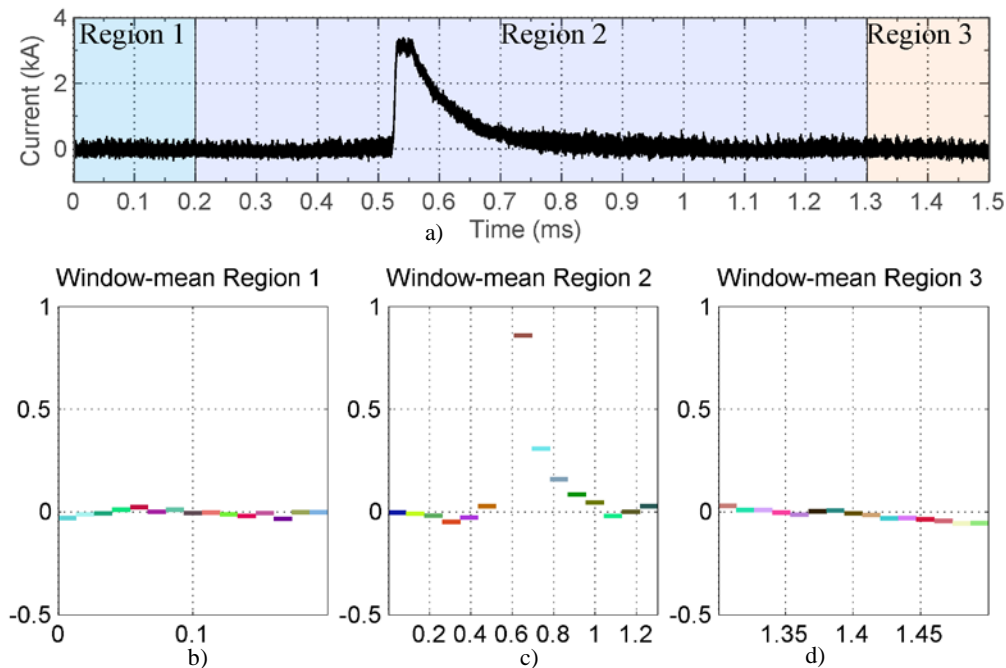


Figure 33. Current pulse definition (a) Overall pulse with shadowed current pulse regions (b,c,d) Test of the stationarity of the mean in different regions. The colors are for illustration purposes only and indicate the length of each segment.

In the first region, we have a stationary signal (noise level). The second region corresponds to the main pulse. Finally the third region where the main pulse has completely decayed and the signal is again stationary.

8.5.1 Stationarity Test

A series can be considered stationary if different windows or segments of the series have equal statistic moments. The segments could be arbitrary within the window length, as long as the number of data is sufficient to be statistically significant. Stationarity test can be done in different ways, among which

- by measuring means and variances in different windows and comparing them (non-parametric tests), or
- by plotting the autocorrelation versus offset (correlogram) and verifying that it decays to zero [10].

The first method is illustrated in Figure 33b where it is seen that for the middle region, the mean value changes considerably whereas in the other regions, it remains nearly constant over the whole region. This method, although graphical and easy to implement, is in general time consuming over large datasets.

A more rigorous way of evaluating stationarity is based on the evaluation of a hypothesis test with a given rejection/acceptation ratio. Among the available tests (e.g., unit root [46], Dickey-Fuller [47], KPSS test [48]), a Dickey-Fuller test was selected and implemented because it allows testing the stationarity of the mean. The stationarity test is implemented into the SENDIS software, in the form of a function in the flash segmentation toolset.

8.5.2 Semi-supervised Segmentation

The segmentation of each flash is performed in a semi-supervised manner, using algorithms that give an initial approximation for the identification of the pulse regions (in terms of start and stop times), and then the user is asked to check each pulse interval verifying the stationarity of the first and last regions. This minimizes the risk of misclassification and eases the analysis and processing of the data by establishing a library of pulses that can be navigated through and analyzed with full resolution and improved speed rather than processing the entire dataset. Furthermore, the detected pulses are embedded into an information packet, associated with a vector of logical and numerical properties that allows extracting each pulse parameters and obtaining statistical data. The segmentation algorithms

will be detailed in the following subsections. An example of the results of the segmentation process is presented in Figure 34.

8.5.3 Threshold Segmentation

A simple and fast segmentation algorithm consisting of setting a threshold after filtering and DC removal is implemented in order to find the intersection points between a given threshold and each current pulse (see Figure). The obtained points are then augmented (a value is added and subtracted to the left and right points) in order to obtain a bounding box for each pulse (Figure 35d).

The threshold segmentation algorithm is very efficient in terms of running time for large datasets. However, it is not optimal when the pulses are different in length and demands from the user many adjustments to make sure that each pulse stationarity criteria is fulfilled. A more advanced algorithm for detecting the pulse start and end points was developed and will be described in the next subsection. The threshold technique is available also as a tool in the developed software.

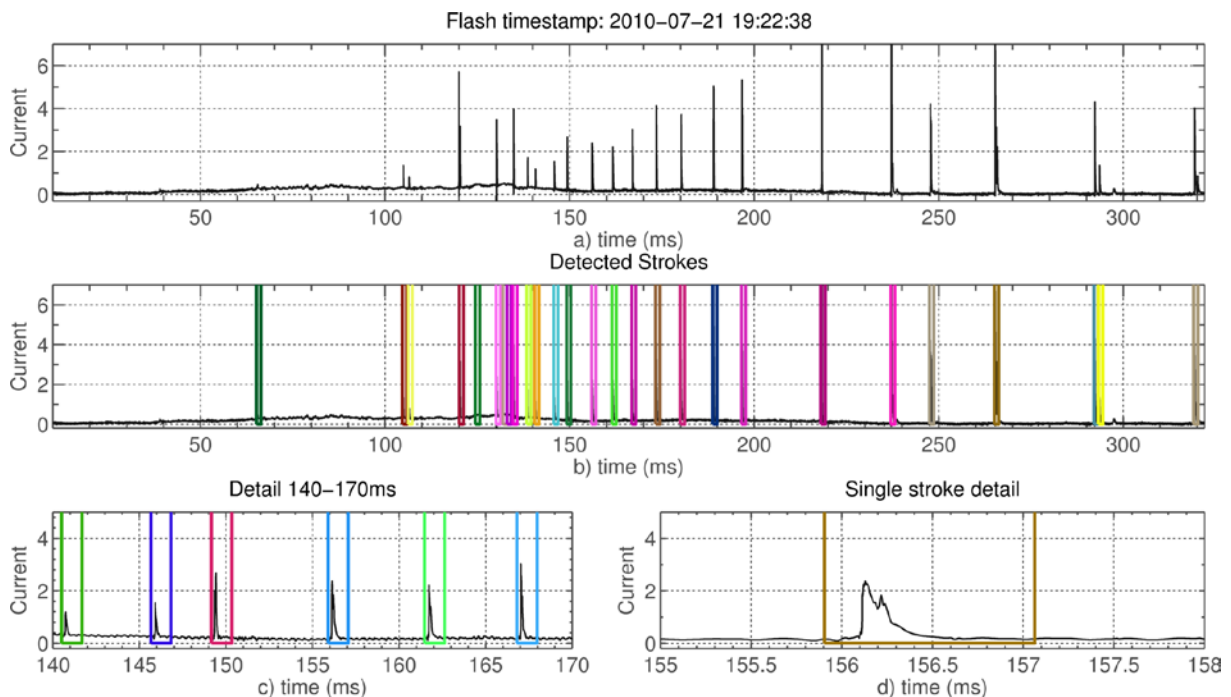


Figure 34. Segmentation of a lightning flash current waveform. (a) Measured waveform. (b) Detected pulse regions. (c) and (d) expanded views of detection pulse regions.

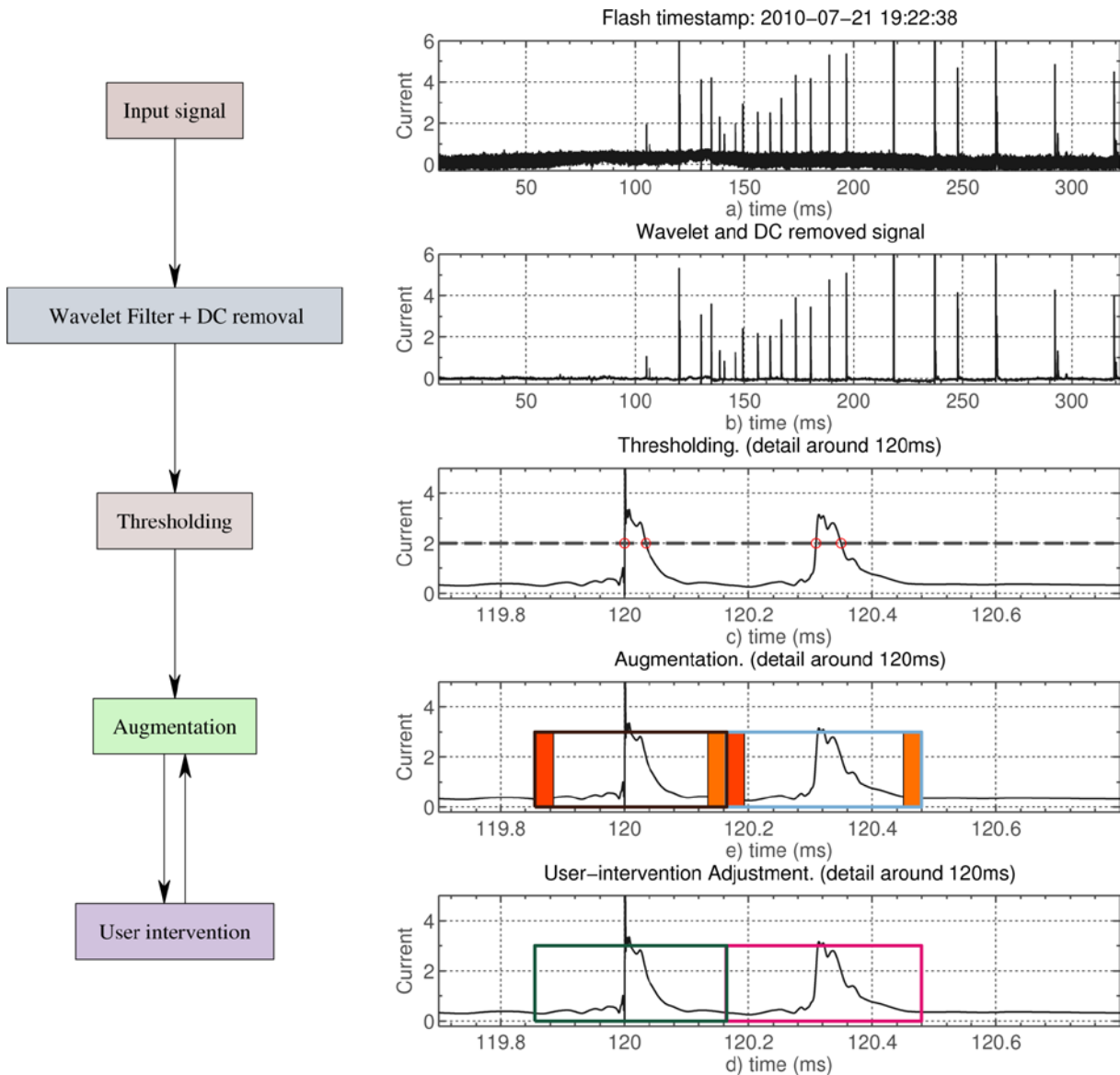


Figure 35. Threshold segmentation. (a) Measured lightning current waveform. (b) Filtered and DC-removed signal, (c) Thresholding. (d) Augmentation. (e) Adjustment by user.

8.5.4 Broken-Sticks Segmentation

A synthetic piecewise signal with noise is presented in Figure 36a, the underline function consists of two first order polynomials $y_1 = t + 1$, $0 \leq t < 5$ and $y_2 = 3t - 9$, $5 \leq t < 10$. This constitutes a typical case when a single regression curve cannot estimate accurately the underlying model. For this case, the identification problem can be written as finding the coefficients of

$$\begin{aligned} \tilde{y}_1 &= a_1 t + b_1, & 0 \leq t < c \\ \tilde{y}_2 &= a_2 t + b_2, & c \leq t < 10 \end{aligned}$$

An optimization algorithm can easily find the solution when the change parameter c is known (the solution is depicted in Figure 36b). In this case, with a small extra computational effort,

the algorithm can also find a good approximation when the change parameter is unknown. Note, however, that for each additional linear regression region (or ‘stick’), three new unknown variables are added, which represent another extra computational effort [49-51].

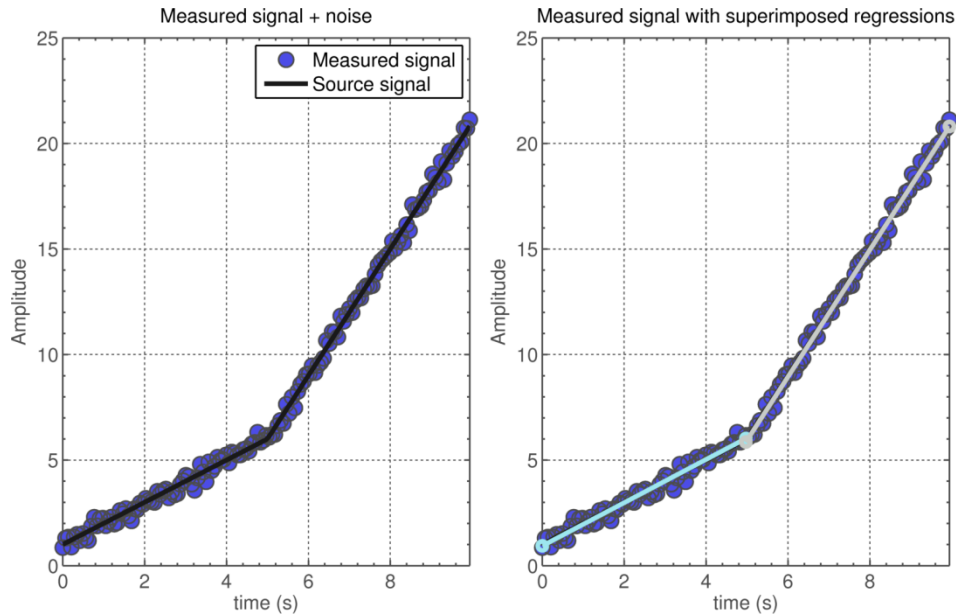


Figure 36. Piecewise regression (a) model and measured signal (b) estimated model

The interest in having local regressions for lightning current signals is the possibility of detecting long valleys between successive strokes for classification purposes. An efficient algorithm would allow the detection of pulses with variable lengths as found in real measurements.

A possible solution is to use bottom-up regression [18, 52]: the whole signal is divided in small windows, over which local regressions are calculated. Local adjacent regressions are then compared in terms of their respective variances. If the difference is smaller than a given threshold, the adjacent regression sticks are merged into a new one.

A parallel implementation of this region growing algorithm was developed which works faster over the flash dataset and gives, in general, better results when compared with basic threshold segmentation. An example of the calculated local regressions output previous to the sticks merging is displayed in Figure 37b. In this case, after the bottom-up merging procedure was over, the two linear segments were recovered.

An example of broken-sticks based classification on a flash data is shown in Figure 38. The last step also involves the user intervention evaluating the stationarity criteria over the classified candidate pulses.

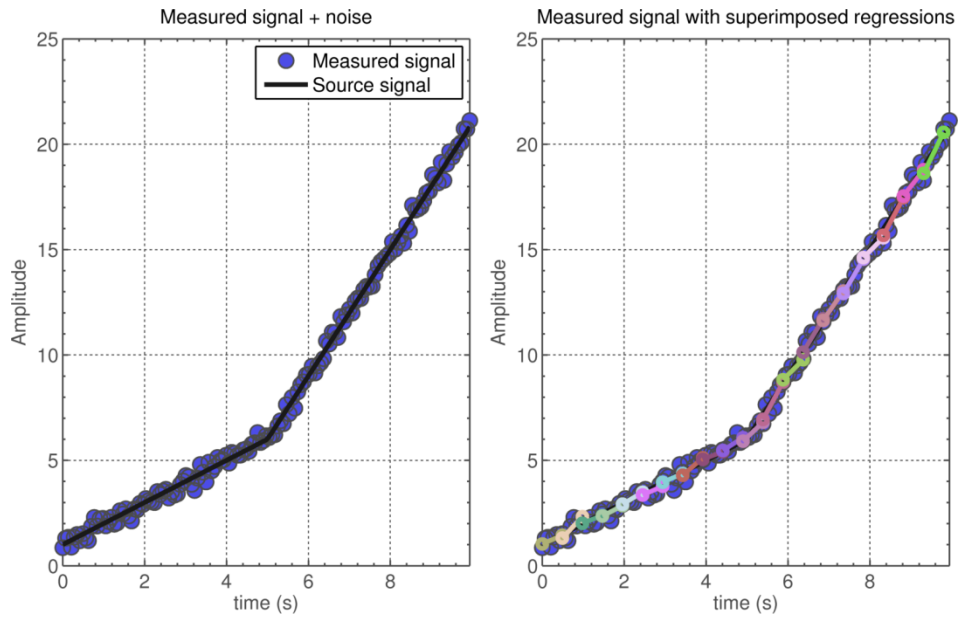


Figure 37. Piecewise regression (a) model and measured signal (b) result previous to segment merging.

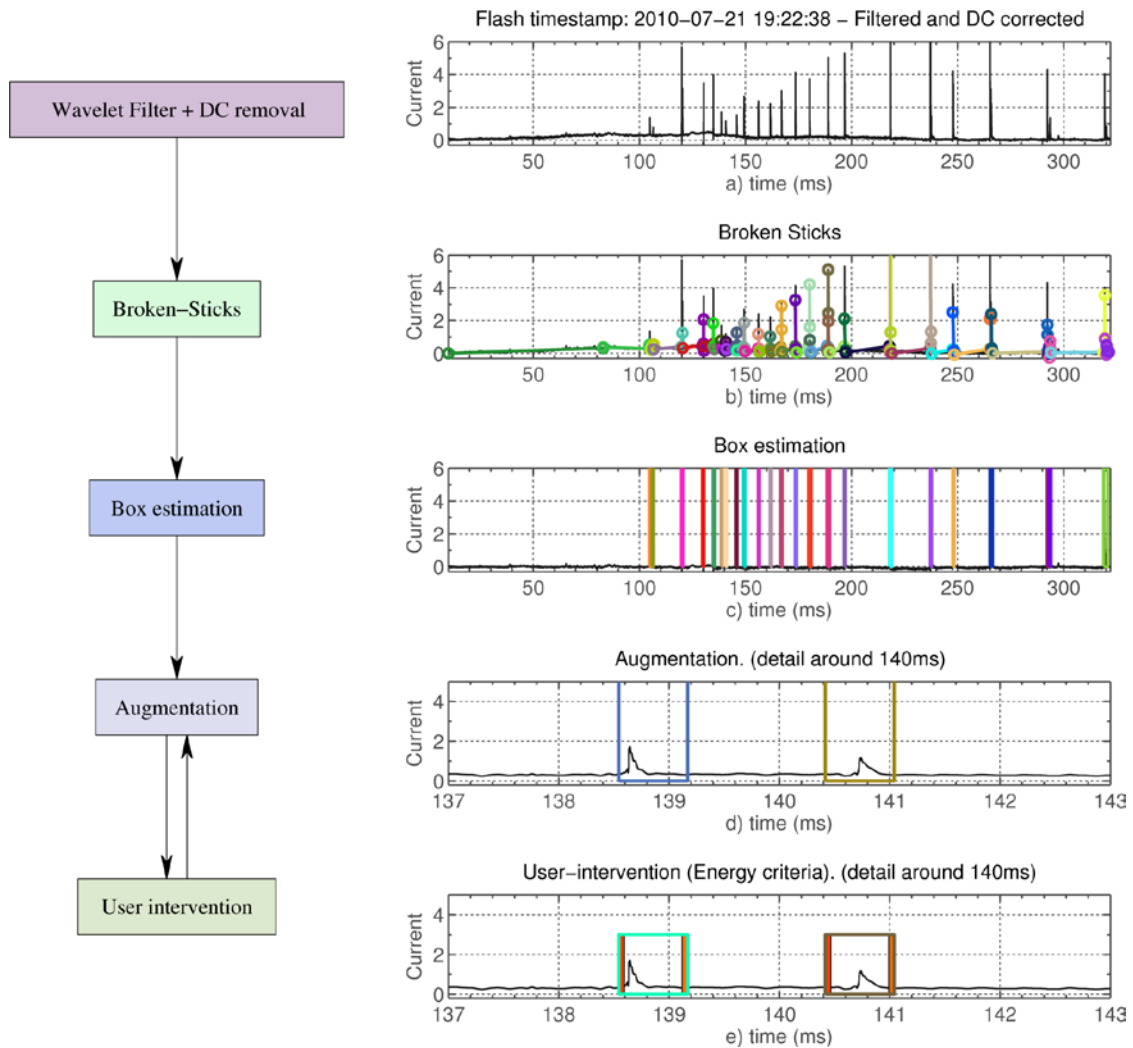


Figure 38. Broken-sticks segmentation. Detail of the steps. (a) Flash current waveform, (b) broken sticks, (c) box estimation, (d) augmentation, and (e) user adjustment.

8.6 Current Waveform Reconstruction

As shown through the spectral analysis, measured lightning currents are characterized by a frequency spectrum extending from DC to a few MHz. While broadband resistive shunts (e.g. [53]) represent an ideal solution for the measurement of lightning currents as their output is a faithful reproduction of the current associated with various phases of a lightning discharge, such a solution was not possible in the case of the Säntis Tower given that modifications of the tower structure were not permitted. Although Rogowski coils can, in principle, have a frequency response down to the Hz or even mHz region and they should be able to record initial continuing currents associated with upward flashes (see i.e. [54]), their high frequency response is limited by the size of the sensor and by its resonance frequency, which might be as low as some hundreds of kHz [18]. As a result, the current rise time and time-derivative might be affected by the high frequency shortcomings of Rogowski coils.

In order to overcome the limited high frequency response of the Rogowski coils, the B-dot sensor signals were used. These have been shown to be very accurate for the measurement of the early-time response of the current derivative. Assuming proportionality between magnetic field and current, the current is obtained by numerical integration of the B-Dot sensor output. The effectiveness of the simultaneous use of Rogowski coils and B-dot sensors for the measurement of lightning currents was demonstrated through laboratory tests carried out in the high voltage laboratory of the Swiss Federal Institute of Technology, EPFL [18].

An algorithm was developed and used for the reconstruction of the impulse current signal from the B-Dot and Rogowski signals (see block diagram shown in Figure 39). The Rogowski coil signal is transformed in the frequency domain by applying an FFT and filtered using a 100 kHz low frequency ZPF Chebyshev Type II filter (described in Section 8.4). This cut-off frequency removes the measured resonance frequency of the Rogowski coils (1.2 MHz [18]). The B-dot sensor signal is integrated before being transformed into the frequency domain and filtered using a 100 kHz high-pass filter (ZPF Chebyshev type II). The two signals are then combined and converted back into the time domain. This approach was tested using different waveforms measured simultaneously by the two systems and found to be very stable. Figure 39 shows an example of waveforms recorded by the Rogowski coil and the B-dot sensor associated with a return stroke in an upward negative flash. An expanded view of the initial 10 μ s of the pulses is shown in the time domain figures. It can be seen that the early time response of the reconstructed current is essentially determined by the B-dot sensor and it does not show the oscillatory behavior of the Rogowski coil which is presumably due to the coil

resonances [18]. On the other hand, the late time behavior of the reconstructed signal follows that of the Rogowski coil.

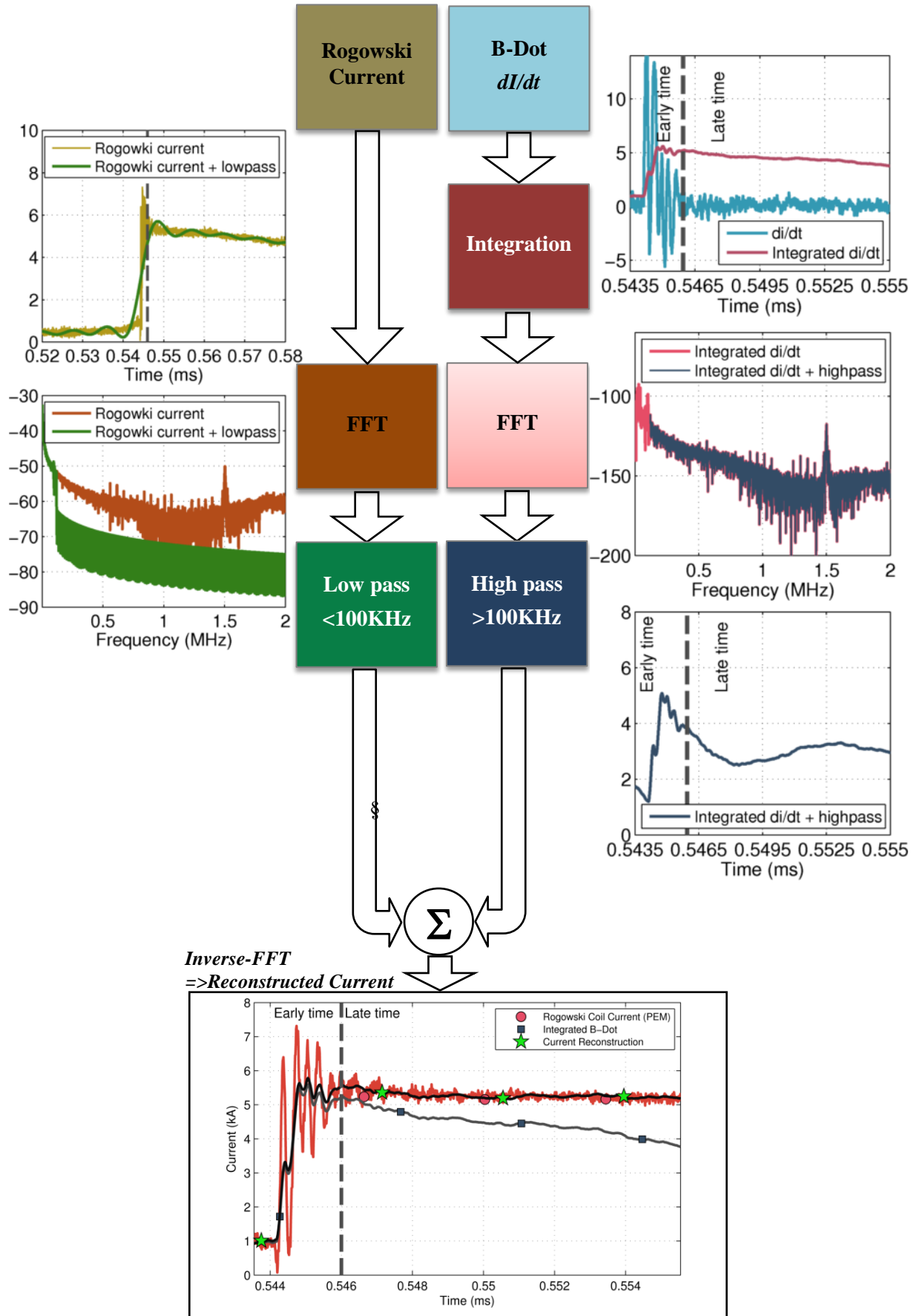


Figure 39. Current Reconstruction Algorithm. Detail of the steps.

References

- [1] C. Romero, A. Rubinstein, M. Paolone, F. Rachidi, M. Rubinstein, P. Zweiacker, *et al.*, "Instrumentation of the Sântis Tower in Switzerland for lightning current measurements," *International Journal of Plasma Environmental Science & Technology*, vol. 4, pp. 79-85, 2010.
- [2] V. A. Rakov, "Transient response of a tall object to lightning," *IEEE Transactions on Electromagnetic Compatibility*, vol. 43, pp. 654-61, 2001.
- [3] D. Pavanello, F. Rachidi, J. L. Bermudez, M. Rubinstein, and C. A. Nucci, "Contribution of the "Turn-On Term" to the Electromagnetic Field Radiated by Lightning to Tall Structures," in *2003 International Workshop on EM Radiation from Lightning to Tall Structures*, Bologna, Italy, 2003, p. 2.
- [4] F. Rachidi, W. Janischewskyj, A. M. Hussein, C. A. Nucci, S. Guerrieri, B. Kordi, *et al.*, "Current and electromagnetic field associated with lightning return strokes to tall towers," *IEEE Transactions on Electromagnetic Compatibility*, vol. 43, pp. 356-367, August 2001 2001.
- [5] J. L. Bermudez and F. Rachidi, "Determination of far radiated field from a lightning return stroke to a tall tower," in *Internal Rapport EPFL-DE-LRE-2001/A*, Swiss Federal Institute of Technology, Lausanne, Switzerland, 2001.
- [6] J. L. Bermudez, M. Rubinstein, F. Rachidi, F. Heidler, and M. Paolone, "Determination of Reflection Coefficients at the Top and Bottom of Elevated Strike Objects Struck by Lightning," *Journal of Geophysical Research*, vol. 108, pp. 4413, doi: 10.1029/2002JD002973, 2003.
- [7] A. Mosaddeghi, D. Pavanello, F. Rachidi, and M. Rubinstein, "Electric and Magnetic Fields at Very Close Range from a Lightning Strike to a Tall Object," in *19th International Zurich Symposium on Electromagnetic Compatibility*, Singapore, 2008.
- [8] R. J. Sasiela, *Electromagnetic Wave Propagation in Turbulence: Evaluation and Application of Mellin Transforms*: SPIE, 2007.
- [9] A. C. V. Saraiva, M. M. F. Saba, O. Pinto, Jr., K. L. Cummins, E. P. Krider, and L. Z. S. Campos, "A comparative study of negative cloud-to-ground lightning characteristics in São Paulo (Brazil) and Arizona (United States) based on high-speed video observations," *J. Geophys. Res.*, vol. 115, p. D11102, 2010.
- [10] A. M. Mathai, *A handbook of generalized special functions for statistical and physical sciences*: Clarendon Press, 1993.
- [11] K. Takezawa, *Introduction to Nonparametric Regression*: John Wiley & Sons, 2005.
- [12] O. I. Marichev, *Handbook of integral transforms of higher transcendental functions: theory and algorithmic tables*: E. Horwood, 1983.
- [13] S. J. Orfanidis, *Optimum signal processing: an introduction*: Macmillan, 1988.
- [14] F. Heidler and J. Cvetić, "A class of analytical functions to study the lightning effects associated with the current front," *European Transactions on Electrical Power*, vol. 12, pp. 141-150, 2002.
- [15] R. G. Lyons, *Understanding Digital Signal Processing (2nd Edition)*: Prentice Hall, 2010.
- [16] A. V. Oppenheim and R. W. Schaffer, *Discrete-time signal processing*: Prentice Hall, 2010.

-
- [17] C. E. Baum, L. Carin, and A. P. Stone, *Ultra-Wideband, Short-Pulse Electromagnetics 3*: Plenum Press, 1997.
- [18] C. Romero, A. Mediano, A. Rubinstein, F. Rachidi, M. Rubinstein, M. Paolone, *et al.*, "Measurement of lightning currents using a combination of Rogowski coils and B-Dot sensors," in *30th International Conference on Lightning Protection (ICLP)*, Cagliari, Italy, 2010.
- [19] *Biostatistics: A Foundation for Analysis in the Health Sciences 8E with SPSS Student Software Version 16. 0*: John Wiley & Sons, Incorporated, 2008.
- [20] L. Marple, "High resolution autoregressive spectrum analysis using noise power cancellation," in *Acoustics, Speech, and Signal Processing, IEEE International Conference on ICASSP '78.*, 1978, pp. 345-348.
- [21] P. Chowdhuri, J. G. Anderson, W. A. Chisholm, T. E. Field, M. Ishii, J. A. Martinez, *et al.*, "Parameters of lightning strokes: a review," *Power Delivery, IEEE Transactions on*, vol. 20, pp. 346-358, 2005.
- [22] P. Liatos and A. M. Hussein, "Characterization of 100-kHz noise in the lightning current derivative signals measured at the CN tower," *Electromagnetic Compatibility, IEEE Transactions on*, vol. 47, pp. 986-997, 2005.
- [23] J. F. Hauer, C. J. Demeure, and L. L. Scharf, "Initial results in Prony analysis of power system response signals," *Power Systems, IEEE Transactions on*, vol. 5, pp. 80-89, 1990.
- [24] T. Lobos, J. Rezmer, and J. Schegner, "Parameter estimation of distorted signals using Prony method," in *Power Tech Conference Proceedings, 2003 IEEE Bologna*, 2003, p. 5 pp. Vol.4.
- [25] H. Yingbo and T. K. Sarkar, "On SVD for Estimating Generalized Eigenvalues of Singular Matrix Pencil in Noise," in *Signals, Systems and Computers, 1990 Conference Record Twenty-Fourth Asilomar Conference on*, 1990, p. 931.
- [26] H. Zhou, G. Diendorfer, R. Thottappillil, H. Pichler, and M. Mair, "Characteristics of upward bipolar lightning flashes observed at the Gaisberg Tower," *J. Geophys. Res.*, vol. 116, p. D13106, 2011.
- [27] P. L. Lewin, T. N. Tran, D. J. Swaffield, and J. K. Hallstrom, "Zero-Phase Filtering for Lightning Impulse Evaluation: A K-factor Filter for the Revision of IEC60060-1 and -2," *Power Delivery, IEEE Transactions on*, vol. 23, pp. 3-12, 2008.
- [28] Z. Staroszczyk, "Correlative zero-phase fundamental component notch filter for power signals," in *Electrotechnical Conference, 2000. MELECON 2000. 10th Mediterranean*, 2000, pp. 587-590 vol.2.
- [29] J. O. Smith, *Introduction to Digital Filters: With Audio Applications*: W3K Publishing, 2007.
- [30] Y. C. Lim and C. C. Ko, "Forward-backward LMS adaptive line enhancer," *Circuits and Systems, IEEE Transactions on*, vol. 37, pp. 936-940, 1990.
- [31] F. Gustafsson, "Determining the initial states in forward-backward filtering," *Signal Processing, IEEE Transactions on*, vol. 44, pp. 988-992, 1996.
- [32] E. L. Crow and K. Shimizu, *Lognormal Distributions: Theory and Applications*: M. Dekker, 1988.
- [33] E. T. Lee and J. W. Wang, *Statistical Methods for Survival Data Analysis*: J. Wiley, 2003.
- [34] I. M. Imiantov and E. V. Chubarina, *Electricity of the free atmosphere: by I.M. Imyanitov and E.V. Chubarina. Translated from Russian*, 1967.
- [35] R. Lhermitte and E. Williams, "Cloud electrification," *Rev. Geophys.*, vol. 21, pp. 984-992, 1983.

-
- [36] E. R. Williams, "Large-Scale Charge Separation in Thunderclouds," *J. Geophys. Res.*, vol. 90, pp. 6013-6025, 1985.
- [37] C. Romero, "Internal Rapport: On the Lognormal Probability Plot," 2012.
- [38] H. Zhou, G. Diendorfer, R. Thottappillil, H. Pichler, and M. Mair, "Characteristics of upward positive lightning flashes initiated from the Gaisberg Tower," *J. Geophys. Res.*, vol. 117, p. D06110, 2012.
- [39] J. M. Chambers, *Graphical methods for data analysis*: Wadsworth International Group, 1983.
- [40] S. Miller and D. Childers, *Probability and Random Processes: With Applications to Signal Processing and Communications*: Elsevier Science, 2012.
- [41] I. MathWorks, *Curve fitting toolbox: for use with MATLAB® : user's guide*: MathWorks, 2002.
- [42] J. M. Wallace and P. V. Hobbs, *Atmospheric Science: An Introductory Survey*: Elsevier Academic Press, 2006.
- [43] W. P. Winn, G. D. Aulich, S. J. Hunyady, K. B. Eack, H. E. Edens, P. R. Krehbiel, *et al.*, "Lightning leader stepping, K changes, and other observations near an intracloud flash," *J. Geophys. Res.*, vol. 116, p. D23115, 2011.
- [44] C. Romero, M. Paolone, F. Rachidi, M. Rubinstein, A. Rubinstein, G. Diendorfer, *et al.*, "Preliminary comparison of data from the Sântis Tower and the EUCLID lightning location system," in *Lightning Protection (XI SIPDA), 2011 International Symposium on*, 2011, pp. 140-145.
- [45] R. A. Houze, *Cloud Dynamics*: Academic Press, 1994.
- [46] A. Bhargava, "On the Theory of Testing for Unit Roots in Observed Time Series," *The Review of Economic Studies*, vol. 53, pp. 369-384, 1986.
- [47] J. Y. Park, "Bootstrap Unit Root Tests," *Econometrica*, vol. 71, pp. 1845-1895, 2003.
- [48] K. Denis, C. B. P. Peter, and S. Peter, "Testing the Null Hypothesis of Stationarity Against the Alternative of a Unit Root: How Sure Are We That Economic Time Series Have a Unit Root?," Cowles Foundation for Research in Economics, Yale University May 1991.
- [49] E. J. Kademan, *Piecewise linear regression through random partitioning*: University of Wisconsin--Madison, 1993.
- [50] M. C. Huang, *Piecewise linear tree-structured regression*: University of Wisconsin--Madison, 1989.
- [51] C. de Boor, *A Practical Guide to Splines*: Springer, 2001.
- [52] E. Keogh, S. Chu, D. Hart, and M. Pazzani, "An online algorithm for segmenting time series," in *Data Mining, 2001. ICDM 2001, Proceedings IEEE International Conference on*, 2001, pp. 289-296.
- [53] G. Diendorfer, H. Pichler, and M. Mair, "Some Parameters of Negative Upward Initiated Lightning to the Gaisberg Tower (2000 - 2007)," *IEEE Transactions on Electromagnetic Compatibility*, 2009.
- [54] A. M. Hussein, M. Milewski, E. Burnazovic, and W. Janischewskyj, "Current Waveform Characteristics of CN Tower Negative and Positive Lightning," in *XInternational Symposium on Lightning Protection (SIPDA)*, Curitiba, Brazil, 2009, pp. 451-456.

Curriculum Vitae

Carlos Romero
Born on June 16, 1978 in Bogotá (Colombia)
Colombian
Married

Education

- 2001 B.Sc. degree in Electronics Engineering from the 'Universidad Distrital', Colombia
2006 M.Sc. degree in Electronics Engineering from the 'Universidad de los Andes', Colombia

Professional experience

- 2007 Engineering Team Leader, Colombian Satellite Project
2002-2006 Assistant Professor 'Universidad Nacional' Colombia, Assistant Professor 'Universidad Central' Colombia

Distinctions

- Sept. 2012 Diploma for high quality presentation of the paper "*Characteristics of Positive and Bipolar Lightning Flashes Recorded on the Sántis Tower in 2010 and 2011*" at ICLP 2012 International Conference on Lightning Protection - Vienna, Austria

Publications

Journal papers

- 2012 Romero, C.; Paolone, Mario; Rubinstein, Marcos; Rachidi-Haeri, Farhad; Rubinstein, Abraham; Diendorfer, Gerhard; Schulz, Wolfgang; Daout, Bertrand; Kälin, Armin, 'A system for the measurements of lightning currents at the Sántis Tower' Electric Power Systems Research (ISSN: 0378-7796), vol. 82, num. 1, p. 34-43 Elsevier, 2012

Romero, C., Mediano, Arturo; Rubinstein, Abraham; Rachidi, Farhad; Rubinstein, Marcos; Paolone, Mario; Mora, Nicolas; Pavanello, Davide; Zweiacker, Pierre; Daout, Bertrand 'Measurement of lightning currents using a combination of Rogowski coils and B-Dot sensors' 2012, Journal of Lightning Research, vol. 4, num. 1, p. 71-77, 2012.

2010 Romero, C., A. Rubinstein, M. Paolone, F. Rachidi, M. Rubinstein, P. Zweiacker, and B. Daout. Instrumentation of the Säntis Tower in Switzerland for lightning current measurements. International Journal of Plasma Environmental Science & Technology, 4(1):79-85, 2010.

Conference proceedings

2012 Romero, C., Marcos Rubinstein, Mario Paolone, Farhad Rachidi, Vladimir A. Rakov, Davide Pavanello. 'Some Characteristics of Positive And Bipolar Lightning Flashes Recorded on the Säntis Tower in 2010 and 2011'. on 31st International Conference on Lightning Protection. 2012.

Romero, C., Mario Paolone, Marcos Rubinstein, Farhad Rachidi, Davide Pavanello, Dave Giri. 'A Statistical Analysis on the Risetime of Lightning Current Pulses in Negative Upward Flashes Measured at Säntis Tower'. on 31st International Conference on Lightning Protection. 2012.

H.M.Manesh, G. Lugin, R. Razzaghi, C. Romero, F. Rachidi and M. Paolone, F. Rachidi, 'A New Method To Locate Faults In Power Networks Based On Electromagnetic Time Reversal' on 13th IEEE International Workshop on Signal Processing Advances in Wireless Communications 2012.

2011 Romero, C. Paolone, M. , Rachidi, F. ; Rubinstein, M. , Rubinstein, A. , Diendorfer, G. , Schulz, W. Bernardi, M. , Nucci, C.A. 'Preliminary comparison of data from the Säntis Tower and the EUCLID lightning location system' Conference: Lightning Protection (XI SIPDA), 2011 International Symposium on Date of Conference: 3-7 Oct. 2011 On Page(s): 140 - 145

Romero, C., M. Paolone, F. Rachidi, M. Rubinstein, V. A. Rakov et al. 'Current Waveforms Associated with Positive Flashes Recorded on the Säntis Tower in Summer 2010'. XIth International Symposium on Lightning Protection (SIPDA), Fortaleza, Brazil, 2011.

Romero, C., A. Rubinstein, M. Paolone, F. Rachidi and M. Rubinstein et al. 'First Direct Lightning Current Measurements on the Newly Instrumented Säntis Tower in Switzerland'. 29th International PIERS Symposium, Marrakesh, Morocco, 2011.

2010 Romero, C., A. Rubinstein, M. Paolone, F. Rachidi, M. Rubinstein, P. Zweiacker, and B. Daout, "Instrumentation of the Säntis Telecommunication Tower in Switzerland for Lightning Current Measurement", 2010 American Electromagnetics International Symposium AMEREM, July 5-9, Ottawa, Canada.

Romero, C., A. Mediano, A. Rubinstein, F. Rachidi, M. Rubinstein, M. Paolone, N. Mora, D. Pavanello, P. Zweiacker, and B. Daout, "Measurement of lightning currents using a combination of Rogowski coils and B-Dot sensors", 30th International Conference on Lightning Protection (ICLP), September 13-17, 2010, Cagliari, Italy.

M. Rubinstein, C. Romero, F. Rachidi, A. Rubinstein and F. Vega. 'A Two-Station Lightning Location Method based on a Combination of Difference of Time of Arrival and Amplitude Attenuation'. 2010 Asia-Pacific Symposium on Electromagnetic Compatibility, Beijing, China, 2010

2009 M. Rubinstein, C. Romero, F. Rachidi and F. Vega. 'Lightning Location by Relative Radiation Field Peak Attenuation'. 10th International Symposium on Lightning Protection, Curitiba, Brazil, 2009.

A. Rubinstein, C. Romero, M. Paolone, F. Rachidi and M. Rubinstein et al. '*Lightning measurement station on Mount Säntis in Switzerland*'. 10th International Symposium on Lightning Protection, Curitiba, Brazil, 2009.

2005 Romero, C., '*Fuzzy Control and Sliding-Mode Control in DC-DC Converters*', ISBN 958-33-6534-3 on Andean IEEE Conference 2005.

Romero, C., '*Digital Signal Processing System for human blink detection*', ISBN 958-33-8404-6. on Andean IEEE Conference 2005.

Supervised student projects

Master's projects

2012 Y. Liu, "*Relativistic Doppler Effect in Lightning Discharges*", EPFL, Jan 2012.

2011 L. El Ouali, "*Evaluation du Système Européen de Détection et de Localisation de la Foudre*", EPFL, June 2011.

2011 S. Chorowicz, "*Risetime Analysis of Säntis Tower Pulses*", EPFL, June 2011.

2009 B. Rioja, "*Design of Magnetic Sensors for the Measurement of Lightning Current at Säntis Tower*", EPFL, Dec 2009.